NUREG/CR–3816 (4 of 4)
SAND84–1072 (4 of 4)
R3, R7
Printed September 1985

Reactor Safety Research Quarterly Report October – December 1984 Volume 32

Reactor Safety Research Department 6420

Prepared by
Sandia National Laboratories
Albuquerque, New Mexico 87185 and Livermore, California 94550
for the United States Department of Energy
under Contract DE-AC04-76DP00789

Prepared for
U. S. NUCLEAR REGULATORY COMMISSION

Available from

Superintendent of Documents
U.S. Government Printing Office
Post Office Box 37082
Washington, D.C. 20013-7982

and

National Technical Information Service
Springfield, VA 22161

NUREG/CR-3816 (4 of 4)
SAND84-1072 (4 of 4)
Vol. 32
R3 and R7

REACTOR SAFETY RESEARCH QUARTERLY REPORT October-December 1984

Reactor Safety Research Program

Printed: August 1985

APPROVED:

Manager, Reactor Safety Research

Director, Nuclear Fuel Cycle Programs

Sandia National Laboratories
Albuquerque, NM 87185
Operated by
Sandia Corporation
for the
U.S. Department of Energy

Prepared for Division of Accident Evaluation
Office of Nuclear Regulatory Research
U.S. Nuclear Regulatory Commission
Washington, DC 20555
Under Memorandum of Understanding DOE 40-550-75
NRC FIN Nos.
(A-1016, A-1019, A-1030, D-1124, A-1181, A-1218, A-1227, A-1246, A-1263, A-1264, A-1335, A-1336, A-1340, A-1342, A-1383, A-1385, A-1390)

PREVIOUS DOCUMENTS IN SERIES

Reactor Safety Research Quarterly Report, January-March 1984, NUREG/CR-3816 (1 of 4), SAND84-1072 (1 of 4), Volume 29, Sandia National Laboratories, October 1984.

Reactor Safety Research Quarterly Report, April-June 1984, NUREG/CR-3816 (2 of 4), SAND84-1072 (2 of 4), Volume 30, Sandia National Laboratories, December 1984.

Reactor Safety Research Quarterly Report, July-September 1984, NUREG/CR-3816 (3 of 4), SAND84-1072 (3 of 4), Volume 31, Sandia National Laboratories, May 1985.

FOREWORD

Sandia National Laboratories is conducting, under the USNRC's sponsorship, phenomenological research related to the safety of commercial nuclear power reactors. The research includes experiments to simulate the phenomenology of accident conditions and the development of analytical models, verified by experiment, which can be used to predict reactor and safety systems performance and behavior under abnormal conditions. The objective of this work is to provide NRC requisite data bases and analytical methods to (1) identify and define safety issues, (2) understand the progression of risk-significant accident sequences, and (3) conduct safety assessments.

The collective NRC-sponsored effort at Sandia National Laboratories is directed at enhancing the technology base supporting licensing decisions.

CONTENTS

LIST OF FIGURES

LIST OF FIGURES (Continued)

LIST OF FIGURES (Continued)

LIST OF FIGURES (Continued)

LIST OF FIGURES (Continued)

LIST OF FIGURES (Continued)

LIST OF FIGURES (Continued)

LIST OF TABLES

ACRONYMS

ACRR	Annular Core Research Reactor
BCL	Battelle-Columbus Laboratory
BNL	Brookhaven National Laboratories
BWR	Boiling Water Reactor
CEA	Commisariat a L'Energie Atomique
CDA	Core Disruptive Accident
CMCI	Core Melt-Coolant Interaction
CMOT	Clad Motion Code
CORCON	Core/Concrete Interaction Code
DCC	Degraded Core Coolability
DC	Dry Capsule
DF	Damaged Fuel
DFR	Damaged Fuel Relocation
ECCS	Emergency Core Cooling System
EURATOM	European Atomic Energy Community
EXO-FITS	Outside of Fully Instrumented Test Sites
FCI	Fuel-Coolant Interaction
FITS	Fully Instrumented Test Site
FLAME	Flame Acceleration Measurements
HECTR	Hydrogen Event: Containment Transient Response
HEDL	Hanford Engineering Development Laboratory
HIPS	High Pressure Streaming
INEL	Idaho National Engineering Laboratory
INPO	Institute of Nuclear Power Operation
IRIS	Inductive Ring Susceptor Technique
KfK	Kernforschungszentrum Karlsruhe
LANL	Los Alamos National Laboratory
LCS	Limestone/Common Sand
LMF	Large Melt Facility
LMFBR	Liquid Metal Fast Breeder Reactor
LWR	Light Water Reactor
MELPROG	Melt Progression Code
NRC	Nuclear Regulatory Commission
NTS	Nevada Test Site
ORNL	Oak Ridge National Laboratory
PIE	Postirradiation Examination
PNC	Power Reactor and Nuclear Fuel Development Corporation
PRA	Probabilistic Risk Assessment
PWR	Pressurized Water Reactor
QUEST	Quantitative Uncertainty Evaluation for the Source Term
RSR	Reactor Safety Research
RPV	Reactor Pressure Vessel
S/A	Subassembly
SEALS	Steam Explosions at Large Scale
SHIP	Small-Scale High Pressure
SPIT	System Pressure Injection Test
STAR	Sandia Transient Axial Relocation
SWISS	Sustained Water Interactions with Stainless Steel
TMBDB	Thermal Margin Beyond Design Basis

TRAN	Transition Phase
TURC	Transient Urania Concrete
TWT	Transient Water Tests
ULOF	Unprotected Loss of Flow
UT	Ultrasonic Thermometer
VGES	Variable Geometry Experimental System

EXECUTIVE SUMMARY

1. CONTAINMENT LOADING AND RESPONSE

In the analysis of severe accidents, several scenarios lead to the release of molten-core material and the subsequent interactions involving molten fuel, coolant, structural material, potential in core retention systems, the reactor vessel, and the reactor cavity boundary. The present program seeks to identify the results of these interactions. The results also will be used to support model development for the containment code CONTAIN, the melt progression code MELPROG, and the phenomenological models CORCON and VANESA and to provide data for their verification.

1.1 Ex-Vessel Core Debris Interactions

1.1.1 The SWISS Test Series

The interaction of molten fuel, fuel cladding, and core structures with a concrete basemat has been recognized since the Reactor Safety Study as an important aspect of severe reactor accidents. Although the conditions necessary for such an interaction to take place are improbable, an assessment of the physical source terms resulting from the interaction is needed if a comprehensive evaluation of the risks posed to reactor containments are to be made. If containments should fail, core debris-concrete interactions will pose a fundamental source of radioactive release to the environment. Over the past several years, an intensive study of these core debris-concrete interactions has been sponsored at Sandia National Laboratories by the NRC's Office of Nuclear Regulatory Research.

The first sustained water interaction with stainless steel experiment (SWISS-1) was performed. This test consisted of an inductively heated molten pool of stainless steel interacting with concrete in which water was poured over the top of the resulting molten pool crust and investigated the effect of this water pool on the melt-concrete interaction.

The experimental results indicated a continuous steady erosion rate that was weakly coupled to the power generation rate for the duration of the test. Water addition showed no effect upon the erosion rate. This rate was attributed to the presence of a thick crust that effectively insulated steel melt from the water. A CORCON calculation indicated only half the erosion observed, implying the need for further code development and refinement.

1.1.2 The Hot Solid Test Series

Experiments and models for both molten core-concrete and hot solid-concrete interactions are examined to provide a better understanding of the transition between the two accident phases and how the results of the current effort might be incorporated into a single analytical tool that handles both.

The HSS-3 test was run to determine whether or not the geometry and diagnostics developed in steel/concrete interaction experiments could be applied to an experiment using UO_2 as the slug material.

The HSS-3 experiment was successful in producing and recording the axial penetration of hot solid UO_2 through a concrete basemat material. However, several design changes are indicated before a fully instrumented hot solids test can be run. Additional containment to facilitate measurements of water vapor and gas evolution is a first priority improvement and should be accomplished with the addition of a second ceramic sleeve outside of the alumina sleeve now used. Once the design changes are made, fully instrumented tests will be run using both steel and UO_2 for solid attack.

1.2 High-Pressure Melt Ejection and Direct Containment Heating

Several safety studies indicate that molten core debris can potentially be ejected into the reactor cavity if the reactor pressure vessel (RPV) fails while the primary system is at elevated pressure. Experiments have been performed to determine the influence of water in the reactor cavity during the ejection of the core debris. The safety analyses assume that the presence of water has an insignificant effect on the dispersal of debris into the containment region. This assumption presumes that the water is simply pushed out of the cavity as a slug, that is then followed by the debris. The test results confirm that the water is removed from the cavity, partly as a slug but the bulk of material is in the form of dispersed droplets. The creation of the drops is attributed to the same mechanisms that cause debris removal from the cavity during blowdown of the primary system, primarily particle entrainment by the high-velocity blowdown gases.

Pressure records from gauges installed in the cavity sidewall indicate relatively slow risetimes compared to energetic fuel-coolant interactions. Peak pressures on the order of 4 to 6 MPa are recorded in time intervals of 150 to 300 ms after melt entry into the water pool. Effervescing

gas and steam surrounding the melt probably prevent the intimate mixing of the debris and water necessary for a more energetic interaction. In both tests, the peak pressure may not have been attained due to premature failure of the cavity structure.

The rapidly developed relief paths may have prevented continued pressure increase. The energy transferred to the water is sufficient to completely destroy the concrete cavity and eject pieces weighing several kg up to 100 m from the test site.

The potential for direct heating of the atmosphere by the expelled debris may threaten the integrity of some containment structures. This scenario will be studied experimentally by developing a large simulated containment volume to contain the expelled debris during HIPS experiments. The design for this facility has been completed and the acquisition process initiated.

1.3 CORCON

One of the important elements of severe accident analyses is the predictions of loads placed on the reactor containment and radionuclide release brought on by the interaction of reactor core debris with concrete. CORCON is a state-of-the-art, mechanistic model of core debris attack on concrete. It predicts the concrete erosion, gas generation, and heat transfer that occur during the interactions of debris with concrete.

CORCON predictions were compared to results of some of the recent TURC (transient urania-concrete) tests. The TURC tests involved deposition of nominally 200 kg of high-temperature melt onto a limestone/common sand concrete slug held in a magnesia annulus.

Both CORCON mod1 and CORCON mod2 predict well the rate and extent of concrete erosion observed in the TURC1T test. Both CORCON mod1 and CORCON mod2 underpredict by about a factor of two the concrete erosion observed in TURC1SS. Both CORCON mod1 and CORCON mod2 greatly overpredict the extent of concrete erosion observed in TURC2.

A notable feature of the test comparison has been the similarity of predictions from CORCON mod1 and CORCON mod2. Only in the case of test TURC2 was there a significant difference between predictions by the two versions of CORCON.

The underprediction of concrete ablation for test TURC1SS is being attributed to the model of heat transfer from the melt

to the concrete. CORCON uses the "gas film" model, which was devised many years ago based on experiments in which hot liquids were poured onto dry ice. The model devised from the simulant experiment has retained a certain credibility, largely because of its analytic simplicity. Alternative models exist in the literature. Some of these alternatives include models in which the incipient melt layer on the surface of the concrete limits heat transfer, models based on the relative density differences between melt and concrete, and models based on the local convection created by formation and detachment of bubbles at the melt-concrete interface. However, none of these recognize the unique features of concrete and the attack on concrete by high-temperature melts.

Clearly, one area where CORCON will need modification is in melt-to-concrete heat transfer. Recent thoughts on liquid-liquid heat transfer with bubble agitation suggest that the interlayer heat transfer coefficients (heat transfer between the oxidic and the metallic phases of a melt) also need reexamination.

The overprediction of concrete erosion in the TURC2 test is due to the model's failure to predict an interfacial crust that forms immediately upon melt-concrete contact in the experiment. Two features of CORCON merit examination to correct this failure: (1) the interfacial contact temperature models in CORCON appear incorrect, and (2) the rates at which the liquidus and solidus properties of the oxide phase change as concrete is incorporated into the melt need to be examined.

1.4 Molten Fuel-Coolant Interactions

The objective of this program is to develop an understanding of the nature of fuel-coolant interactions (FCIs) during hypothetical accidents in light water reactors (LWRs). FCIs can occur in the core region, in the reactor lower plenum, or in the cavity below the vessel. They can occur when melt falls into water or when water falls into melt. The understanding of FCIs achieved in this program should be sufficient to resolve the key reactor safety issues for both terminated and unterminated accidents. Models are being developed to determine:

1. The rates and magnitude of steam and hydrogen generation due to FCIs,

2. The probability and consequences of direct containment failure by steam explosions,

3. The influence of FCIs on accident progression and the nature of the source term (including fission-product chemistry, release rate, particle size, and dispersal),

4. The consequences of pouring water on the melt in order to terminate an accident, and

5. The characteristics of the debris produced by FCIs, including particle size distributions, porosity, and coolability.

1.4.1 Experiments, Data Reduction, and Analysis

Construction of the new EXO-FITS (fully instrumented test site) has been completed. This facility has been designed to deliver 50-kg iron/alumina charges to various-sized water chambers from various drop heights. Three experiments were conducted to develop the capability of preparing and delivering a 50-kg iron/alumina thermite charge into a 61-cm water chamber. Steam explosions were observed in all three experiments. The delivery of a 50-kg iron/alumina charge appears similar to that of the 20-kg melt. In the first experiment, a small amount of molten thermite leaked from the crucible prior to drop, but the main mass appeared to enter the water as a relatively coherent mass. In the second experiment, the melt dropped with no problems. From the x-rays taken during this experiment the melt appeared to be in one uniform mass at melt/coolant contact. In the third experiment, the melt did not release from the crucible at the time of drop. The high-speed camera data revealed that the stainless steel lid fell free at the time of drop, but the graphite lid did not.

The water-phase pressure data from these three experiments are being analyzed. To validate the water-phase pressure measurements, a series of high-explosive experiments that will simulate a steam explosion are planned.

The analysis of the FITS particle debris to determine the oxidation state continued. To date, x-ray fluorescence, x-ray diffraction, and scanning electron microscopy have been unable to quantitatively define the oxidation state of the iron/alumina material. Mössbauer is currently being pursued and results are expected in the near future. If the Mössbauer techniques do not produce quantitative results, we will then have wet-chemistry analyses of the debris performed.

1.4.2 Model Development and Applications

The hydrodynamics code CSQII was used to estimate the peak pressures, impulse, and kinetic energy in the proposed SEALS (steam explosions at large scale) facility. These calculations indicated that the peak pressure at the top of the vessel was ~19 MPa at 12 ms from the trigger. This initial pressure pulse is followed by a 16-MPa peak pressure pulse at 14 ms, corresponding to the time of impact of the two-phase slug with the upper head. Peak kinetic energies in the system were calculated to be ~27.5 MJ at 9.8 ms, resulting in a peak conversion ratio of 0.4 percent. These results were based upon input parameters and initial conditions of the 20-kg experiments previously modeled with CSQII.

The SEALS facility was also modeled using a version of the BUBBLE program used at Los Alamos to approximate the behavior of an expanding two-phase bubble of fuel in a pool of sodium in an LMFBR (liquid metal fast breeder reactor). The peak kinetic energy calculated using this code was 29 MJ at 5 ms. The slug impacted the head with a velocity of 105 m/s, which corresponded to a conversion ratio of 0.9 percent.

Work also continued on the nonequilibrium parametric explosion model. The TEXAS computer code has been modified to more accurately represent the multiphase system; e.g., a modified flow regime map, more realistic drag coefficients, mass and heat transfer coefficients, and constitutive relationships. Analyses of some of the FITS experiments were performed. The importance of eight initial conditions will be considered in the upcoming months. These eight initial conditions are: (1) slug mass, (2) coolant mass in the interaction zone, (3) initial volume ratio of coolant vapor to liquid in the interaction zone, (4) mixing time, (5) initial mixing diameter, (6) fragmentation time, (7) local fragmentation diameter, and (8) mass of fuel fragmented locally. Constitutive relations and consistent methodology were developed to determine the initial conditions of the experiment. The influence of fuel composition, mass ratio, subcooling, ambient pressure, and chamber confinement will also be considered during the study.

Modeling of the film collapse and fuel fragmentation of the small-scale single droplet experiments has conceptually been divided into four stages: (1) film boiling around the fuel droplet, (2) film collapse and jet penetration, (3) jet penetration and entrapment, and (4) expansion and fragmentation of the fuel. A baseline experiment which was conducted by Nelson was modeled. The results indicate that even though

the peak acceleration rate is high at high peak trigger pressure, the instability does not grow linearly with peak pressure. The single-droplet FCI experiment 11-75-1 was also analyzed. In this case, the vapor bubble undergoes four cycles of expansion and collapse and results in a 1 percent conversion ratio. Even though the analysis technique is still approximate, the results are within the limit of the experimental results.

1.4.3 Program Development and Planning

In preparation for the Steam Explosion Review Group (SERG) meeting held in Harpers Ferry, we proposed a research program that includes the development of FCI models and a comprehensive experimental program. The experimental program addresses four current questions about FCI processes. We ranked these four into priorities according to our perception of the immediate needs of the NRC. The first priority of the proposed program was large-scale (2000-kg) experiments conducted in the SEALS facility to determine the effects of scale on coarse mixing and conversion ratio. The second and third priorities were FITSX (FITS extended) and the SHIP (small-scale highpressure) facilities, respectively.

The SEALS facility is proposed to be built in three phases, optimizing the experimental information and cost. In the first phase, we will construct a facility similar to the current EXO-FITS facility. In the second phase, we will construct a right circular cylinder of a half-linear-scale reactor vessel and attach the delivery system developed in the first phase. In the final phase, we will finish construction of the half-linear-scale reactor vessel, which will measure conversion ratios and other data important to alpha-mode failure.

1.5 Hydrogen Behavior

The major concerns regarding hydrogen in LWRs (light water reactors) are that the static or dynamic pressure loads from combustion may breach containment or that important, safety-related equipment may be damaged due to either pressure loads or high temperatures. In order to assess the possible threats, it is necessary to understand how hydrogen is produced, how it is transported and mixed within containment, and how it combusts.

The objectives of this program are (1) to quantify the threat to nuclear power plants (containment structure, safety equipment, and the primary system) posed by hydrogen

combustion; (2) to disseminate information on hydrogen behavior and control; and (3) to provide programmatic and technical assistance to the NRC on hydrogen-related matters.

The HECTR (hydrogen event: containment transient response) code is a reactor analysis tool used to compute transport and combustion of hydrogen. Initial development of a diffusion flame model has begun. Calculations have been performed on plume flames in a BWR (boiling water reactor) Mark III containment. HECTR assessment continued against data from the large-scale experiments performed at NTS. Calculations of global deflagrations of premixed atmospheres both with and without containment sprays were completed.

A substantial amount of useful data on premixed and continuous injection hydrogen deflagrations in air and steam has been provided by the large-scale tests performed at the Nevada Test Site (NTS). These burns were conducted at sufficient scale to aid in the validation of hydrogen combustion codes. Sandia has completed a detailed evaluation of the quality and self-consistency of some of the data from the premixed tests in conjunction with the HECTR assessment effort. This was done in order to judge the utility of these data in characterizing hydrogen burn environments.

The FLAME (flame acceleration measurement experiments) facility is a large-scale channel designed to study hydrogen combustion problems relevant to nuclear reactor safety. Initial tests examined the effects of transverse venting on combustion in an obstacle-free channel. Activities this period included repair of the facility and resumption of testing. As a result of a detonation during test F-14, the steel door at the end of FLAME and part of the supporting concrete were damaged by unexpectedly high-pressure loads. Permanent repairs have been completed and testing has resumed.

Small-scale experiments, performed at McGill University, examined transition to detonation in the wake of an obstacle and the transmission of detonation through circular orifices. The objective of the first study is to establish criteria for transition and to provide experimental data suitable for model calibration. A single orifice plate is placed in a 30-cm tube. Upstream overpressure and the number and diameter of orifice holes are varied in order to vary both the turbulence length scale and intensity. Transition to detonation has been demonstrated in the wake of a single orifice for relatively insensitive H_2-air mixtures (20 percent H_2 with 1 bar upstream overpressure).

Propagation of detonation is studied to examine near-limit phenomena. The objective is to establish criteria for the propagation limit.

The relative detonability of H_2-air-steam mixtures that are predicted to occur following a reactor accident is being studied in the Heated Detonation Tube (HDT). Prior to the HDT experiments, the effects of initial pressure and temperature were believed to be small for the ranges expected during a reactor accident. We have found, however, that the initial thermodynamic conditions have strong influences on the detonability of a given mixture. During this period, measured detonation cell sizes, which are used to characterize the relative detonability of a mixture, have been compared to computed values over a wide range of steam concentrations. A single point normalization procedure appears to provide consistent predictions.

1.6 Hydrogen Mitigative and Preventive Schemes

The objective of the Hydrogen Mitigative and Preventive Schemes Program is to provide the NRC with information to evaluate proposed equipment concepts and operational schemes to prevent or mitigate the effects of hydrogen combustion during hypothetical LWR accidents. To provide this information, we are investigating the operability and consequences of operation of deliberate ignition systems and their components during hypothetical hydrogen-producing accidents. We are studying the effects produced by operating the containment water spray system while the deliberate ignition system is activated. We recently completed an experimental study of the behavior of resistance-heated hydrogen igniters exposed to water sprays and gas flows. A report on this work is being prepared.

To complement this study, the flow of air in nuclear reactor containment buildings due to the introduction of water sprays is being investigated numerically and theoretically. The particular geometry studied is that of Sequoyah, a pressurized water reactor equipped with an ice condenser. Given the water spray flux specified for Sequoyah, peak flow velocities of approximately 12 to 14 m/s are possible in an empty building. This velocity is reduced substantially when account is taken of the presence of ice condensers and steam generators. A draft report on this study has been submitted to the Nuclear Regulatory Commission for review.

We are also studying the effects of liquid water dispersed as drops on the combustion of hydrogen-air mixtures. We are investigating the use of rotating disc generators in the 5.6 m^3 FITS combustion chamber to generate monodisperse

damaged nuclear plant. Current estimates of the release of the principal fission-products over the range of relevant accident conditions are subject to significant uncertainty (e.g., QUEST). A key element in reducing the uncertainty in predicted releases is an improved understanding of fission products from the fuel under severe fuel damage conditions. The ACRR Source Term Program is being developed to provide a data base for fission-product release over a range of fuel temperatures, system pressures, and fuel damage states, where little or no data currently exists, to allow the development of improved fission-product release models for use in consequence evaluation. This program is related to out-of-pile programs at ORNL and BCL.

A primary objective of the ST experimental design effort is to provide the capability to examine a range of fuel temperatures, gas pressure and composition, and fuel-clad damage states in a relatively low-cost experiment. Two general approaches are being examined: a conventional, once through design (boiler-condenser) and a recirculation system. A series of system design studies and component tests was initiated to provide the basis for system selection.

Another major objective of these tests is to sample fission products as close as possible to the point of release to minimize transport and mitigation effects that require unfolding in order to interpret the results as has been the case in previous in-pile tests. A unique fission-product filter sampler has been designed to provide this capability for the ST tests. These samplers are operated sequentially to provide time-dependent information. A series of demonstration and diagnostic tests to support the final sampler design has been initiated. The ST fission-product sampler design includes both passive filter sections (for particulate) and active filter sections designed to remove specific fission-product species by chemical reactions.

2. FISSION-PRODUCT SOURCE TERM

2.1 High-Temperature Fission-Product Chemistry and Transport

The purpose of the Fission-Product Chemistry and Transport Program is to obtain data on the chemistry and processes that affect the transport of fission-products under accident conditions. Baseline thermodynamic and reactivity data are being collected for compounds of fission-product elements of particular interest. An experimental facility has been built to allow the chemistry of fission-products in prototypic steam-hydrogen environments to be studied. The interaction of fission-products with reactor materials such as stainless steel can be examined in this facility. Results of these experimental studies are compared to predictions of thermochemical models to determine if reaction kinetics play an important role in fission-product transport.

A report was drafted that describes the experimental results of the reaction of cesium iodide with 304 stainless steel and Inconel 600 in a steam and hydrogen environment. The report results show that some cesium, but essentially no iodine, was retained with the oxide formed on the Inconel 600. Formation of a cesium silicate was indicated. Essentially no cesium or iodine was detected in the oxide layers formed on 304 stainless steel in sharp contrast to the retention of cesium in previous experiments when cesium hydroxide vapor was used. Surface reaction rate constants (or their limiting values) are given for these reactions in the report.

At the request of Idaho National Engineering Laboratory (INEL), thermodynamic calculations were made for the tellurium-oxygen-hydrogen system in order to predict the major tellurium species that could be released under TMI-2 accident conditions. These calculations indicate that H_2Te is the thermodynamically preferred tellurium containing vapor species for the provided accident conditions. The formation of H_2Te is favored by the presence of excess hydrogen and by high total system pressures. This species is also favored when the tellurium content of the gas phase is reduced or diluted. Increasing the system temperature to >1200 K will tend to dissociate H_2Te, depending on other system parameters.

2.2 ACRR Source Term Tests

Release of radionuclides during fuel degradation in a core uncovery accident is the first stage in the determination of the amount and nature of the radioactive release from the

3. LWR DAMAGED FUEL PHENOMENOLOGY

Sandia's LWR Damaged Fuel Phenomenology Program includes analyses and experiments that are part of the integrated NRC Severe Fuel Damage (SFD) Research Program. Sandia is investigating, both analytically and in separate-effects experiments, the important "in-vessel" phenomenology associated with severe LWR accidents. This investigative effort provides for two related research programs: the Damaged Fuel Relocation (DFR) Program and the Damaged Core Coolability (DCC) Program. The focus of these activities is to provide a data base and improved phenomenological models that can be used to predict the progression and consequences of LWR severe core damage accidents. The DFR experiment program provides unique data on in-vessel fuel damage processes that are of central importance in determining the release and transport of fission-products in the primary system. The DCC experiment program provides data on the ultimate coolability of damaged fuel configurations.

3.1 ACRR Damaged Fuel Relocation and Quench

The focus of the LWR DFR experiment program is directed toward providing separate-effects phenomenological data on important severe in-vessel fuel-damage processes to aid in the development of second generation severe accident analysis codes. The core damage configuration, hydrogen generation, and fission-product release are the primary areas of interest. The DF test series uses photography to record the damaged fuel configuration during an in-pile experiment in which accident conditions are simulated in a small LWR rod bundle. The decay heating in these experiments is simulated by fission heating of the fuel in the ACRR. Steam conditions similar to expected accident conditions are provided.

The DF-2 experiment was run successfully in the ACRR. A short bundle of nine PWR fuel rods was disrupted by fission-simulated decay heat and the rapid oxidation of zircaloy cladding in steam. The experiment is distinguished from the earlier DF-1 test by higher early clad oxidation (15 percent instead of 10 percent), and by 40 percent lower steam input. The primary purpose of the experiment was to investigate the effect of higher early clad oxidation on the mode and extent of fuel disruption.

The fuel and clad temperatures in DF-2 rose at up to 10°C per second (only 40 percent of the DF-1 result). Indicated peak temperatures reached 2500 K, in the same range as DF-1. Corrected temperature estimates to account for actual thermocouple response indicates peak temperatures of 2700 K

(single diameter) water drops with suspended water densities in excess of 100 g/m^3. Significant advantages over nozzle-generated drops are expected, particularly avoiding turbulence in the combustion gases. A pair of these generators has been tested both in a transparent plastic mockup and in the FITS chamber. Downward water drop fluxes as measured by rain gauges indicate a strongly nonuniform distribution of dispersed water across the chamber. Since this cannot be observed visually, other methods for determining drop uniformity are being investigated.

We are also studying the effects on deliberate ignition of hydrogen-air mixtures that contain aerosols produced in containment by core overheating, breakup of jets of core melt, or core-melt/concrete interactions. To measure these effects, we have prepared the 5.3 m^3 VGES (variable geometry experimental system) chamber for the combustion of hydrogen in the presence of aerosols, simulants of both core materials and fission products. This effort has involved installation of extensive aerosol generating and sampling equipment. We extended the combustion experiments with Al_2O_3 aerosols to experiments with Fe_2O_3 aerosols. Neither oxidic aerosol had a major effect on the pressure rise or impulse produced by the burns of 6.5 H_2-air mixtures. This was confirmed in small-scale tests over a wide range of experimental conditions. However, in one experiment with a metallic iron aerosol, both pressure rise and impulse were increased significantly.

We also performed experiments in the VGES chamber in which a 10 w/o CsI-90 w/o Al_2O_3 aerosol was exposed to hydrogen burns from 6.5 to 29.5 percent H_2 in air. Extensive formation of elemental iodine was observed.

The feasibility of constructing a nonpowered hydrogen igniter from catalytically active platinum has been demonstrated. Some parametric optimization produced a device that ignited mixtures as lean as 5.5 v/o hydrogen in air in laboratory tests. The possibility of using devices such as these to continue deliberate ignition during station blackout is being examined.

for both DF-1 and DF-2. Analysis indicates the temperature rise was stopped in the upper bundle region by relocation of molten zircaloy at 35 to 40 percent oxidation.

The hydrogen production rate was measured from the temperature rise of copper oxide recombiners. The peak hydrogen production rate matched the total bundle steam flow, indicating that the zircaloy-steam reaction was steam-starved during the most severe part of the transient.

Extensive aerosol production began when the cladding temperature exceeded 2000 K. The aerosol is presumably tin released by melting zircaloy as found in DF-1.

Posttest radiographs show much less fuel liquefaction and relocation of fuel and clad, to the lower part of the bundle, than in the earlier DF-1 experiment.

3.2 ACRR LWR Degraded Core Coolability

The LWR Degraded Core Coolability (DCC) Program investigates the coolability of damaged core debris in water. The debris is fission heated in the ACRR to simulate the decay heat expected in an LWR severe core-damage accident. The governing phenomenological uncertainties being investigated are pressure effects, deep bed behavior, particle size distributions, stratified beds, bottom coolant feed, and material effects. Each DCC experiment will determine the coolability in three thermal regimes: (1) convection/boiling, (2) dryout, and (3) extended dryout. The staff is using experimental results to confirm and/or modify the present analytical models used to predict degraded core coolability.

The Leverett function used in the DEBRIS model for describing the capillary pressure as a function of saturation may be incorrect for broad particle size distributions. A series of tests was initiated to measure the capillary pressure on glass-water and UO_2-water beds. Initial results indicate that for narrow particle size distributions, the data was in good agreement with the Leverett function. For broad particle size distributions the capillary pressure curve changed significantly. This has implications on channeling calculations and relative permeabilities, as well as incipient dryout heat fluxes for the DCC experiments.

The scoping calculations for the DCC-3 experiment, which examines the effects of particle stratification and bottom inlet flow, were completed. Most of the hardware has been procured and some testing on instrumentation and the pumping system for the inlet flow began.

4. MELT PROGRESSION PHENOMENOLOGY

The objective of this program is the development of a mechanistic computer model for the in-vessel phases of severe accidents in LWRs. This model, MELPROG, is implicitly linked with the TRAC-PF1 RCS thermal hydraulics models to provide a complete, integrated treatment of the reactor primary system from accident inception up to and through release of core materials and fission products from the reactor vessel. The model also provides materials and thermohydrodyamic input to the CONTAIN reactor containment analysis model.

MELPROG consists of several explicitly linked modules which, in turn, are comprised of models that represent and treat the physical processes that occur during a severe core-damaging accident. These modules only interact through well-defined interfaces. Any module can be run stand-alone. Similarly, any module in the code can be removed and replaced by dummy interfaces and the code will continue to run. Hence, improving or substituting new models into the code, as warranted, is relatively easy.

The first version of MELPROG, MELPROG-PWR/MOD0, was completed and is now being tested prior to release. This version uses a one-dimensional fluid dynamics model (FLUIDS) and contains a PWR core structure model (STRUCTURES). This version also includes the DEBRIS module for debris bed analysis, the RADIATION module for radiation heat transfer analysis, and the PINS module for fuel and control rod analysis.

The second version, MELPROG-PWR/MOD1, is currently under development and will include all features of the original code plus many significant enhancements. In particular, this version will include a two-dimensional fluid dynamics model, a fission-product module (VICTORIA), an improved core structures model, a melt-water interaction model, and a melt ejection model. This version will still be intended for PWR analysis, but represents a major improvement over the original version.

5. ADVANCED REACTOR ACCIDENT ENERGETICS

The Advanced Reactor Accident Energetics Program addresses the key issues in an LMFBR core-disruptive event that determine the progression and severity of the accident. This program involves a series of in-pile experiments and analyses that focus on key phenomena in two general areas:

1. Initiation Phase--Fuel/Clad Dispersal Experiments,

2. Transition Phase--Fuel Freezing and Streaming Experiments.

5.1 Initiation Phase

The Sandia Fuel Dynamics Program provides needed experimental data and analysis for the initiation phase of an LMFBR core-disruptive accident. The motion of clad and fuel in the initiation phase of an LOF accident is an important consideration in the subsequent progression of the accident. Early fuel dispersal can lead to neutronic termination while limited dispersal and blockage formation continues the accident into the transition phase and the possibility of further neutronic activity.

To obtain data on the important phenomena involved in this phase of an LMFBR accident, the USNRC is sponsoring the Sandia Transient Axial Relocation (STAR) experiments in the ACRR test facility. Kernforschungszentrum Karlsruhe (KfK), FRG is cosponsor of this program.

The third experiment in the jointly-sponsored (NRC-KfK) STAR experiment program was performed. This was the first STAR experiment to be performed with preirradiated fuel. The purpose of this experiment was to examine fuel and clad motion behavior in an irradiated fuel experiment that reproduced unprotected loss of flow (ULOF) accident heating conditions for an LMFBR. The experiment was performed successfully, and high-speed films of the fuel behavior show a strong tendency for early axial fuel dispersal.

The STAR-3 experiment used one preirradiated fuel pin and one fresh pin. The power transient and fuel type were chosen to represent a low void coefficient ULOF accident scenario, which results in fuel failure at relatively low power levels (near nominal power). Consequently, the power transient was designed to cause early clad relocation prior to fuel motion) while at nominal power (P_o). Later, when fuel melting occurs at 6 x P_o, it was expected to cause fuel disruption due to fuel frothing or foaming. Because of

the slow transients and low power levels, the STAR-3 experiment simulated lower bound accident heating conditions of a generic ULOF accident. The STAR-4 power history will simulate high-power ULOF scenarios and, therefore, will represent an upper bound ULOF. The fuel used in STAR-3 was preirradiated to medium burnup (5.7 a/o). This fuel (in terms of its burnup, linear heat rating, microstructure, and fission-product content) represents the end-of-life fuel characteristics in an LMFBR.

The results of the STAR-3 experiment show that clad relocation will be delayed, causing fuel and clad relocation to occur simultaneously. Furthermore, when clad motion does occur, significant drop entrainment should be expected because of the nonwetting behavior of fuel and molten cladding. These conditions, therefore, minimize the chances for clad blockage formation and delayed fuel dispersal. Also, fission gases and volatile fission products cause early fuel disruption and dispersal. Fuel dispersal at moderate power levels (without significant fuel vapor pressure) involves substantial axial fuel sweep out. Thus, whole core safety analysis for an end-of-life core should be able to include fuel dispersal mechanisms due to fission products and sodium vapor entrainment. In other words, the fuel motion analysis (for preirradiated fuel) does not rely on fuel vapor pressure to cause fuel dispersal.

5.2 Transition Phase

Current heterogeneous core designs are characterized by relatively low-sodium void coefficient and incoherent behavior in the initiation phase. These features generally increase the likelihood of a "transition" or "meltout" phase during a core-disruptive accident. The key questions in the transition phase are whether fuel or clad blockages form, leading to a confined or "bottled" core configuration, and the behavior and reactivity implication of this pool of fuel-steel in the core region of the fuel blockages lead to this state.

The TRAN program addresses the question of fuel-inventory reduction by penetration into upper core structure and through subassembly gaps to the lower core structure. If deep penetrations occur, nonenergetic shutdown is probable while shallow penetration will lead to a transition phase and the possibility of further energetics. First-of-a-kind in-pile experiments, sponsored jointly by the USNRC and the Japanese Power Reactor and Nuclear Fuel Development Corporation (PNC), are being conducted to provide data to evaluate the various models describing fuel penetration.

EXECUTIVE SUMMARY

Assembly of the multipin flow channel experiment B-4 is underway. Final ACRR safety committee approval has been obtained. Final calculations are being performed in support of the preexperiment diagnostic work which will determine the actual experiment-ACRR energy coupling factor and the optimum ACRR fuel melting pulse. Also being performed are SIMMER-II and PLUGM calculations for the anticipated fuel melting and flow conditions. A sensitivity study revealed that double pulsing of the fuel in the melting phase in the experiment tends to minimize the undesired early motion by driving off the gas contained in the open fuel porosity. Precalculations using the PLUGM code indicate that a coherent bulk flow of fuel is likely to result through the entire length of the freezing channel without the slug blow-through experienced in the earlier mass-limited TRAN experiments.

Modifications to the GAP-2 design were performed that will lead to an experiment coupling factor of about 11 J/g/MJ. This configuration will allow use of an ACRR fuel melting design pulse, which is well within the capabilities of the ACRR.

6. POSTACCIDENT HEAT REMOVAL

6.1 Debris Bed Coolability

The objective of the Debris Bed Coolability Program is to develop experimentally validated models for the behavior of LMFBR core debris after a severe accident. The primary tools in pursuing this objective are coolability experiments using conditions as prototypic as possible so as to determine all the important phenomena needed to develop models to predict coolability limits. Fission heating of UO_2 is the only heating method currently available that can provide an adequate simulation of decay heat for many of the expected debris and coolant configurations. Fission-heated coolability experiments provide the foundation of the debris bed coolability research at Sandia. The program is funded jointly by the UNSRC, EURATOM (JRC, Ispra), and the PNC (Japan).

Preparations continued for the D-13 experiment, which is the last experiment in the program. D-13 complements the recently conducted D-10 experiment. The experiments are identical, except that the debris in D-13 is in a stratified (layered by particle size) configuration rather than a uniformly loaded bed. Much of the work this period centered on setting up a new assembly area for handling large quantities of special nuclear material. Extensive security upgrades are required for protection of the material during loading into and assembly of the experiment. The new area also required accommodating hot sodium operations.

The operational procedures for conduct of D-13 have been reviewed and approved by all sponsors. The sequencing of operations is critical for D-13 in order to preserve the stratified geometry until the packed bed incipient dryout measurements, as a function of bottom flow, have been obtained.

Preliminary calculations of the experiment have been performed, and indicate that with sufficient bottom cooling, the debris is coolable for the decay heat power levels associated with most reactor accident scenarios.

6.2 Dry Debris Melt Progression

In order to establish the release time frame and quantity of radioactive materials following a severe accident, it is necessary to determine the fuel melt dynamics and the characteristics of melting attack by molten fuel on reactor structure and containment barriers should postaccident debris heat removal not be adequate. Simulation of those

portions of debris beds undergoing extended dryout and melting is necessary to support modeling activities. This study is aimed at providing such data through in-core experimentation with typical reactor material undergoing sustained, intrinsic heating at temperatures of interest. Models developed are provided to the LWR severe accident code MELPROG as well as to direct analyses of LMFBR debris coolability. This work is cosponsored by the NRC, the Japanese PNC, and EURATOM (JRC, Ispra).

Both experiments in the series have been completed, and work this quarter involved disassembly of the experiment packages and sectioning of the debris. A vertical cut was made through the center line of the debris. In DC-1 a large pool of molten UO_2 was formed surrounded by a dense linticular crust and a large overlying void. In DC-2 the steel on melt wetted the UO_2 and exhibited only localized agglomeration and interconnection. The large migrations of molten steel observed in previous experiments was not observed. The thermal conductivity in the bed increased by 40 percent after steel melting. These experiments provide excellent data on heat transfer in dry debris and in molten configurations and also provide phenomenological understanding on the mechanics of melt progression.

1. CONTAINMENT LOADING AND RESPONSE

1.1 Ex-Vessel Core Debris Interactions

(D. A. Powers, 6422; D. R. Bradley, 6425; J. E. Brockmann, 6422; E. R. Copus, 6422; J. E. Gronager, 6422)

1.1.1 Preliminary Results of the SWISS-1 Test

1.1.1.1 SWISS Experimental Apparatus

The SWISS experimental apparatus, shown in Figure 1.1, consists of an interaction crucible, melt generator, instrumented expansion chamber, and water storage tank (not shown). The melt generator is constructed of MgO castable material and is mounted above the interaction crucible. The instrumented expansion chamber is bolted to the top of the melt generator. Induction coils are placed around both the melt generator and the crucible. The melt charge is a solid cylinder of 304 stainless steel having a mass of 46 kg. The charge is instrumented with both type C and type K thermocouples.

The stainless cylinder is slowly heated inductively until a superheat of 500 to 700 K is attained. At this point the melt is teemed into the interaction crucible by fracturing a ceramic diaphragm in the melt generator. The crucible is typical of the "1-D crucible" used in the TURC tests with different dimensions. The crucible is instrumented with type K thermocouples to monitor temperature profiles and to infer heat flux. Upon delivery, inductive power is applied to the melt in order to provide sustained heating for the remainder of the experiment. Some period of time after melt delivery, water is injected on top of the molten debris through a pipe cast into the side of the crucible. Water flow is adjusted during the experiment to maintain a subcooled water pool above the melt. The water pool temperature is measured using exposed type K thermocouples cast into the side wall of the interaction cavity. The excess water in the crucible flows over a weir, through a pipe, and into a water storage tank mounted on load cells. Gas and aerosols evolving from the experiment are collected.

1.1.1.2 SWISS-1 Experiment Results

The SWISS-1 experiment results presented here are preliminary in nature and are not complete. Although extensive analysis of the complete experiment will be performed, only

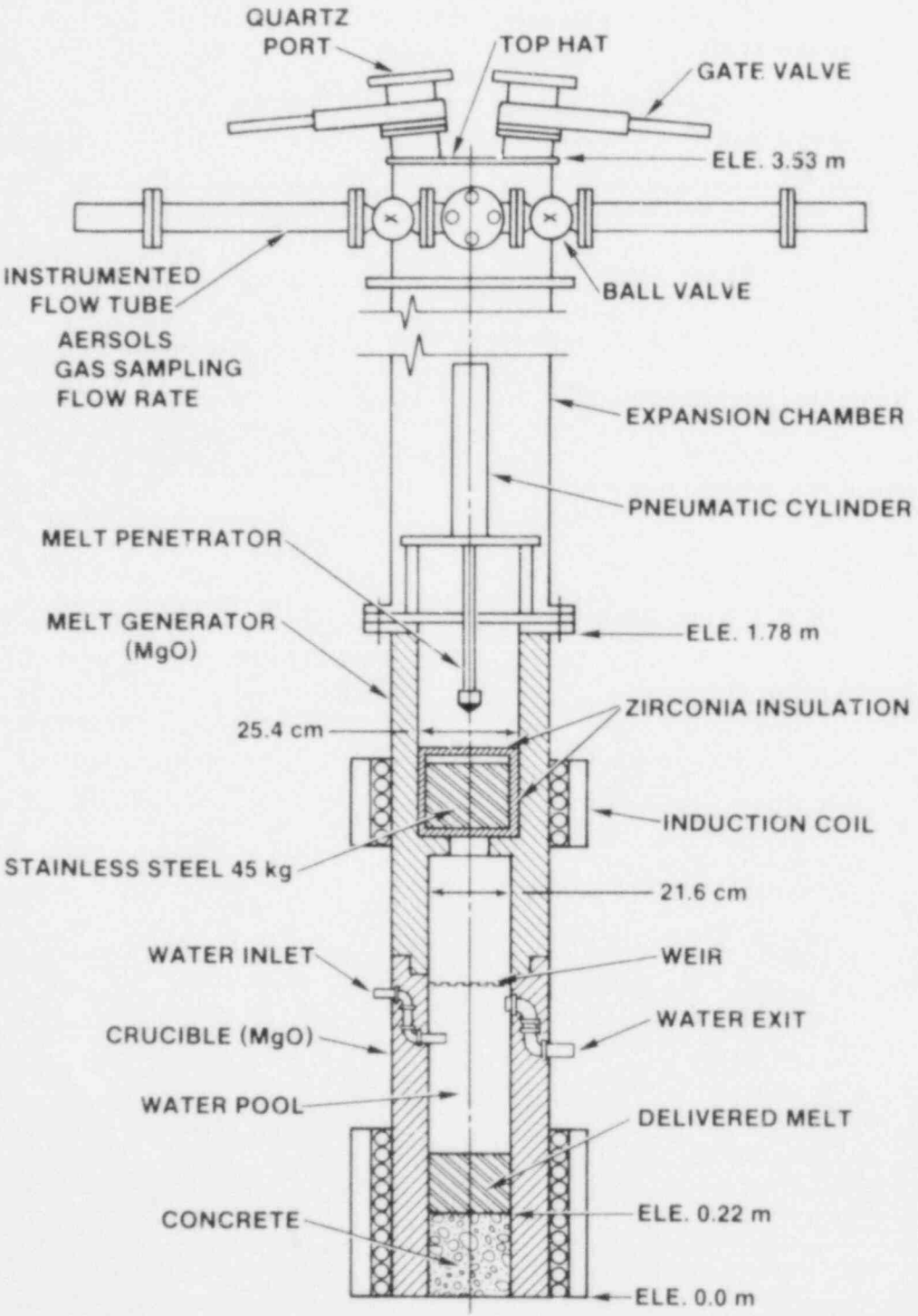

Figure 1.1. SWISS Experimental Apparatus

the concrete ablation by the melt and qualitative look at the role of the water pool on concrete ablation will be presented.

The SWISS-1 test was initiated by heating a 46-kg 304SS charge through melting to a temperature of 20,530 K. The melt was then teemed into the interaction crucible and inductively heated throughout the experiment. The melt power history is shown in Figure 1.2. Due to a trip of a circuit breaker, power was lost to the inductive power supply for approximately 3.5 min. After 12 cm of concrete had been eroded, water was injected into the crucible to form a water pool above the molten debris. In less than 6 min the steel debris had eroded through the base of the concrete slug, thus terminating the experiment.

1.1.1.3 SWISS-1 Thermal Response of Concrete

The SWISS-1 test eroded 17 cm of concrete before termination. Figure 1.3 shows the eroded front location during the course of the experiment. Critical events during the test are labeled. The erosion of the concrete was initially delayed at incipient melt-concrete contact. The delay was most likely caused by remelting a layer of steel that had frozen on the concrete surface. A small amount of steel had leaked from a crack in the melt generator prior to teeming. This was followed by a period of erosion at a rate of 0.5 cm/min for 14 min. Loss of power for 3.5 min slowed or terminated ablation until the power was restored. Following the power interruption, the erosion rate was constant at 0.66 cm/min until test termination.

As shown in Figure 1.3, water was injected at 31.5 min into the crucible with no observable effect on the erosion rate. The water injection temperature was 2950 K. A considerable amount of steam production occurred initially, but this was primarily due to the quenching of hot surfaces within the interaction crucible. Once the water pool was established, a subcooled pool temperature was maintained at 358 K. Due to the termination of the experiment 2 min after the pool was established, the stability of pool temperature has not been confirmed.

During posttest examination the interaction crucible was cut to reveal an axial cross section. A thick crust, 5 to 8 cm, had insulated the molten pool from the water above. The top of the crust was convoluted but with no evidence of crust fragmentation. The molten pool side or bottom of the crust was glassy smooth and showed clear signs of being molten. The physical characteristics of the crust have not yet been determined.

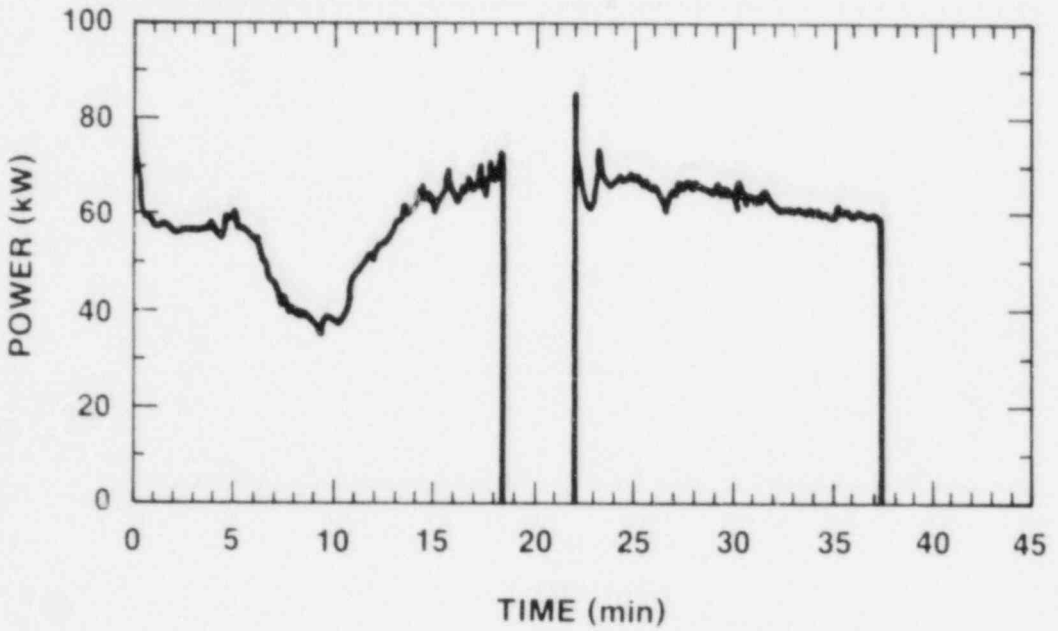

Figure 1.2. The SWISS-1 Experiment Power History

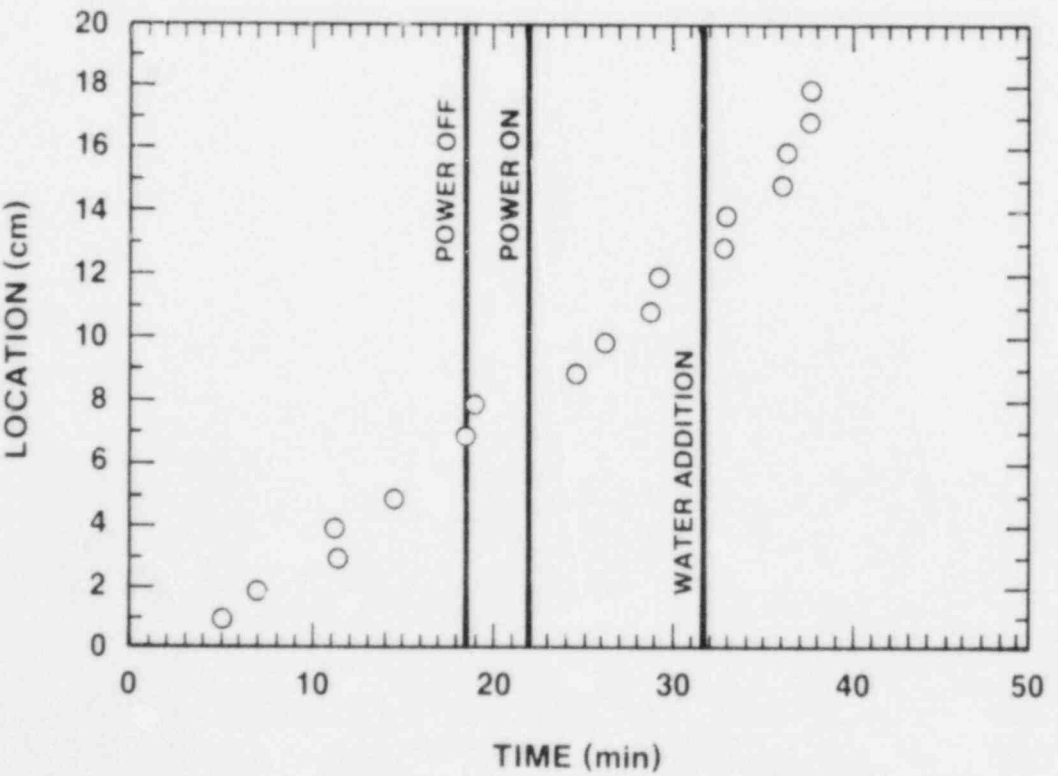

Figure 1.3. The Ablation Front History of the SWISS-1 Experiment

Figure 1.4 is a plot of the various calculated heat losses for the SWISS test. The dominant heat loss in this case is to the MgO sidewall. This is partly due to the fact that as the steel erodes the concrete new cold sidewall is exposed to the pool. In addition, the small diameter of this test leads to a relatively large sidewall area for heat transfer.

Figure 1.5 is a prediction of the thermocouple traces for the SWISS test. The predicted pool temperature remains close to the melt temperature of the stainless steel (1700 K).

A constant ablation rate was observed. The heat balance of the SWISS test indicates that the rate of ablation was set by the power generation. This conclusion is derived from the pool temperature prediction from the heat balance calculation. If a penetration rate greater than that which could be supported by the power generation were to occur, then freezing of the pool would occur and penetration would cease. The continued power generation would remelt the pool and the cycle would begin again. In contrast, if the penetration rate were slower than that set by the power generation, then pool superheating would occur and this should have been predicted by the heat balance calculations. The penetration rate is not tightly coupled to the power generation rate because in the experiment there were variations in the power but not in the ablation rate. Thus, thermal inertia probably plays a significant role in smoothing out the ablation rate data.

The SWISS-1 test was a sustained stainless steel/concrete interaction test with water addition. The experimental result indicated a continuous steady erosion rate that was weakly coupled to the power generation rate for the duration of the test. Water addition showed no effect upon the erosion rate. This was attributed to the presence of a thick crust that effectively insulated steel melt from the water. A CORCON calculation indicated only half the erosion observed, again implying the need for further code development and refinement.

1.1.2 Interaction of Hot Solid Core Debris with Concrete

1.1.2.1 Background

In the unlikely event of a reactor core melt-down which is followed by failure of the reactor pressure vessel, the interaction of core debris with the concrete basemat can occur. Although the probability of this type of accident is small, an assessment of the interaction is desirable for the

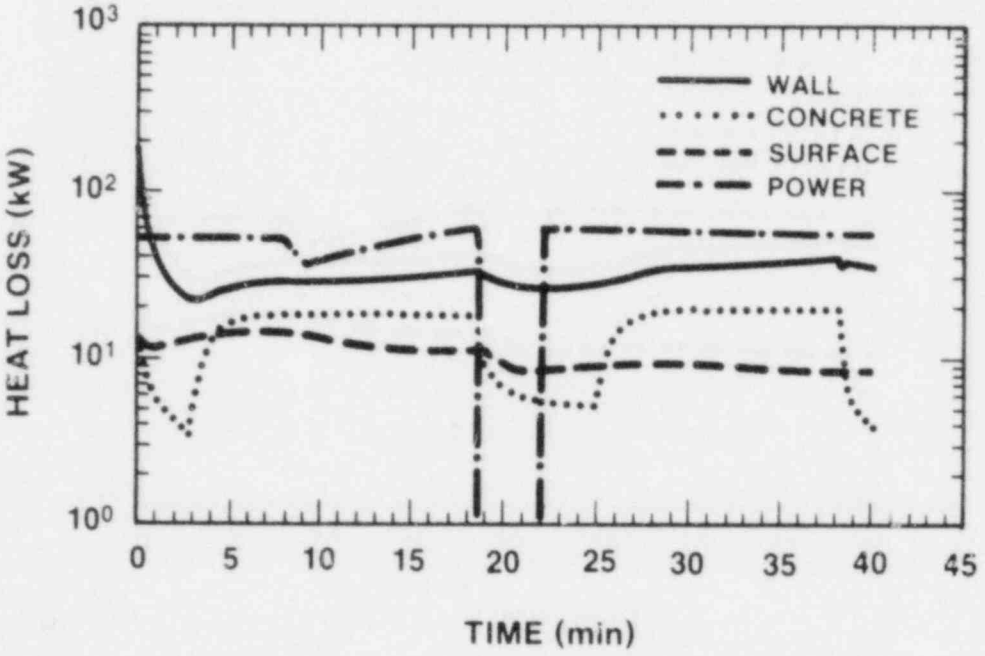

Figure 1.4. The Predicted Heat Losses in the SWISS-1 Experiment

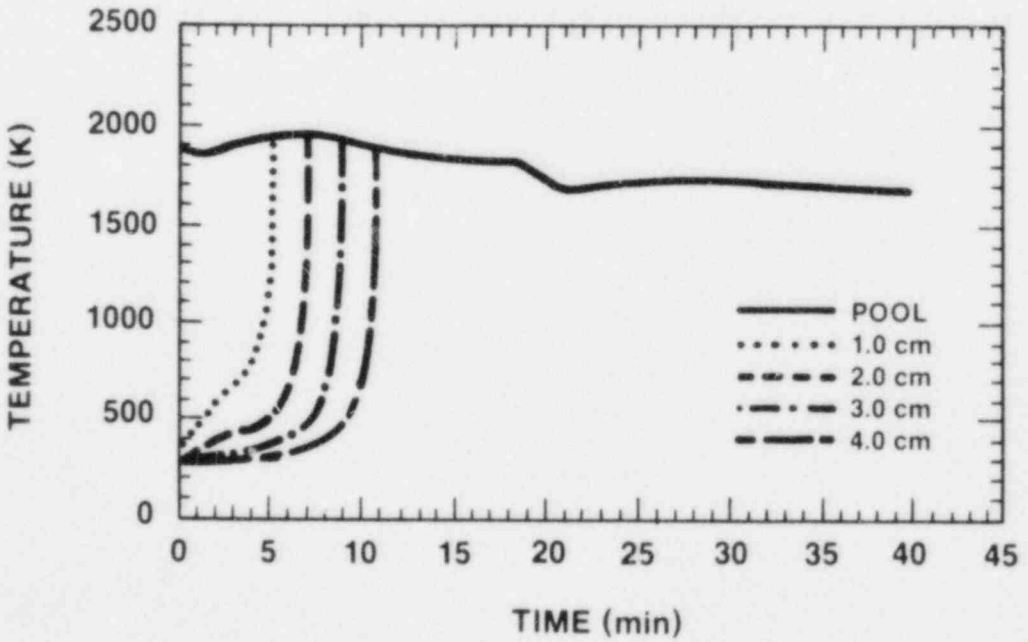

Figure 1.5. The Predicted Thermocouple Response in the SWISS-1 Experiment

proper evaluation of the risks of nuclear power. The interaction of core debris heated internally by the decay of fission products with structural concrete has been identified as a little understood aspect of such accidents.

Following melt-through of the reactor pressure vessel, the accident may proceed in several different directions. If coolant is present in the reactor cavity, the molten core material may cause a steam explosion which fragments all or part of the melt. The Zion and Indian Point Probabilistic Safety Studies propose additional fragmentation mechanisms which may be operative instead of, or in combination with, a steam explosion. Rapid quenching of the melt will accompany extensive fragmentation and the core material will exist as a debris bed cooled by the remaining water in the cavity. Depending on the configuration of the debris (bed height and particle size) and the decay power generated in the bed, localized dryout and remelting can occur. If, on the other hand, heat transfer within the debris is sufficient to prevent remelting, the accident will proceed as a hot solid interaction with concrete. The ZPSS and IPPSS reports also indicate that rapid quenching of the melt may occur even if no fragmentation takes place, as long as sufficient coolant is present in the cavity. Here again, the core debris would interact with the concrete in the form of an internally heated solid material.

Vastly different accident scenarios can result if no coolant is present in the reactor cavity at the time of pressure vessel melt-through. Here, no fragmentation or quenching occurs and the molten core material begins to interact with the concrete immediately. As the concrete is heated and subsequently ablates, steam and carbon dioxide are released in sufficient quantity to cause vigorous stirring of the melt. Although some analyses assume that the melt rapidly becomes stratified into separate oxidic and metallic layers (which would be the case in a quiescent pool), some experimental results indicate that the two phases are intermixed by the gas stirring. Regardless of the configuration of the melt, its decay power will eventually drop below the heat losses to the surrounding structure and atmosphere, and the melt will solidify. In this scenario, as in the previous one, the long-term phase of the reactor accident is governed by the interaction of hot solid core debris with structural concrete.

Regardless of whether the core debris is molten or solidified, fragmented or monolithic, there are several phenomena which must be well understood before the ex-vessel phase of the accident can be assessed. The following is a list of

those phenomena which have the greatest influence on the progression of a core-concrete interaction and its related risk evaluation:

1. Heat transfer to the concrete and to the containment atmosphere,

2. Heat conduction in the concrete,

3. Gas release from the concrete and corresponding changes in concrete properties,

4. Reduction of the gases (H_2O and CO_2) as they pass through the debris,

5. Ablation (melting) of the concrete,

6. Transport of the molten concrete/released gas mixture,

7. Crust and/or slurry formation as the molten debris cools (transition to the hot solid-concrete interaction),

8. Fission-product redistribution within the debris,

9. Aerosol production during the core-concrete interaction, and

10. Accident termination either by coolant addition or natural cooling.

The driving force in the interaction is the rate at which heat is transferred to the concrete. As the concrete heats up, several of its constituents ($CaCO_3$, $Ca(OH)_2$) undergo chemical reactions which liberate steam and carbon dioxide. In addition to this, free water which has remained in the pores of the concrete evaporates, providing another source of steam. As these concrete decomposition events occur, gas is released and thermophysical properties change. Most important of these are the concrete density, specific heat, and thermal conductivity. As the concrete temperature continues to rise, its chemical components begin to melt. Once melted, the concrete is quickly displaced from the debris-concrete interface by the combined force of the weight of the debris and the flow of released gas. The ultimate location of this slag material will affect the long-term heat transfer characteristics of the debris. For example, if a slag crust forms at the top surface of the debris it will reduce radiation heat loss and may also prevent the debris from being quenched by coolant which is added later.

The core-concrete interaction influences not only the containment structure adjacent to the debris, but also the containment atmosphere above the debris. The concern here is the ability of the containment to withstand the long-term pressurization that occurs during the interaction. The pressure increases both as a result of direct heating of the atmosphere by the debris and released aerosols, and also by the addition of noncondensable gases produced during concrete decomposition. As released H_2O and CO_2 pass upward through the debris, they are reduced to H_2 and CO by oxidation of the metallic components of the debris. These two gases not only add to the pressure in the containment, but because they are flammable, they may cause rapid overpressurization and failure of the containment if ignited. If the containment fails, the risk to the public is greatly affected by the magnitude and nature of the aerosols released during the interaction.

Based on previous experimental work at Sandia, aerosol production appears to be a strong function of the debris temperature and the net heat flux to the concrete. When the debris is molten and very hot, dense aerosol clouds have been observed, while for lower temperature solid debris, aerosol production appears to be much smaller. The composition of these aerosols is also of great importance, especially with respect to their radioactive fission-product content. Related to this is the question of fission-product redistribution within the debris. Fission products that become trapped within the concrete slag layer on the top of the debris have a much greater probability of release in aerosol form than if they reside well below the surface.

Another question related to fission-product relocation is the distribution of decay heat within the debris. Correct thermal modeling of a core-concrete interaction requires a prior knowledge of the location and magnitude of the energy sources within the debris. This is another aspect of the interaction about which more data are required.

Finally, of special concern is the question of when the core-concrete interaction terminates. Namely, how long will the interaction proceed and is it possible to quench the debris and thus stop the interaction by adding coolant to the reactor cavity. Current severe accident scenarios are open-ended, i.e., once the core-concrete interaction has begun, it is assumed to continue for some unspecified period of time. Eventually, decay heat generation within the core debris will drop below the heat losses to the surroundings and the accident will terminate naturally. However, it is not known whether the time required for this to occur is

hours, days, weeks, or even months. Other times of importance correspond to termination of CO_2/CO production and finally of H_2O/H_2 production. When gas production from core-concrete interactions ceases, the threat to containment integrity is reduced.

Prior to natural termination, it may be possible to stop the core-concrete interaction by introducing coolant into the reactor cavity. The heat removal capability of the coolant depends on several factors, the more obvious of which are the magnitude of the heat flux and the debris surface area available for heat transfer. If boiling heat transfer is assumed, the heat flux to the coolant can vary over at least an order of magnitude depending on the debris surface temperature and the subcooling of the coolant. Of even greater importance is the surface-to-volume ratio for the debris. For a deep, monolithic debris formation the available surface area may be small enough and the depth large enough that erosion of the concrete floor is essentially unaffected by the coolant. On the other hand, for a shallow, fragmented debris bed a quenched configuration might be maintained for a long period of time.

The goal of the Hot Solids Program is the development and experimental verification of a computer model which incorporates all of the phenomena just mentioned. In order to understand how this effort meshes with our current level of knowledge, it is instructive to review both the existing data base and the models and computer codes presently in use. In this discussion, experiments and models for both molten core-concrete and hot solid-concrete interactions will be examined to provide a better understanding of the transition between the two accident phases and how the results of the current effort might be incorporated into a single analytical tool which handles both.

1.1.2.2 Hot Solid UO_2/Concrete Interaction Experiment (HSS-3)

The HSS-3 experiment was designed as a scoping test. The main objectives for HSS-3 were to determine whether or not the geometry and diagnostics developed in the steel/concrete interaction experiments could be applied to an experiment using UO_2 as the slug material.

HSS-3 used a 10-kg slug of 80 percent UO_2/20 percent ZrO_2 to simulate hot solid attack. This slug was inductively heated using embedded tungsten rings. The UO_2 slug stood 18 cm high and 13 cm in diameter and was instrumented with C and S-type thermocouples. All other aspects of the experimental configuration were exactly as in HSS-1.

Power to the induction coil (Figure 1.6) was applied more gradually in HSS-3 than in HSS-1. After 3 hours, erosion began when the interface temperature reached 1300°C. Erosion continued at an approximately constant rate for 4 more hours. Unlike HSS-1, ablation was symmetric at all times and was not accompanied by substantial crust growth or formation. After 4 hours, the erosion front reached the practical limit for measuring thermocouple responses and the test was terminated.

Posttest disassembly of the HSS-3 package showed that both the UO_2 slug and the alumina sleeve had remained essentially intact during the test. Hairline cracks appeared in both structures, however, and the embedded rings in the UO_2 slug were exposed to the atmosphere. A gray UO_2/concrete slag material filled the gap between the UO_2 slug and the alumina sleeve for a height of 2 to 3 cm above the original concrete interface. These observations correlate with the x-ray imaging data.

Analysis of the thermocouple data (Figure 1.7) again showed general agreement with the x-ray erosion data (Figure 1.8). These results indicated that the tungsten ring assembly was able to absorb roughly 75 percent of the power applied to the induction coil. The 10-kg slug of 80 percent UO_2/20 percent ZrO_2 ablated 5.5 cm of limestone/common sand concrete in approximately 4 hours at an average debris temperature of 1650°C. Once again, the rate of erosion was fairly constant throughout the course of the HSS-3 experiment.

The HSS-3 experiment was successful in producing and recording the axial penetration of hot solid UO_2 through a concrete basemat material. However, several design changes are indicated before a fully instrumented hot solids test can be run. Additional containment to facilitate measurements of water vapor and gas evolution is the first priority improvement and should be accomplished with the addition of a second ceramic sleeve outside of the alumina sleeve now employed. Once the design changes suggested from the results of HSS-1 and HSS-3 have been made, fully instrumented tests will be run using both steel and UO_2 for solid attack.

1.2 High-Pressure Melt Ejection and Direct Containment Heating

(W. W. Tarbell, 6422; D. A. Powers, 6422)

The High-Pressure Melt Ejection and Direct Containment Heating task is a study of phenomena that might take place should core debris be expelled into a reactor cavity from a

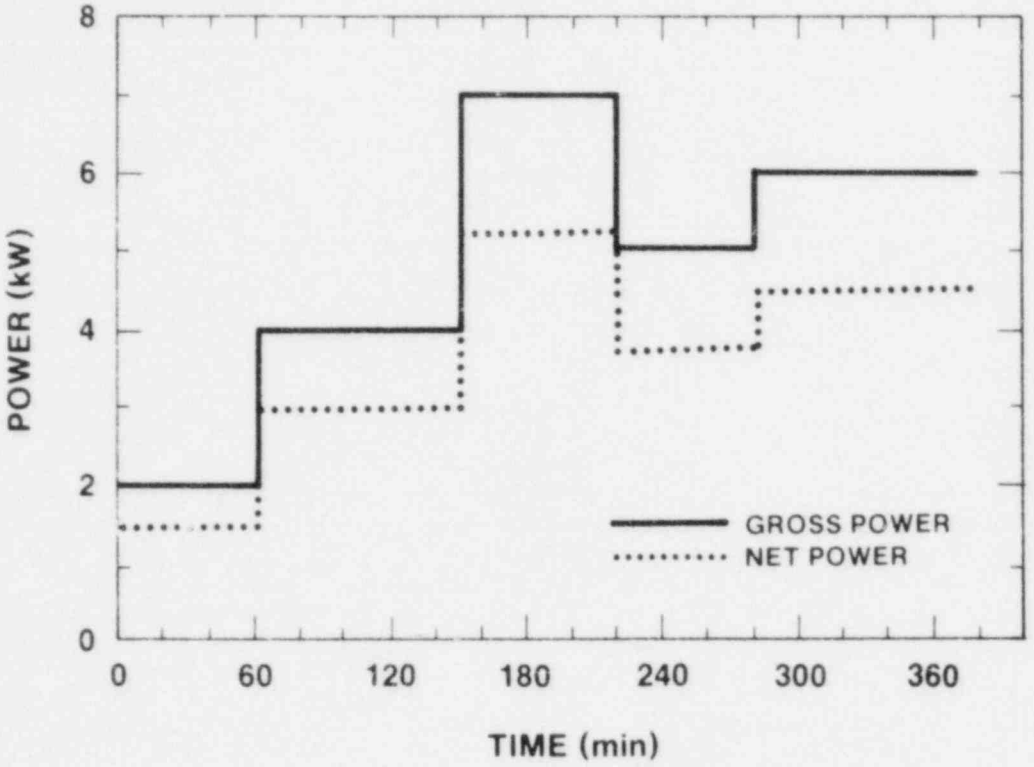

Figure 1.6. HSS-3 Power History

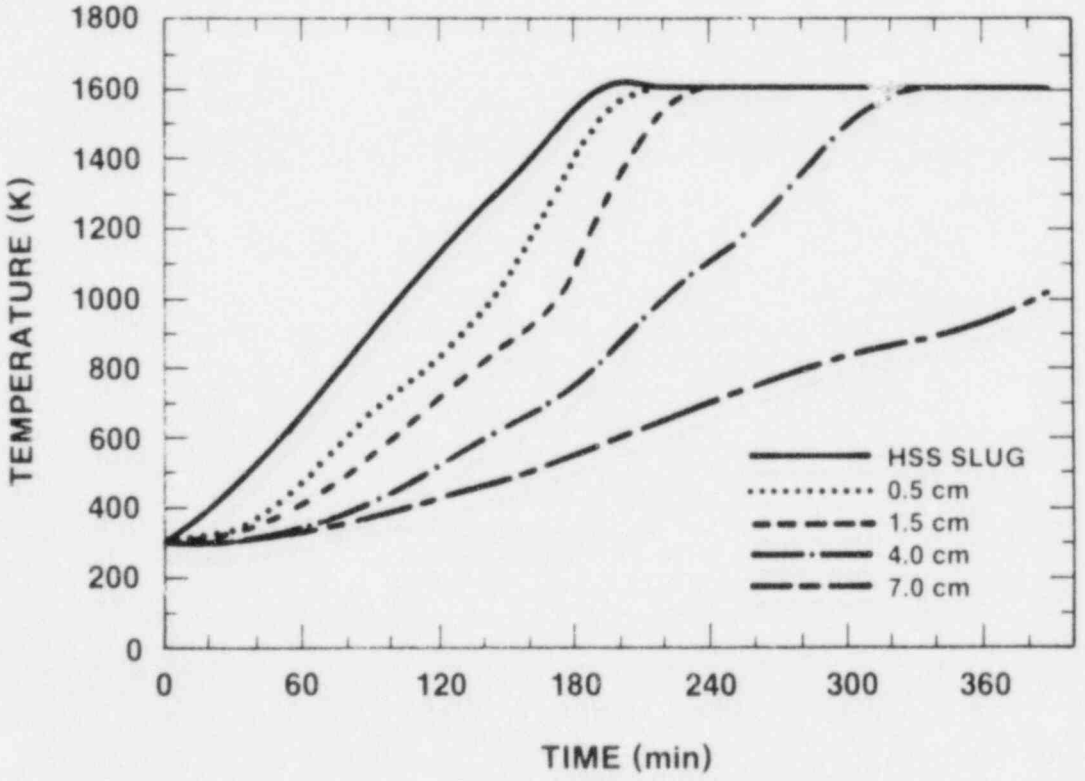

Figure 1.7. HSS-3 Thermal Profile

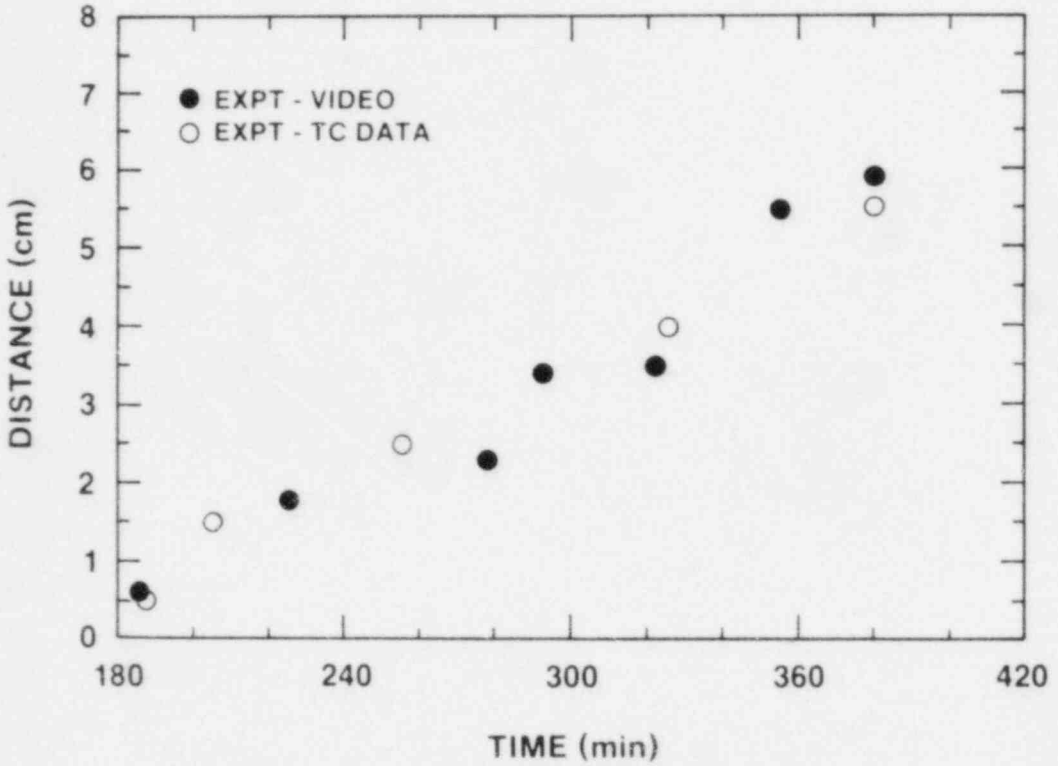

Figure 1.8. HSS-3 Erosion Distance

pressurized reactor vessel. Early experiments have established that molten materials can be expelled from the cavity into the containment atmosphere. The early experiments have shown also that expulsion of melt from the vessel and from the cavity is accompanied by intense aerosol generation, and that debris lofted from the cavity into the atmosphere can react chemically with the atmosphere and can exchange heat with the atmosphere rapidly. Crude analyses of the reactions and the heat transfer have suggested the containment pressurization by rapid heating of the atmosphere could be critical.

Progress was made in the High-Pressure Melt Ejection and Direct Containment Heating task in three areas during the report period:

1. A large-scale test (Test HIPS 6W) of pressurized melt ejection into a wate filled reactor cavity model was run.

2. Design of a containment model to allow quantitative evaluation of the atmosphere heating by expelled debris was completed.

3. Development of models of the ejection process, based on results of past tests, was undertaken.

In the early, analytic exploration of the pressurized melt ejection phenomena (Zion Probabilistic Safety Study, Commonwealth Edison, 1981) it was contended that water in the reactor cavity would not interfere in the dispersal of debris from the cavity. Test HIPS 6W was intended to verify this hypothesis. The test involved the expulsion of 80 kg of molten iron and aluminum oxide into a model at 1:10 linear scale of the reactor cavity of a modern, large, pressurized water reactor. The cavity was completely filled with water. A previous test in the program analogous to HIPS 6W had been interrupted because steam generation within the cavity overpressurized and failed the test fixture. For test HIPS 6W, the test fixture was strengthened substantially to avoid interruption of the test.

The early events of test HIPS 6W proceeded as predicted. A water slug was expelled from the cavity opening. Analyses of videotape records of the tests suggest that the water in this slug was highly fragmented. The cause of the fragmentation is not known. The water was moving at too low a velocity to disintegrate into fine droplets as a result of so-called "Weber breakup."

The emerging water slug was followed by expelled melt. The melt was actually traveling faster than the water slug. The two slugs intersected above the cavity opening.

About 300 msec after the start of pressurized melt ejection, a violent explosion occurred. The explosion hurled the upper portion of the test apparatus about 11 ft into the air. The lower portion of the reinforced concrete and steel fixture had been ripped away from the upper portion of the fixture. The general impression gleaned from test records is that a violent melt/coolant interaction (steam explosion) took place. Crude estimates based on the damage to the test fixture and the loft of the upper portion of the test fixture indicate that at least 4 percent of the available thermal energy from the melt was converted into mechanical work during the explosion.

The explosion leaves the question of the effects of water on debris dispersal incompletely answered. Early in the expulsion process, it appeared both melt and water were being expelled from the cavity. Fragmentation of the water slug and intermixing of the water above the cavity opening had not been anticipated and could have ramifications on the ability of expelled debris to raise the atmospheric temperature. However, interruption of the test by the steam explosion makes it impossible to say if all the debris expelled from the cavity would be intermixed with water. A steam explosion, so damaging to the test fixture, would be unlikely to damage most reactor cavities. Debris lofted into the containment atmosphere by a steam explosion would have, however, a qualitatively different effect on containment pressure than debris unassociated with water.

The steam explosion in test HIPS 6W as well as the overpressurization in a previous, similar test make it apparent that the existing test apparatus is inadequate for studying the effects of water on debris dispersal. Strengthening the cavity model for test HIPS 6W simply allowed a greater pressure rise in the cavity and consequently a more violent disassembly of the apparatus. Consequently, further studies of the effects of water on debris dispersal are being deferred in the program until a more suitable test fixture can be designed.

Discounting the remaining questions concerning the effects of water on debris dispersal, it is apparent that behavior of the debris following dispersal is the critical unknown in the pressurized melt ejection process. Analyses to date of the postdispersal have been crude simply because of lack of data. Among the unknown features of debris behavior are:

1. The trajectory of expelled debris particles and droplets, especially when structures with reactor containments block easy pathways for the debris.

2. The rate of heat transfer from the debris to the ambient atmosphere.

3. The rate of reaction of the atmosphere with the debris and the competitive reaction rates of steam and oxygen with the debris.

To investigate these unknowns it is necessary to confine the expelled debris into a chamber analogous to a reactor containment. A chamber of this sort was designed for the program during this report period. The chamber is to be made of steel. It will have a volume of about 93 m^3. Its height and diameter are 13 and 4 m, respectively. It will have a pressure rating of 150 psig and a maximum service temperature of 345°C. The vessel will be steam jacketed so it can be used with steam atmospheres. Many penetrations

varying in diameter from 1 to 3 ft are provided in the chamber for instrumentation and visual diagnostics. Structures analogous to those found in reactor containments may be assembled within the chamber.

Analyses of the pressurized melt ejection process during the report period have focused on the behavior of melt within the vessel and during expulsion from the vessel. Draft copies of the findings in these studies have been forwarded to the NRC program monitor. Some especially substantive results are as follows:

1. Ablation of the hole in the vessel by streaming melt has been modeled and the model has been found to compare well with experimental data. The model predicts ablation at a rate about twice that predicted by earlier models.

2. Recoil of the vessel during pressurized melt expulsion, while large, is unlikely to be of safety significance during an accident.

3. Simultaneous melt and gas expulsion through a penetration in the vessel can occur, but only when the head of the melt becomes small. Thus, if all the core is molten, simultaneous gas and melt expulsion will occur once nearly 80 percent of the melt has been expelled.

The latter point, simultaneous melt and gas expulsion, is quite important. Some have suggested that this simultaneous expulsion might prevent some of the more dire direct heating consequences of pressurized melt expulsion. Quite the opposite, simultaneous expulsion of gas and melt would cause the melt to be finely fragmented and easily transported out of the cavity region into the larger containment volume. The analytic result obtained concerning simultaneous expulsion suggests relatively small amounts of the melt would be subjected to this efficient fragmentation process. Even so, the result suggests the aerosol source term associated with pressurized melt ejection, currently thought to amount to 1 to 2 percent of the expelled melt, may be as much as 20 percent of the expelled melt.

1.3 CORCON

(D. A. Powers, 6422; D. R. Bradley, 6425)

CORCON predictions were compared to results of some of the recent TURC tests. The TURC tests involved deposition of nominally 200 kg of high-temperature melt onto a limestone/common sand concrete slug held in a magnesia annulus. Four tests were run in the TURC test series:

TURC1T: The melt in this test consisted of iron and aluminum oxide prepared by metallothermic reaction.

TURC1SS: The melt in this test was type 304 stainless steel.

TURC2: The melt was UO_2 plus 25 w/o ZrO_2.

TURC3: The melt was similar to that used in test TURC2 except 10 w/o zirconium metal was added.

All test melts were doped with materials that would be radionuclides in a reactor accident.

Comparisons of CORCON predictions have been made with results of the first three TURC tests. In summary, the results of the comparisons are:

1. Comparison to TURC1T: Both CORCON mod1 and CORCON mod2 predict well the rate and extent of concrete erosion observed in this test.

2. Comparison to TURC1SS: Both CORCON mod1 and CORCON mod2 underpredict by about a factor of two the concrete erosion observed in this test.

3. Comparison to TURC2: Both CORCON mod1 and CORCON mod2 greatly overpredict the extent of concrete erosion observed in this test.

A notable feature of the test comparison has been the similarity of predictions from CORCON mod1 and CORCON mod2. Only in the case of test TURC2 was there a significant difference between predictions by the two versions of CORCON.

The underprediction of concrete ablation for test TURC1SS is being attributed to the model of heat transfer from the melt to the concrete. CORCON uses the so-called "gas film" model. This model was devised many years ago based on experiments in which hot liquids were poured onto dry ice. The wholly inappropriate analogy between the simulant experiments and actual melt attack on concrete has been decried for several years. The model devised from the simulant experiment has retained a certain credibility largely because of its analytic simplicity. Alternative models exist in the literature. Some of these alternatives include models in which the incipient melt layer on the surface of the concrete limits heat transfer, models based on the relative density differences between melt and concrete, and models based on the local convection created by formation and detachment of bubbles at the melt/concrete interface. None of these models really recognize the unique features of concrete and the attack on concrete by high-temperature melts.

Clearly, one area where CORCON will need modification is in the area of melt-to-concrete heat transfer. Recent thoughts on liquid-liquid heat transfer with bubble agitation suggest that the so-called interlayer heat transfer coefficients (heat transfer between the oxidic and the metallic phases of a melt) also need reexamination.

Overprediction of concrete erosion in the TURC2 test comes about because the CORCON model failed to predict an interfacial crust observed to form immediately upon melt/concrete contact in the experiment. Two features of CORCON merit examination to correct this failure:

1. The interfacial contact temperature models in CORCON appear incorrect, and

2. The rates at which the liquidus and solidus properties of the oxide phase change as concrete is incorporated into the melt need to be examined.

1.4 Molten Fuel-Coolant Interactions

(M. Berman, 6427; B. W. Marshall, Jr., 6427)

1.4.1 Experiments, Data Reduction, and Analysis

1.4.1.1 FITSD Experiments

(B. W. Marshall, Jr., 6427; M. S. Krein, 6427; M. Berman, 6427)

No experiments were conducted in the "D" series during this period. We have, however, begun to develop a 50-kg melt-mass capability for use in four of the D experiments. This effort is being conducted in the new EXO-FITS facility described in Section 1.4.1.2, and has been designated as the Melt Development-extended (MDX) series.

1.4.1.2 EXO-FITS Experiments

(B. W. Marshall, Jr., 6427; M. S. Krein, 6427)

Construction of the new EXO-FITS facility (Figure 1.9) is complete, including assembly of the instrumentation wiring, control, and power lines. This facility has been designed to deliver 50-kg iron/alumina charges to various sized water chambers and from various drop heights up to 1.88 m.

Three experiments were conducted to develop the capability of preparing and delivering a 50-kg iron/alumina thermite charge into a 61-cm water chamber. This capability will be used in the completion of the FITS-D series described in Section 1.4.1.1. Secondary purposes are to: (1) ensure experimentally that the water-phase-pressure measurements are correct, (2) measure experimentally the melt temperature during drop, and (3) determine experimentally whether x-rays can be used to define the melt geometry before entry and

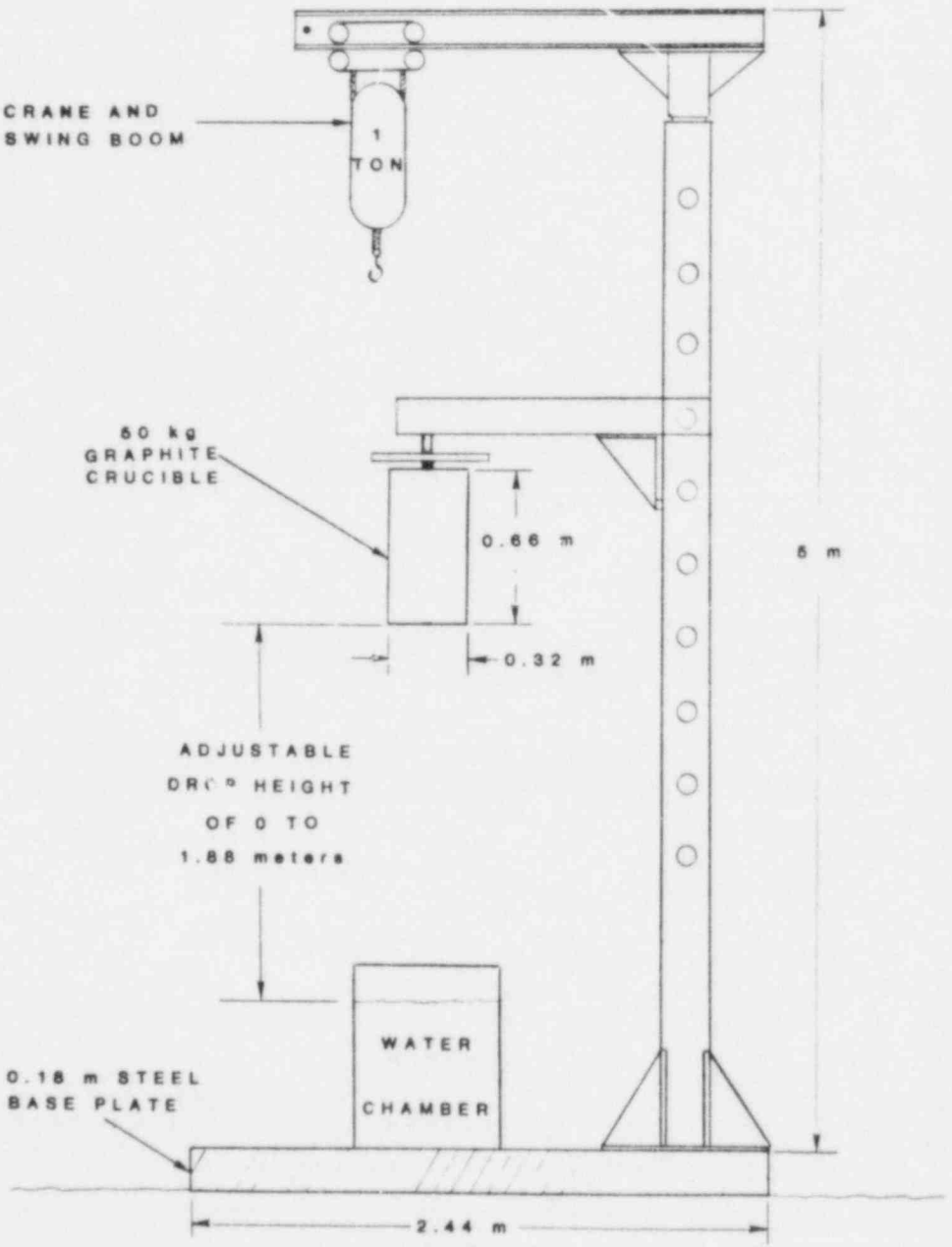

Figure 1.9. 50-kg EXO-FITS Facility

during the fuel-coolant mixing processes. The water-phase gauge measurements will be checked by comparing gauges within the same mounting structure.

This test series has been named the MDX series. The initial conditions of the three experiments conducted to date are shown below.

	MDX-1	MDX-2	MDX-3
Water Chamber	Lucite	Lucite	Lucite
Water Cross Section	61 cm	61 cm	61 cm
Water Depth	61 cm	61 cm	30.5 cm
Water Temperature	290 K	280 K	283 K
Melt Mass (loaded)	50 kg	50 kg	50 kg
Drop Height	1.8 m	1.8 m	1.8 m

The data collected during these experiments included six to ten water phase pressure gauges, a two-color optical pyrometer measurement of the melt temperature, and control signals (i.e., burn probes, drop signal, etc.).

Steam explosions were observed in all three experiments. The new EXO-FITS facility is operating well, with very few problems. The delivery of a 50-kg iron/alumina charge appears similar to that of the 20-kg melt, even though the L/D ratio of the 50-kg crucible is approximately twice that of the 20-kg crucible. The diameters of the two crucibles were chosen to be approximately equal, since the L/D ratio could not be exactly matched (due to geometric constraints within the FITS vessel). In the first experiment, a small amount of molten thermite leaked from the crucible containment prior to drop, but the main mass appeared to enter the water in a coherent state. In the second experiment, the melt dropped with no problems. From 600-keV flash x-rays taken during this experiment (the first time we tried to take x-rays of melt entry) the melt appeared to be in one uniform mass at melt/coolant contact. In the third experiment, the melt did not release from the crucible at the time of drop. The high-speed camera data revealed that the stainless steel lid fell free at the time of drop but the graphite lid did not, allowing only small amounts of molten thermite to escape. This has happened on a few occasions in past FCI experiments. Special precautions in assembly will be taken to prevent this in future FCI experiments.

The water-phase pressure data are currently being analyzed. To further validate the water-phase pressure measurements, a series of high-explosive experiments that will simulate a steam explosion are being proposed. Details of these experiments will be discussed in subsequent reports.

1.4.1.3 Experimental Analysis of the Iron/Alumina Thermite (B. W. Marshall, Jr., 6427; G. B. StClair, 6427)

The major efforts in this area were in the reduction and interpretation of the experimental data from the enclosed thermite burns performed to date. Work is continuing in this area and a topical report is currently being prepared.

The experimental measurement of the heat content of the molten thermite was investigated during this period by the Thermophysical Properties Division. The instrument that will be used is essentially a bomb calorimeter with freon as the heat absorption media. The thermite will be ignited in a small cavity that is surrounded by liquid freon. The measurements of the freon properties (such as temperature, gas generated during the process, etc.) will allow us to calculate accurately the heat content of the thermite. Additional measurements may include specific heat content of the thermite reactants and an estimation of the temperature of the molten material. This work was begun during this reporting period and should be completed by the summer of 1985.

The iron oxidation states of the iron/alumina thermite before and after the baking processes are being evaluated using x-ray diffraction and Mössbauer techniques available at Sandia. The importance of these analyses is that different oxidation states will change the stoichiometry of the mixture and, therefore, the heat content and temperature of the melt. The results from these analyses will also be reported as they warrant.

1.4.1.4 Analysis of the FITSD Experiments (O. Seebold, 6427; B. W. Marshall, Jr., 6427; M. Krein, 6427)

Analysis of the FITS particle debris to determine the oxidation state continued. If the oxidation state of the debris materials can be established with reasonable certainty, the mechanisms for the generation of hydrogen can be experimentally identified. To date, x-ray fluorescence, x-ray diffraction, and scanning electron microscopy have been unable to quantitatively establish the oxidation state of the iron. However, it was qualitatively determined that a substantial amount of the metallic iron had formed an oxidized compound with the alumina, called hercynite ($FeAl_2O_4$).

Further work in this area is currently awaiting the arrival of a cobalt source used in a Mössbauer technique to determine the oxidation states of iron. It is hoped that this technique will provide insight into the oxidation states and possible mechanisms governing the processes during an FCI.

If the Mössbauer study does not provide this information, wet-chemistry analysis of the debris will be pursued.

A Hicks-Menzies thermodynamic model of steam explosions (developed by Dr. K. McFarlane of the (UKAEA) Safety and Reliability Directorate) has been implemented on the VAX for use in analyzing the FITS experiments and for developmental work on the SEALS facility. Seventy input cases have been run and the results are under examination.

In addition to this case study, the initial test parameters for the FITS-5D experiment were input and compared to the test results. As shown in Figure 1.10, if the theoretical final state pressure is plotted against the mass ratio (mass coolant/mass fuel) and compared to the experimental quasi-static pressure plateau, the range of coolant mass that participated in the FCI can be bounded, assuming a given fuel mass (i.e., the melt dropped to the water chamber).

1.4.2 Model Development and Applications

1.4.2.1 Modeling of Explosion Propagation and Structural Loading Using CSQ-II

(K. L. Schoenefeld, 6425; M. Young, 6425)

During this reporting period, the hydrodynamic code CSQII was used to estimate peak pressures, impulse, and kinetic energy in the proposed SEALS facility. Modeling of the FCI was performed, as in previous modeling of the FITS series of FCI experiments, using the high-explosive option in CSQII. The calculation included three materials: steam/water mixture (assumed to be the burning material), water, and air and in the approximate geometry shown in Figure 1.11.

The assumed initial conditions for the CSQII calculations are summarized below:

Steam-Water Mixture ("burning" material)

Mass - 3694 kg
Density - 630 kg/m^3
Temperature - 368 K
Pressure - 0.083 MPa
Total Energy - 3.69 x 10^9 J (total energy released)

Water

Mass - 1992 kg
Density - 997 kg/m^3
Temperature - 298 K
Pressure - 0.083 MPa

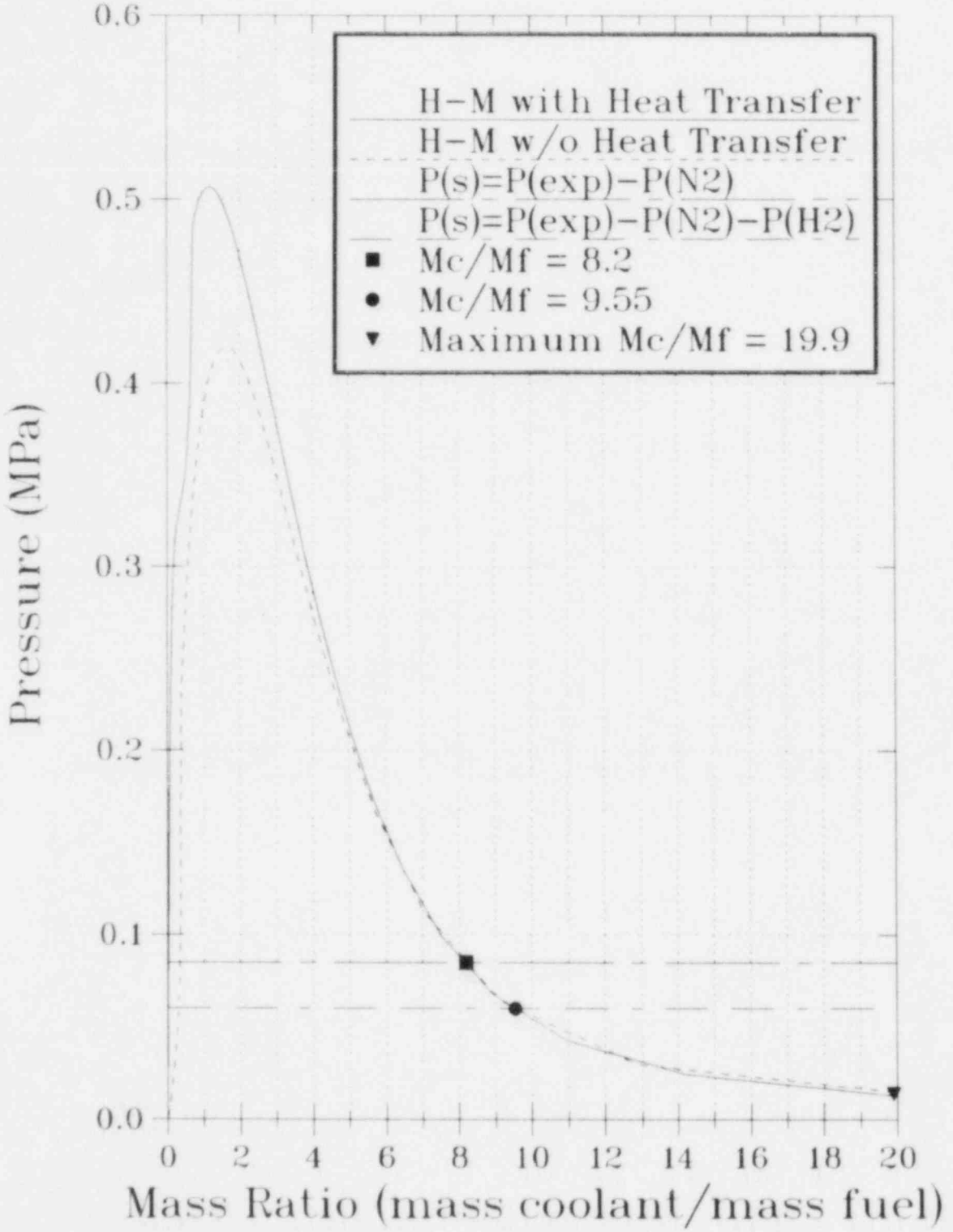

Figure 1.10. FITS-5D: Comparison of Hicks-Menzies Final State Pressure to Quasi-Static Pressure Plateau

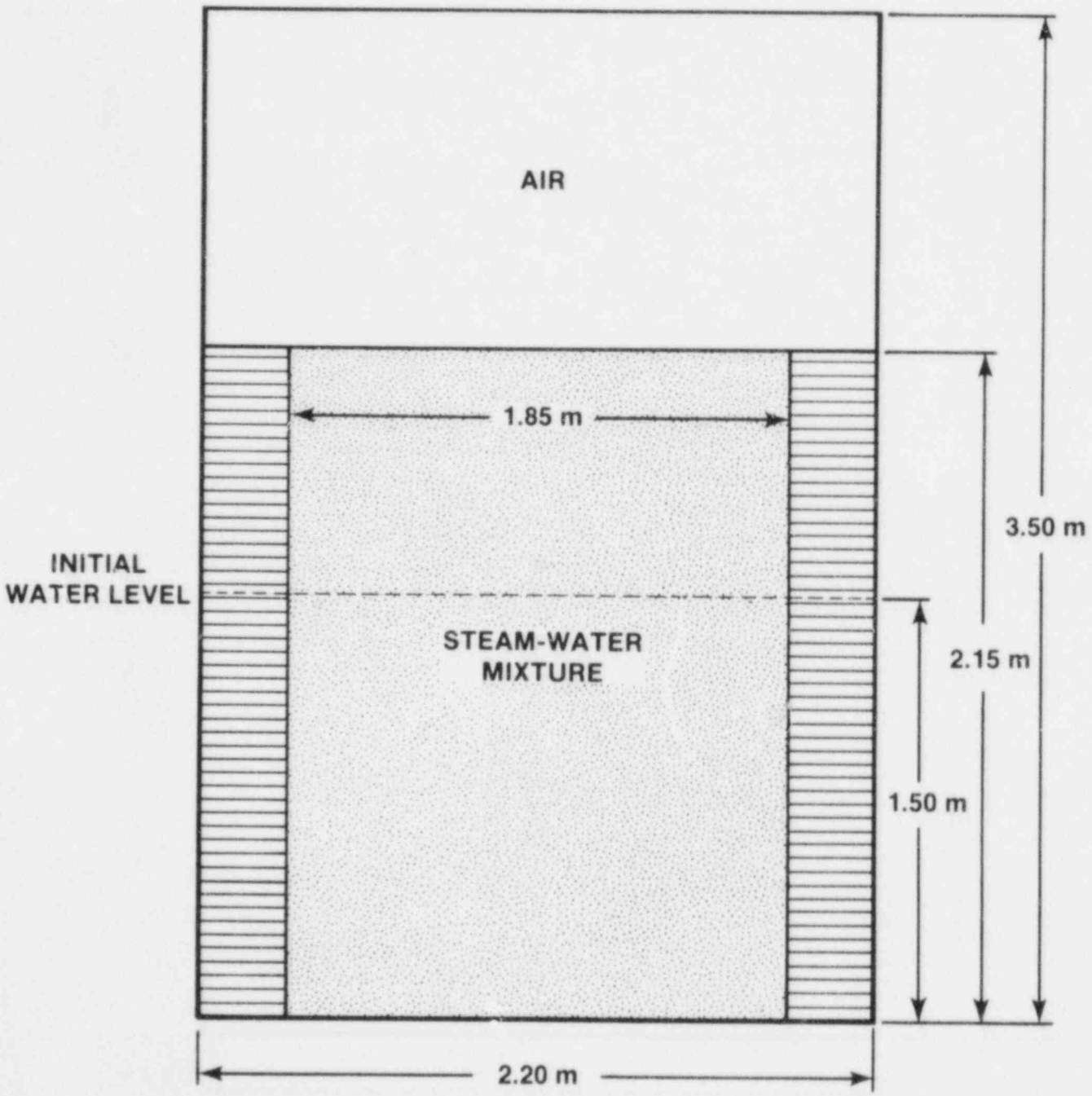

Figure 1.11. SEALS Chamber Geometry for CSQII

Air

Mass - 5.1 kg
Density - 1 kg/m^3
Temperature - 293 K
Pressure - 0.083 MPa

The cell size assumed for the finite difference mesh was 0.05 m x 0.05 m.

The values for the total energy input in the fuel, mass of water in the mixture region, and the macroscopic density and volume of the mixture region were scaled up from the FITS3B test. This was done by determining the ratio of the mass of water in the mixture region to the mass of fuel and the specific energy in the fuel in FITS3B (again from CSQII calculations). The overall geometry and mass ratios in the proposed SEALS facility are close to those in the FITS facility.

The results of the CSQII calculations, shown in Figure 1.12 indicate that the peak pressure pulse at the trigger point (bottom center of the cylindrical mixture region) reaches approximately 9.5 MPa. At the top of the vessel in the center location, a pressure peak of 19 MPa occurs at approximately 12 ms, as shown in Figure 1.13, corresponding to the time of arrival of the shock wave from the water surface. This is followed by a pulse of 16 MPa at 14 ms, corresponding to the time of impact of the two-phase slug with the chamber head. This slug is composed of a water-steam mixture; the pressures transmitted to the chamber head on impact depend on the behavior of the gas-liquid mixture in the slug when impacting the head. The pressure at a point near the bottom of the chamber wall, as shown in Figure 1.14, indicated a ringing in the single-phase water region with a peak pressure of about 77 MPa. Peak kinetic energies in the system as shown in Figure 1.15 were nearly 27.5 MJ at 9.8 ms. The conversion ratio of peak kinetic energy to input thermal energy for this system is 0.4 percent. Density plots shown in Figure 1.16 indicate that the material moving upward along the chamber wall is moving more rapidly than that in the center of the region.

1.4.2.1.1 BUBBLE Modeling of SEALS

The SEALS facility was also modeled using a version of the BUBBLE program. The approach was first used at LANL to approximate the behavior of an expanding two-phase bubble of fuel in a pool of sodium in a LMFBR as a check on the SIMMER hydrodynamics code. The current version is adapted to the behavior of an expanding two-phase bubble of water-steam in

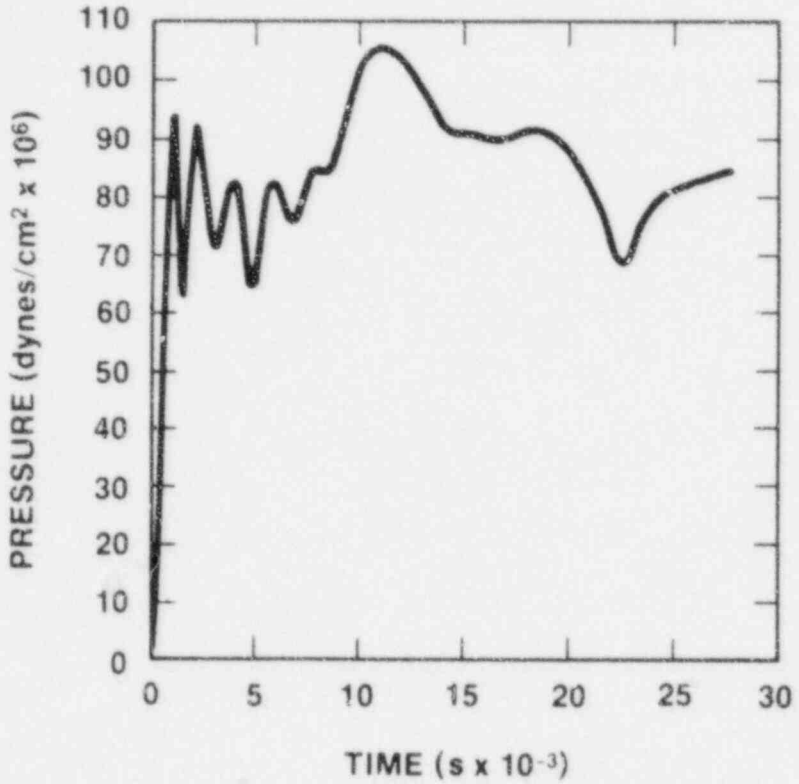

Figure 1.12. Pressure at Bottom Center of Mixture Region

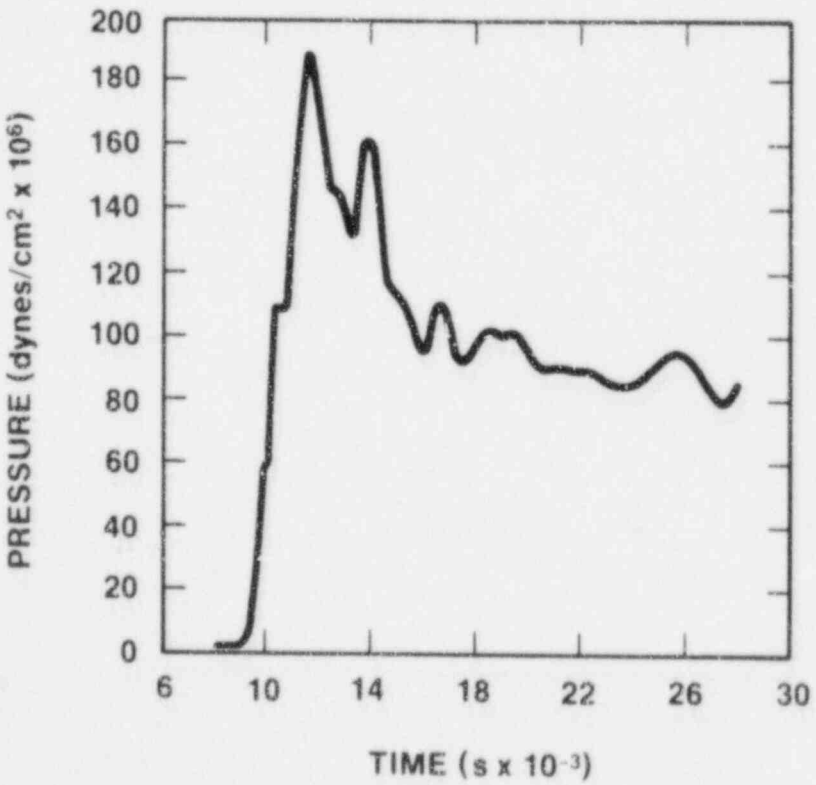

Figure 1.13. Pressure at Top of Vessel

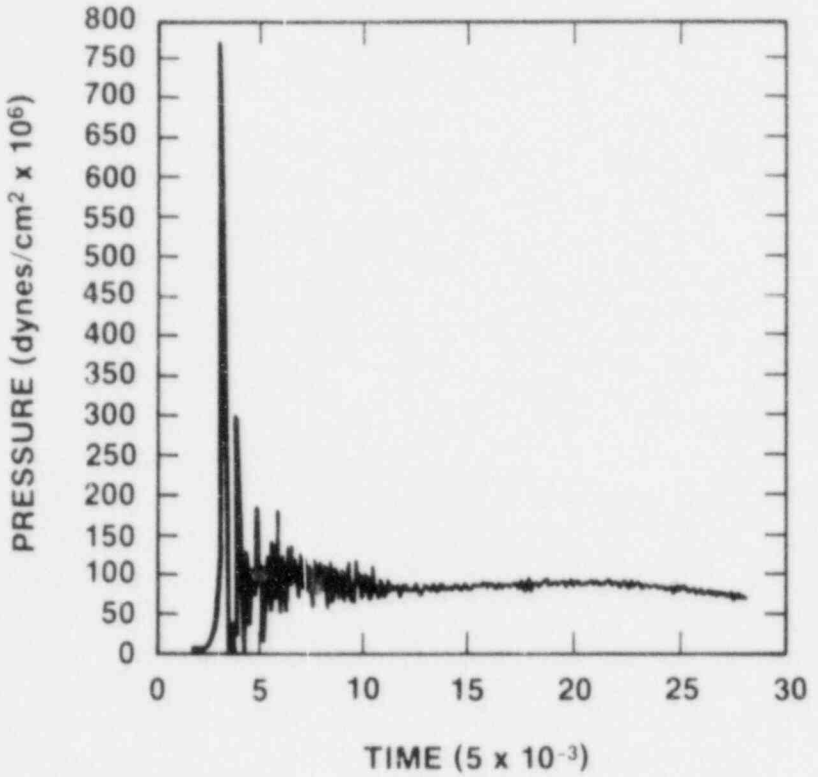

Figure 1.14. Pressure Generated Along Vessel Wall Near Bottom

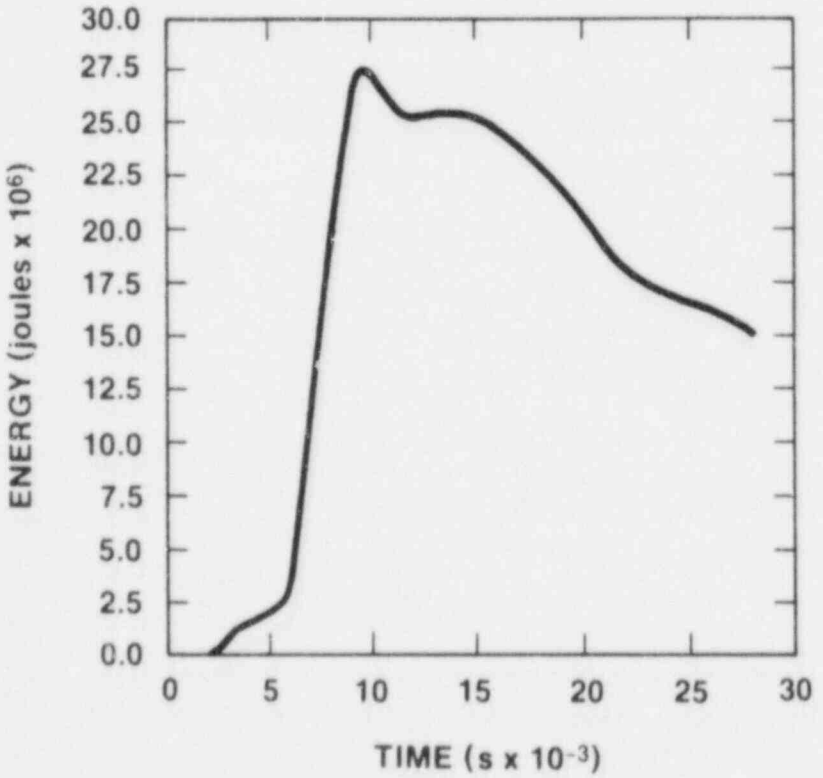

Figure 1.15. Kinetic Energy of All Materials

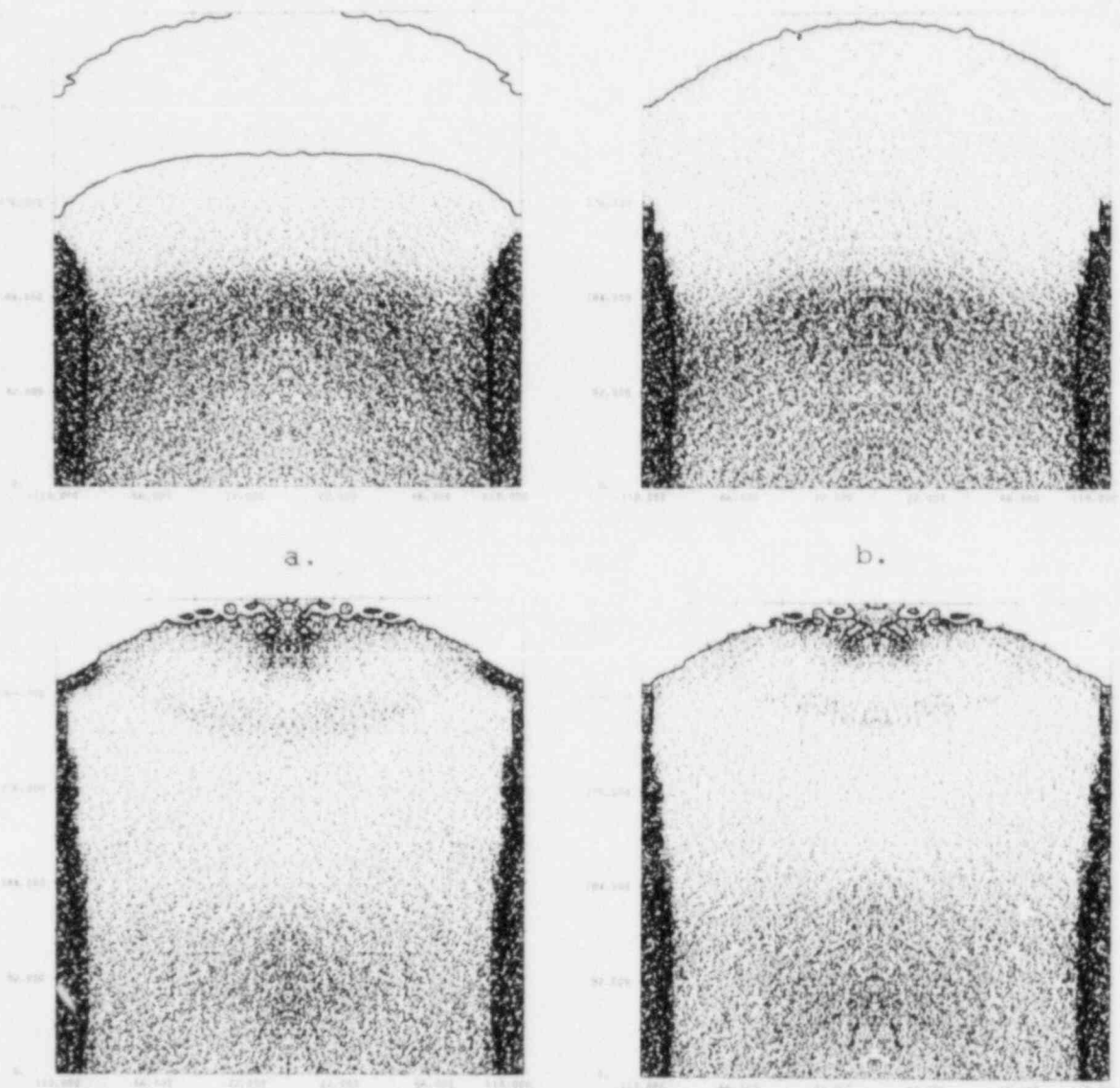

Figure 1.16. Material Density Plots Within SEALS Vessel at Times: (a) 0.008 s, (b) 0.010 s, (c) 0.016 s, and (d) 1.83 s

a water pool. A compressible volume of air above the pool is also included for these calculations.

The BUBBLE code assumes that the behavior of an FCI in a pool can be treated as a heatup of a two-phase mixture on the saturation curve; the bubble pressure (not to be confused with the wall pressures) is then totally determined by the internal energy of the mixture. Further assumptions are made that the expansion of this two-phase mixture is essentially that of a spherical bubble expanding isentropically, and that the rate of expansion can be determined by the Rayleigh equation. The initial rise time is assumed to be primarily determined by the heat transfer rate from the hot fuel to the two-phase mixture.

Using a total change in the water-steam energy of 3.2×10^9 J and the same initial conditions described above in Section 1.4.2.1, the peak bubble pressure was 13.7 MPa at 1.4 ms as shown in Figure 1.17. The peak kinetic energy was also calculated to be 29 MJ at 5 ms just before the slug hit the top of the chamber, with a velocity of 105 m/s (Figure 1.18), which corresponds to a conversion ratio of 0.9 percent.

1.4.2.1.2 Discussion of the Calculations

The energy change in the water-steam mixture, given above for the BUBBLE calculation, is actually the same as that occurring in CSQII for the total energy input to CSQII; the apparent difference is due to the way that the models in CSQII and BUBBLE approximate the explosion. CSQII heats up the entire mass of water-steam in the finite difference cells containing the mixture; this results in a heating of the two-phase mixture to a peak temperature of 605 K, corresponding to a saturation pressure of 13 MPa and a change in the internal energy of the two-phase mixture of 10^6 J/kg. A greater total energy is needed in CSQII since the code must raise the temperature of the water substituting for the iron/alumina thermite in the actual experiment as well as that of the water-steam mixture. In BUBBLE, the fuel is treated as an inert mass to be accelerated and its heatup is not modeled; therefore, the energy input corresponds to that needed to change the temperature of the water-steam only.

The motion of the bubble boundary has a small (20 percent) effect on the peak pressure, in that the energy input must be raised a few percent from that predicted on the basis of the thermal equilibrium of the fuel and water and the saturation pressure equation. As noted before, the rise time of the initial pressure peak in BUBBLE (and in the experiment) is basically the characteristic heat transfer time constant. In CSQII, the rise time is a function of the cell size and propagation speed, as the energy released from

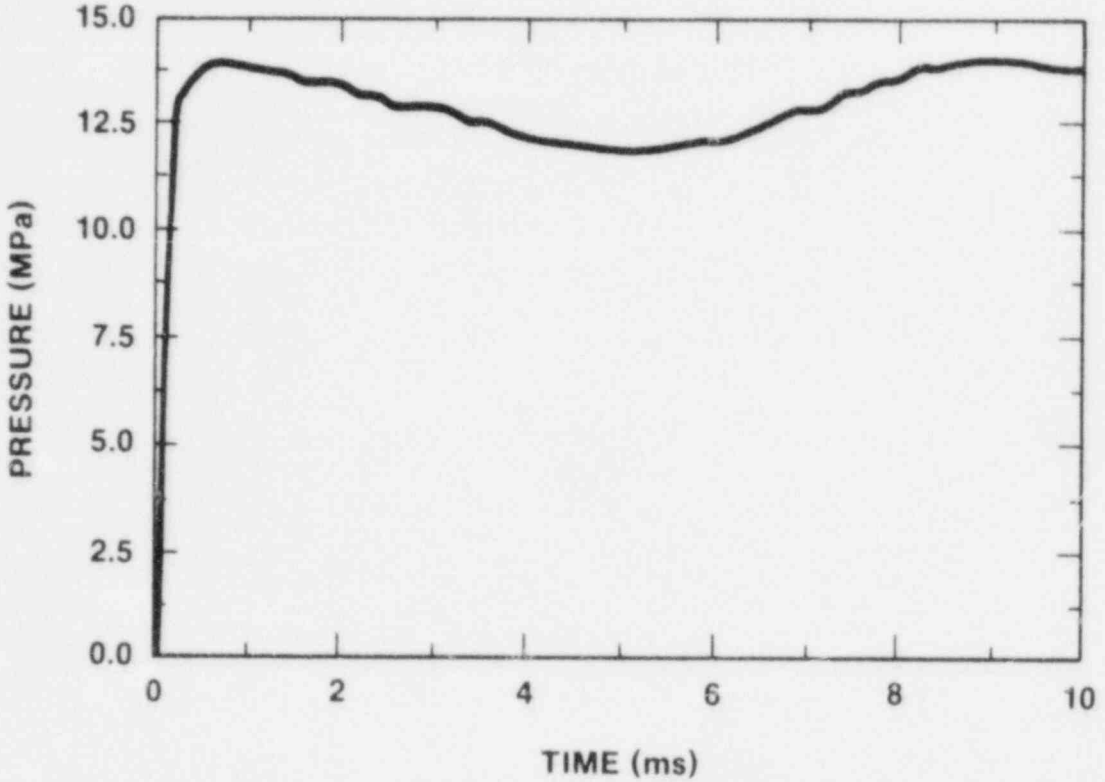

Figure 1.17. BUBBLE Mixture Pressure

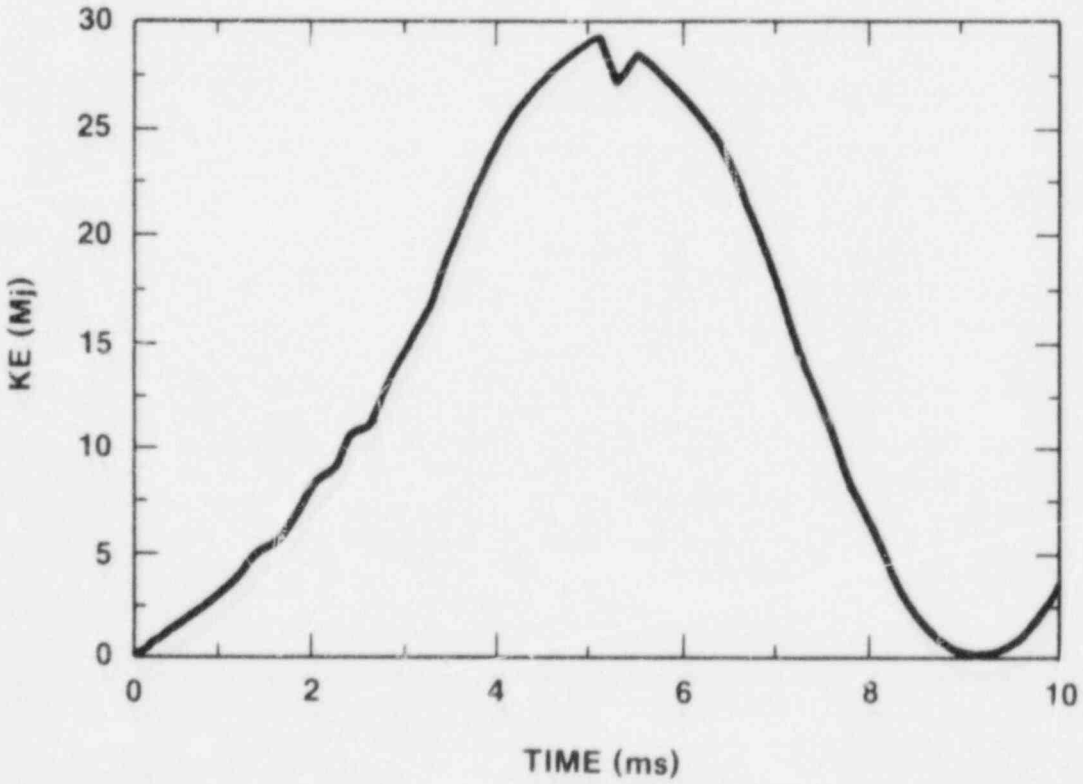

Figure 1.18. BUBBLE Kinetic Energy of All Materials

the iron is equilibrated with the entire cell contents instantly.

The impact times predicted by the two models seem fairly different (5 ms for BUBBLE vs. 14 ms for CSQII); most of this difference is from the acoustic relief time axially in the mixture region (about 11 ms), which is not included in the BUBBLE model. The material in the mixture region cannot move as a slug until this time has elapsed. The impact time from BUBBLE corresponds to the difference between the acoustic transit time and the CSQII impact time (14 ms), which is then seen to be fairly close to CSQII (3 ms). The BUBBLE results are also seen to oscillate because slowing of the slug in BUBBLE is solely by adiabatic compression of the cover gas, with no heat transfer, collapse of vapor bubbles in the slug, or other dissipative effects; the slug then behaves essentially as a harmonic oscillator. BUBBLE does not predict the impact pressure at the top of the chamber. This can be estimated from the slug velocity and material properties of the slug and head. Using typical values for the top (iron) and the two-phase mixture, and a velocity of 100 m/s at the slug top boundary, the impact pressure is roughly 50 MPa for a two-phase slug. However, as the slug collapses, its internal vapor bubbles and the slug properties approach those of a single-phase material (water). When this occurs, the impact pressure can rise to around 150 MPa.

1.4.2.2 Modeling of Coarse Fragmentation and Steam and Hydrogen Generation (WISCI)
(M. L. Corradini and C. Chu, UW)

We continued to modify the TEXAS computer program to include specific models for fuel fragmentation and mixing. The model initially installed into TEXAS will be the hydrodynamic fragmentation model of Chu. In addition to this modeling, we have found it necessary to change significantly the majority of the constitutive relations used in TEXAS to represent more accurately the multiphase system we are modeling; e.g., a modified flow regime map (similar to TRAC), more realistic drag coefficients, mass and transfer coefficients. We are initiating some benchmark calculations to compare the computer calculations to analytical results and experimental data.

1.4.2.3 Modeling of Coarse Fragmentation and Explosion Phases (TEXAS)
(M. L. Corradini and M. Oh, UW)

1.4.2.3.1 Nonequilibrium Parametric Explosion Model for Hemispherical Expansion

In our parametric model we included a more realistic hemispherical inertial constraint that can be applied to

weak wall chambers; e.g., like those used in FITS. The previous planar inertial constraint can be altered to this spherical geometry and still maintain the one-dimensional nature.

The mass and the energy balance equations do not change for the hemispherical expansion, compared to the planar expansion case.

The macroscopic momentum balance equation for the slug is altered to the form

$$\frac{dV_s}{dt} = \frac{R_o}{R_i^2 + R_o R_i}\left[\frac{P_i - P_o}{\rho_s} - \frac{2g}{\pi}(R_o - R_i) - V_s^2\left(\frac{3}{2} + \frac{R_i^4}{2R_o^4} - \frac{2R_i}{R_o}\right)\right] \tag{1.1}$$

where V_s = velocity of slug

g = acceleration due to gravity

R_i = inner radius of hemispherical shell-type slug

R_o = outer radius of hemispherical shell-type slug

P_i = pressure in the interaction zone

P_o = ambient pressure

ρ_s = density of liquid slug

t = time.

We again consider the breakup of the slug when the continuous phase of the interaction zone is vapor during the hemispherical expansion. We assume that the slug breaks apart when the critical Taylor instability wavelength is greater than the thickness of the hemispherical slug during the explosion expansion,

$$\delta_s = R_o - R_i < 2\pi \left|\sigma_f / a(\rho_s - \rho_g)\right|^{1/2} \tag{1.2}$$

where δ_s = thickness of the slug

σ_f = surface tension of coolant

a = acceleration of inner or outer interface

ρ_g = density of vapor phase.

1.4.2.3.2 A Local Fragmentation Model for the Explosion

In the original nonequilibrium model we chose to describe the fuel fragmentation process using an exponential rate law similar to what was done in the Cho-Wright FCI model.[1.1] However, we now have a conceptual picture of the fragmentation process for which the exponential model seems inadequate.

The explosion and fuel fragmentation process is composed of two parts: (1) fragmentation during the explosion propagation, and (2) fragmentation during the explosion expansion. We only model the first fragmentation and neglect the second fragmentation event since it occurs much later in time and would generate larger fragments that cool more slowly and do not significantly contribute to the conversion ratio.

We define the local fragmentation time, T_{frag}, as the actual time for fragmentation. This represents the times for coolant entrapment, expansion, overexpansion, collapse and cyclic repeating of this process until the system depressurizes and fragmentation ceases.

The diameter of the fuel fragment, D_{frag}, due to the explosion is not the mass average size as measured in FITS and as originally used in the previous Nonequilibrium Parametric Model. One can relate this D_{frag} to $D_{f,mass\ avg}$ by

$$D_{f,mass\ avg} = \frac{D_{frag}\Delta m_{f,frag} + (m_f - \Delta m_{f,frag})\, D_{non,frag}}{m_f} \qquad (1.3)$$

where

$$D_{non,frag} = \left[\frac{6(m_f - \Delta m_{f,frag})}{\pi N_{mix}\rho_f}\right]^{1/3} \qquad (1.4)$$

$$N_{mix} = \left[\frac{6m_f}{\pi\rho_f D_{mix}^3}\right] . \qquad (1.5)$$

In this model we assume a bimodal fragment distribution where large fragments are not to be fragmented past D_{mix} and small fragments are set parametrically to a value of $\Delta m_{f,frag}$.

Thus, the important question is how much of the mass is fragmented, $\Delta m_{f,frag}$, during the fragmentation time, T_{frag}.

From Equations (1.1) through (1.3), we find

$$0 = \left(m_f - \Delta m_{f,frag}\right)^{3/4} \left(\frac{D_{mix}^3}{m_f}\right)^{1/3} + \Delta m_{f,frag} D_{frag} - m_f D_{f,mass\ avg} \quad . \tag{1.6}$$

Therefore, one can solve for the unknown $\Delta m_{f,frag}$, which satisfies Equation (1.4), using Newton's numerical method.

We introduce a linear fragmentation model into the parametric model to mechanistically account for breakup to this size.

$$m_{fr} = \frac{m_{f,frag}}{T_{frag}} \qquad (t < T_{frag}) \tag{1.7}$$

$$= 0 \qquad (t > T_{frag}) \quad .$$

1.4.2.3.3 Analysis of the FITS Experiments

To use the Nonequilibrium Parametric Explosion Model in FITS experimental analysis, a consistent methodology to determine the initial and boundary conditions for the calculation was developed.

The important initial conditions for the parametric model are:

1. Mass of the slug, m_{slug}.
2. Mass of the coolant in the interaction zone, m_c.
3. Initial volume ratio of vapor coolant to liquid coolant in the explosion zone, V_{gi}/V_{ci}.
4. Mixing time, T_{mix}.
5. Initial mixing diameter, D_{mix}.
6. Fragmentation time, T_{frag}.

7. Local fragmentation diameter, D_{frag}.

8. Mass of fuel involved in the local fragmentation, $\Delta m_{f,frag}$.

Mass of the Slug

The slug is composed of the mixture of fuel and coolant. Therefore, the mass of the slug is equal to the sum of the mass of fuel and the mass of coolant.

$$m_{slug} = m_f + m_c \quad . \tag{1.8}$$

Mass of the Coolant in the Interaction Zone

It is important to estimate how much of the total coolant is involved in the actual interaction. The volume of water displaced in the interaction zone is

$$V_d = V_{mix} - V_{water} \tag{1.9}$$

where $$V_{mix} = V_{fuel} + V_{water} + V_{steam} \quad . \tag{1.10}$$

Using some simple FITS correlations,[1.2] we also know that

$$V_{mix} = 3\ (T^+)^2\ V_{fuel} \tag{1.11}$$

$$V_{water} = 1.5\ (T^+)^2\ V_{fuel} \tag{1.12}$$

where V_{mix} = volume of the mixture

V_{fuel} = volume of fuel

T^+ = dimensionless mixing time given by

$$T^+ = \frac{U_f T_{exp}}{D_{fo}} \left[\frac{\rho_c}{\rho_f}\right]^{1/2} \quad .$$

The average relative velocity of fuel, $U_{f,avg}$, can be obtained by the simple balance of inertial force, drag force, and gravity force which results in

$$\dot{U}_f = g - \frac{4}{3}\frac{C_d}{D_{fo}}\frac{\rho_c}{(\rho_f - \rho_c)} U_f^2 \qquad (1.13)$$

where U_f = relative velocity of the fuel in coolant

C_d = drag coefficient depending on Reynolds number

D_{fo} = initial diameter of entering fuel

g = acceleration due to gravity

ρ_f = density of fuel

ρ_c = density of liquid coolant.

Based on the above analysis, the maximum possible mass of coolant which can be involved in the interaction is:

$$m_c = \rho_c V_{water}$$

$$= 1.5 (T^+)^2 V_{fuel} \cdot \qquad (1.14)$$

The use of this correlation to predict the coolant involved in the explosion is a very rough estimate. We are currently developing a more theoretically based approach.

Initial Volume Ratio of Coolant Vapor to Liquid

This ratio is necessary to determine the initial vapor volume fraction around the premixed fuel particles.

From Equations (1.1) through (1.4), the volume of steam in the zone is

$$V_{gi} = 1.5 (T^+)^2 V_{fuel} - V_{fuel} \cdot$$

Also the volume of coolant in the zone is

$$V_{ci} = 1.5 (T^+)^2 V_{fuel} \cdot$$

Therefore the initial volume ratio is given by

$$V_{gi}/V_{ci} = \frac{1.5\ (T^+)^2 - 1}{1.5\ (T^+)^2} \quad . \tag{1.15}$$

Initial Mixing Diameter

We believe that hydrodynamic effects may be more dominant that the thermal effects during the premixing stage of the fuel-coolant interaction. The important variables in the coarse mixing stage are the dimensionless mixing time and the Weber number.

Based on the hydrodynamic mixing model developed by Chu,[1.2] an exponential correlation of mixing diameter can be formulated as

$$D_f/D_{fo} = \mathrm{EXP}(-C(T^+)^m(We)^n) \quad , \tag{1.16}$$

$$\text{at } T^+ = 0 \quad D_f = D_{fo}$$

where $C = 0.163$, $m = 0.772$, $n = 0.246$

T^+ = dimensionless mixing time

We = Weber number given by

$$We = \frac{\rho_c\ U_f^2\ D_{fo}}{\sigma_f} \quad .$$

The upper bound of the mixing diameter would be the initial entering diameter of the falling fuel. From the detailed computer calculations of Chu or the simplified correlation one can find the mixing diameter as

$$D_{mix} = D_f \quad (<D_{fo}) \quad . \tag{1.17}$$

Mixing Time

The mixing time is the experimental time measured from the time of fuel entry into the coolant to the initiation of explosion in the experiments.

Fragmentation Time

The shock wave forms in the interaction zone due to rapid heat transfer and propagates through the mixture, with a velocity greater than the sound speed of the mixture, to the low-pressure free surface and transmits a low-pressure rarefaction wave back to the high-pressure interaction zone with the same velocity. As a result, the interaction zone responds by an expansion to equilibrate the pressure difference. Therefore, one can roughly equate this travel time as the fragmentation time.

$$T_{frag} = \frac{2L}{V_{prop}} \tag{1.18}$$

where V_{prop} = propagation velocity measured in the experiment

L = length from the interaction zone to the free surface.

Local Fragmentation Diameter

The local fragmentation time (discussed in Section 1.4.2.3.2) is defined as the time when the local rapid fragmentation occurs, which is the same as T_{frag}.

If the fuel fragmented is essentially quenched in a time of order $\sim T_{frag}$, D_{frag} can be estimated from simple transient conduction considerations. The quenching temperature of the fragmented fuel is a function of the Biot number and the Fourier modulus.

Let

$$\frac{T_f - T_c}{T_{fo} - T_c} = f(Fo,Bi) = 0.01 \tag{1.19}$$

where Fo = Fourier modulus

Bi = Biot number.

From the transient conduction chart for a sphere of Heisler,[1.3] the Fourier modulus can be obtained using the known values of quenching temperature and Biot number. To calculate the Biot number we need the information of heat transfer coefficient between the fuel particle and the surrounding medium.

The single-phase convective heat transfer coefficient for a sphere[1.4] is given by

$$h = \frac{k_c}{D_f}\left[2 + 0.6\left(\frac{D_f V_{rel}\rho_c}{\mu_c}\right)^{1/2}\left(\frac{C_p\mu_c}{k_c}\right)^{1/3}\right] \qquad (1.20)$$

where V_{rel} = local relative velocity between the fuel fragment as a sphere and the surrounding medium

D_f = diameter of fragmented fuel particle

ρ_c = density of coolant

μ_c = viscosity of coolant

C_p = heat capacity of coolant

k_c = thermal conductivity of coolant.

The minimum Biot number is obtained by assuming no relative velocity between fuel particle and coolant. In that case the heat transfer coefficient becomes

$$h = \frac{2k_c}{D_f} \quad . \qquad (1.21)$$

The minimum Biot number becomes

$$Bi = \frac{hD_f}{2k_f} = \frac{k_c}{k_f} \qquad (1.22)$$

where k_f = thermal conductivity of fuel.

Therefore, the maximum Fourier modulus is obtained from Heiser's chart. From the definition of Fourier modulus the minimum diameter of local fragmentation becomes

$$\text{min. } D_{frag} = \left[\frac{\alpha_f T_{frag}}{F_o}\right]^{1/2} \qquad (1.23)$$

where α_f = thermal diffusivity of fuel.

If we assume a large relative velocity between fuel particle and coolant, the heat transfer coefficient becomes large and provides an upper bound Biot number. Then the Fourier modulus converges to one, under the condition of fixed center temperature of fuel. Therefore, the maximum diameter of local fragmentation is:

$$\max. D_{frag} = \left|\alpha_f T_{frag}\right|^{1/2} . \qquad (1.24)$$

Based on the above analysis, we can estimate the upper bound and the lower bound of local fragmentation diameter.

Mass of Fuel Involved in the Local Fragmentation

This value can be obtained using the local fragmentation concept proposed in Section 1.4.2.3.2.

We focus on a subset of the many FITS experiments conducted to date to investigate the following effects on the FCI.

1.	Composition;	Iron-Alumina/Corium
2.	Mass ratio;	$1.5 < m_c/m_f < 50$
3.	Subcooling;	$0°C < T_{sub} < 80°C$
4.	Ambient pressure;	$1 \text{ bar} < P_{amb} < 11 \text{ bars}$
5.	Chamber confinement;	planar/hemispherical
6.	Scale effect;	$5 \text{ kg} < m_f < 50 \text{ kg}$

Composition

Test MD-19 for Iron-Alumina and MDC-2 for corium will be investigated to examine the difference between iron-alumina molten core simulant and the corium A+R thermites.

Mass Ratio

A major objective of the FITS-B experiments was to study the effect of initial water/fuel mass ratio on the triggering and conversion ratio of the iron-alumina system. Test FITS-7BR will be analyzed for the low mass ratio and test FITS-9B for the high mass ratio case.

Subcooling

Test FITS-6B will be analyzed to investigate the effect of saturated water on the FCI characteristics and test FITS-3B for the effect of subcooling on the FCI.

Ambient Pressure

Test FITS-5A was done to study the effect of high ambient pressure on triggering and to determine if an external trigger source would initiate an explosion.

Chamber Confinement

Most of the FITS and EXO-FITS experiments were done with the weak chamber walls like lucite. The lucite chambers offered no structural resistance to the expansion phase of the steam explosion process. Therefore, the geometrical expansion characteristic was nearly a hemispherical expansion. Test RC-2 was a rigid wall confinement experiment, which determined the effect on the explosion phase of the FCI due to radial confinement by a steel wall.

1.4.2.4 Modeling of Film Collapse and Fine Fragmentation (M. L. Corradini and B. Kim, UW)

The modeling of small-scale single droplet fuel-coolant interactions is conceptually divided into four stages:

1. Film boiling around a molten fuel droplet: As soon as the fuel droplet submerges in the coolant, film boiling begins instantly due to the high heat flux from the fuel droplet. This was investigated in our previous work. The film boiling around the sphere enters into a steady-state condition after some initial oscillations of the vapor-coolant interface as a result of the rapid evaporation, overexpansion, and collapse of the film. Under certain conditions these oscillations may be prolonged and violent. This film growth stage provides the initial conditions for subsequent fuel-coolant interactions.

2. Film collapse and jet formations: Due to some triggering mechanism (for example, an external pressure pulse, contact with the solid wall or overexpansion of the film and condensation), the vapor film begins to collapse. When the vapor-coolant interface is accelerated toward the coolant, the interface becomes unstable and the Taylor instability disturbance grows. The spikes of the interfacial instabilities form an array of coolant jets directed toward the fuel all over the surface.

3. Jet penetration and entrapment in the fuel: Under certain conditions, the jets grow so fast that they contact the fuel surface and even penetrate the fuel. As a result of these needle-like jet penetrations, numerous tiny coolant drops with vapor film surrounding them are entrapped in the fuel near the surface, which seems to form a shell of the mixture of vapor and coolant drops.

4. Expansion and fragmentation of the fuel: Violent evaporation of the entrapped coolant drops leads to the expansion of the mixture against the surrounding fuel. The outer portion of the fuel seems to be separated from the parent fuel droplet and forms a shell with vapor film. During the continuous expansion of the mixture, any one side of the fuel shell is subjected to a Rayleigh-Taylor instability. The growth of surface disturbances finally results in the breakup of the outer fuel shell.

Consequently, this mixture of vapor, coolant drops, and fragmented fuel particles forms around the parent fuel droplet and expands. The high heat transfer rate from fragmented fuel particles enables the film to grow enormously. However, as the vapor film expands rapidly into the coolant, the condensation rate at the interface increases, the film stops growing and collapse begins again starting the whole process anew.

Because of the cyclic nature of the process, an initially small disturbance can grow. Under certain conditions the second and subsequent cycles may be weaker than the preceding ones and in these conditions the initial disturbance of the interface is stable and does not lead to an explosion. Under other conditions subsequent cycles are more energetic than the preceding ones and an explosion occurs.

Detailed accounts of each stage are as follows:

1. Film Boiling Around Fuel Droplet

Qualitative characteristics of the film growth and collapse were reported previously and the effects of the boundary conditions were also studied in detail.

2. Film Collapse and Jet Formations

As the film collapses due to an external pressure pulse, the vapor-coolant interface becomes unstable and any initial disturbances grow. Since the wavelength seems to be far smaller than the vapor film radius, planar Rayleigh-Taylor instability growth rate was initially used. In the linear mode, the amplitude of the disturbance grows exponentially.[1.5]

$$\frac{\eta}{\eta_o} = \exp(nt) \tag{1.25}$$

where η_o is an initial amplitude of the disturbance. The linear growth constant is given as[1.6]

$$\eta = \left[4k^2 \frac{(\mu_c+\mu_v)^2}{(\rho_c+\rho_v)^2} + \frac{(\rho_c-\rho_v)\, gk - \sigma k^3}{(\rho_c+\rho_v)} \right] - 2k^2 \frac{(\mu_c+\mu_v)}{(\rho_c+\rho_v)} \tag{1.26}$$

where subscripts c and v describe the coolant and vapor. As the amplitude grows beyond a distance equal to its wavelength linear growth rate is no longer valid. In the nonlinear growth stage, constant-velocity growth of the amplitude is observed and correlated as

$$V = C\sqrt{\lambda g} \tag{1.27}$$

where γ = wavelength

g = acceleration.

Lewis[1.7] reported the constant C to be 0.78 and Emmons 0.3.[1.8]

The linear growth phase is assumed to be dominated by the fastest-growing wave number, which is given as

$$k = \left| \frac{g(\rho_c-\rho_v)}{3\sigma} \right| . \tag{1.28}$$

As the radius of the film decreases, the planar theory becomes unreasonable in its application. Instability growth in spherical geometry is necessary for the understanding of the characteristics of the collapsing bubble, such as apparent heat transfer area increase and possible entrainment rate.

3. Jet Penetration and Entrapment

The resistance of a solid or liquid to the penetration by a liquid jet is a function of jet velocity and the geometry of the target. If the jet has a high enough velocity, the depth of penetration is controlled by the inertia of the target, but for lower velocities the mechanical strength of

the solid is the dominating factor. In the current modeling the fuel is assumed to remain as a liquid during the interactions; the temperature of fuel surface is higher than the melting temperature of the fuel.

Let a jet of density ρ_j and finite length l impinge with a velocity V_j on a fixed target, so that the jet length diminishes at the rate of $V_j - u$.[1.9] Relative to an observer moving with penetration velocity u, the phenomenon is stationary; the jet and the target approach a common stagnation point with velocity $V_j - u$ and u. Hence Bernoulli's equation applies in both media. Equating pressure at the stagnation point, one gets for inviscid flow

$$\frac{1}{2}\rho_j(V_j-u)^2 = \frac{1}{2}\rho_t u^2 \quad . \tag{1.29}$$

When the breakup factor, a dimensionless number which takes account of the jet breaking into particles, is included, the velocity of penetration is given by

$$u = V_j \Bigg/ \left[1 + \left(\frac{\rho_t}{\gamma\rho_j}\right)^{1/2}\right] \quad . \tag{1.30}$$

In fact, the breakup factor accounts for all the factors that produce changes from the simple derivation of Equation (1.30) from Equation (1.29) and varies from 0 to 1. The penetration depth is given by

$$L = l\left(\frac{\gamma\rho_j}{\rho_t}\right)^{1/2} \quad . \tag{1.31}$$

In this simple potential theory the effects of surface tension and viscosity are neglected. The process is assumed to be adiabatic where the vaporization of the jet during the penetration is not considered at all.

4. Expansion and Fragmentation of the Fuel

As a result of the jet penetration in the fuel and the breakup of jets, the fuel droplet has a cloud of vapor and coolant drops entrapped within it near the surface. The expansion of the mixture by the evaporation of the coolant drops induces the outer fuel shell to expand like a balloon. As it expands, the outer fuel shell becomes thinner.

A Rayleigh-Taylor instability can then grow on either side of this fuel shell. Consequently, the growth of the disturbance and the stretching of the fuel shell leads to the eventual breakup of the fuel shell. Under certain conditions it takes time for the fuel shell to be fragmented since the acceleration rate seems to be relatively low compared to tnat during the film collapse stage.

Let the breakup velocity, V_b, be defined as the velocity of the fuel particles when they break apart from the fuel shell. They are assumed to travel through the vapor film and surrounding coolant with initial velocity V_b. The time scale of heat transfer for the fuel particles in the vapor film is determined by V_b. The diameter of the fuel debris is approximately given as one-half of the Rayleigh-Taylor wavelength during the expansion. From the conservation of the fuel mass, the number of the fuel debris is given as

$$N = \frac{3R_o^2 L}{R_{fr}^3} \tag{1.32}$$

where R_o is the initial radius of the fuel droplet at each cycle and L is the depth of jet penetration.

The possible travel or mixing distance of the fuel debris can be found from the energy balance; kinetic energy of each fuel particle at the moment of the breakup is equal to the viscous dissipation during the movement of the fuel particles through the vapor film and the surrounding coolant.

Consequently, the main vapor film around the unfragmented parent fuel drop grows enormously due to the heat input, not only from the fuel droplet but also from the numerous fragmented fuel particles. When the vapor film grows beyond its equilibrium point and all the fuel particles leave, the movement of the film retards and begins to collapse. Collapse of the film triggers another cycle of fuel-coolant interactions. This cycle will be repeated until the parent fuel droplet is too small to cause interactions or the penetration of coolant ceases. For the fragmented particles which are relatively large, they may possibly undergo another boiling-related breakup or purely hydrodynamic fragmentations during their travel through the coolant.

The initial conditions for the calculations were those used by Nelson in his baseline experiments, which are given in Table 1.1. When the film boiling around the spherical fuel droplet enters its steady state, whose variables are given in Table 1.2, a triggering pressure is applied. The trigger

Table 1.1

Baseline Variables in FCI Experiments

Diameter of fuel droplet	2.8 mm
Temperature of fuel droplet	2233 K
Temperature of coolant	300 K
Ambient pressure	1 bar

Table 1.2

Variables at Steady State of Film Boiling

Temperature fuel surface	2060 K
Pressure of vapor-film	1 bar
Mean temperature of vapor	1055 K
Thickness of vapor film	0.3 mm
Mass of vapor	1.8×10^{-9} kg

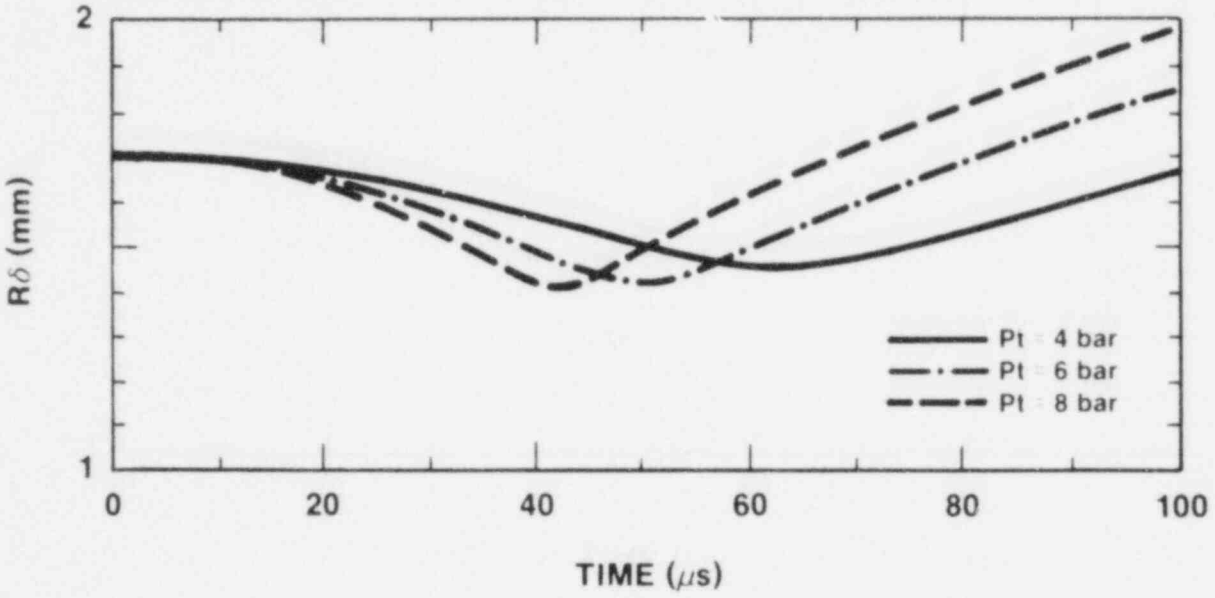

Figure 1.19. Film Radius-Time History at Different Peak Trigger Pressures

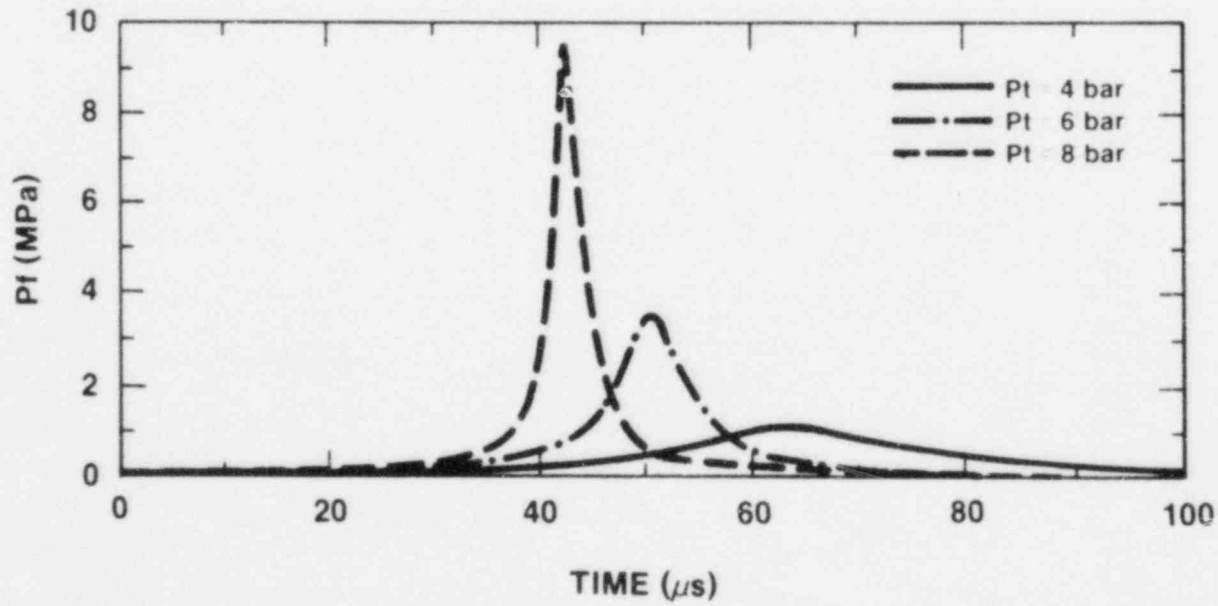

Figure 1.20. Film Pressure-Time History at Different Peak Trigger Pressures

pressure has a sharp increase up to a certain peak pressure and decays exponentially. Figures 1.19 and 1.20 show the vapor-film radius and pressure history at a given trigger pressure. The coolant hardly contacts the fuel surface even at large trigger pressures; rather the vapor reaches its supercritical state where the process is very complicated. During the later stage of film collapse and early stage of film expansion vapor-coolant interface accelerates toward the coolant as shown in Figure 1.21. The interfacial instability then grows as shown in Figure 1.22. Even though the peak acceleration rate is high at high peak trigger pressures, the instability does not grow linearly with peak pressure since the time duration of positive acceleration decreases with trigger pressure.

The initial amplitude of disturbance is unknown. Since evaporation or condensation occurs at the vapor-coolant interface, it should not be smaller than the critical nucleation embryo for the evaporation or condensation which is 10 μm for the homogeneous nucleation and 2.5 x 10 μm for the heterogeneous nucleation at 1 atm. Obviously, it should be smaller than the vapor film itself. Also, it can be approximated as some fraction of the momentum boundary layer thickness of the flow over the spherical vapor film. In this calculation it is assumed to be 10 μm. Figures 1.23 and 1.24 show the history of jet velocity and penetration velocity at different peak trigger pressures, where the penetration velocity increases with peak trigger pressures. Figures 1.25 and 1.26 show the penetration depth and corresponding wavelength of the instability. Due to the assumption that the instability grows at the fastest-growing wave number, the wavelength decreases with the acceleration rate. When the penetration depth is larger than the half of the corresponding wavelength, which is the approximate diameter of coolant drop at 0 breakup factor, jets can be completely entrapped in the fuel. Therefore, only when the peak trigger pressure is larger than certain values can the fuel droplet undergo energetic interactions, which is approximately 5 bar under the baseline initial conditions given in Table 1.1. Figures 1.27 and 1.28 show the effect of the breakup factor on the penetration velocity and the penetration depth of the jets. In this case the diameter of the coolant drops which can be entrapped in the fuel may be less than the half of the wave number and is dependent on the breakup factor.

1.4.2.5 Modeling of the Single Droplet Experiments (M. L. Corradini and B. Kim, UW)

In this section, the results of small-scale single droplet fuel-coolant interactions experiments are currenty analyzed. The aim is to obtain an approximate estimate of area increase during the interaction. The size and number of

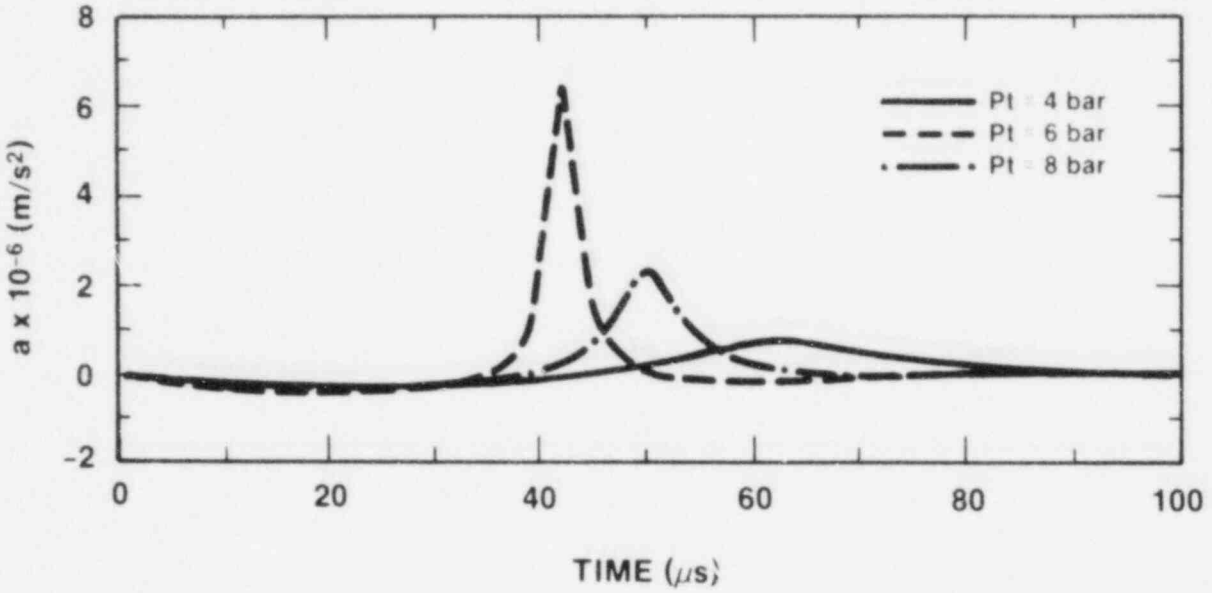

Figure 1.21. Acceleration of Vapor-Coolant Interface

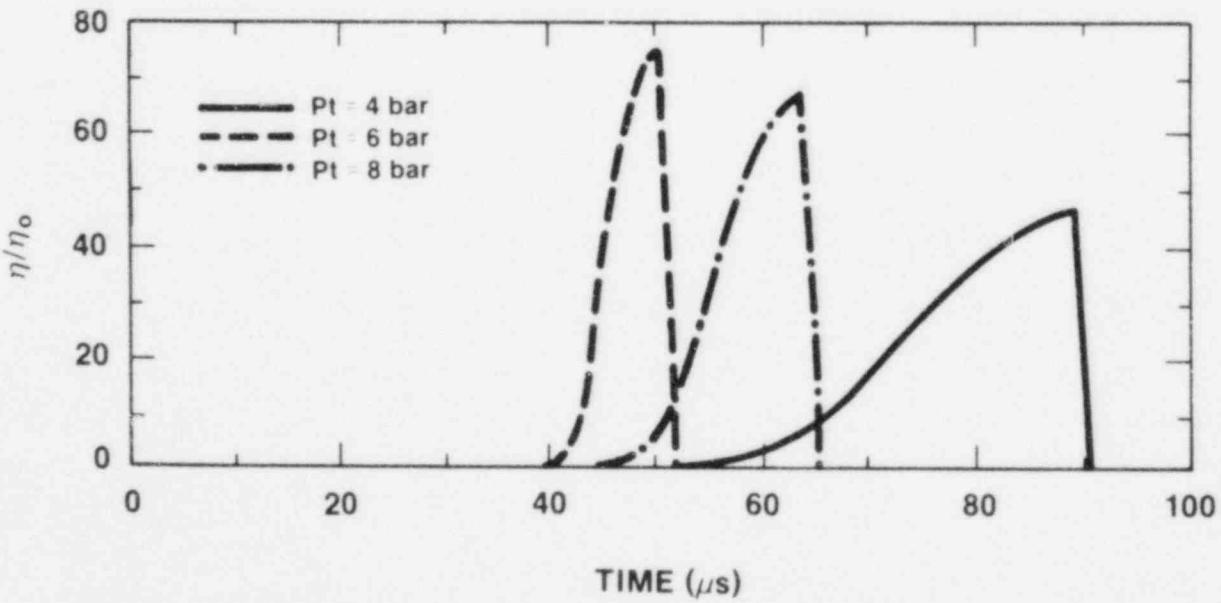

Figure 1.22. Instability Growth Rate

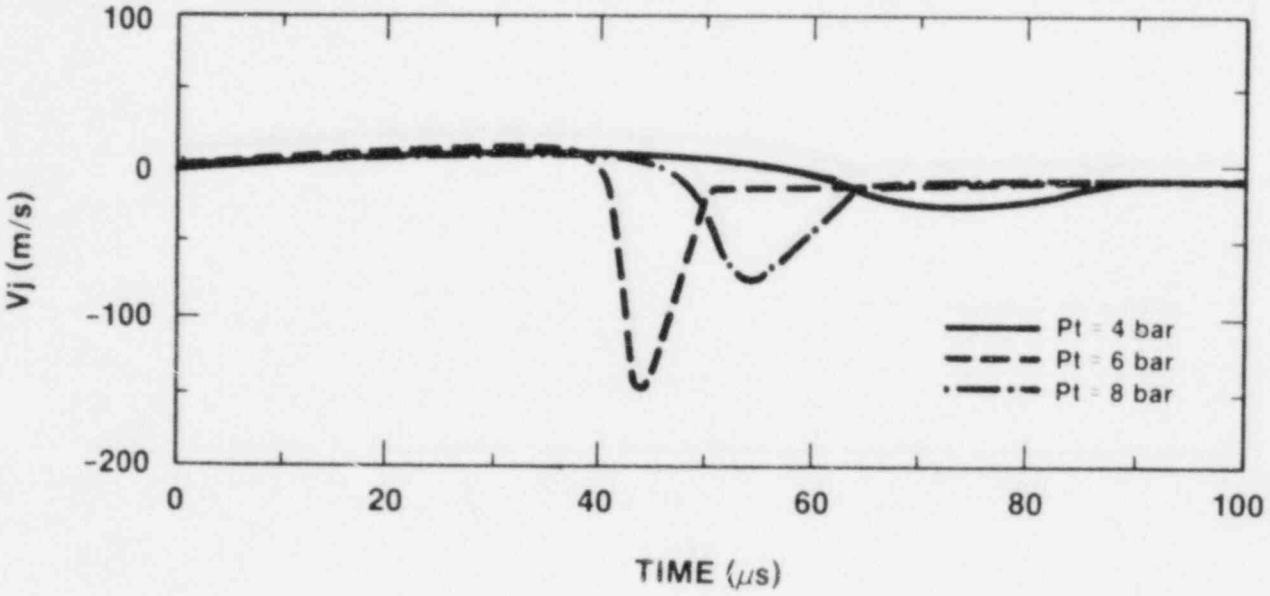

Figure 1.23. Velocity of Coolant Jet-Time History

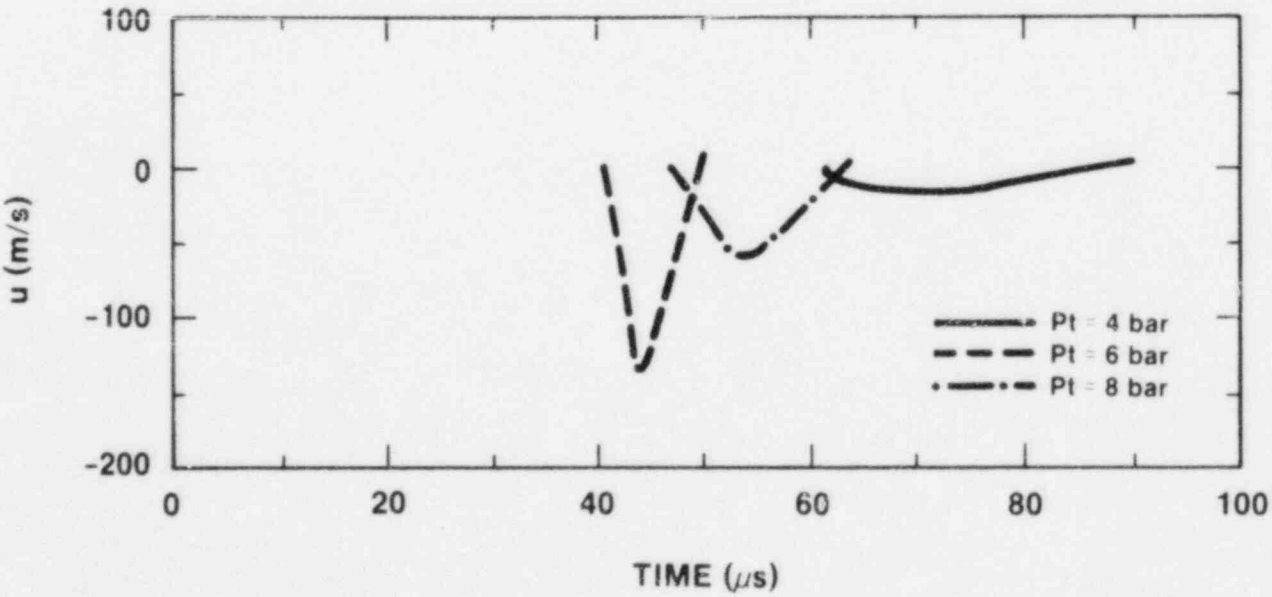

Figure 1.24. Penetration Velocity-Time History

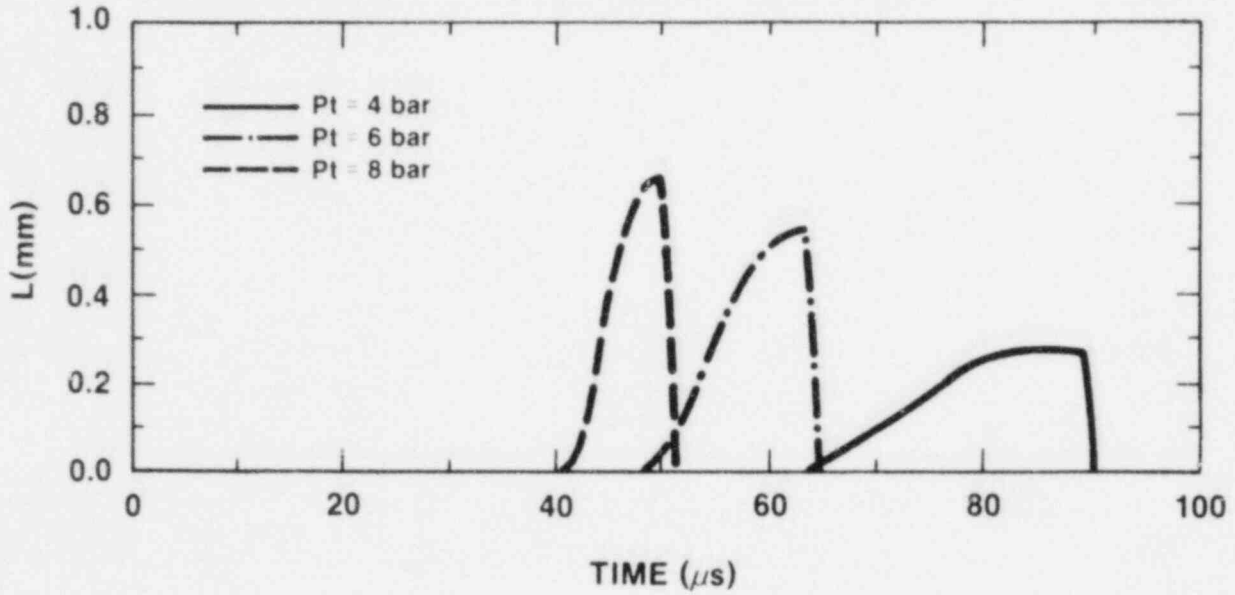

Figure 1.25. Penetration Depth-Time History

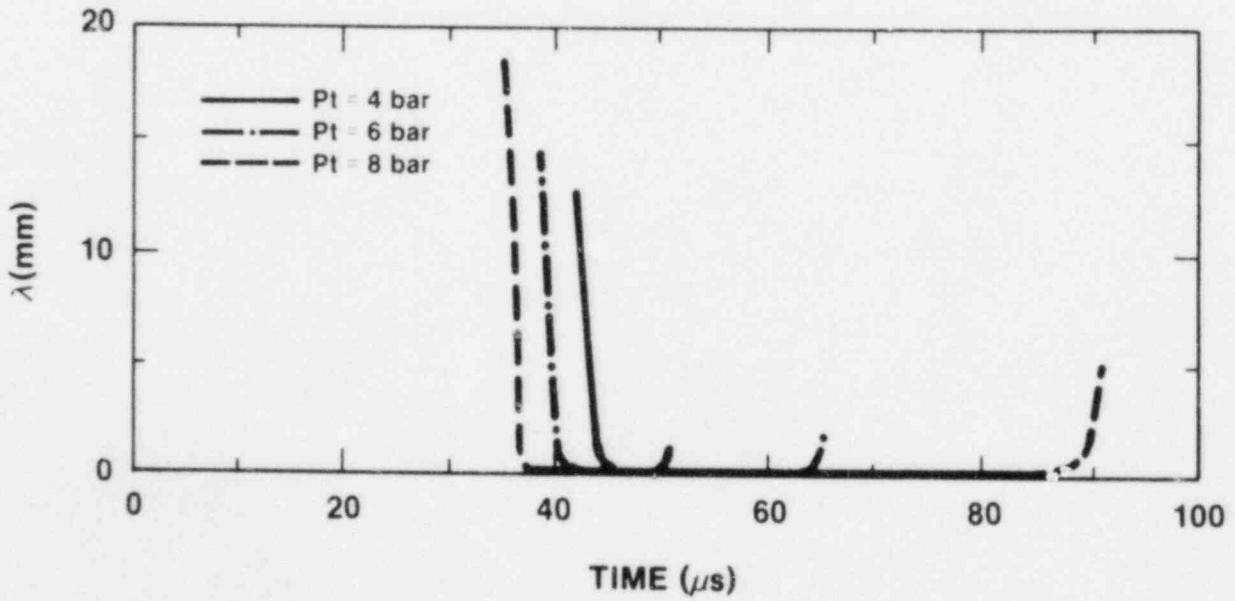

Figure 1.26. Wavelength-Time History

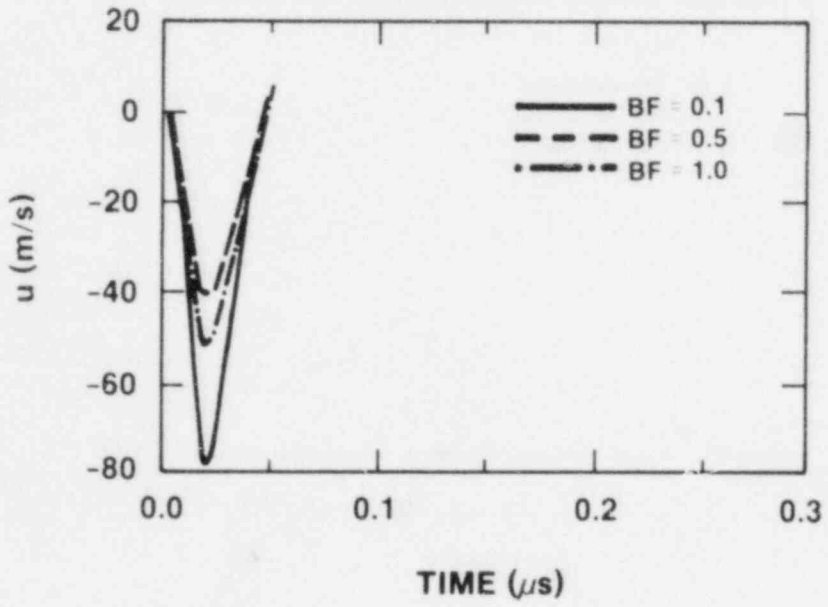

Figure 1.27. Effect of Breakup Factor on Penetration Velocity

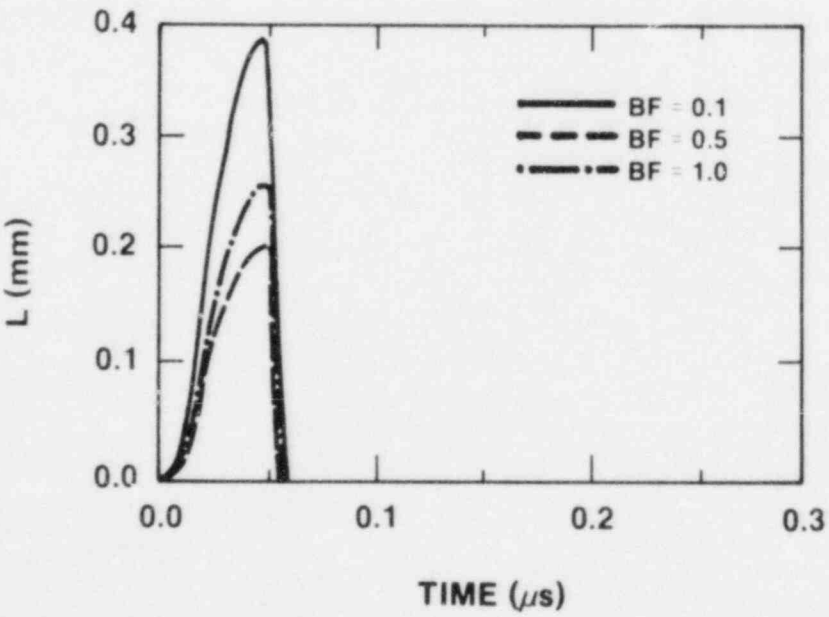

Figure 1.28. Effect of Breakup Factor on Penetration Depth

fuel debris are estimated based on the bubble diameter history in the fuel-coolant interactions.

The approach adopted here is to:

1. Obtain an estimate of the heat transfer needed to give the observed growth of each vapor bubble;

2. Estimate the area and hence the equivalent particle size and number needed to give the above heat transfer rate.

Heat Transfer from the Oxide Drop

The heat which is transferred from the hot oxide droplet and particles goes into mechanical work done by the expanding bubble, change of the internal energy of vapor film, and heating of the bulk coolant.

In order to calculate the total heat transfer from the fuel each of these terms was calculated for each bubble expansion.

Work done by the expanding vapor bubble goes into increasing the kinetic and potential energy of the coolant. When the bubble reaches its peak diameter, the kinetic energy of the coolant is zero and the work done is therefore equal to the potential energy of the coolant. This potential energy is approximately given

$$E = P_{\infty} \cdot \Delta V \tag{1.33}$$

where P is the bulk coolant pressure and ΔV is the change in the volume of the steam bubbles during the expansion.

In order to calculate the energy of the vapor at any moment, it is necessary to know the pressure, volume, and temperature of the vapor. In principle, it should be possible to calculate the vapor film pressure from the bubble diameter history and Rayleigh equation given as

$$\ddot{R}_{\delta} = \frac{1}{R_{\delta}} \left[\frac{P_f - P_{\infty} - \frac{2\sigma}{R_{\delta}} - \frac{4\mu_c}{R_{\delta}} \dot{R}_{\delta}}{\rho_c} - \frac{3}{2} \dot{R}_{\delta}^2 \right] . \tag{1.34}$$

In practice, however, no reasonably consistent values could be obtained since the photographic data provided from the experiments are too sparse; i.e., the errors in calculating

the velocity and particularly the acceleration of the interface are unacceptable.

An alternative approach is to assume that the vapor behaves as a perfect gas and undergoes an adiabatic and reversible expansion. Since the work done by the expanding bubble is already known, the pressure of the vapor bubble is given as

$$P = \frac{(1-\gamma)W}{V^{\gamma}\left|V_o^{1-\gamma} - V_i^{1-\gamma}\right|} \qquad (1.35)$$

where W = expansion work

γ = specific heat ratio

V = volume of the steam bubble

subscripts i and o describe the initial and final stage of bubble expansion.

The mean temperature of the vapor bubble is also unknown, but supposed to be in a superheated state.

In this simple calculation it is assumed that the change of internal energy of the vapor during the expansion of the bubble is negligible compared to the work done by the expanding bubble. In other words, most of the energy dumped from the fuel particles into the vapor is used in the expansion of the vapor bubble and heating of the bulk coolant.

The heating of the bulk coolant has been estimated by using the heat transfer correlation of the flow over the spherical drop, which is given as

$$Nu = 2.0 + 0.6\ Re^{1/2} Pr^{1/3} \qquad (1.36)$$

where the Reynolds number is based on the drop fall velocity in the coolant. Since the heat transfer coefficient and the area is a function of the diameter of the vapor bubble, the heat transfer rate for each bubble expansion is obtained by integration from the minimum radius to maximum radius of the expanding bubble.

Heat Transfer Area

Having calculated the heat transfer from the fuel for each cycle, if an effective heat transfer time and heat transfer rate are known we can calculate the required heat transfer area for each cycle. The heat transfer rate from the

fragmented fuel particles is assumed to be that of steady-state heat conduction in vapor which is given as

$$Nu = 2 \quad . \tag{1.37}$$

The heat transfer time is considered to be one-half of the expansion time of each cycle since the fragmented fuel particles travel with a certain velocity through the film. The average temperature difference between the fuel debris and the vapor is assumed to be

$$\Delta T = \frac{1}{2} (T_f - T_c) \tag{1.38}$$

where subscripts f and c describe fuel and coolant.

Size and Number of Fuel Debris

The size and the number of fragmented fuel particles are calculated from the total heat transfer area required. It is assumed that the diameter of the fuel debris is uniform independent of the cycles. Therefore, the diameter of the fuel debris is given as

$$d = \frac{\pi D^3}{A} \tag{1.39}$$

where D is the initial diameter of the fuel droplet and A is the required heat transfer area. The number of the fuel debris can be calculated from the conservation of the fuel mass. Since the fragmented fuel particles have certain velocities and transfer heat to the vapor only during the expansion of the bubble, the heat transfer rate during the collapse is not considered in the calculations.

Results

Small-scale single droplet FCI experiments 11-75-1 were analyzed. In this case the vapor bubble undergoes four cycles of expansion and collapse. The results of the calculations are given in Table 1.3.

Even though the analysis itself is very simple and approximate, the results are within the limit of experimental findings. For a more complete analysis of the FCI data from the experiments, more data at higher sampling frequencies are required such as the bubble diameters at every 10 to 20 μs

which can be used to find out the pressure history of the steam bubble.

1.4.2.6 Monte Carlo Analysis
(M. Berman, 6427; O. Seebold, 6427)

A version of the Monte Carlo code used in the NUREG/CR-3369 has been implemented on the Area 5 VAX. The new version of the code was tested using identical input that had been used to test the earlier version. The results from the new version appeared to qualitatively agree with the results from the earlier version. In order to strictly compare the results of the current version with the results from the original version, it must be run on the same computer and operating system because of the differences between the random number generators on the two operating systems.

Table 1.3

Results of FCI Experiment Analysis

Work done	1.1 N·m
Conversion ratio	1.0%
Heating of bulk coolant	0.5 N·m
Heat from parent drop	0.04 N·m
Heat from fuel debris	1.56 N·m
Heat transfer area	9.5×10^{-5} m^2
Diameter of debris	0.1 mm
Number of debris	12,000

1.4.3 Program Development and Planning

1.4.3.1 Research Program Plan
(M. Berman, 6427; B. W. Marshall, Jr., 6427)

In preparation for the Steam Explosion Review Group (SERG) meeting held in Harpers Ferry on November 27 and 28, 1984, we proposed a research program that includes the development of FCI models and a comprehensive experimental program. The experimental program addresses four current questions about FCI processes. We then ranked these four into priorities according to our perception of the immediate needs of the NRC. The results of this ranking and a brief description of each is given below.

Priority 1: SEALS Facility (Steam Explosions At Large Scale)

Objective: Determine the effects of scale on coarse mixing and conversion ratio for steam explosions at an ambient pressure of one Albuquerque atmosphere (0.83 bars).

Description: Use up to 2000 kg of iron-alumina thermite in an open (no external containment building) geometry, rigid (steel) and weak-walled (lucite) water chambers (one-half linear scale replicas of a PWR lower plenum), subcooled and saturated water. Some tests might use corium thermites and prototypical (PWR and BWR) structures in the lower plenum.

Priority 2: FITSX Facility (Extension of current FITS system)

Objective: Investigate FCI behavior for up to 50 kg of various thermitic melts in the existing FITS vessel. Measure conversion ratio, steam and hydrogen generation, debris characteristics, and fission-product release for normal (melt dropped into water) and alternate (water onto melt) contact modes.

Description: Oxidic (iron oxide) and mixed oxide-metal melts (corium, iron-alumina, UO_2-molybdenum) would be thermitically prepared and brought into contact with saturated and subcooled water; ambient pressure would be varied between 0.83 and 11 bars. The influence of many important initial and boundary conditions on FCI behavior would be quantified.

Priority 3: SHIP Facility (Small-scale HIgh Pressure)

Objective: Determine the dependence of explosion triggering and conversion ratio on ambient pressure up to 170 bars.

Description: Prepare single-droplet oxidic and metallic metals in a high-pressure chamber, using a laser and an inductive melter. Measure the pulse characteristics (peak pressure, rise time, duration) necessary to trigger explosions, and the resulting yield of those explosions.

Priority Unknown: ELVIS (Enclosed Large-Vessel Interaction System)

Objective: Investigate FCI behavior in a scaled-up version of the FITS facility, using inductively-prepared oxidic and metallic melts.

Description: Prepare approximately 400-kg melts and deliver them into water chambers inside of a larger containment chamber. Investigate the influence of the important initial and boundary conditions.

The assignment of priorities is based on our estimates of the impact and importance of the possible experimental results. With respect to vessel and containment failure, we believe that the SEALS facility is extremely important for issue resolution. Much of the current uncertainty with respect to alpha-mode failure derives from the extrapolation of small-scale data to the reactor situation. If the large-scale SEALS tests confirm that physical limits on explosion yields exist, then we will have removed a major contributor to risk from further consideration; i.e., alpha-mode failure at ambient pressure.

If the SEALS results are not positive, then the research would address other potential mechanisms for limiting or preventing containment failures; e.g., more detailed experiments and analyses of the melt progression, and the way that melt pours into the lower plenum; and improved simulation of the geometry and structures in the lower plenum, especially for BWRs. The required scale of additional experiments would be strongly influenced by the as-yet-unknown results of the SEALS tests.

SEALS is not intended to be an all-purpose facility for addressing generic FCI questions. The relatively high cost of individual tests will limit the number and scope of the tests. SEALS will primarily address the influence of increasing melt mass on the probability and consequences of steam explosions. FITSX is intended to be the primary facility for assisting in the development and assessment of FCI models important for reactor safety analyses.

1.4.3.3 Preliminary Design and Cost Study for SEALS
(B. W. Marshall, Jr., 6427; M. Berman, 6427; M. Krein, 6427)

This section describes a facility (the SEALS facility) that can experimentally determine the limits to fuel-coolant mixing. SEALS will address the amount of melt that can mix and participate in a steam explosion by means of measuring the conversion ratio as a function of several important parameters. SEALS will be capable of preparing and delivering

thermitic melts, mostly iron/alumina thermite, up to 2000 kg into a one-half scale reactor lower plenum. Corium and purely oxidic thermites may also be investigated in later testing.

The selection of 2000 kg of molten fuel is based upon the following considerations:

1. This mass, as generally agreed at the Molten-Core Coolant Interaction Research Review Group in New Orleans, LA, is large enough to unequivocally distinguish the difference between the current mixing models.

2. This mass is large enough to approach the range of masses that might threaten the integrity of the reactor vessel or the containment building if an energetic steam explosion occurs.

3. Although 2000 kg represents an increase of two orders of magnitude over the current FITS capabilities, we believe that it is possible to build and operate such a facility.

We are proposing the SEALS facility to be constructed in a three-phase approach. In the first phase, we will construct a facility similar to EXO-FITS (shown in Figure 1.29), that will be used to gather information about the proposed melt preparation and delivery system for the second and third phases. In addition, preliminary information about mixing limits and conversion ratios will be gathered to check the design and instrumentation capabilities of the one-half scale facility to be built in the second phase. In the second phase, shown in Figure 1.30, we will construct a right circular cylinder of a half-linear-scale reactor vessel and attach the delivery system developed in phase one to the water vessel. This vessel is the cylindrical section of the final SEALS facility. In the final phase, shown in Figure 1.31, we will finish construction of the half-linear-scale reactor vessel which will measure conversion ratios, and other data important to alpha-mode failure.

The first phase will measure conversion ratios to an accuracy quite similar to the earlier EXO-FITS[1.10,1.11] and open-geometry[1.12] experiments conducted at Sandia. It will also provide estimates of conversion ratios, water phase pressurization, swell level, films of the explosion propagation phase, and tracer particle velocities. All of the tests will be conducted using lucite water chambers, and will be the only ones in which the mixing processes will be directly photographed.

In the second phase, the cylindrical section of the one-half scale vessel will be used as the water vessel. An

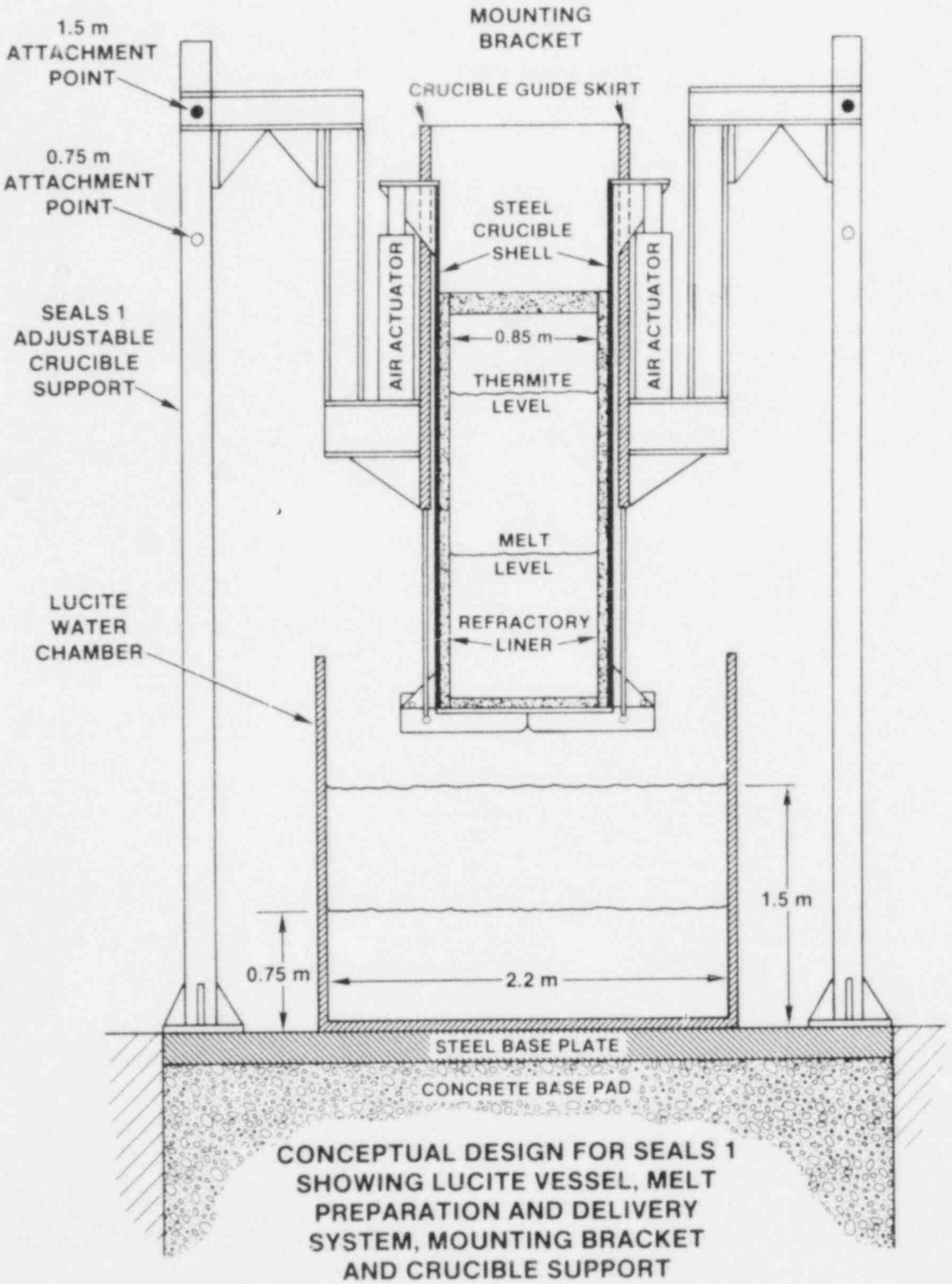

Figure 1.29. SEALS - Phase 1

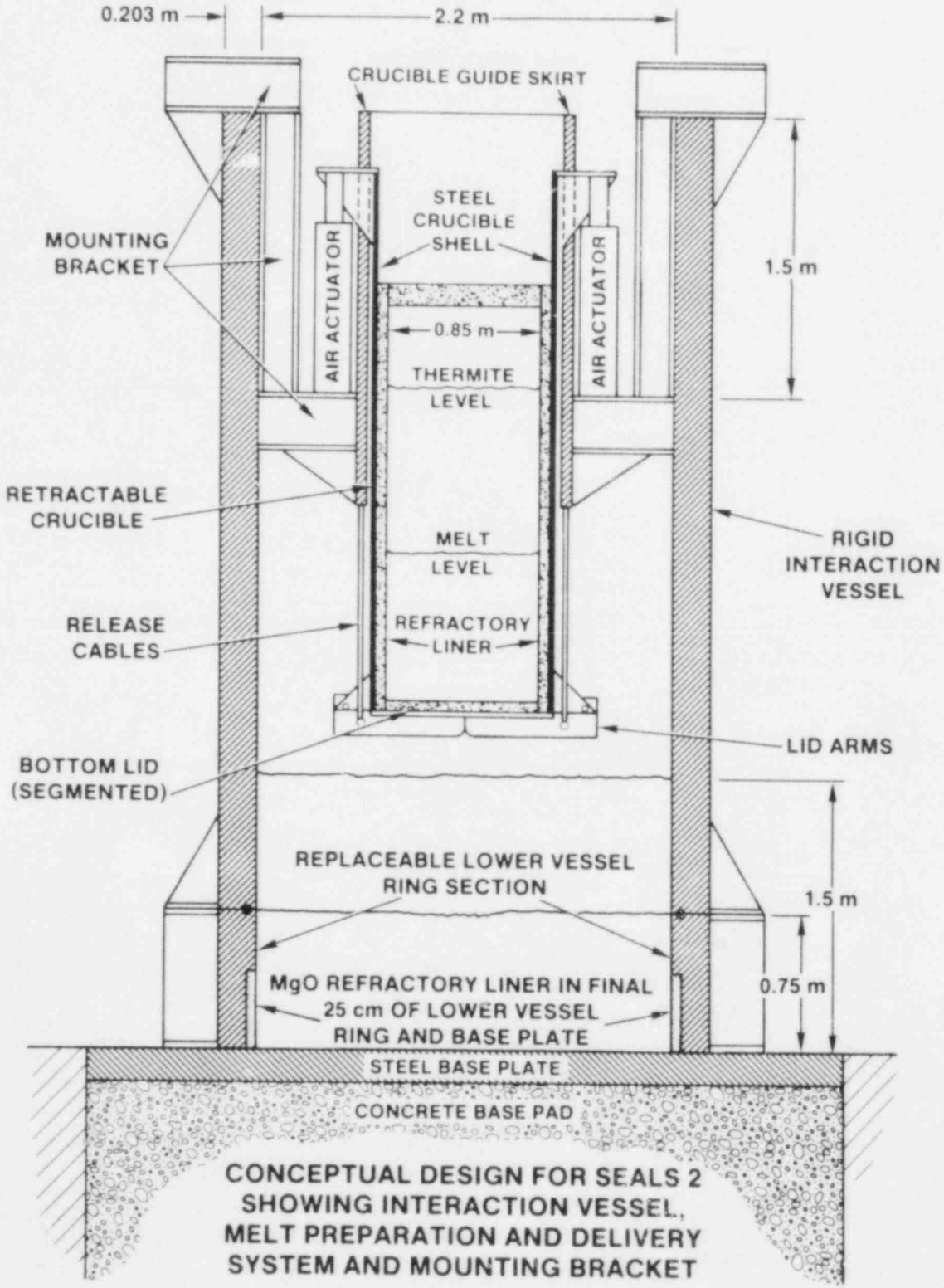

Figure 1.30. SEALS - Phase 2

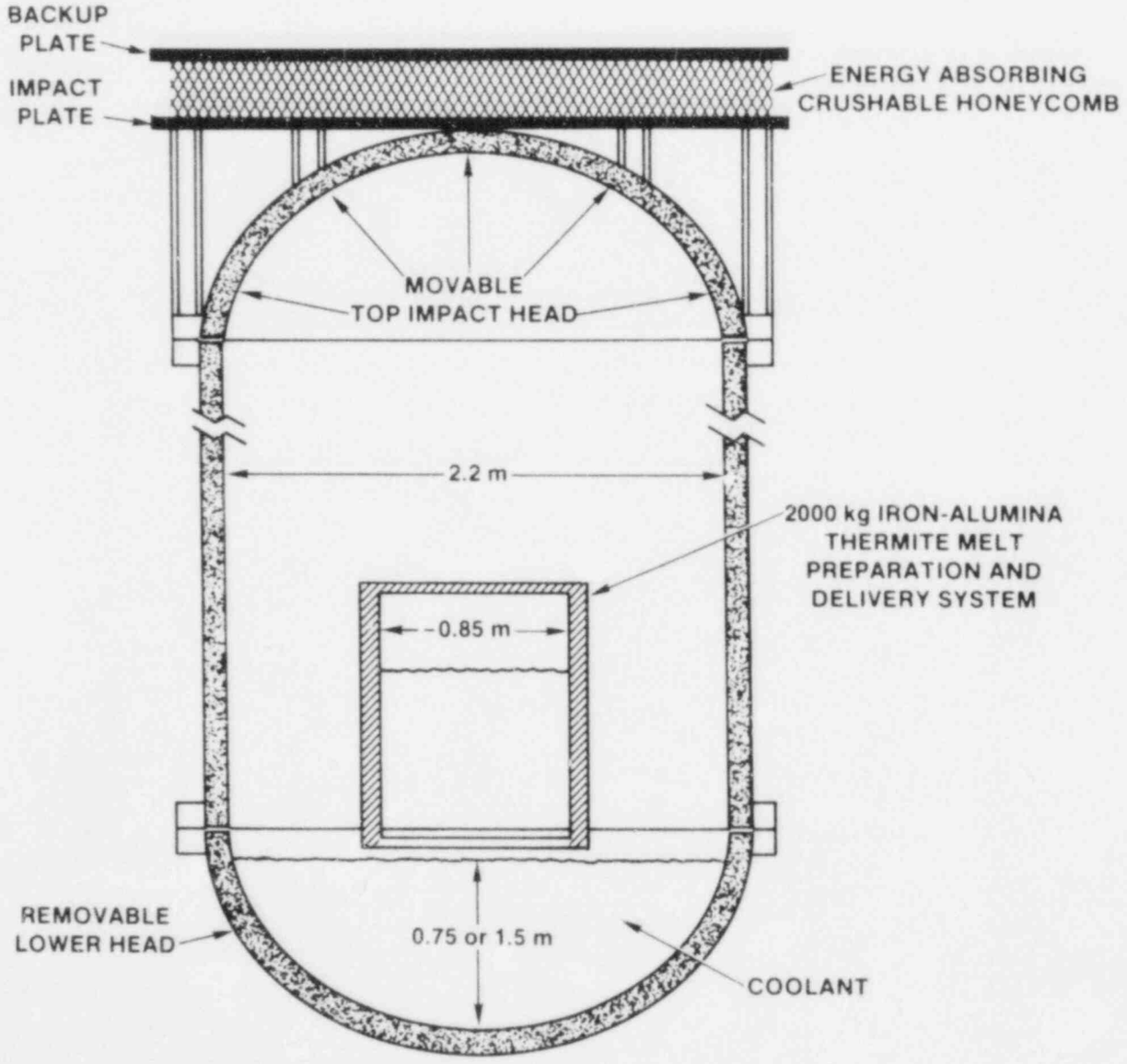

Figure 1.31. SEALS - Phase 3

experimental program will be performed that will define the FCI characteristics for a "fully vented" system. Acoustic methods may be employed to estimate the shape of the mixing region within the opaque steel chamber. The mass involved in an explosion will be estimated by subtracting the residual mass in the water chamber from the delivered mass. Also, the instrumentation discussed in the first phase will be included in these experiments.

The final phase of SEALS (SEALS3) will provide a more accurate measurement of conversion ratio within a half-linear-scale reactor vessel. This facility will provide information about conversion ratios and vessel pressurization during a steam explosion in addition to the basic set of measurements described for the first two phases. Additional instrumentation will include strain gauges and accelerometers.

This systematic approach to the SEALS facility will optimize both the data acquisition at large scale in addition to the cost of acquiring the data. In the first phase, limits to mixing and approximate conversion ratios will be checked in lucite water chambers. If mixing limits appear in this mass range (i.e., no explosion or only very weak explosions occur for such large melt masses), it may not be necessary to continue to the subsequent phases. On the other hand, if energetic steam explosions occur, the data gathered in the first phase will be useful check points for the design criteria assumed for the final phases. We also feel that it is necessary to approach the design and construction of the SEALS facility in a cautious manner, since we are increasing the fuel delivery system by two orders of magnitude beyond present capabilities.

Frequent separate multiple explosions will be easy to observe in the first phase of SEALS. The conversion ratio in this case would be of little importance to reactor safety since relatively small amounts of fuel are contributing to each explosion. In the case of saturated water, steam explosions may or may not occur spontaneously. If the explosion is triggered externally, great care will be required in artificially simulating triggers that may occur in a reactor vessel. The occurrence of a large-scale steam explosion will possibly be dependent on the characteristics and nature of the external trigger source. If explosions can be externally triggered when most or all of the melt is in the water, then large conversion ratios are expected. Experimentally, the design and implementation of these external triggers might be an important part of the steam explosion.

The above discussion implies that the first phase of SEALS may be adequate to accomplish the scaling objective if the results are similar to some of the pretest predictions. If, on the other hand, large-scale coherent steam explosions are observed, then the second and third phases of the facility

will be built to measure more accurately the important parameters for the reactor. Further, the data from the first phase will provide useful checks for the design strength and experimental flexibility of the final two phases. However, if the final phase of the SEALS facility is built initially and the subsequent experiments demonstrate mild or nonexplosive results, then the cost for this information would be excessively high.

1.5 Hydrogen Behavior

(J. T. Hitchcock, 6427; M. Berman, 6427)

1.5.1 Deflagrations

1.5.1.1 HECTR Diffusion Flame Model

(C. C. Wong, 6427)

During a degraded core accident, hydrogen generated from metal-water reaction or radiolysis can combust as a standing flame at the point-of-release of the hydrogen-steam mixture into the containment. The jet of steam and hydrogen will entrain and mix with the containment atmosphere, and possibly burn as a turbulent diffusion flame. The ignition source can be accidental (arcing switch contacts) or deliberate (glow plugs), and if the jet mixture is hot enough, spontaneous ignition can occur (autoignition). The primary threat from diffusion flame combustion is the high thermal loads imposed by the flame on safety-related equipment and containment penetration seals.

The character of a diffusion flame can be determined by the basic flow field, which will be either a jet or a plume. We distinguish between jets and plumes on the basis of the role of buoyancy in the flow. Jet-like flows are dominated by the initial momentum of the jet. In plume-like flow, the initial momentum is negligible compared to that induced by buoyancy. For example, hydrogen released during a degraded core accident through a stuck-open valve (2 to 10 cm) of a PWR will probably result in momentum-dominated jets of hydrogen and steam, driven initially by very high pressure (1000 to 2000 psia) and expanding into a containment at or near atmospheric pressure. On the other hand, hydrogen released into a BWR containment will come from spargers in the suppression pool. These flows will be at low pressure, spread over a relatively large area (3-m-diameter) and have a small steam content relative to the PWR cases. The basic flow is buoyancy-dominated.

Our initial development efforts on diffusion flame modeling are directed toward evaluating and extending the earlier work performed for the NRC Containment Loads Working Group (CLWG). The diffusion flame model developed for the CLWG[1.13] is relatively simple, but highly problem-dependent and very difficult to use. In this model one or more connected flame

compartments are specified along with the hydrogen injection rate into each compartment. The flow loss coefficients at the junctions between the flame compartments are adjusted iteratively, until the flow rate at the top of the flame compartments approximately is equal to the flow rate predicted by the empirical correlation developed by Zukoski.[1.14] Sometimes many calculations are performed in order to obtain the designated flow rate as predicted by the Zukoski correlation.

This model was tested on BWR Mark III containment compartmentalized as shown in Figure 1.32.

As part of a sensitivity study, we varied the flow loss coefficients at the top of the flame compartments and found that HECTR results are very sensitive to changes in the flow loss coefficient (Table 1.4).

1.5.1.2 NTS Calculations
(C. C. Wong, 6427; J. F. Kotas, 6427)

We continued to assess HECTR against the large-scale hydrogen combustion experiment conducted at the Nevada Test Site (NTS). Current work has concentrated on the two premixed tests, P20 and P21. These two tests were among the last conducted at the NTS test facility and are of particular interest because of the high initial hydrogen concentration. The main difference between P20 and P21 was that P20 had no sprays on but P21 had sprays on continuously throughout the test. Since the initial conditions were nominally the same for each test, the results illustrate the effect of sprays upon hydrogen deflagrations in a large-scale test vessel. HECTR calculations were performed to assess the containment spray model in the code. A secondary objective of these calculations was to examine the HECTR heat-transfer and combustion models.

The initial conditions for tests P20 and P21 were:

Test Name	P_o (kPa)	T_o (K)	H_2 (%)	H_2O (%)
NTS P20	104.2	342.0	12.9	27.8
NTS P21	102.3	341.3	13.2	27.4

The combustion duration and combustion completeness were taken from Reference 1.15. Both tests had 100 percent combustion completeness, consistent with the HECTR combustion model. However, the measured burn times of 2.1 s and 1.7 s for tests P20 and P21, respectively, do not agree with the default combustion model in HECTR, and the EPRI burn time data were used in the calculations.

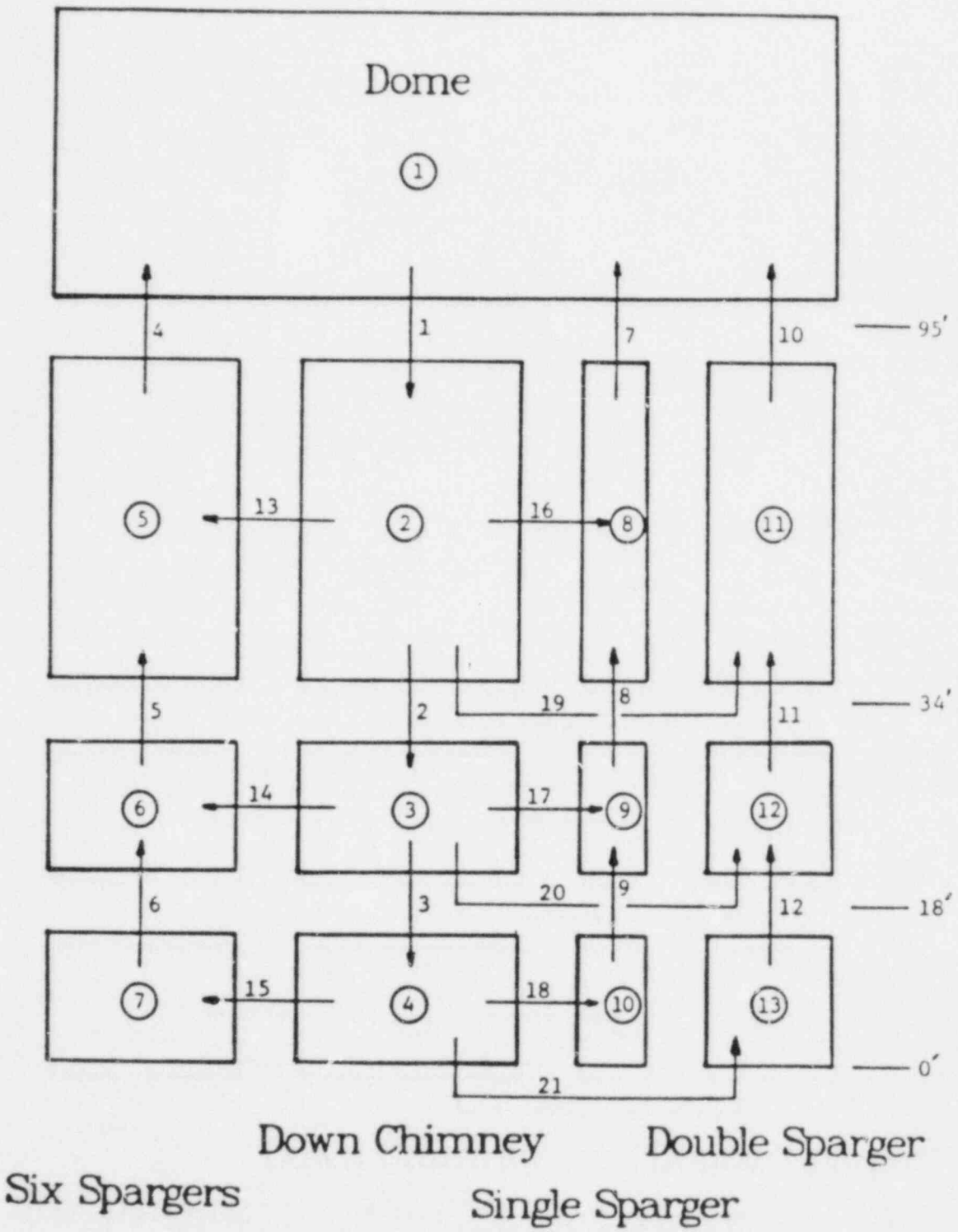

Figure 1.32. Compartmentalization for Nine-Sparger Cases

Table 1.4

Flow Loss Coefficient Sensitivities

Cases	Maximum Pressure (kPa)	Max Flame Comp Temp (K)	Max Drywell Wall Temp (K)
40 lb/min Hydrogen:			
1. Standard Problem Results	153.	510.	468.
2. Same as 1, but loss* coeffs. in annulus equal 0.1	147.	466.	438.
75 lb/min Hydrogen:			
3. Standard Problem Results	167.	602.	526.
4. Same as 3, but loss coeffs. in annulus equal 0.1	165.	522.	476.
5. Same as 3, but loss coeffs. in annulus equal 0.025	161.	503.	463.
100 lb/min Hydrogen:			
6. Standard Problem Results	174.	661.	560.
7. Same as 6, but loss coeff. in annulus equal 0.1	171.	560.	499.

* For all cases, loss coefficients in annulus refer to all junctions in nine-sparger model (Figure 1.32)

In the HECTR calculations, the NTS dewar was modeled as one compartment with two major surfaces, the dewar wall and the water pool at the bottom of the vessel. The dewar wall surface area consisted of both the actual wall surface, plus the area of the scaffolding and catwalk within the vessel volume. Both calculations were run to approximately 450 s.

1.5.1.2.1 HECTR Calculation of NTS Test P20

The HECTR predicted gas pressure is shown together with NTS pressure transducer P102 data in Figure 1.33. The HECTR calculated peak pressure is 428 kPa compared to 401 kPa measured by P102. This represents a 6.6 percent overprediction by HECTR. In the postcombustion phase of the transient immediately following the peak, the HECTR pressure follows the P102 data very closely. The excellent agreement of the slopes of the two curves in the 30-s period following the peak pressure indicates that the heat transfer from the gas to the dewar wall and internal structures is computed very well by HECTR. At 100 s, the HECTR predicted gas pressure falls below the measured pressure and at the end of the calculation is approximately 10.7 kPa low, indicating that the total energy loss from the gas predicted by HECTR is greater than that observed in the experiment.

THE HECTR predicted gas temperature (Figure 1.34) essentially follows the same trends seen in the pressure plot. HECTR predicts a peak gas temperature of 1470 K, compared to a temperature of 1412 K measured by thermocouple 101. This represents an overprediction of 4.1 percent. In the postcombustion transient phase, the HECTR result coincides with the data until 50 s when HECTR underpredicts the temperature for the remainder of the transient.

The surface wall temperature predicted by HECTR is compared against data obtained from thermocouple T120 in Figure 1.35. Note that HECTR predicts a quicker and higher surface wall temperature peak than T120 measures. This difference may be due to the limitations of the HECTR one-compartment model, where the surface wall temperature is calculated to be uniform everywhere and respond identically at every location. In reality, thermocouple T120 is at a specific location and may not be representative of the average surface wall temperature of the dewar. There is reasonable agreement between HECTR and T120 during the burn and approximately 40 s after ignition. The late-time behavior deviates, but the data appears to be suspect.

Although energy deposition data from NTS is not yet available, total energy transfer predicted by HECTR is shown in Figure 1.36. The total energy transferred from the gas to the wall is displayed together with the radiative and convective components. This plot is typical of all HECTR NTS

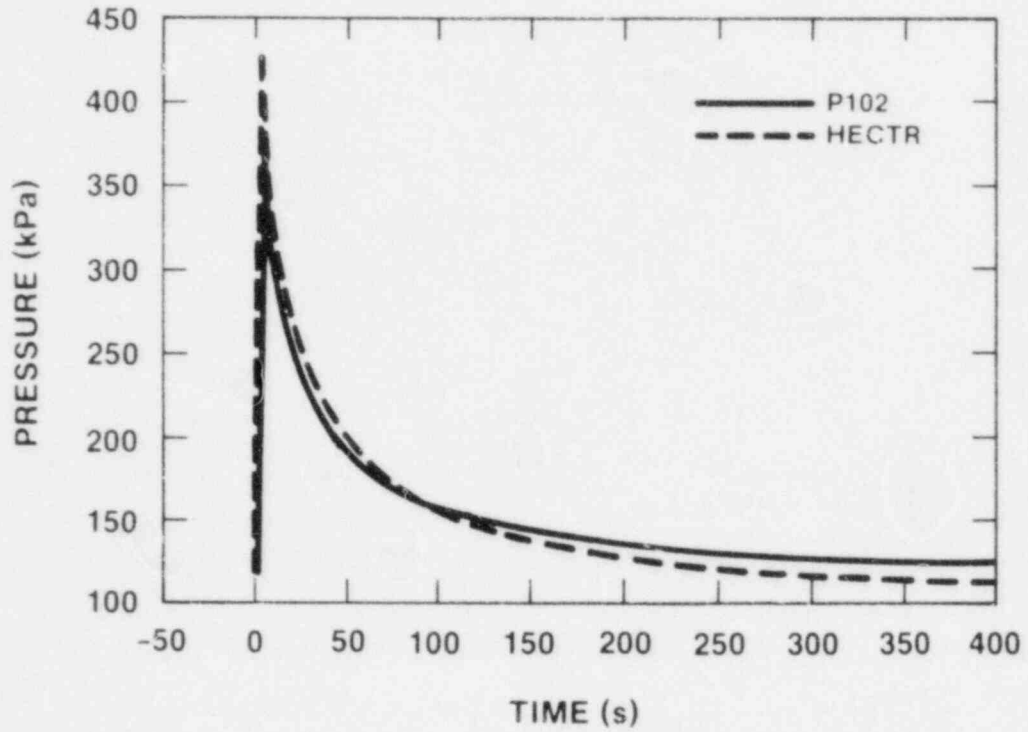

Figure 1.33. Gas Pressure vs. Time for NTS Test P20

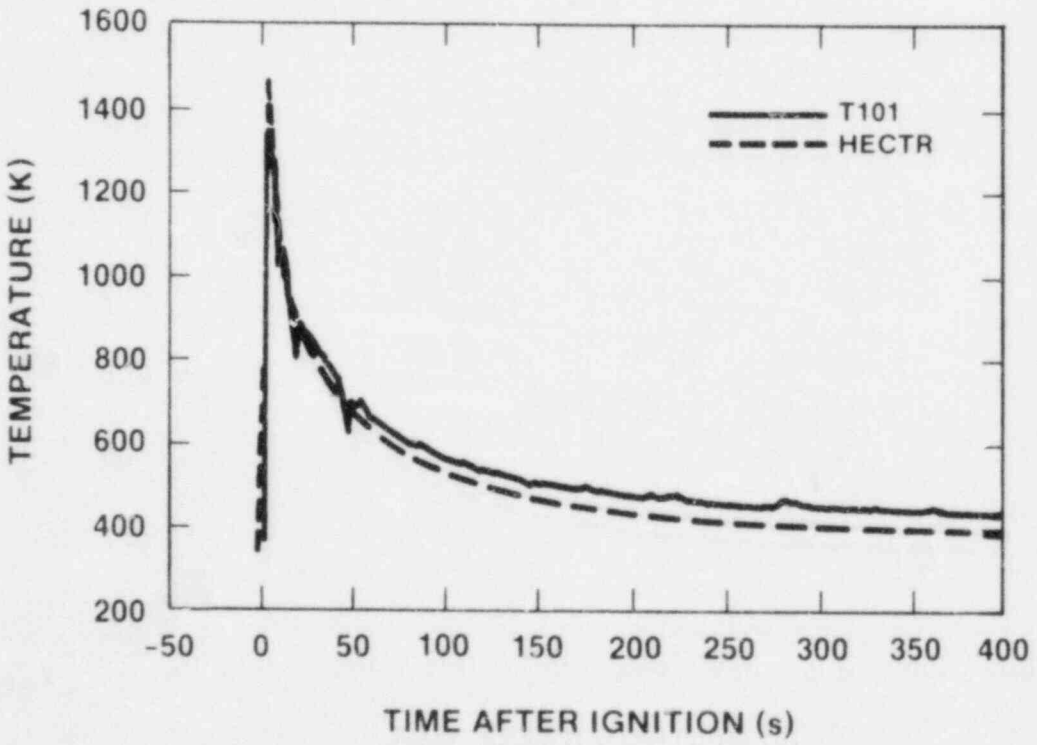

Figure 1.34. Gas Temperature vs. Time for NTS Test P20

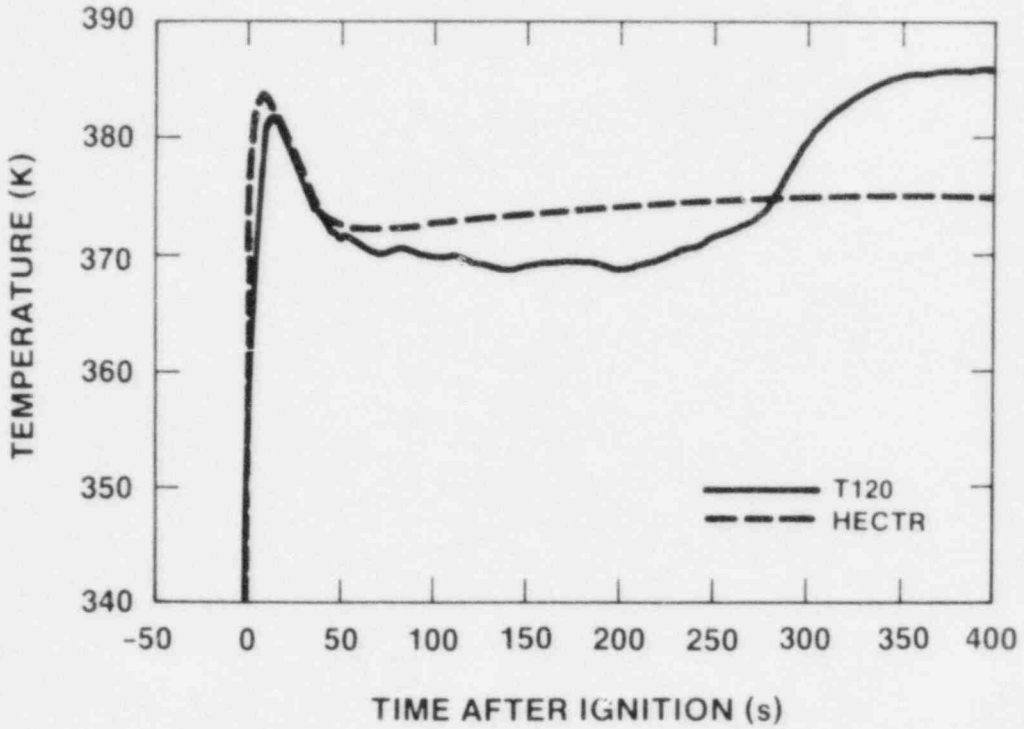

Figure 1.35. Surface Temperature vs. Time for NTS Test P20

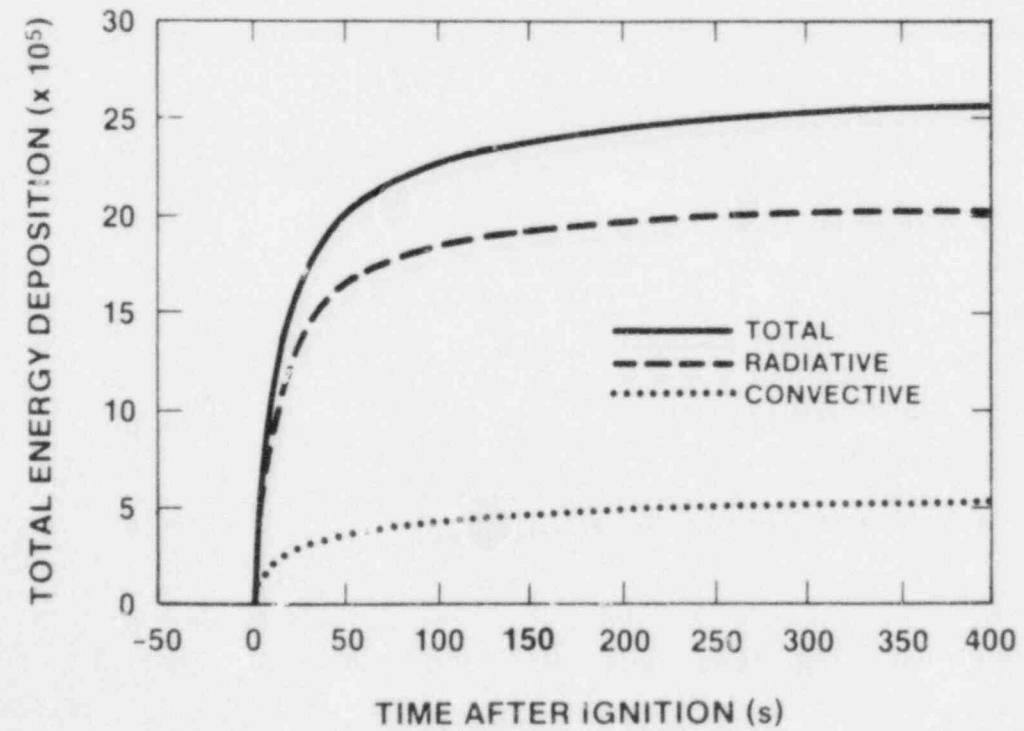

Figure 1.36. Total Energy Deposition vs. Time for NTS Test P20

calculations performed to date, with radiative transport accounting for 80 percent of the total energy transfer.

1.5.1.2.2 HECTR Calculation of NTS Test P21

As previously mentioned, the HECTR P21 calculation was performed much like the P20 calculation but with the spray model activated and heat transfer from gas to spray calculated. The comparison between the HECTR predicted gas pressure and pressure transducer P102 is shown in Figure 1.37. HECTR predicts a peak gas pressure of 426 kPa, representing a 7.3 percent overprediction of the peak pressure of 397 kPa measured by P102. The HECTR and P102 results coincide until 30 s when HECTR begins to underpredict the pressure. This underprediction continues until 70 s when HECTR begins to overpredict the pressure slightly. By the end of the transient, there is only an 8.2 kPa difference between HECTR and P102. A "kink" occurs in the HECTR curve at 42 s, the point when the steam mass fraction at the drop surface falls below the steam mass fraction in the bulk gas. This causes the mass transfer from the droplet to the gas to turn around, resulting in a net mass transfer to the droplet from condensation of steam. Thus, the droplet begins to grow as it condenses steam on its downward journey. This process effectively shuts off further cooling of the gas-steam mixture in the atmosphere, evidenced by the sudden plateau of the pressure curve at this point.

The gas temperatures are plotted in Figure 1.38. Note that thermocouple T101 falls approximately 300 K short of the HECTR peak. This deviation may be due to its location in the dewar and/or to an insulation effect caused by the water spray. Other thermocouples measured a peak gas temperature near 1400 K. The HECTR result represents a 4.8 percent deviation from this value. The HECTR predicted gas temperature follows the same trends as the pressure and makes the same sudden turn at 42 s after ignition.

Figure 1.39 shows a 20 K difference between the HECTR predicted surface wall temperature and thermocouple T120. This underestimation may be due to an overestimation of the liquid film thickness on the surface, increasing thermal resistance thereby reducing heat transfer and surface temperature. The surface condensation model and liquid drainage computation must be studied and corrected, if necessary.

HECTR computed energy depositions are shown in Figure 1.40. One interesting feature of Figure 1.40 is the abrupt halt of radiative energy transport to the dewar wall at 32 s after ignition. This is a result of the rapid gas cooldown by the spray droplets. Radiative transport is thus only 60 percent of the total energy transfer from the gas to the dewar wall.

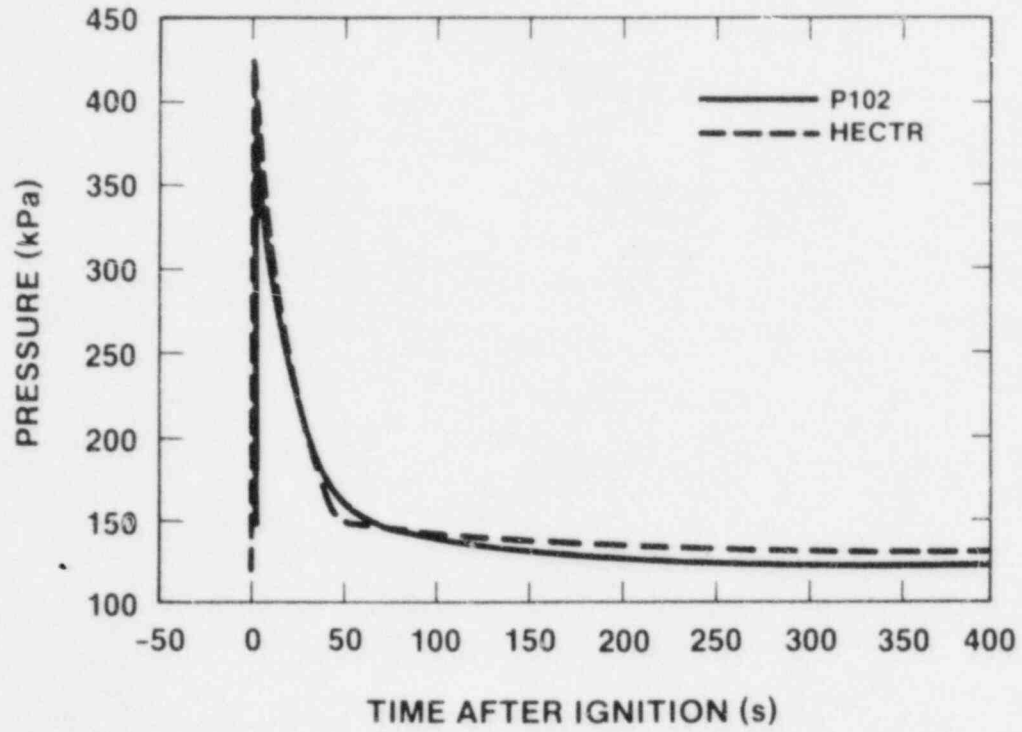

Figure 1.37. Gas Pressure vs. Time for NTS Test P21

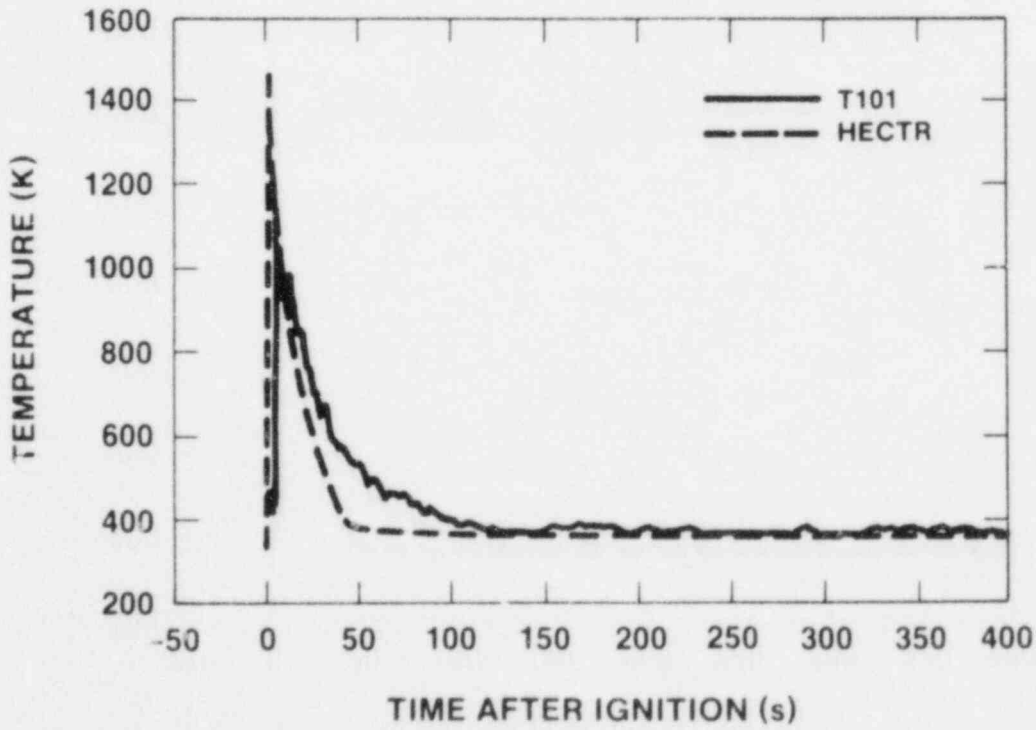

Figure 1.38. Gas Temperature vs. Time for NTS Test P21

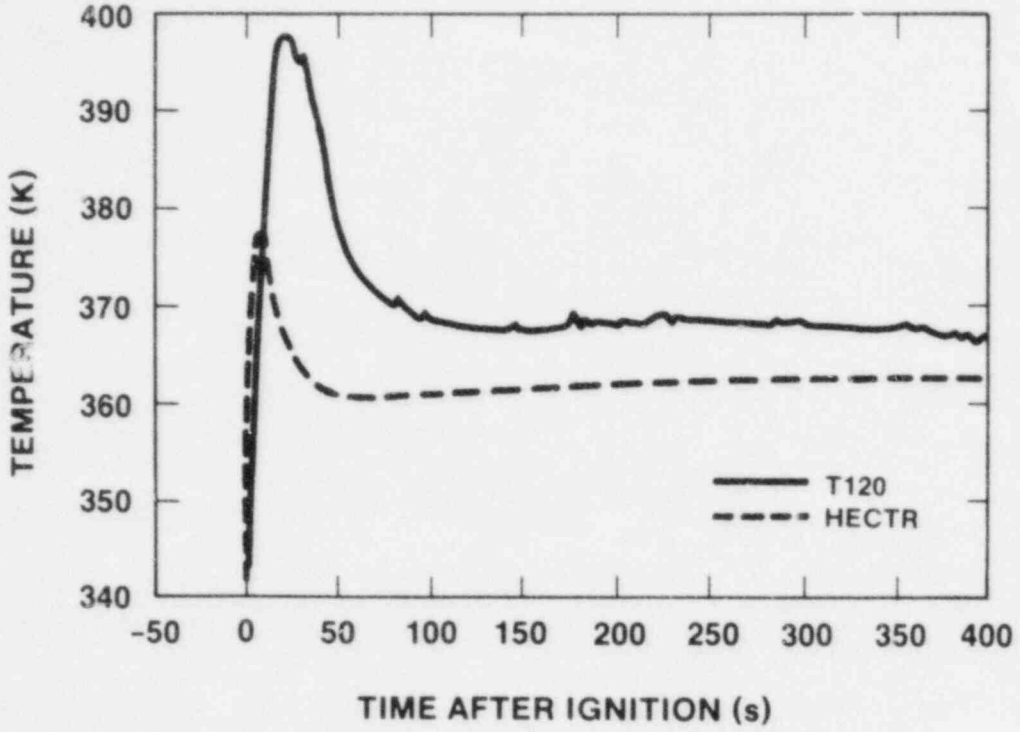

Figure 1.39. Surface Wall Temperature vs. Time for NTS Test P21

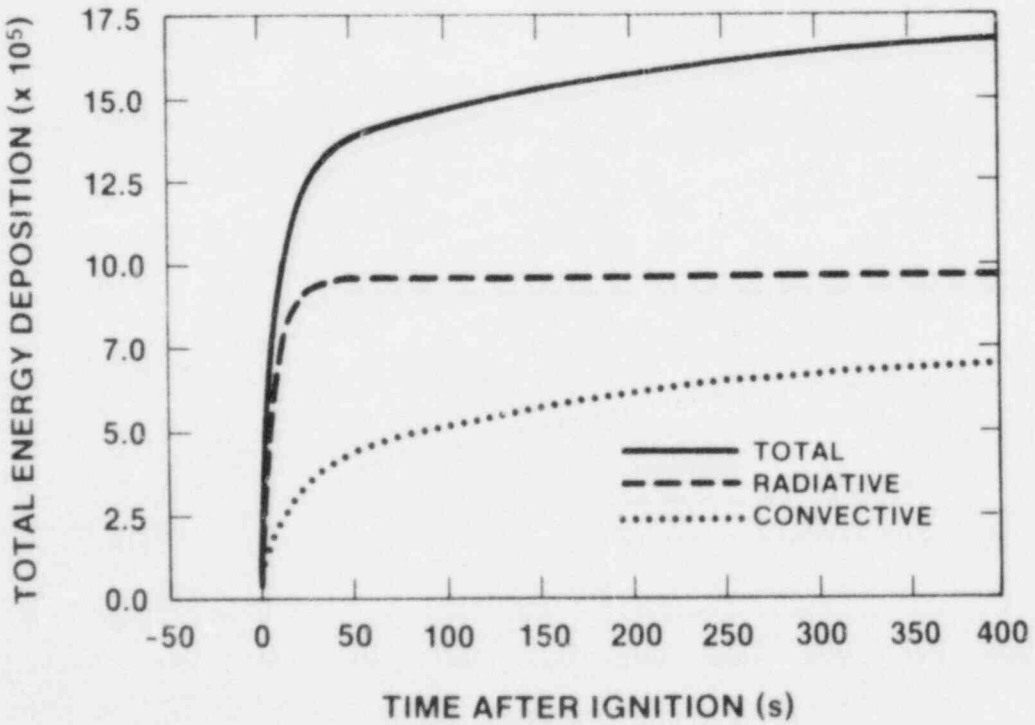

Figure 1.40. Total Energy Deposition vs. Time for NTS Test P21

1.5.1.2.3 Comparison of HECTR P20 and P21 Calculations

Since the initial conditions are nominally the same for each test, with the only difference being the activation of the sprays in test P21, a comparison of the two calculations provides insight into the effect of containment spray. Because containment spray is an important engineered safety feature and is expected to be operative in emergency situations requiring the removal of saturated steam from the containment environment, it is important to critically assess the containment spray model in the HECTR code.

The gas pressure and temperature time histories as computed by HECTR for both tests are shown in Figures 1.41 and 1.42, respectively. The burn times and hydrogen combusted are nominally the same, resulting in close peak pressures and temperatures (423 kPa, 1470 K for P20; 426 kPa, 1464 K for P21). This is consistent with the experimental data which indicate that sprays have a small effect during the short burn duration. In the 40-s time period following the end of the burn, the spray effect becomes more pronounced as the P20 and P21 gas pressures and temperatures begin to diverge. During this time period, radiative energy transport diminishes as the gas begins to cool down. This decrease is intensified by the evaporation of the spray droplets removing heat from the containment atmosphere, evidenced by the more rapid decline of the test P21 gas pressure and temperatures than those of test P20. At 42 s, spray droplet evaporation stops and condensation begins. Since condensation is the dominant heat transfer mechanism at this point in the transient, the gas pressures and temperatures in test P21 cease their decline, and a quasi-steady state thermal equilibrium between sprays and vessel is reached. The gas pressures and temperatures in test P20, however, continue to decline since the heat transfer mechanism to spray droplets is not present.

The steam molar fraction is plotted in Figure 1.43 for both tests. Since both tests combust approximately the same amount of hydrogen into steam, the difference between the P21 peak of 0.58 and the P20 peak of 0.43 is simply the amount of vapor added by the evaporation of spray droplets. The P20 vapor content remains essentially constant after the burn, although a slight increase occurs over an 80-s time period caused by the evaporation of surface wall condensate. In P21 after the driving potential between the vapor fraction at droplet surface and the vapor fraction within the bulk gas becomes zero at 42 s, the spray begins to condense steam, and the steam fraction begins a slow decline for the remainder of the transient.

Total, radiative, and convective/condensation energy deposition to the dewar wall are plotted in Figures 1.44, 1.45, and 1.46, respectively, for both tests. These figures

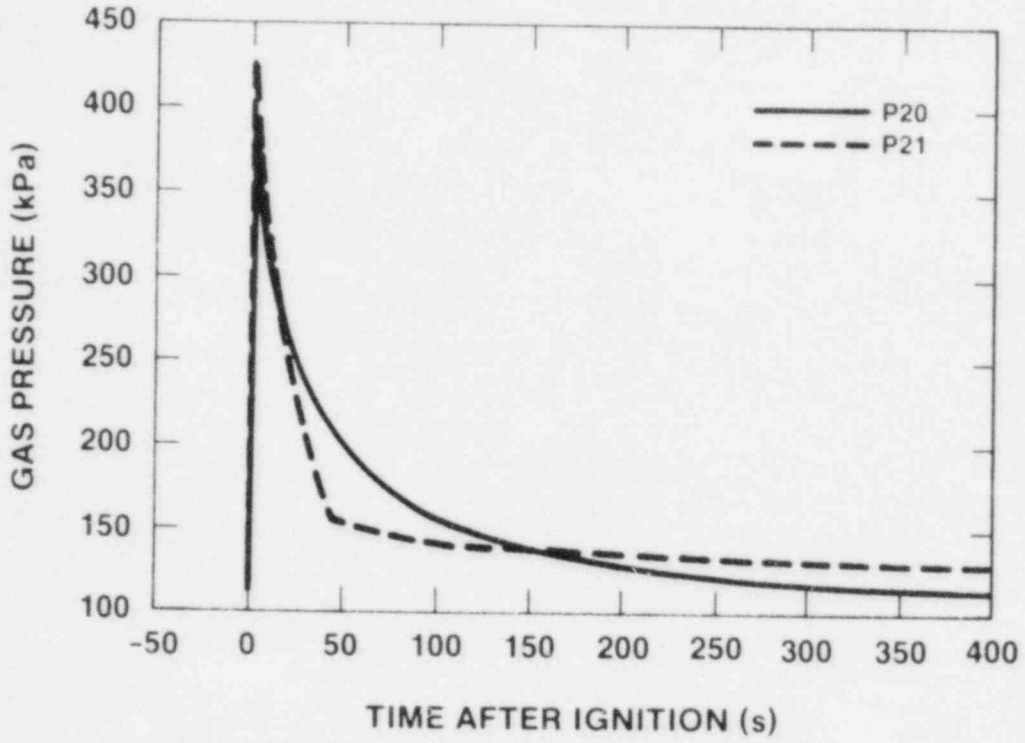

Figure 1.41. Comparison of the Calculated Gas Pressure vs. Time Between NTS Tests P20 and P21

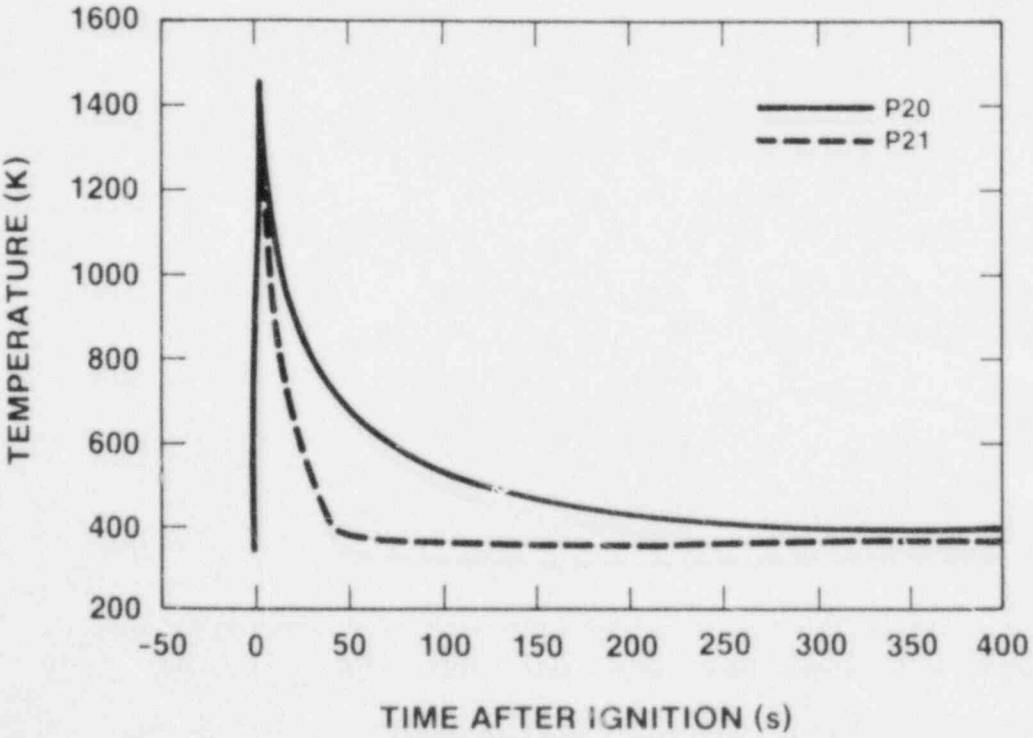

Figure 1.42. Comparison of the Calculated Gas Temperature vs. Time Between NTS Tests P20 and P21

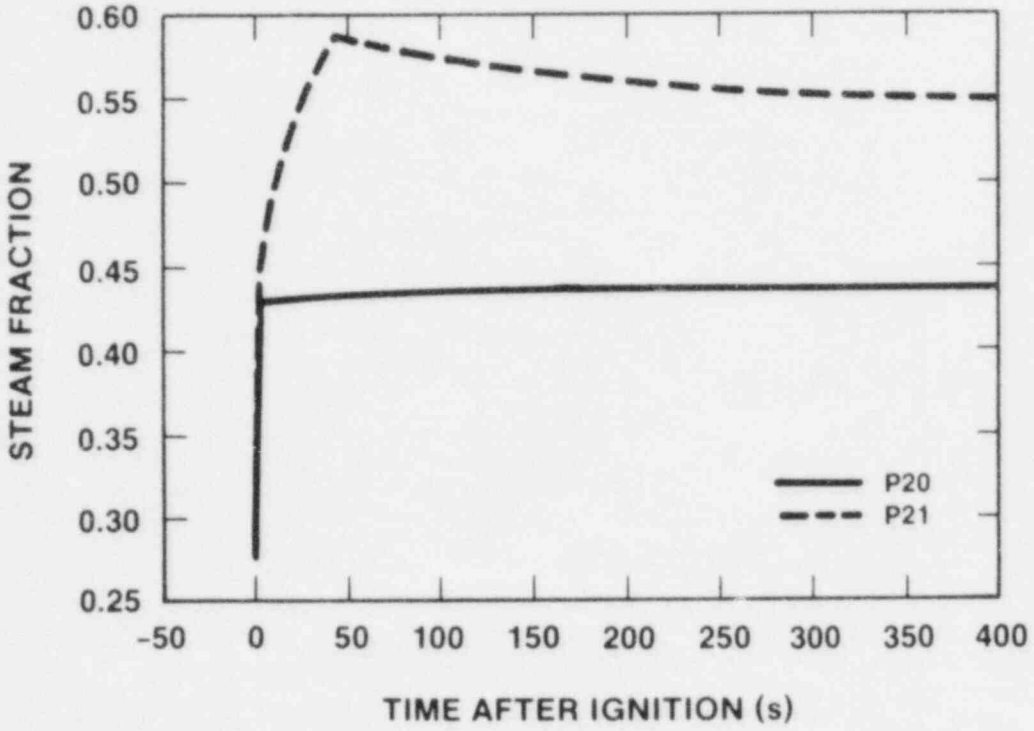

Figure 1.43. Comparison of the Calculated Steam Molar Fraction vs. Time Between NTS Tests P20 and P21

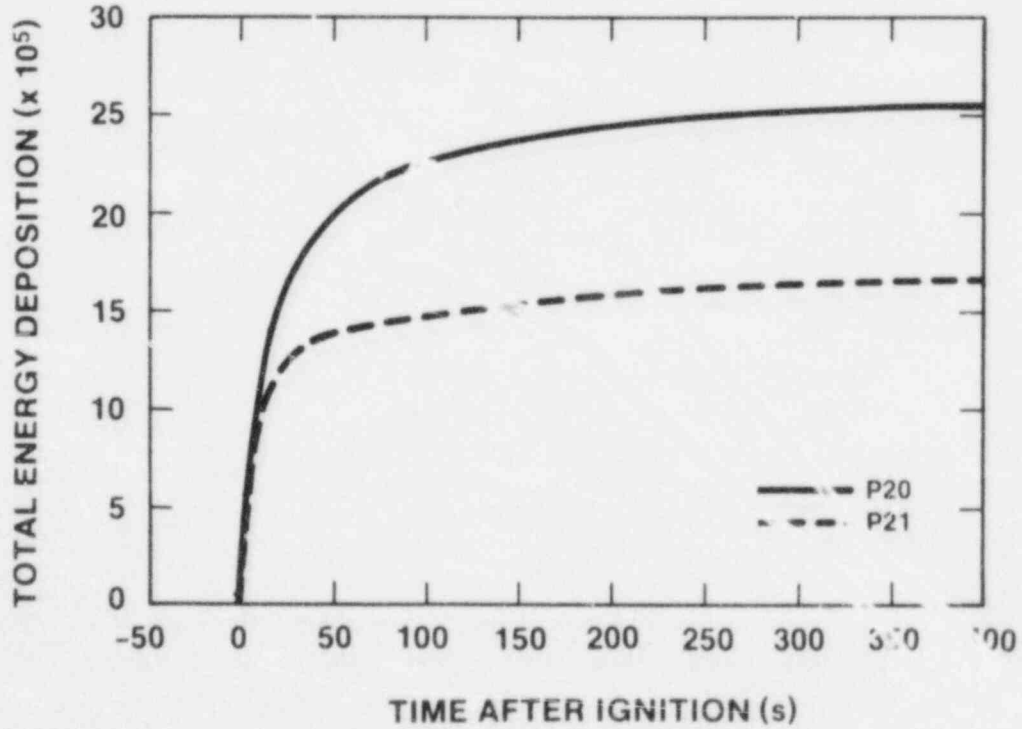

Figure 1.44. Comparison of the Calculated Total Energy Deposition to Surfaces vs. Time Between NTS Tests P20 and P21

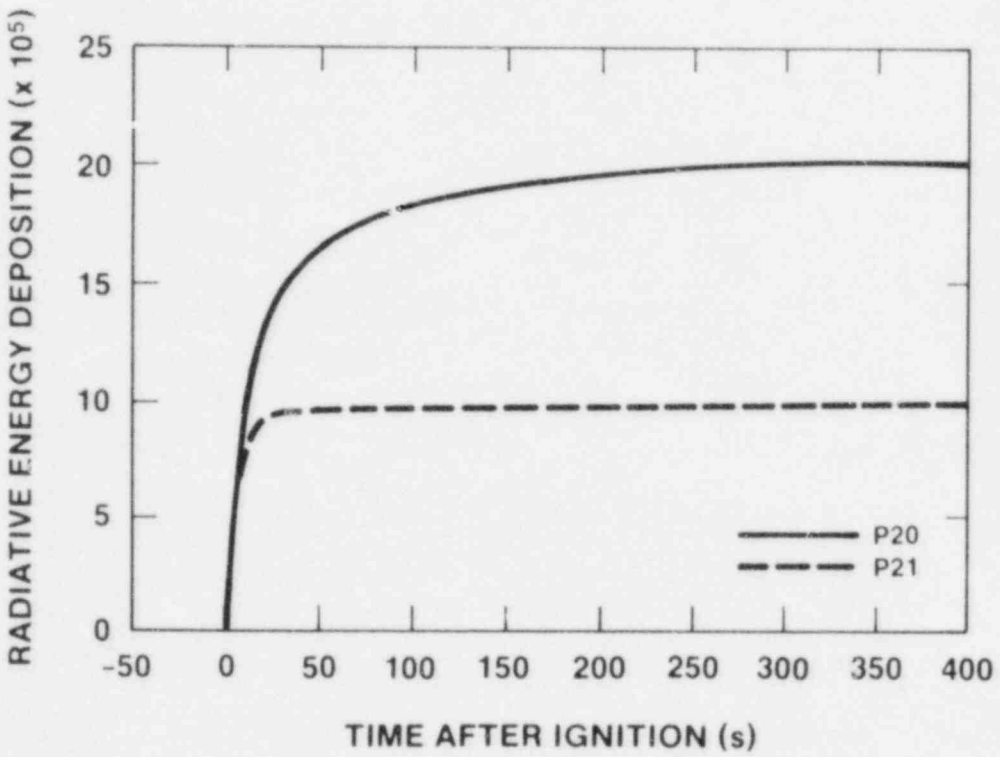

Figure 1.45. Comparison of the Calculated Energy Deposition to Surfaces From Radiation vs. Time Between NTS Tests P20 and P21

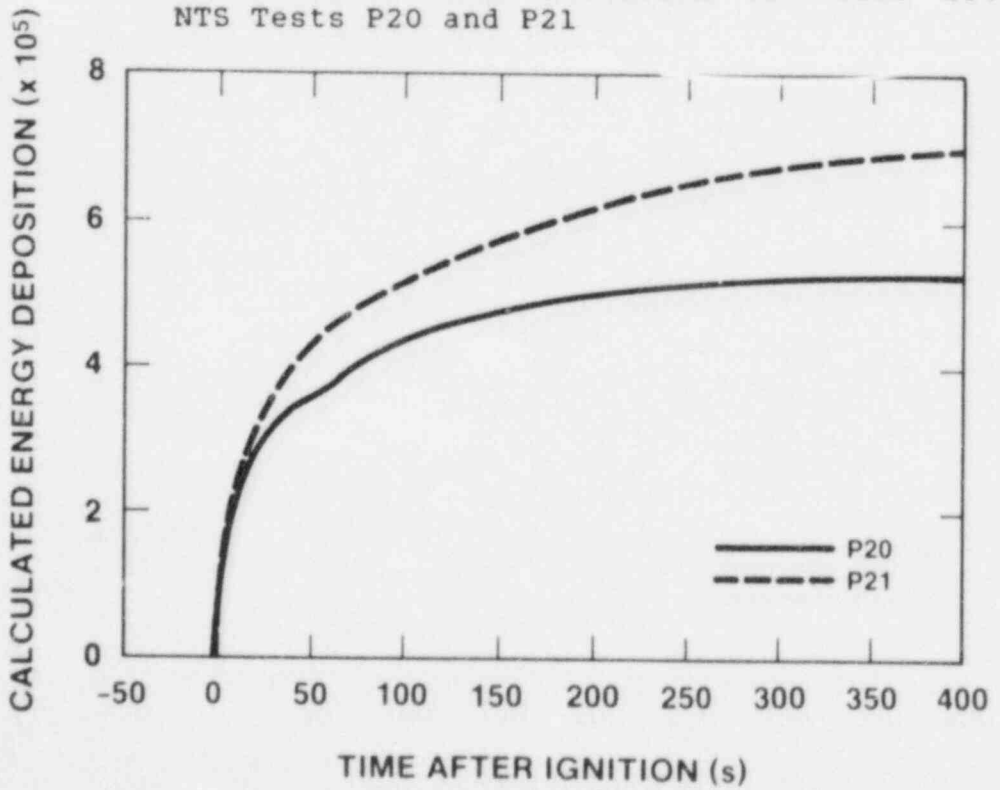

Figure 1.46. Comparison of the Calculated Energy Deposition to Surfaces From Convection/Condensation vs. Time Between NTS Tests P20 and P21

summarize the results shown in Figures 1.36 and 1.40. As expected, the total energy deposition is greater in test P20 because there is no heat transfer to droplets, and all energy released from the gas is absorbed by the dewar. Thus, the difference in the total energy deposition of 8.8×10^5 J/m between tests P20 and P21 is energy absorbed by the sprays. The effect of the sprays upon radiative energy deposition (Figure 1.46) is quite dramatic as the more rapid gas cooldown in test P21 shuts off radiative transport. Without sprays, the P20 bulk gas temperature cools at a slower rate and more energy is radiated away as a result. The convective energy deposition for test P21, however, is greater than that of test P20 (Figure 1.46) because of the greater condensation rate of the liquid film on the vessel wall. This is confirmed by Figure 1.47 which shows a positive condensation rate from the vessel wall in test P21 for the entire test. The test P20 rate of surface condensation, however, is -8 s after ignition when the liquid film on the wall begins to evaporate.

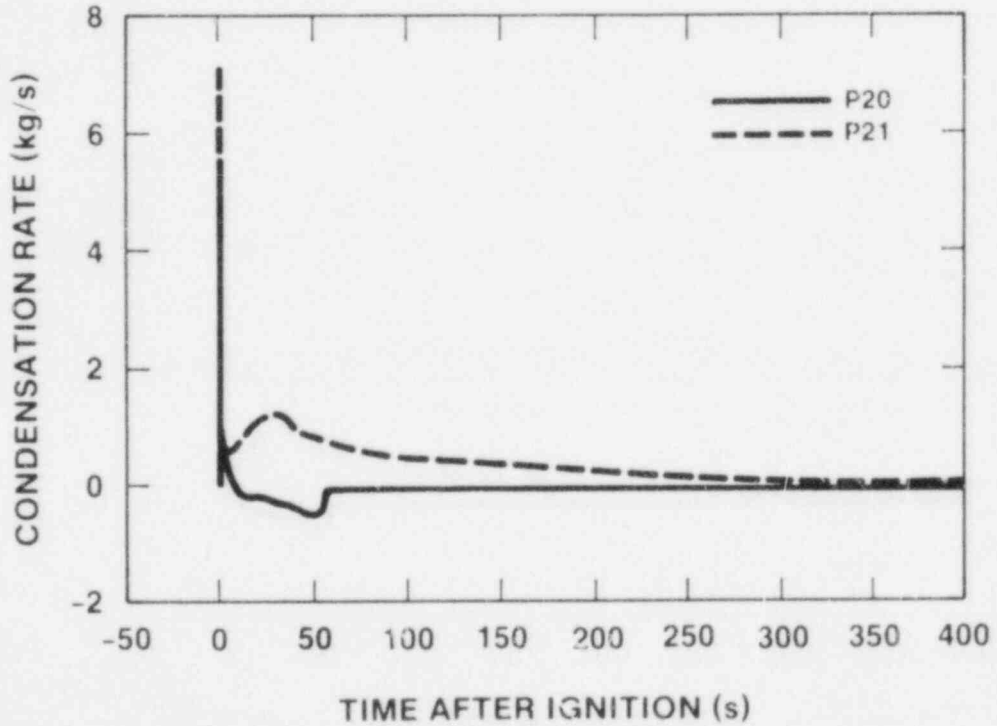

Figure 1.47. Comparison of the Calculated Condensation Rate at the Vessel Wall vs. Time Between NTS Tests P20 and P21

1.5.1.2.4 Future Modeling

Several processes, possibly important for the prediction of the effects of sprays, are not currently modeled in HECTR.

First, the experimentally observed enhanced turbulent mixing caused by the downward movement of the spray droplets is not modeled. It has the dual effect of shortening burn time and increasing peak gas pressures. Second, the interaction of water drops with combustion is not included. This has the opposite effect: increasing burn time and lowering the pressure. These are areas where future modeling efforts are required.

1.5.1.3 HDR Test V44 Calculation
(C. C. Wong, 6427; J. F. Kotas, 6427)

HDR is a decommissioned reactor facility near Frankfurt, West Germany used by Kernforschungszentrum Karlsruhe (KfK) to conduct reactor-scale steam blowdown experiments during the fall of 1982. This particular experiment, V44 (German Standard Problem No. 6) was one of a series of water and steam blowdown experiments which simulate full-scale, design-basis, loss-of-coolant accidents.

The prediction of containment pressures and temperatures during and following a large break LOCA requires accurate modeling of containment heat sinks, condensation on structures, intercell flow, and air-steam thermodynamics. Condensation heat transfer correlations (e.g., Uchida correlations) obtained from small-scale experiments are not adequate for predicting peak containment pressures.[1.16] Significant progress has been made in the past several years in incorporating more realistic condensation models to predict containment response. In particular, a condensation model has been developed for the HECTR code, which is applicable over a broad range of conditions. This model handles both condensation and evaporation, both forced and natural convection conditions, and includes the effects of condensate film and boundary layer. Test V44 is a good experiment to assess this new condensation model at large scale.

Initial preparation of the HECTR HDR test V44 calculation has begun with the creation of the HECTR input deck. The compartmentalization is identical to that used in the CONTAIN calculation of the same test.

1.5.1.4 NTS Test Data Reduction and Analysis
(A. C. Ratzel, 1513; J. E. Shepherd, 1512)

A substantial amount of useful data on premixed and continuous injection hydrogen deflagrations in air and steam has been provided by the large-scale tests sponsored by the U.S. Nuclear Regulatory Commission and the Electric Power Research Institute and conducted by EG&G at the Nevada Test Site (NTS). These tests were performed to study combustion processes in a large-scale vessel and to evaluate associated safety-related equipment response to the resulting thermal

environments. The experiments were performed in a 2048-cubic-meter spherical vessel (hydrogen dewar) with mixtures of hydrogen, steam, and air ignited by glow plugs or heated resistance coils. Hydrogen concentrations ranged from 5 to 13 percent (by volume) and steam concentrations from 4 to 40 percent. Several tests also incorporated spray systems and/or fans which enhanced the combustion rate and significantly altered the postcombustion gas cooling. Additional tests addressed the effects of localized combustion from diffusion flames which were generated by ignition of streams of steam-hydrogen mixtures injected into the dewar.

These burns were conducted at sufficient scale to aid in the validation of hydrogen combustion codes. We are performing a detailed evaluation of the quality and self-consistency of some of the data from the premixed tests in conjunction with the HECTR assessment effort. This is being done in order to judge the utility of these data in characterizing hydrogen burn environments. The quality of the data from different types of instrumentation varies greatly, and care must be exercised in interpreting the results.

A draft topical report on this evaluation is nearing completion. The information provided in this report should be useful for "benchmarking" existing computer codes used in modeling nuclear containment response to degraded core accidents and also to resolve issues pertaining to functionability of safety-related equipment in containment during such accidents. The results obtained from this study coupled with results obtained from intermediate-scale combustion testing (e.g., such as from the FITS and VGES facilities at Sandia) should also be useful in future modeling activities to upgrade the combustion and heat transfer models currently used in reactor safety computer simulations.

1.5.2 Flame Acceleration and Transition to Detonation

1.5.2.1 The FLAME Facility

(M. P. Sherman, 6427; S. R. Tieszen, 6427; W. B. Benedick, 1131)

FLAME is a heavily reinforced "U"-shaped channel designed to study hydrogen combustion problems relevant to nuclear reactor safety. The internal dimensions are 30.5-m-long by 2.44-m-high by 1.83-m-wide (100 x 8 x 6 ft). Movable steel plates on top of the channel provide various degrees of transverse venting. Low energy ignition occurs at the closed end, and the flame propagates toward the open end of the channel. The floor and side walls of FLAME are covered with hundreds of high-strength embeds to which obstacles can

be attached. Planned experiments include the investigation of flame acceleration mechanisms and the transition to detonation in simulated reactor containment geometries.

The initial tests in FLAME have examined the effects of transverse venting on combustion in an obstacle-free channel. In small-scale tests at McGill University, limited to 12.7 percent hydrogen, even small degrees of top venting, ~8 percent, led to a great reduction in flame acceleration. The purpose of our tests is to quantify the effective flame speeds, overpressures, and danger of transition to detonation at large scale.

Prior to this reporting period a total of 16 tests had been completed. The first series used 50 percent top venting area with no obstacles placed in the channel (other than instrumentation and two small mixing fans). These tests were relatively benign with no transition to detonation, even for 28 percent hydrogen. The overpressures were low. The second series of tests used a closed top and no obstacles. With no top venting the flame speeds and overpressures were much higher. In two tests, at 24.7 percent and 30.0 percent hydrogen, transitions to detonation occurred. The F-14 test at 30 percent hydrogen resulted in damage to the FLAME structure. The current series of tests is using 13 percent top venting area. This value is of interest because it is close to the value where venting began to have a substantial mitigating effect in the small-scale experiments. Two tests had been run at up to 17.6 percent hydrogen. Further tests at higher hydrogen concentrations awaited permanent repairs to the FLAME facility caused by the detonation in F-14.

During this reporting period repairs to FLAME were completed and two additional tests were run, F-17 and F-18. The hydrogen mixtures in these two tests, 14.9 percent and 18.1 percent, were below those projected, and covered the same ground as the previous two tests. There was an air leak in the compressed air lines used to drive the mixing fans. Some of the air passing through these lines, instead of venting outside FLAME, went into the channel, diluting the mixture. The problem was discovered and corrected. Testing will resume in January.

It is highly desirable to relate the experimental results from FLAME to theoretical models in order to be able to extrapolate the results to conditions of interest in reactor containments. We view the problem of understanding FLAME results in four parts:

1. Perform a more complete analysis of the data, incorporating it into a form useful for theoretical modeling.

2. Use turbulent combustion theory and/or correlations to be able to predict flame speeds as a function of hydrogen concentration, transverse venting, and obstacle configuration.

3. Determine the overpressure in the channel, for given flame speeds.

4. Determine the conditions for transition to detonation, given the results of problems 1-3.

We made significant progress in improving the analysis of the FLAME data. These results will be described in following paragraphs. We have been examining turbulent flame speed literature and comparing the results to our experimental work. However, this work is still incomplete. Work on the comparison of the experimental and theoretical overpressures for tests with no transverse venting will be described. Transition to detonation will be considered in the next quarterly.

1.5.2.1.1 New Analysis of Experimental Results

In the past we have shown flame shapes for a few selected tests based on linear interpolation of time-of-arrival data taken from hand-drawn time versus axial distance graphs. We now have a set of computer programs that will determine flame shapes, flame speeds, and accelerations from tabular time-of-arrival data using linear interpolation of flame time-of-arrival data. Some results are shown in Figures 1.48 a-d.

In the first series of tests with 50 percent top venting area, the speed of propagation of the flames was nearly constant down the channel after an initial transient. We plot "typical speed of flame propagation" (axial distance traveled by the flame divided by the difference in time of arrival) versus hydrogen concentration. For tests with no top venting, the flame accelerated down the channel. The "typical flame propagation speed," based on some mean speed in the later part of the channel near midheight, began to lose its significance. To use a less arbitrary velocity, and for comparison to theory for planar flames, we define an "equivalent planar flame speed" as the volumetric burning rate divided by the channel cross-sectional area. In Figure 1.49 we show the peak value of this quantity versus hydrogen concentration. The equivalent planar flame speed for the 50 percent top venting area case is much lower than for the comparable case with no top venting. With 13 percent top venting area, the speed is intermediate between the other two cases.

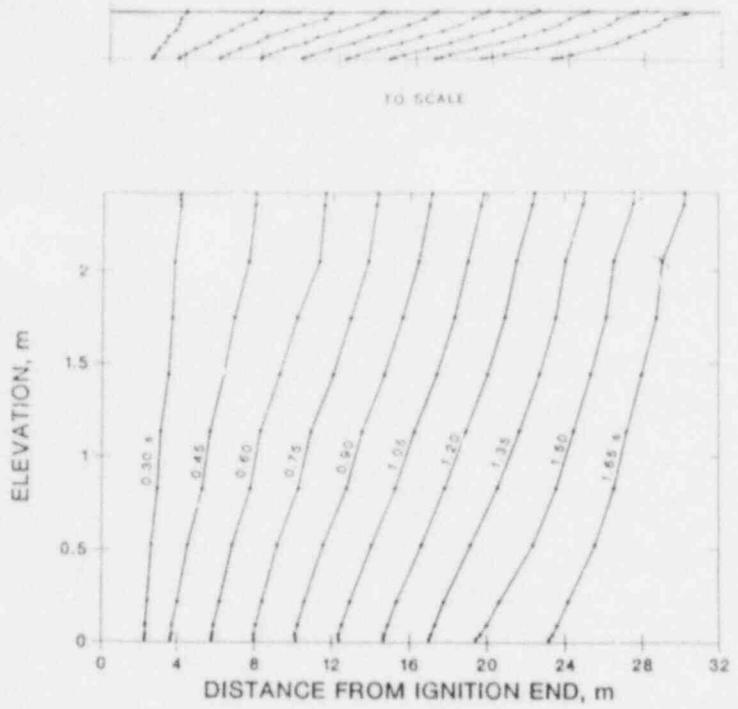

Figure 1.48a. FLAME Test F-6, Combustion Front Profiles, 15.5 Percent Hydrogen, 50 Percent Top Venting

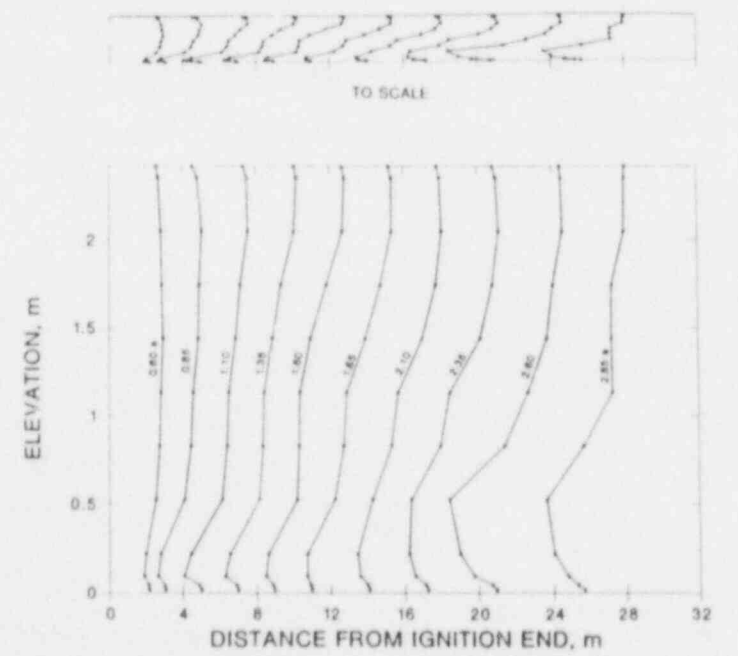

Figure 1.48b. FLAME Test F-7, Combustion Front Profiles, 12.0 Percent Hydrogen, No Top Venting

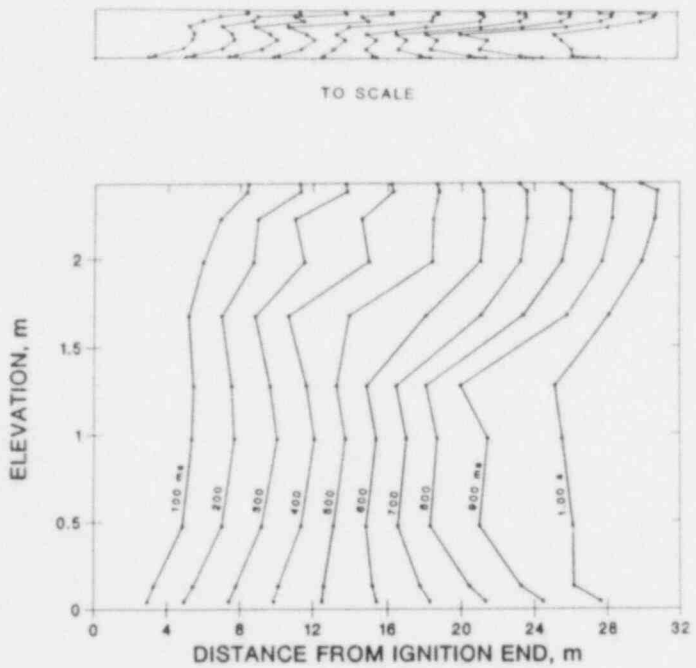

Figure 1.48c. FLAME Test F-15, Combustion Front Profiles, 15.4 Percent Hydrogen, 13 Percent Top Venting

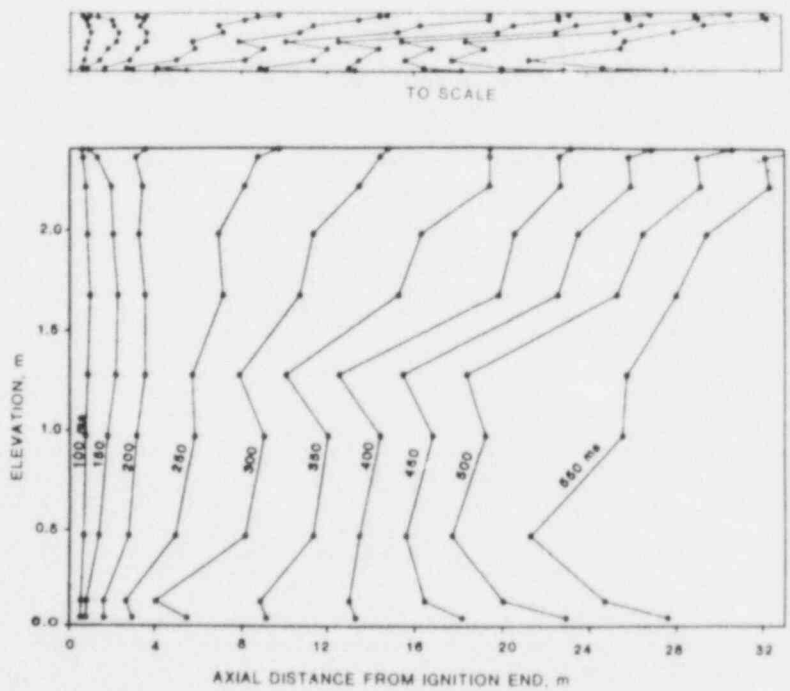

Figure 1.48d. FLAME Test F-16, Combustion Front Profiles, 17.6 Percent Hydrogen, 13 Percent Top Venting

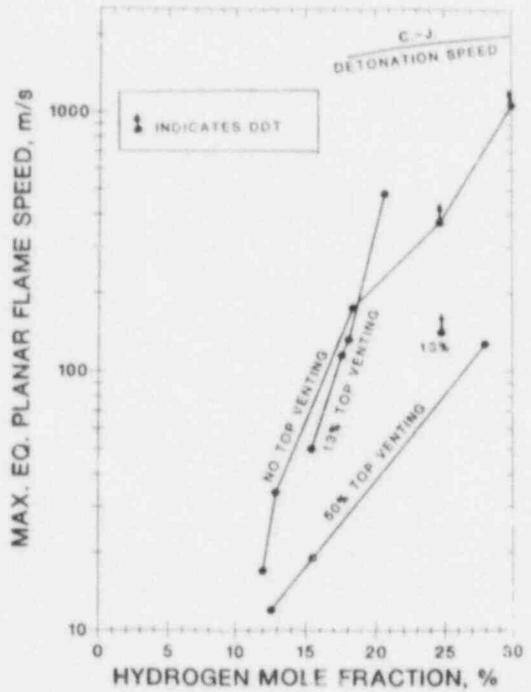

Figure 1.49. Maximum Equivalent Planar Flame Speeds

1.5.2.1.2 Overpressure Analysis

For deflagrations in a long channel open at the far end with no transverse venting, a useful upper bound on the overpressure is that caused by an "equivalent" planar flame. We have defined "equivalent planar flame speed" as the volumetric burning rate divided by the channel cross-sectional area. Using this definition, the main difference between a deflagration in FLAME and a planar flame, is that in a finite length channel like FLAME, as an overpressure builds up, pressure relief waves from the open end will reduce the overpressure.

Several papers have treated the "blast wave" from one-dimensional flames.[1.17-1.21] Usually the analyses contained a parameter "j," where j = 0 for planar flames, 1 for cylindrically symmetric flames, and 2 for spherically symmetric flames. Emphasis in these analyses is on spherically symmetric flames; the examples usually given are for j = 2. However, these analyses can be carried out for the simpler planar case. Most references consider constant speed flames. Some references also consider some classes of variable flame speed. For our work we used the paper of Kuhl, Kamel, and Oppenheim.[1.17] In examining it, and previous papers by

the same authors, several misprints in the equations given were found and corrected.[1.22,1.23]

The results of this study are shown in Figure 1.50. The theoretical curve of overpressure for a constant velocity planar flame is based on the theory in Reference 1.17 using thermodynamic properties for the burned gases taken from property tables at 2000 K. The theoretical overpressure is only a weak function of the variation in thermodynamic properties of the mixture. The experimental points show the peak deflagration overpressure versus the peak equivalent planar flame speed for tests with no top venting. In all cases, the peak overpressures are below the theoretical curve. On this logarithmic scale the experimental values appear to be closer to the theoretical curve at the higher flame speeds. This is in accordance with the expectation that pressure relief from the open end of the channel will be less effective with the shorter burn time.

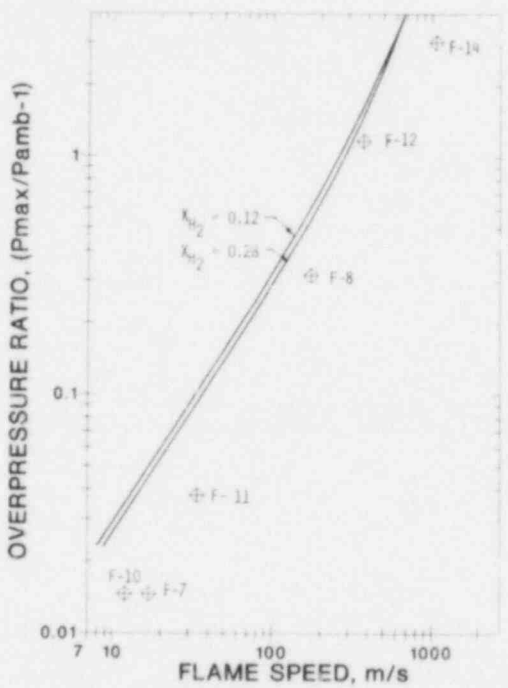

Figure 1.50. Comparison of Peak Measured Flame Pressure With Theory of Planar Steady Flame

For no top venting, this work could be extended to variable flame speed. A model for a finite length channel would doubtless require a numerical unsteady one-dimensional model. Work on modeling FLAME using a complex unsteady two-dimensional computer code called CONCHAS-SPRAY is underway.

We are examining simpler models used to predict vented overpressures that might be suitable for predicting overpressures with top venting. There is extensive literature on determining, or at least limiting, the overpressure in vented explosions.

1.5.2.2 Transition to Detonation at the Wake of an Obstacle (J. H. Lee, R. Knystautas, C. K. Chan, and C. Guirao, McGill University)

For insensitive fuel-air mixtures, transition from deflagration to detonation (DDT) is usually not observed in smooth tubes even after the flame has propagated a distance of hundreds of tube diameters. However, if suitable obstacles are placed in the path of a flame, DDT is greatly facilitated. It has been demonstrated in small-scale experiments[1.24-1.26] and accidentally in large-scale situations[1.27] that DDT can occur at the wake of an obstacle for very sensitive mixtures. Even though it has not been observed, there is reason to believe that DDT can also occur for less sensitive fuel-air mixtures if appropriate conditions are achieved.

Some of the mechanisms leading to DDT have been recently reviewed by Lee.[1.27] Qualitatively, DDT in the wake of an obstacle is well understood. The hot combustion products and the unburned gas are being intensely mixed in the wake region. Depending on the turbulent intensity, this may lead to the formation of pockets of partially reacted mixtures. The local conditions of these pockets correspond to the different stages in the induction period leading to autoignition. The shock wave generated by a localized explosion can be rapidly amplified in the gradient field of induction time produced by the turbulent mixing process. If the size of the mixing region is sufficiently large, the shock can amplify to a strength which is large enough to cause autoignition of the mixture itself, and the onset of detonation can occur. This mechanism is known as Shock-Wave Amplification by Coherent Energy Release (SWACER).[1.28] Another mechanism for DDT is shock merging as observed by Oppenheim.[1.29] This can result from multiple local explosions or by reflection of a shock off surrounding walls. For DDT in a confined region such as inside a tube, both mechanisms are believed to play dominant roles.

In the present study, orifice plates are used as flow perturbing obstacles since the flow structure of the wake downstream of an orifice is well documented. Ignition of the explosive mixture downstream of the obstacle is by the hot combustion products emerging from the orifice in the form of a hot jet. Successful transition to detonation

depends on the mixture sensitivity as well as the mixing process occurring at the wake of this hot turbulent jet. Such a process is very often encountered in industrial accident scenarios. This can be achieved by propagation of a flame through multiple chambers or by rupturing of a containment due to an explosion within. Thus, an understanding of the basic mechanism of DDT at the wake of an obstacle is essential for the assessment of the potential danger in any accident situation. This report summarizes some of the recent results on the study of DDT at the wake of an orifice obstacle and elucidates the possible mechanisms.

1.5.2.2.1 Experimental Apparatus

A schematic of the experimental apparatus is shown in Figure 1.51. The experiments were performed in a tube 30 cm in diameter, 14 m in length, closed at both ends. An orifice was mounted at 2 m from the ignition end dividing the tube into two separate chambers. The gas mixture was ignited by a weak electrical spark in the first chamber. The mixture in the second chamber was subsequently ignited by the hot combustion products shooting out through the orifice. To vary the burning rate and the overpressure achieved in the first chamber, an obstacle array in the form of a series of orifice plates was inserted into the tube near the ignition end for some experiments. These orifice plates had a blockage ratio of 0.28 and were spaced one tube diameter apart. The flame speeds and the pressure developments in both chambers were monitored using ionization gauges and pressure transducers mounted along the length of the tube. Since the main interest in the present study is on the flame behavior in the wake region downstream of the orifice plate, all the probes are placed within 3 m from the obstruction. So far, only H_2-air mixtures have been examined. The gas mixture was prepared by means of a partial pressure method. This process consisted of first evacuating the tube to the desired pressure and charging the tube with hydrogen until the tube is at atmospheric pressure (after each experiment, the apparatus was purged with compressed air). The mixture in the tube was recirculated at least five times by an external pump until the mixture was uniform throughout. Five orifice plates were examined in the present study. In order to obtain a wider range of turbulent length scales downstream of the obstacle, two of the orifice plates used have multiple holes. By varying the diameter of the holes as well as their number, it was possible to vary the turbulent length scale in the wake while keeping the blockage effect relatively similar. The configurations of the orifice plates are summarized in Table 1.5.

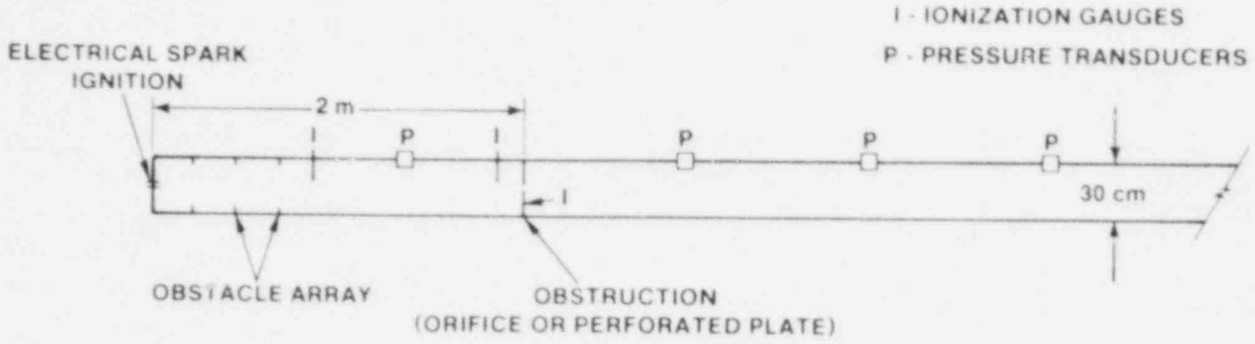

Figure 1.51. Schematic of Apparatus

Table 1.5

Obstacle Configurations for DDT Experiments

	Hole Diameter (cm)	Number of Holes	Open Area (cm^2)	Blockage Ratio
Orifice	5.1	1	20.4	0.972
Orifice	8.9	1	62.2	0.915
Orifice	20.3	1	323.6	0.556
Perforated plate	3.81	7	79.8	0.891
Perforated plate	0.635	318	100.6	0.862

1.5.2.2.2 Results and Discussion

A trajectory for a 24 percent H_2-air flame propagating through a perforated plate (318 holes, 0.635 cm diameter hole) is shown in Figure 1.52. The relative location of the probes is also indicated in the figure. The averaged flame velocity in the first chamber is about 125 m/s. The overpressure at the time of arrival of the leading flame front at the perforated plate is about 1.0 bar. The overpressure in the first chamber drops very quickly as the flame emerges from the plate and the flame velocity jumps to about 900 m/s. The flame propagates at the same velocity for the next 3 m. Transition to detonation does not occur for this case. For 25 percent H_2 (shown in Figure 1.53), the average flame velocity in the first chamber is the same as in the previous case. However, the flame velocity increases rapidly to 1950 m/s upon emerging from the perforated plate. The normal Chapman-Jouguet detonation velocity for 25 percent H_2 is 1850 m/s. This result shows that transition to detonation occurred as a result of enhanced combustion in the wake region. From the flame trajectory, transition to detonation is estimated to have occurred at roughly 0.5 m from the perforated plate. Experiments with other orifice plates also show that the onset of detonation occurs between 0.5 m to 1 m from the obstacle. In a previous study on the initiation of detonation by a hot turbulent jet,[1.27] it was observed that for initiation of unconfined spherical detonation at the wake of a grid plate, the onset of detonation always occurs just a few centimeters from the plate where the turbulent mixing is the most intense. Furthermore, only transitions to detonation for those very sensitive C_2H_2-O_2 mixtures have been observed. The present result indicates that the wall that surrounds the wake region may also play an important role in assisting transition to detonation.

As an indication of whether transition to detonation has occurred, the flame velocities at 2 m downstream from the orifice are shown in Figure 1.54 for all the experiments performed. The corresponding overpressures in the first chamber are also included in the same figure. These results show that if transition to detonation has occurred, the flame velocity at 2 m from the orifice is very close to the C-J detonation velocity. If transition to detonation does not occur, the flame velocity is about half the corresponding C-J detonation velocity. Without further obstructions to generate turbulence, the enhanced combustion cannot maintain itself and the flame velocity is expected to decelerate as it continues to propagate down the tube. The present experiments show that successful DDT depends on both the orifice diameter and the upstream overpressure. For the experiments performed with the 8.9 cm diameter orifice, insertion of an obstacle array in the first chamber increases the upstream

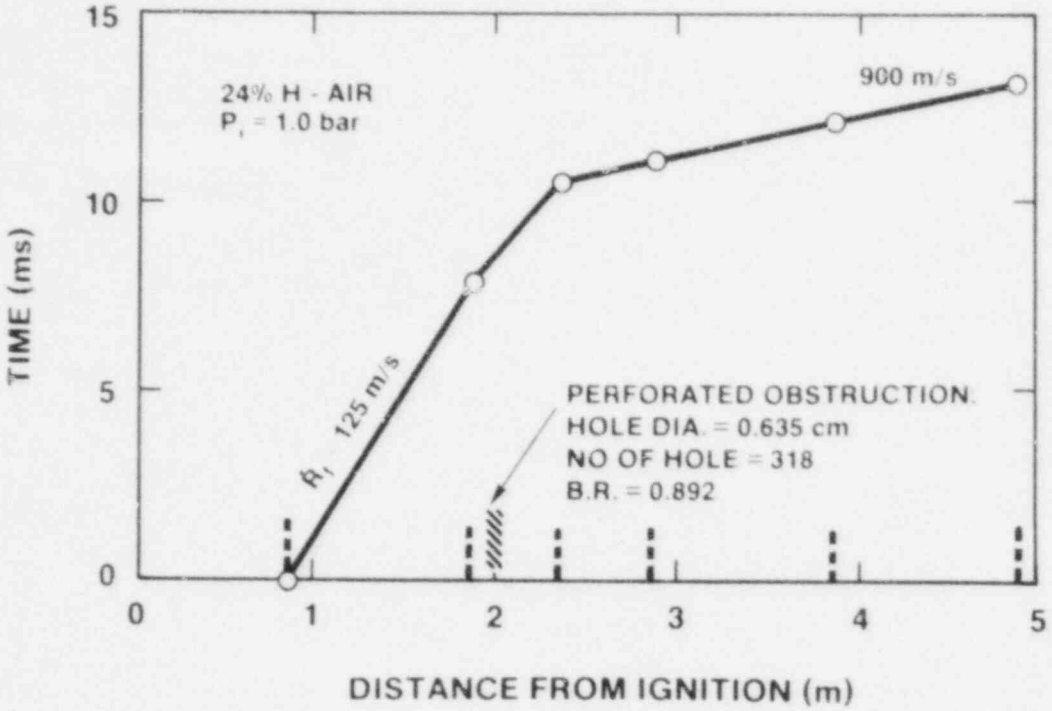

Figure 1.52. Flame Trajectory for 24 Percent Hydrogen-Air Mixtures

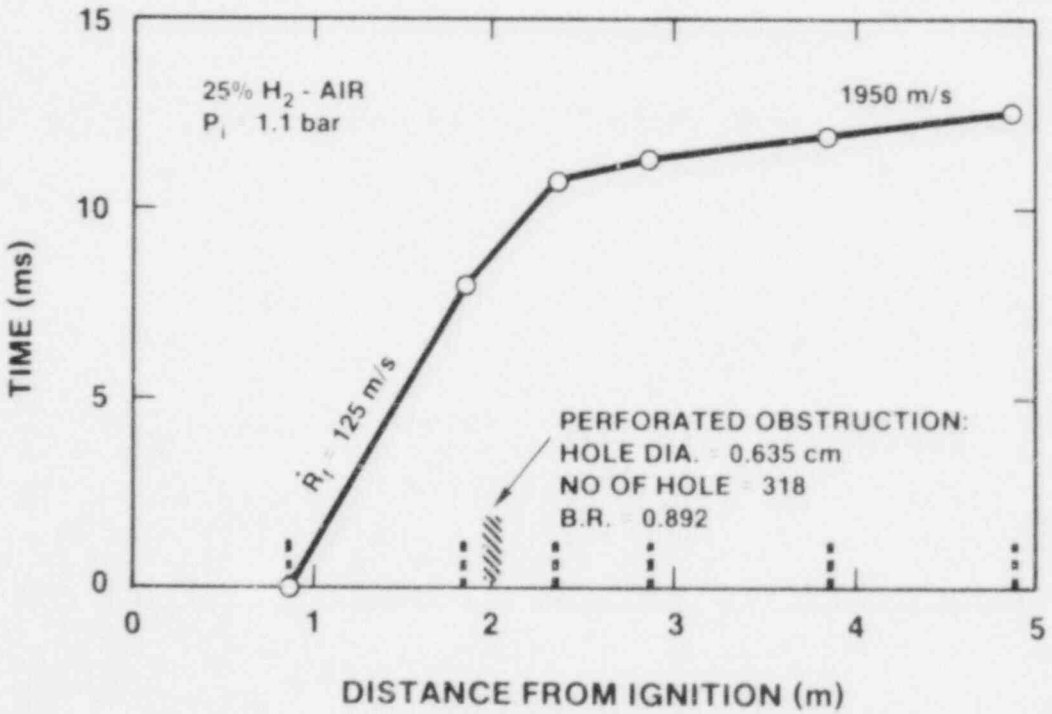

Figure 1.53. Flame Trajectory for 25 Percent Hydrogen-Air Mixtures

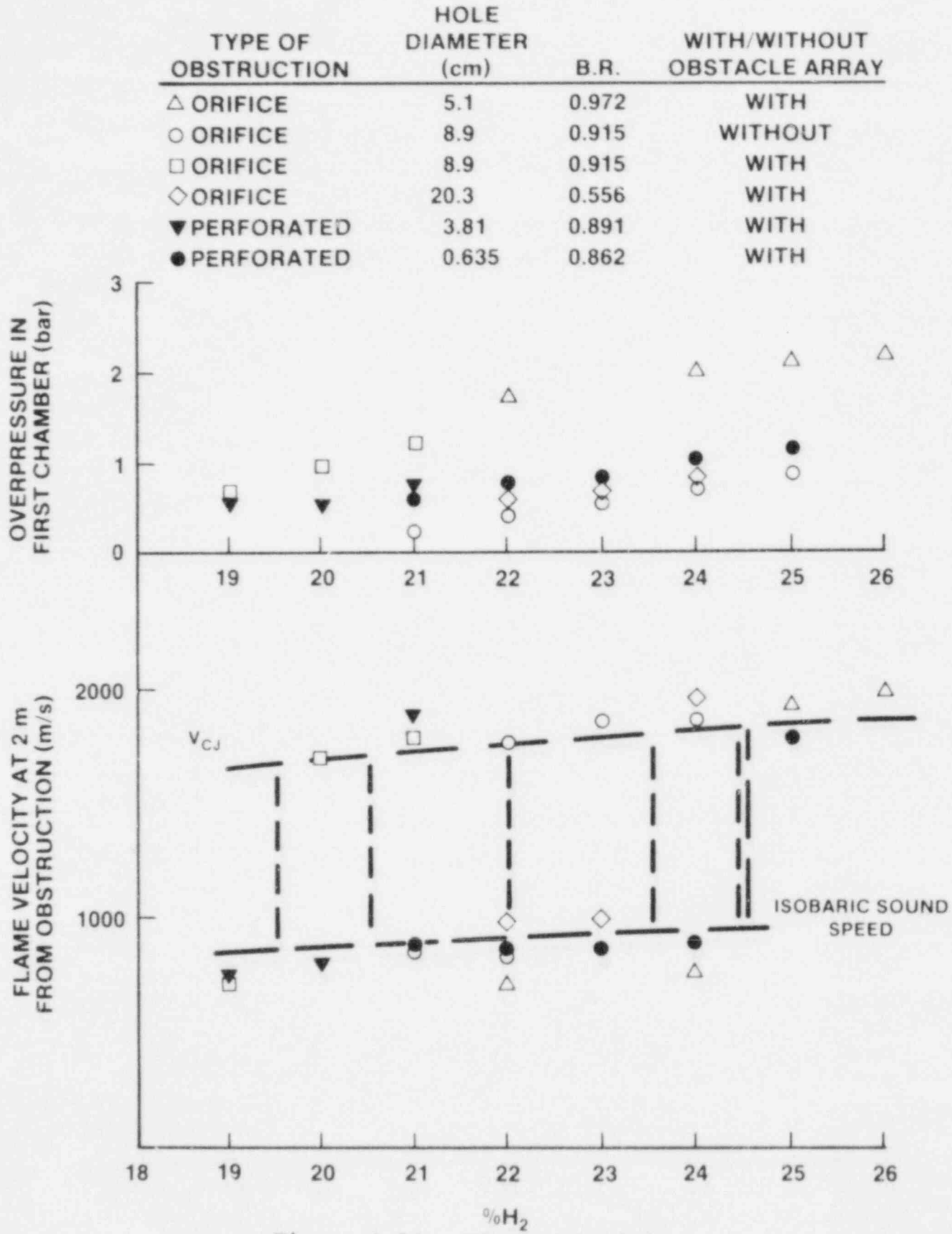

Figure 1.54. Flame Velocities

overpressure from 0.4 bar (without an obstacle array) to 0.95 bar. Higher overpressures result in faster rates of venting of the hot combustion products into the second chamber, which in turn increases the turbulent intensity in the wake region. Keeping the turbulent length scale the same while increasing the turbulent intensity facilitates the transition process. For the present experiments, increasing the upstream overpressure by 0.55 bar changes the condition for DDT from 22 percent H_2 to 20 percent H_2. However, upstream pressure is not necessarily the dominant mechanism for transition. Experiments at 24 percent H_2 show transition to occur for a 9-cm orifice but not for a 5-cm orifice, although upstream pressure is much greater. The overpressure can be increased even further by increasing the number of obstacles in the first chamber to create a higher overall burning rate or by increasing the volume of the first chamber. Ideally, the overpressure can be very close to the constant volume combustion overpressure. One can expect DDT to occur for even less sensitive or leaner H_2-air mixtures.

Another interesting comparison can be made with the results of experiments using perforated plates. The total opened area of the perforated plates and the 8.9-cm orifice plate are about the same. The overpressure in the first chamber and hence the turbulent intensity in the wake are expected to be similar. However, holes of different diameters produce turbulence of different length scale. The hole diameters of the orifice plate and perforated plates are 8.9 cm, 3.81 cm, and 0.635 cm, respectively. The corresponding conditions for DDT are 20 percent H_2, 21 percent H_2, and 25 percent H_2. These results seem to suggest that DDT occurs more easily in regions of larger turbulent length scales. However, this observation should be interpreted carefully. As pointed out earlier, one of the required mechanisms for DDT is the generation of local explosions in the turbulent mixing region. This can only occur if the mixing rate is about the same as the chemical reaction rate. The mixing rate depends on the turbulent length scale as well as the turbulent velocity. Therefore, depending on the turbulent intensity in the mixing region, larger turbulent length scale does not necessarily imply easier DDT.

Transition to detonation in the wake of a single orifice obstacle is possible for relatively insensitive H_2-air mixtures. Preliminary results indicate that beside the orifice configuration and the upstream overpressure which determine the turbulent mixing rate in the wake region, the surrounding walls which confine the wake region also facilitate the transition process. Definitive conclusions regarding the criteria for transition to detonation cannot be obtained based on the present preliminary results. More

extensive studies are needed to achieve a quantitative prediction of the phenomenon.

1.5.3 Detonation Research

1.5.3.1 Heated Detonation Tube
(S. R. Tieszen, 6247; M. P. Sherman, 6427; W. B. Benedick, 1131)

The purpose of the Heated Detonation Tube (HDT) program is to develop an experimental data base with which models can be developed to assess the probability of detonation inside containment. Strong dynamic shock pressures associated with detonations have the potential to cause early containment failure and/or considerable damage to safety-related equipment.

The direct consequence of the nonlinear coupling between the exothermic chemical reaction and the shock-induced hydrodynamic flow field in a detonation wave is the three-dimensional transverse wave structure, commonly characterized by the cell width λ. Extensive evidence shows that all self-sustaining gaseous detonation waves have this structure and that every detonable mixture has a scale of structure. The cell width is believed to be representative of the chemical length scale of a given explosive mixture under detonative conditions and can thereby be used to define the explosion sensitivity of that particular mixture. Moreover, in recent years the broader fundamental significance of the detonation cell width has been demonstrated via the quantitative links that have been established with the other "dynamic" detonation parameters such as the critical initiation energy and the critical tube diameter. It also has direct relevance to establishing criteria for transmission of detonation, onset of transition, and definition of detonability limits.

Recent experimental evidence indicates that the possibility of a detonation within the nuclear containment buildings may not be as remote as originally thought. The basis for this assessment derives from the recent observations of Lee,[1.30] Pförtner,[1.31] and Sherman et al.,[1.32] that turbulence-induced transition to detonation can occur even in off-stoichiometric mixtures, not only under confined, but also under partially confined conditions. In view of the possible damage that a detonation wave poses to the structural integrity of the nuclear reactor containment buildings and safety-related equipment, the study of the detonation susceptibility and detonation properties of the range of mixtures that can be encountered in all possible accident sequences is of major importance.

For several severe accident scenarios hydrogen-air-steam mixtures for a range of concentrations, initial temperatures,

and pressures may exist throughout the containment building. Prior to this work there was no experimental information on the detonability of hydrogen-air-steam mixtures. The main objectives of the present work has been to develop the facilities and to carry out a systematic series of tests which provide a broad range of basic detonability data for H_2-air and H_2-air-diluent mixtures relevant to nuclear reactor safety.

1.5.3.1.1 Apparatus and Procedure

The heated detonation tube is a 0.43 m internal diameter by 13.1-m-long heated and insulated stainless steel tube. The apparatus is shown in Figure 1.55. The temperature of the tube is elevated by electrical resistance tapes mounted under insulation on the outside surface of the tube. Temperature uniformity at elevated temperatures is maintained by computer-controlled feedback from thermocouple measurements of the temperature of the tube under the heaters. Thirty additional thermocouples monitor the tube temperature away from the heater tapes.

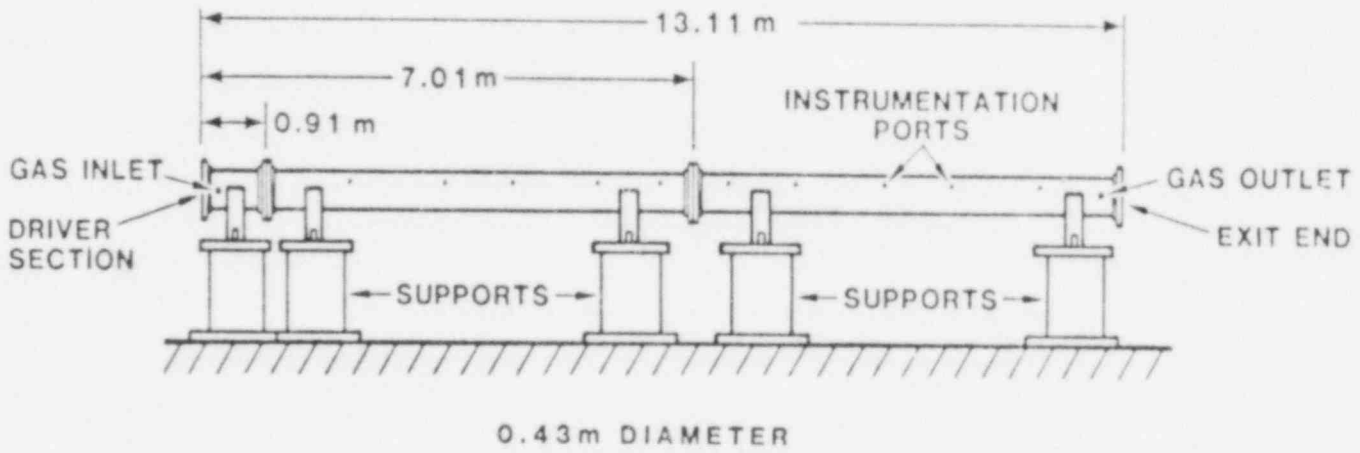

Figure 1.55. Heated Detonation Tube

To ensure a homogeneous mixture, the gases are recirculated from one end of the detonation tube to the other by a bellows pump through a heated secondary recirculation line. Noncondensable gases are introduced into the recirculation line from gas cylinders. Steam is produced by vaporizing a measured volume of water into the recirculation line.

After the explosive initiator and smoked foil are installed at the two ends of the detonation tube, and the ends bolted shut, the tube is evacuated. Dry bottled air is then introduced. After the air temperature in the detonation tube has reached steady state, the air pressure is adjusted to yield the proper air density. The air temperature and pressure are recorded. Hydrogen is slowly added to the recirculation line and the temperature and pressure are again measured after steady-state conditions have been established. In tests with CO_2, the CO_2 is added prior to adding the hydrogen. The mixture is constantly recirculated through the detonation tube via the heated recirculation line. For the 100°C tests, the tube is uniformly heated and then steam is added to the recirculation line. The temperature and pressure are measured when steady state is established prior to initiating the detonation. The gas temperature is measured with a K-type thermocouple probe inserted through the detonation tube wall; the pressure is measured with a 0 to 340 kPa (0 to 50 psia) absolute pressure gauge.

1.5.3.1.2 Modeling

The characteristic reaction zone length for H_2-air-diluent detonations was determined by calculating the steady-state reaction zone structure with the ZND model. A detailed model of hydrogen oxidation integrated along the Rayleigh line was used in these computations. As first suggested by Shchelkin[1.33] and demonstrated by Lee et al.[1.34] for hydrogen-air-carbon dioxide mixtures and by Westbrook and Urtiew[1.35] for hydrocarbon-air mixtures, the characteristic reaction zone length L may be approximately proportional to the cell size, λ,

$$\lambda = AL \quad .$$

This proportionality was used to predict cell sizes from calculated values of L. The value of L we have used is based on the location of Mach number 0.75 in the flow within the reaction zone. The constant A is determined by normalization to data at the stoichiometric point for H_2-air detonations at STP initial conditions. A value of A = 22 was found in this way which is comparable to the value of 20 suggested by Westbrook and Urtiew.[1.35] Alternative definitions of L are possible and result in different coefficients.

1.5.3.1.3 Results

Results of the gaseous detonation tests performed in the detonation tube are shown in Figures 1.56 through 1.58. Uncertainty in detonation cell size for any single measurement of a smoked foil for any single test is ±100 percent. This uncertainty can be reduced by multiple independent smoke foil measurements, by multiple tests, and by assuming smoothness in the "U"-shaped curve. A good discussion of uncertainty in irregular H_2-air detonation cell measurement is given in Reference 1.36.

An extensive series of tests was carried out to measure the detonation sensitivity of H_2-air-steam mixtures. All experiments containing steam were carried out at elevated initial temperature conditions, nominally at T = 100°C in the HDT. To simulate the nuclear reactor environment in the event of hydrogen release, the initial air partial density of the mixture was fixed at air conditions at NTP (i.e., an initial air density of 41.6 moles/m^3). The hydrogen and steam were then added which results in initial mixture pressures which were superatmospheric and ranged from 1.5 to 3 atm depending on the amounts of H_2 and steam added. A range of H_2-air mixtures, to which 10, 20, or 30 percent steam has been added, was studied in the HDT. The results for these tests are displayed in Figure 1.56, where the detonation cell width, λ, is plotted as a function of equivalence ratio and steam mole fraction. The role of steam is to desensitize the mixture by a substantial factor. At stoichiometric composition for H_2-air, the addition of 10, 20, and 30 percent of steam leads to an increase in the detonation cell width, λ, by the corresponding factors of 6, 30, and 60. According to the Zeldovich criteria, where dependence of the mixture sensitivity is related to the inverse cube of the chemical length scale, the addition of 10, 20, and 30 percent steam corresponds to a reduction in detonability by factors of 220, 2.7×10^4, and 2.2×10^5, respectively.

Detonations were recorded with 30 percent steam for equivalence ratios of 0.9 and 1.0. Early predictions by Shapiro and Moffette[1.37] were that 33 percent steam would completely inert a detonation. For the stoichiometric mixture at 100°C, saturation corresponds to a steam mole fraction of 35.6 percent. In the present tests with a stoichiometric H_2-air mixture and 30 percent steam dilution, the detonation cell width that was measured was well below the detonation limit of the tube characterized by the onset of single-head spin. Consequently, we believe that a stoichiometric steam-saturated mixture could be detonated in our facility. The detonation cell width data measured in the

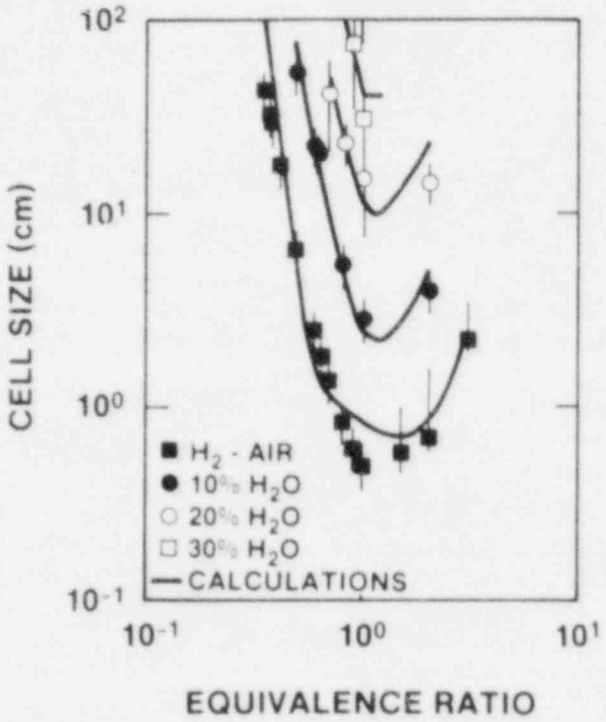

Figure 1.56. H_2-Air-H_2O Detonations

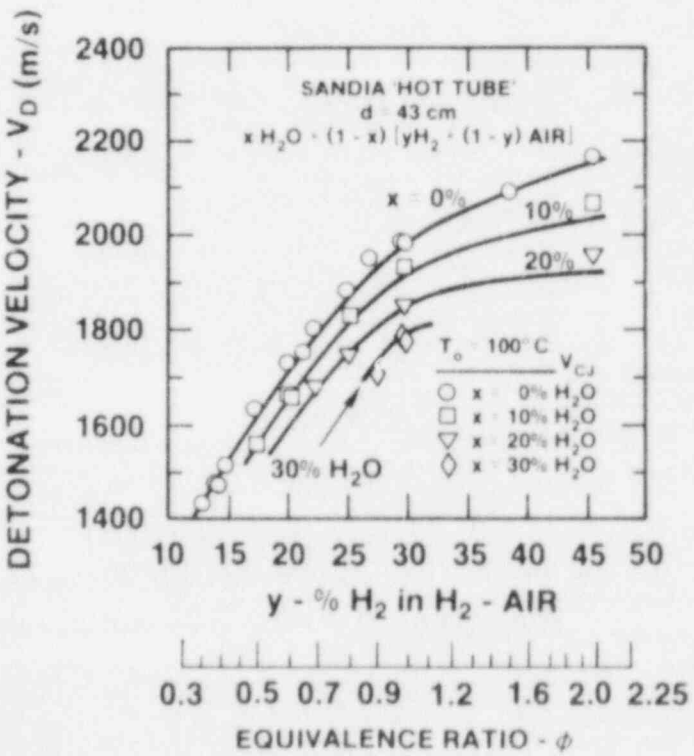

Figure 1.57. Detonation Test Results

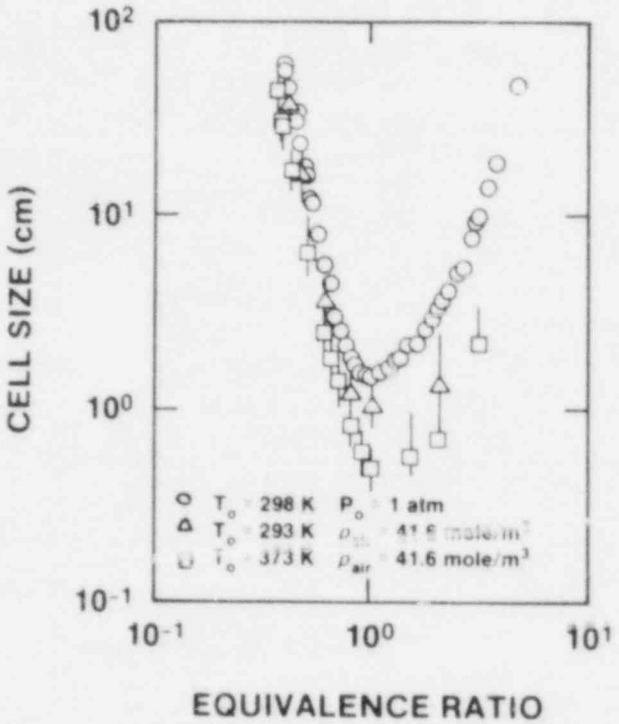

Figure 1.58. H_2-Air Detonations

HDT for H_2-air-steam mixtures have been correlated with our kinetic model. The agreement is very good in spite of the preliminary nature of this type of extrapolative correlation. The kinetic model correlation recovers the essential qualitative features of the experiment results.

Detonation velocity measurements have also been made in the HDT for H_2-air-steam mixtures. The results are displayed in Figure 1.57, together with the C-J velocity calculated from the Gordon-McBride code.[1.38] All the results indicate that the measured detonation velocities, even in marginal H_2-air-steam mixtures, are within a few percent of the calculated C-J values. No significant velocity deficit can be observed in any of the present tests.

Finally, the effectiveness of steam addition to H_2-air mixtures in reducing detonation sensitivity is affected by the initial temperature and pressure. The addition of steam in significant quantities requires elevated temperatures; the addition of steam to a fixed volume of H_2-air mixture raises the pressure. Evidence indicates that both of these conditions--the increased initial temperature and pressure--over and above NTP tend to sensitize the detonable mixture. A comparison of the three sets of experimental points are

shown in Figure 1.58. For the lower two sets of points, the difference in detonation cell size at a given equivalence ratio is due to the temperature difference at constant mixture density. For the upper two sets of points and curves, the difference in detonation cell size at a given equivalence ratio is due to the difference in mixture density at constant temperature.

1.5.3.1.4 Conclusions

1. For a given initial temperature, air density and equivalence ratio, the addition of steam to an H_2-air mixture greatly decreases the detonability of the mixture.

2. At 100°C and an air density of 41.6 mol/m^3, detonation of H_2-air mixtures with up to 30 percent steam have been recorded.

3. For H_2-air mixtures, the detonability increases with increasing initial temperature at constant density. Consequently, the diluent effect of the addition of steam to a fixed volume of an H_2-air mixture in reducing detonability is partially offset if there is a concomitant temperature increase.

4. At 100°C and an air density of 41.6 mol/m^3, a 13.0 percent H_2-air mixture has been detonated.

1.5.3.2 Transmission of Detonation Through Adjacent Circular Orifices
(J. H. Lee, R. Knystautas, C. K. Chan, and C. Guirao, McGill University)

A series of experiments has been performed to study the transmission of detonation through an array of adjacent circular orifices. It is well known that the transmission of a planar detonation wave through a single circular opening follows the relationship $d_c \approx 13\lambda$ where d_c is the critical orifice diameter and λ is the detonation cell width.[1.39,1.40] It is expected that for multiple openings there may be an interference effect when the diffracted waves collide downstream of the orifice plane. The laterally colliding diffracting hemispherical waves would lead to Mach reflections which, if sufficiently strong, would enhance the capability of successful transmission. Figure 1.59 presents a simulated illustration of this. Two spherical waves initiated by simultaneous spark discharges at adjacent spark gaps collide at the mid-plane. The conditions here turn out fortuitous that the collision on one side leads to a Mach stem which is sufficiently strong to generate a detonation wave; the other side of the collision process does not manage to produce a detonation wave. Without the collision process, both waves would have failed to produce a detonation

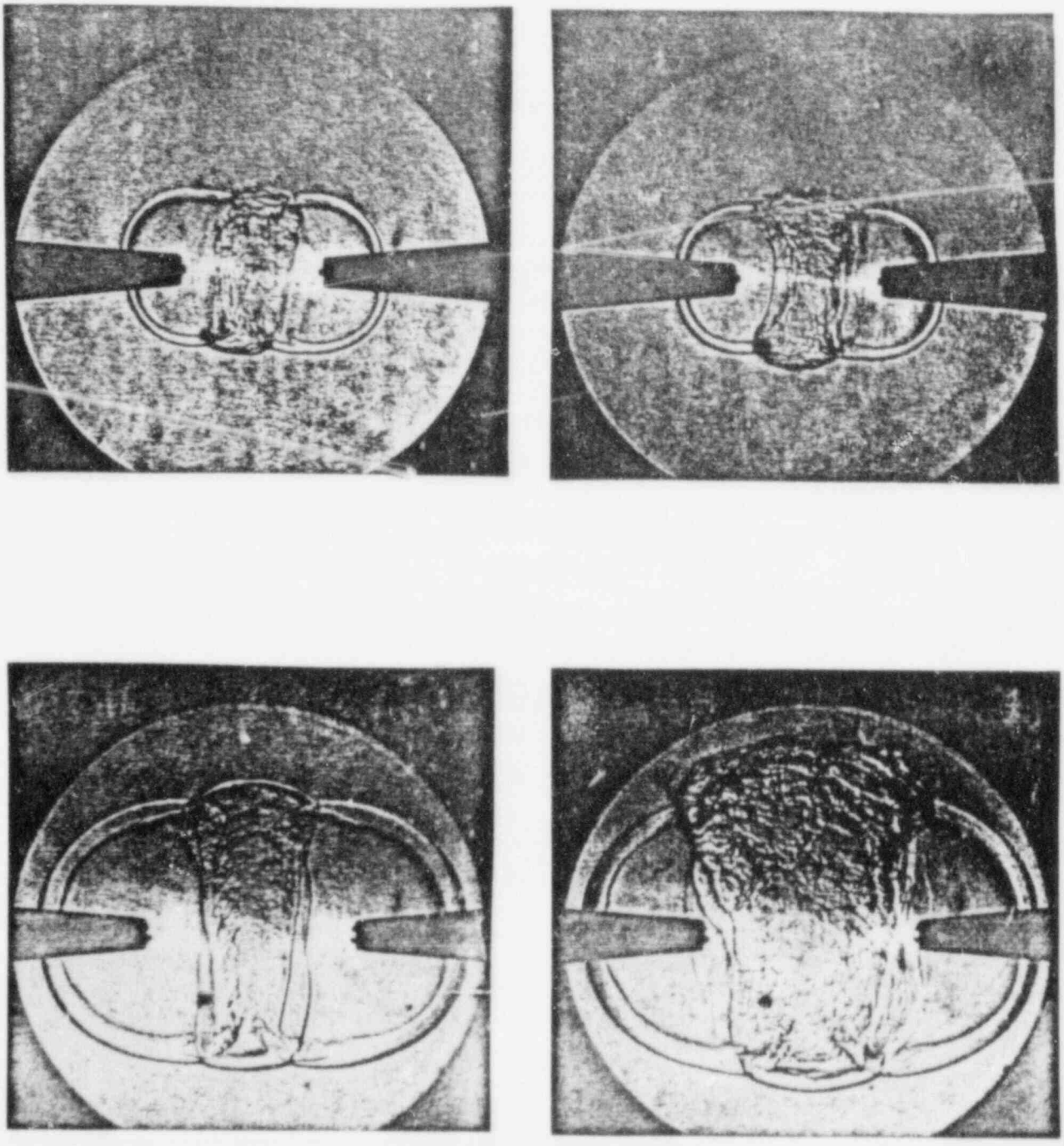

Figure 1.59. Schlieren Photographs of Collision of Two Spherical Waves

wave. These photographs clearly illustrate the reinforcement role of the interactive collision process when the collision is strong enough. If the spherical waves are too far apart, the collision will be too weak to produce a detonative Mach stem.

The results of an extensive study of the collision of diffracted waves from two adjacent circular orifices are reported below. In this case, the orifice diameters, d, are equal and are separated by a distance, s, measured edge to edge as illustrated in Figure 1.60. The actual experiment consisted of a 20-cm diameter tube connected to a 58-cm diameter x 76-cm long detonation chamber. Removable orifice plates with two adjacent circular openings (d = 5 cm) and various spacings, s, could be inserted at the interface between the tube and the chamber. A planar detonation wave initiated in the 20-cm diameter tube was then transmitted through the orifice openings into the chamber. A range of mixtures using hydrogen and ethylene as fuels were used with oxygen and nitrogen to produce a range of mixture sensitivities characterized by the cell width, λ. The variations of orifice diameter, d (normalized with the critical detonation cell size λ), with respect to orifice spacing, s (normalized with the orifice diameter), have been plotted in Figure 1.61.

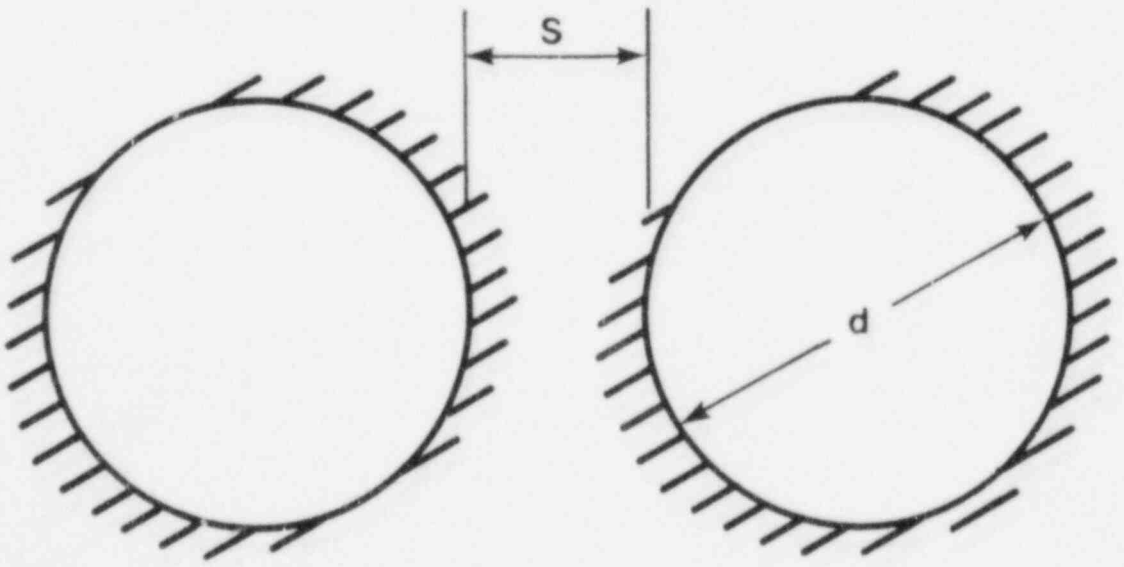

Figure 1.60. Two-Hole Orifice

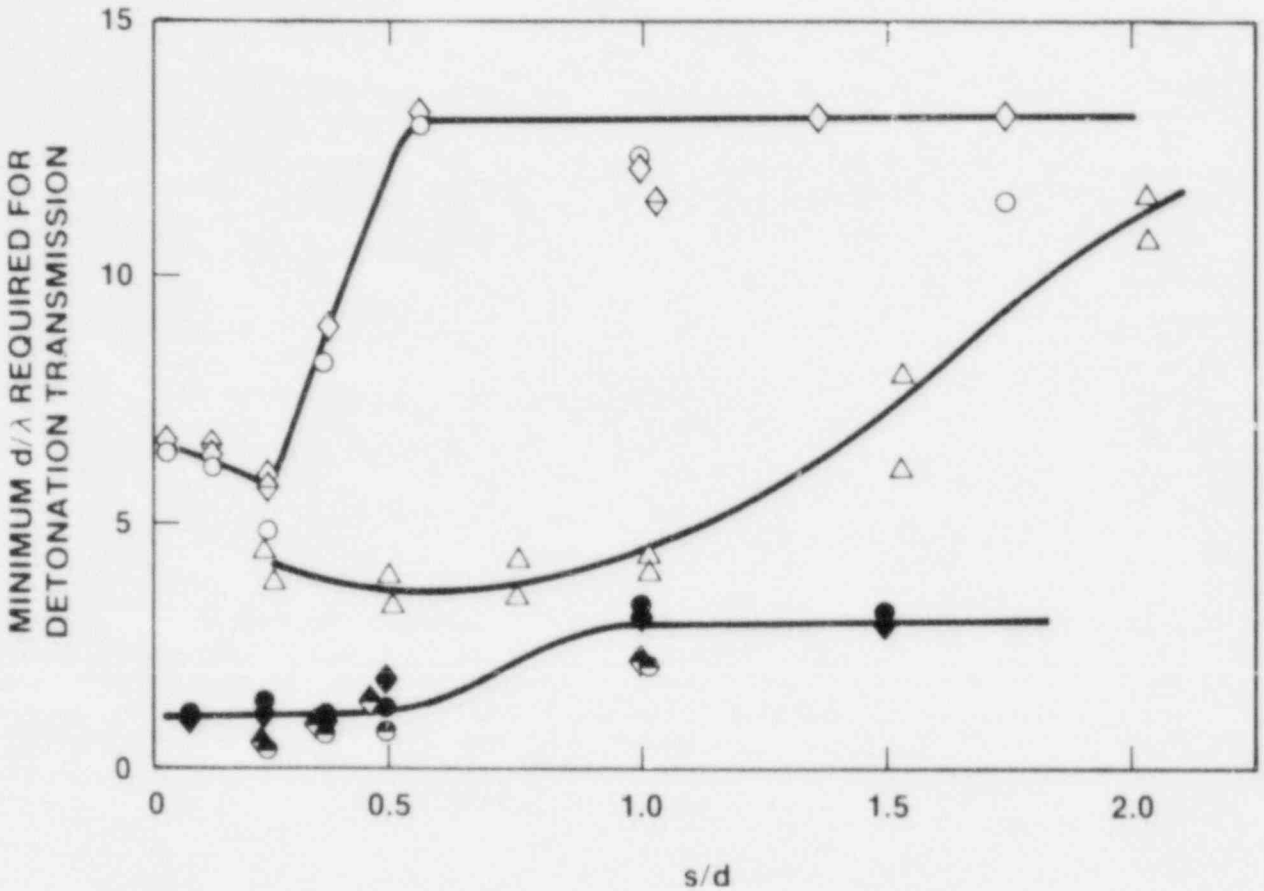

FUEL	ORIFICE DIAMETER (inch)	NUMBER OF HOLES
○	2	2
△ H_2	1.5	3
●	0.5	37-61
◓	0.25	151-211
◇◇	2	2
◆ C_2H_4	0.5	37-61
◆	0.25	151-211

Figure 1.61. Variation of Critical Orifice Diameter With Orifice Spacing

Figure 1.61 clearly illustrates that, for $s/d < 0.5$ the reflective interference effect via the detonative Mach stem enhances the transmission capability of the detonation wave. For $s/d > 0.5$, the transmission effect through two orifice openings becomes identical to the transmission through one, i.e., $d_c \rightarrow 13\lambda$, since now the interference effect is too weak and the two transmitted waves do not couple in a manner which reinforces them sufficiently to lead to a detonative Mach stem.

The results for the transmission of detonation through three adjacent circular openings, whose arrangement is shown in Figure 1.62, have also been plotted in Figure 1.61 for comparison. Again, the circular openings have equal diameters, d, and are spaced a distance, s, apart. As expected, it is evident that the positive interference effect is more pronounced. The three-way collision now produces a Mach plane for the three diffracting hemispherical waves. The reinforcing effect now persists to a hole separation distance in excess of $s/d = 2.0$. Of course, beyond that, the transmission process once again becomes dominated by single-hole characteristics.

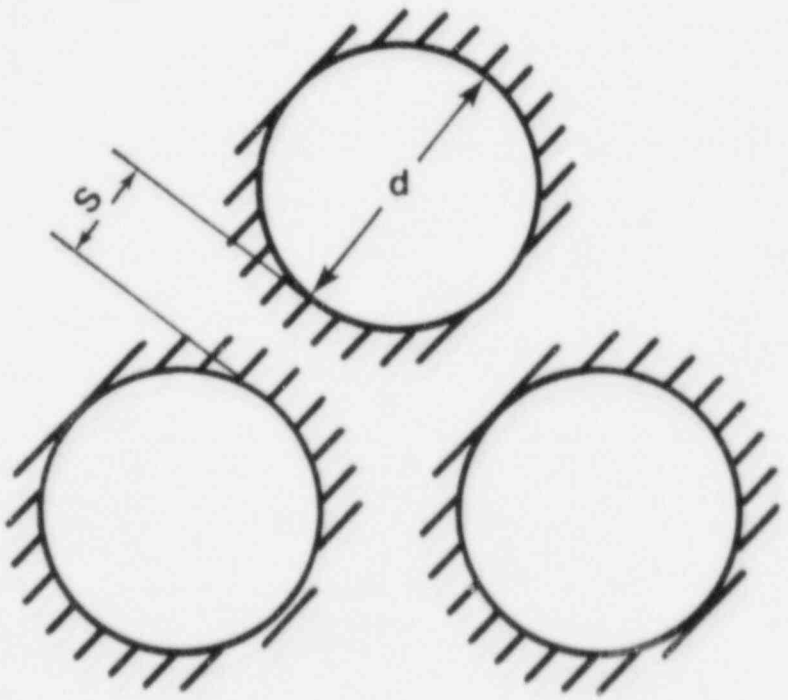

Figure 1.62. Three-Hole Orifice

If now the entire 20-cm diameter orifice plate is perforated by equi-spaced holes of diameter, d, then the transmission process is facilitated even more unless the spacing between holes becomes much larger than $s/d \approx 2.0$. The results are illustrated in Figure 1.62. For $s/d < 0.5$ transmission occurs when the hole diameter is of the order of the detonation cell width (i.e., $d/\lambda \approx 1$). In fact, transmission is observed to occur even when $d/\lambda \approx 1/2$. One would expect that the cell structure should be destroyed by the blockage effect under these conditions. However, s/d is so small in this case that the detonation wave appears to be able to cope with the perturbation imposed on its structure and to all intents and purposes appears not to notice that the interhole blockage is even there. Of course, for larger s/d, this is no longer true and for $s/d > 1$, $d/\lambda \approx 3$. In the limit of $s/d > 2.0$, it is expected that the transmission once again would be controlled by the single orifice transmission criterion, i.e. $d_c \approx 13\lambda$.

1.6 Hydrogen Mitigative and Preventive Schemes

(L. S. Nelson, 6427; M. Berman, 6427)

1.6.1 Effects of Operating the Water Spray System on Hydrogen Igniters

The deliberate ignition system installed in a nuclear reactor containment is used to prevent excessive accumulation of hydrogen produced during a core uncovery accident. However, a second safety-related system, water sprays intended to reduce steam overpressure in similar accidents, may interfere with the proper operation of the numerous hot surface igniters arranged throughout containment as part of the deliberate ignition system.

The effects of the spray operation are thought to be twofold, via direct impingement of spray drops on the igniters, and by driving air currents in the containment by entrainment. We have recently completed an experimental study of the behavior of igniters exposed to water sprays and gas flows. To complement these studies we are using computer modeling to estimate the gas flows that would be induced by the water sprays in typical containments.

1.6.1.1 Air Currents Driven by Sprays in Reactor Containment Buildings

(K. D. Marx, 8363)

This work has been completed. A draft report has been submitted to the Nuclear Regulatory Commission for comments.

1.6.1.2 Behavior of Resistance-Heated Igniters During Operation of Water Sprays in Containment
(L. S. Nelson, 6427; K. P. Guay, 6427)

The experimental portion of this work essentially has been completed. Data analyses and writing of the report are underway.

1.6.2 Hydrogen Combustion in Water Sprays
(L. S. Nelson, 6427; K. P. Guay, 6427)

It has been predicted theoretically[1.41] that during hydrogen combustion, the presence of dispersed water drops in the form of fog or mist will reduce both the peak pressure and peak temperatures produced during the burn. Instantaneous suspended water densities on the order of 100 g/m^3 are required according to this analysis.

The most common way to produce dispersed water drops, by the use of nozzles, generates turbulence and gas motion in the hydrogen-air mixtures and totally masks the effects of water drops on the burns.[1.42] We have been investigating a different method of dispersing the water in a premixed hydrogen-air mixture--spinning disk generators.[1.43] These generators produce large quantities of drops of a single diameter and are expected to produce suspended water densities in the usable range as predicted by theory. Moreover, these generators inject the water into the combustion chamber in a gentle sideways motion compared to the violent downward entry of sprays used in the large chamber experiments.[1.43] By using the monodispersed drops, we intend to compare experimental values with codes that treat hydrogen burns on reactor scale, in particular HECTR. It should be emphasized that these experiments are not intended to test spray systems used in containments, but rather to examine, diameter-by-diameter, the effects of water drops and their concentrations on hydrogen burns independent of the effects of gas motion normally produced by sprays.

As described in Reference 1.44, we are investigating a pair of spinning disk drop generators, obtained from Atmospheric Physics, Inc. These generators were tested in the plastic bag mockup shown in Figure 1.36 of Reference 1.44 and later in the FITS hydrogen combustion chamber. We spent considerable effort characterizing the downward fluxes of the water drops produced by these generators. We used a series of rain gauges in both the plastic mockup and the actual FITS chamber. In Figures 1.63a and b we show the downward flux recorded as a function of distance across the chamber diameter for the plastic bag mockup and the FITS tank, respectively. These figures show the similarity between the

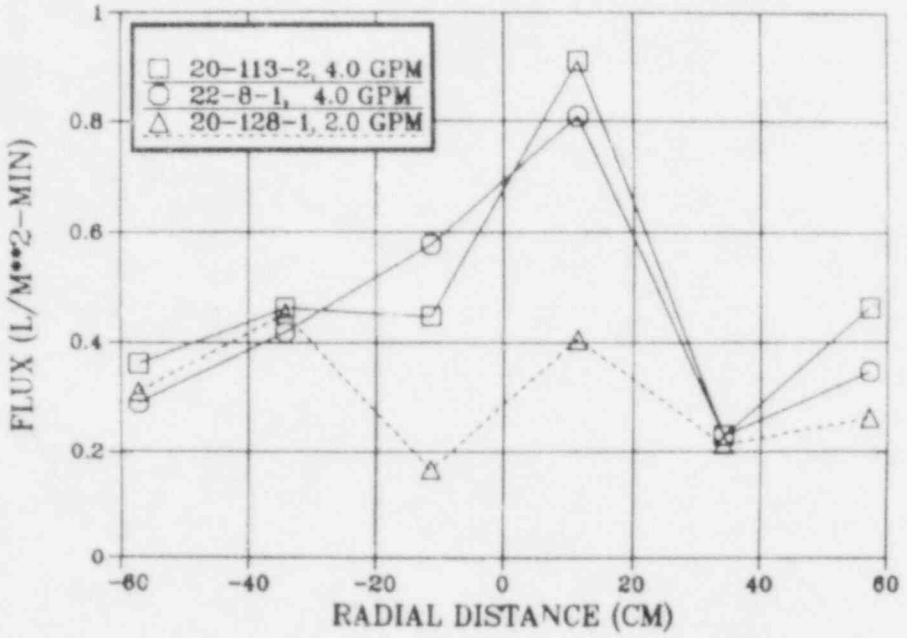

(a) Water Flows of 8 and 16 ℓ/min in Each Generator Were Used

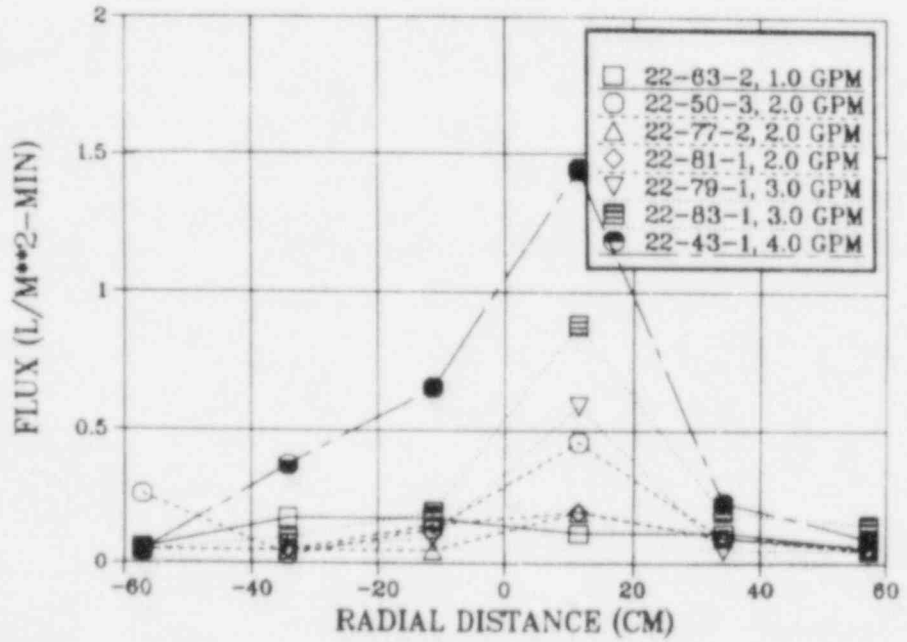

(b) Water Flows of 4, 8, 12, and 16 ℓ/min in Each Generator Were Used

Figure 1.63 Downward Water Fluxes Measured With Rain Gages Across the Diameter of the Plastic Bag Mockup of the FITS Chamber. Spinning disc generators were operated at a speed that produced 100-μm diameter drops.

aflux measurements in the two situations but not quantitative agreement. The flux appears not to be uniform radially in the chamber. Although the curves in Figures 1.63a and b suggest that a dense column of fog exists at the center of the chamber with little at the periphery, this does not agree with visual observations.

We attribute the nonuniformity shown in Figures 1.63a and b to the rotational precession of the clouds of drops (see Figure 1.37 in Reference 1.44) caused by the horizontal injection of the drops into the chamber. We are investigating the possibility that the nonuniformity is caused by the failure of the rain gauges toward the edge of the chamber to collect drops that are passing with considerable horizontal vectors as well as vertical vectors due to the precession of the cloud. We are setting up to investigate the uniformity of the drop cloud with an optical device which does not depend on downward fall of drops through an orifice.

1.6.3 The Effects of Aerosols on Hydrogen Combustion

We continued our studies of the effects of oxidic and metallic aerosols on the combustion of lean hydrogen-air mixtures. We performed experiments with both oxidic and metallic aerosols in the 5.1 m^3 VGES chamber; we also performed a sequence of smaller scale experiments with only an oxidic aerosol in the 0.18 m^3 chamber at McGill University.

1.6.3.1 Experiments in the VGES Chamber
(L. S. Nelson, 6427; G. D. Valdez, 6427)

These tests were performed with the Ansul dispersal system. This device was used to disperse the aluminum oxide aerosols. It is a pressurizable chamber which contains the powders to be dispersed. An opening at the bottom of the chamber is connected to a forked pipe leading to two dispersal nozzles. The exit pipe is initially closed with a burst disk which opens when the powder-filled tank is pressurized. The powder is discharged vertically upward when the ruptured disks break. Photographs of this device are shown in Figures 1.64.

During this quarter, we performed six combustion experiments, three with an iron oxide aerosol, one with a metallic iron aerosol, and two control experiments without aerosols but with similar combustion procedures. In the iron oxide experiments, between 150 and 290 g of oxide was discharged into the VGES chamber, while in the experiment with the metallic iron aerosol, 727 g of metal was discharged. We used premixed concentrations of 6.5 v/o hydrogen in air in each of the VGES tests discussed in this section.

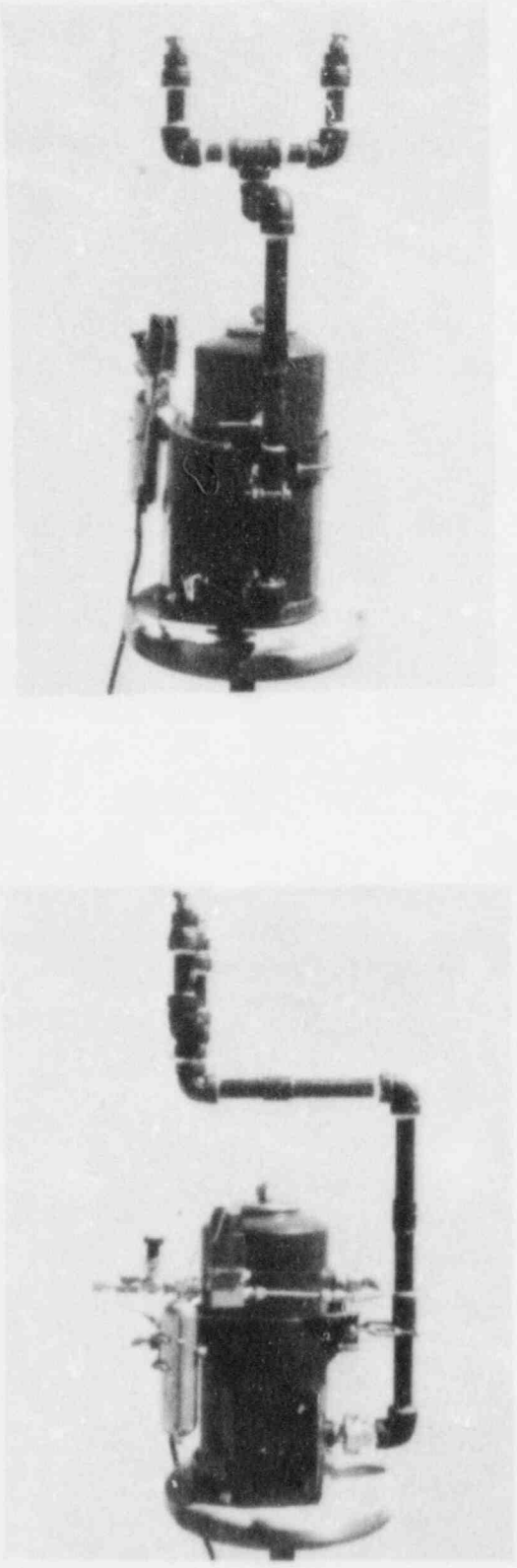

Figure 1.64. Front and Side Views of the Ansul Powder Disperser Used in the VGES Chamber Experiments

The results of these experiments may be summarized as follows: compared to the control experiments without aerosol, the oxidic aerosol had only small effects on the combustion, yielding slightly lowered peak pressures and somewhat lengthened decays on the pressure-time records. However, the metallic iron aerosol produced a significantly higher peak pressure with a steeper rise time than either the control experiment without the aerosol or the iron oxide aerosols. Representative pressure-time traces are shown in Figure 1.65.

From the upper trace in Figure 1.65, it seems possible that an oxidizable aerosol, such as the metallic iron aerosol studied here, might add significantly to the vigor of the combustion of the lean hydrogen-air mixture in which it is dispersed. That is, the finely dispersed oxidizable material might ignite and add its enthalpy of oxidation to that of the hydrogen-air mixture. This observation is based on only one experiment, however, it will be checked more rigorously in the VGES chamber next quarter.

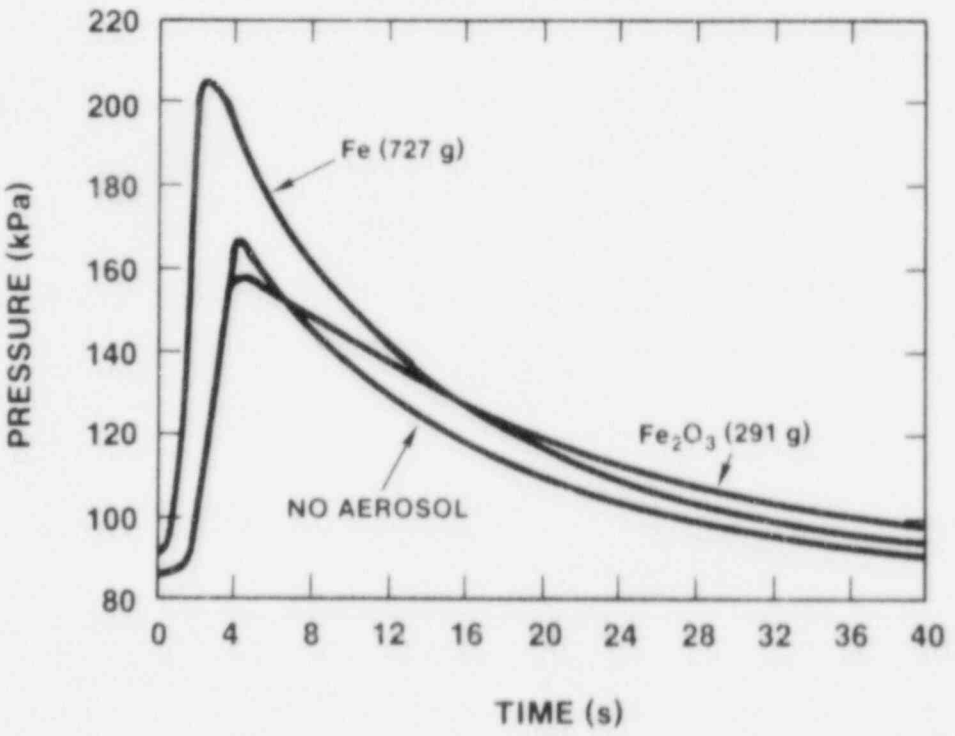

Figure 1.65. Pressure Traces from VGES Experiments in Which Fe_2O_3 and Fe Aerosols Were Injected Prior to Ignition. Also included is a trace from a control experiment in which aerosol was not injected, but otherwise similar procedures were used.

1.6.3.2 Laboratory-Scale Experiments (J. H. Lee, R. Knystautas, and M. Fresco, McGill University)

In order to test further the observations on the iron oxide aerosol described in Section 1.6.3.1 above, a sequence of small-scale experiments was performed in the Department of Mechanical Engineering at McGill University, Montreal, Canada. These experiments were performed in an 0.180 m^3 combustion chamber in which a bowl-type powder dispersal system was used. The apparatus is shown schematically in Figure 1.66. In this apparatus, the same iron oxide used in the VGES experiments was dispersed with up to 1200 g/m^3 concentration. The diagnostics in this chamber consisted of a pressure transducer-oscilloscope combination. The powder was dispersed by firing high-pressure air into the dust bowl shown at the bottom of Figure 1.66 and shortly afterward igniting the hydrogen-air mixture with an exploding wire. The mixture was assumed to be turbulent at the time of ignition.

The laboratory-scale investigations consisted of measuring maximum overpressure and maximum rate of pressure rise as a function of hydrogen concentration for turbulent burns with and without iron oxide at a concentration of 300 g/m^3, and for comparison quiescent burn without iron oxide. The data obtained are shown in Figures 1.67a and b for the maximum pressure rise and the maximum rate of pressure rise as a function of hydrogen concentration. These two figures show that the effects of the iron oxide on the burns are not major, although in both figures the pertinent parameters are reduced somewhat in the presence of the aerosol. The lean ignition limit of hydrogen in air at 4 percent is not affected by the aerosol.

Also investigated were the maximum overpressures and the maximum rate of pressure rise as a function of iron oxide concentration holding the composition of the hydrogen-air mixture to 10 percent. These results are shown in Figures 1.68a and b. Again, the changes produced by the presence of the iron oxide aerosol are not major, although there are significant downward trends for both parameters.

The essential agreement between the numerous laboratory-scale experiments and the smaller number of large-scale VGES experiments provides a good picture of the effects cold oxidic aerosols have on hydrogen burns, namely, that only small changes are produced by even very concentrated aerosols. No catalytic effects seem to be present which might lead to premature ignition or steepening of the pressure-time traces.

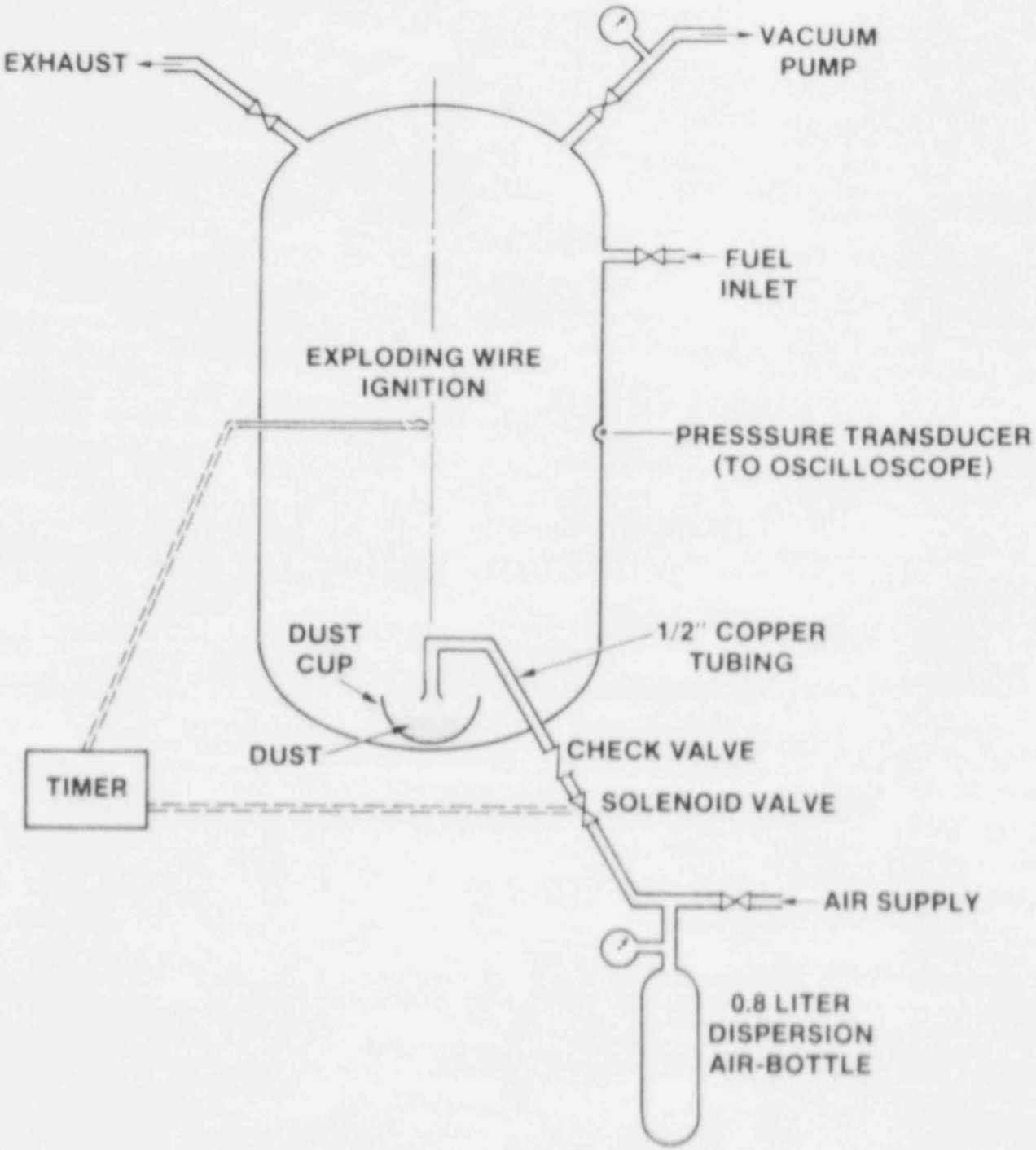

Figure 1.66. Schematic Diagram of the Aerosol Test Apparatus at McGill University

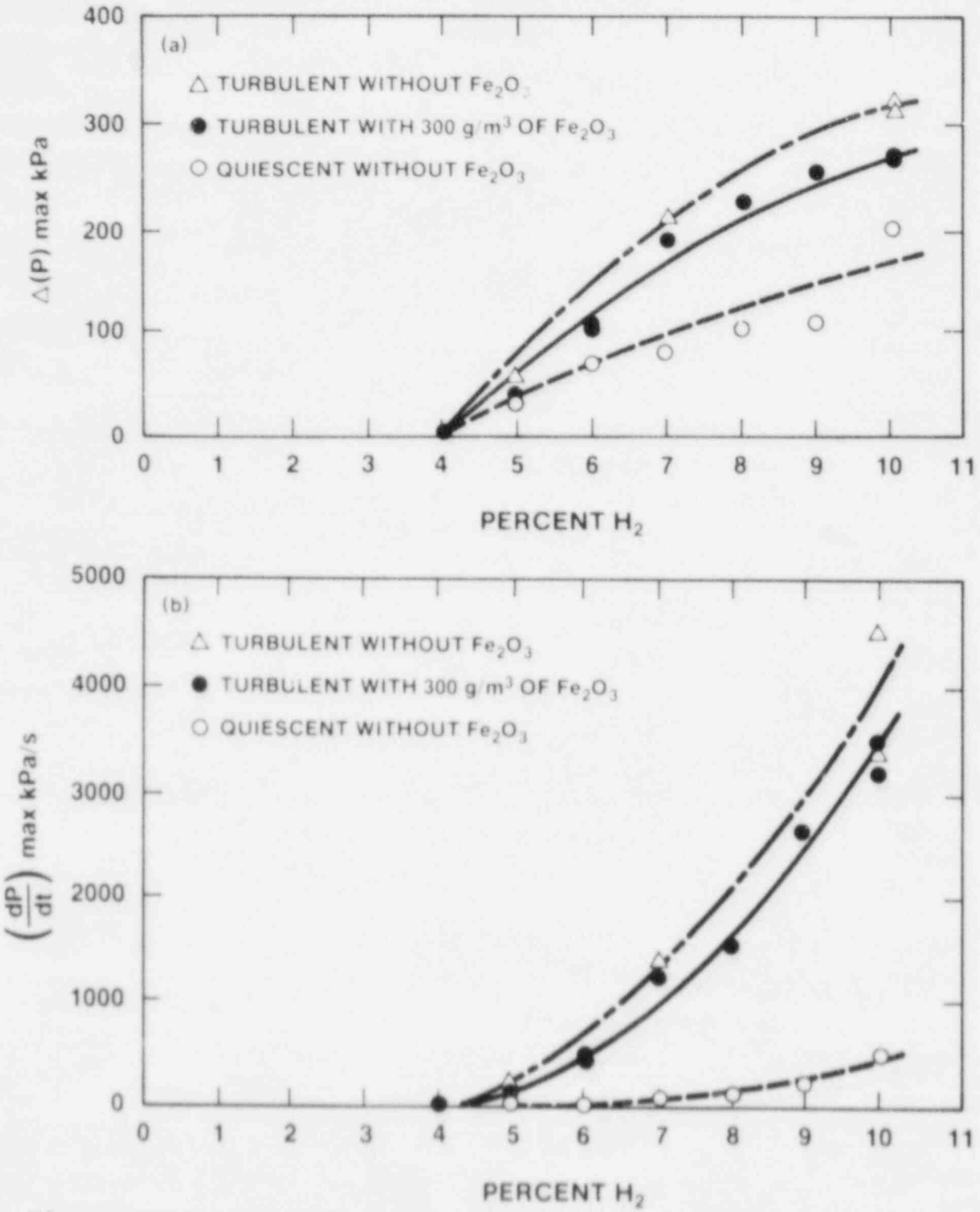

Figure 1.67. Maximum Overpressure (a) and Maximum Rate of Pressure Rise (b) vs. Percent Hydrogen in Air for Turbulent Combustions With and Without 300 g/m^3 of Fe_2O_3 Aerosol Present in the 0.18 m^3 McGill Chamber. For comparison, results for quiescent combustions without aerosol are indicated.

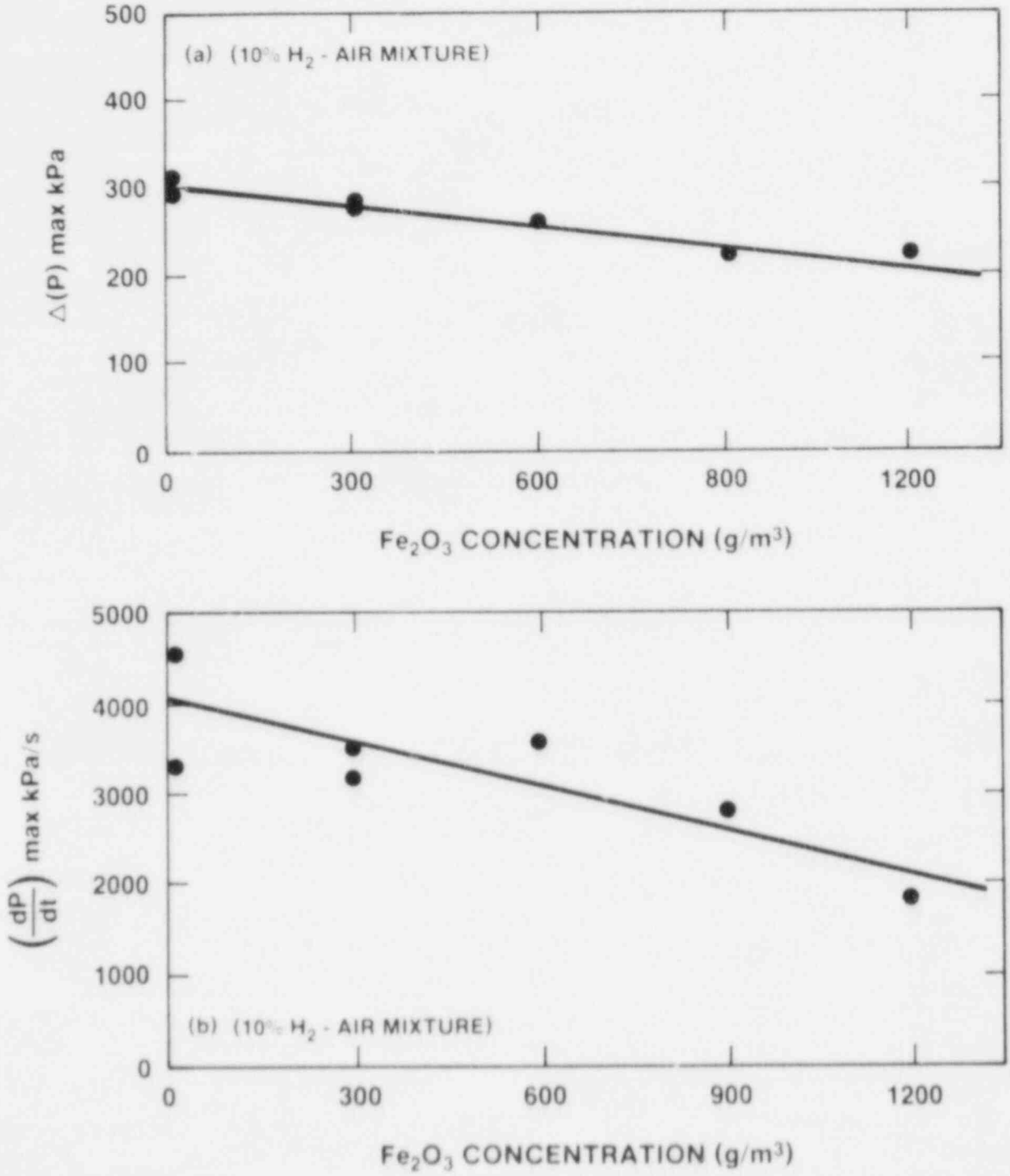

Figure 1.68 Maximum Overpressure (a) and Maximum Rate of Pressure Rise (b) vs. Fe_2O_3 Concentration for Turbulent Combustions of 10 Percent Hydrogen-Air Mixtures Performed in the McGill Chamber

1.6.4 Effects of Hydrogen Combustion on CsI-Containing Aerosols

(L. S. Nelson, 6427; G. D. Valdez, 6427)

We constructed a new type of aerosol-dispersing apparatus. This is comprised of six hemispherical bowls 15 cm in diameter arrayed at three levels in the VGES chamber. One-sixth of the total powder to be dispersed is placed in each bowl for a given experiment. The powder is dispersed by a jet of gas fired downward into the bowl on command. A schematic diagram of this aerosol dispersal system is shown in Figure 1.69.

With this new dispersal system, we performed six experiments using a 10 w/o CsI-90 w/o Al_2O_3 mixture. Experiments were performed by dispersing 1 kg of this mixture for 2 s and 1 s later igniting the combustion with a bridgewire. The combustions were performed over the range of compositions 6.5 to 29.6 percent hydrogen in air. (The latter is the stoichiometric composition.)

In each of these combustions, molecular iodine was produced by oxidation of the CsI. This was observed in several ways. The first was qualitative; upon removing the head from the VGES chamber, a strong halogen-like odor was detected. Moreover, all fallout samples retrieved from the chamber (these samples were removed from three petri dish collectors, the six bowls from the dispersing apparatus, and the bottom of the chamber itself) showed an intense brown coloration. In many of these samplers this coloration appeared as a surface layer above a white layer beneath. When samples from these collectors were placed in water and starch solution added, an intense blue indication of molecular iodine was observed.

As soon as the head could be removed from the VGES chamber, the fallout samples were analyzed to obtain the concentration of molecular iodine in each batch. The amounts of iodine produced range from very small values to over 3 percent by weight in the stoichiometric mixture. (Complete conversion of the 100 g of cesium iodide to molecular iodine would generate 4.8 w/o of elemental iodine.)

We performed a second analysis to measure the quantity of iodide ions and also measured the amount of cesium present by atomic absorption spectroscopy. The ratios of cesium ions to iodide ions are an indicator of how much iodide ion was converted to molecular iodine. A ratio of 1 indicates no conversion, while as the iodine is oxidized and removed from the ionic state, the ratio will increase. This ratio approached 3 in the material collected from the bottom of the VGES chamber when the combustion was performed at stoichiometric hydrogen-air composition.

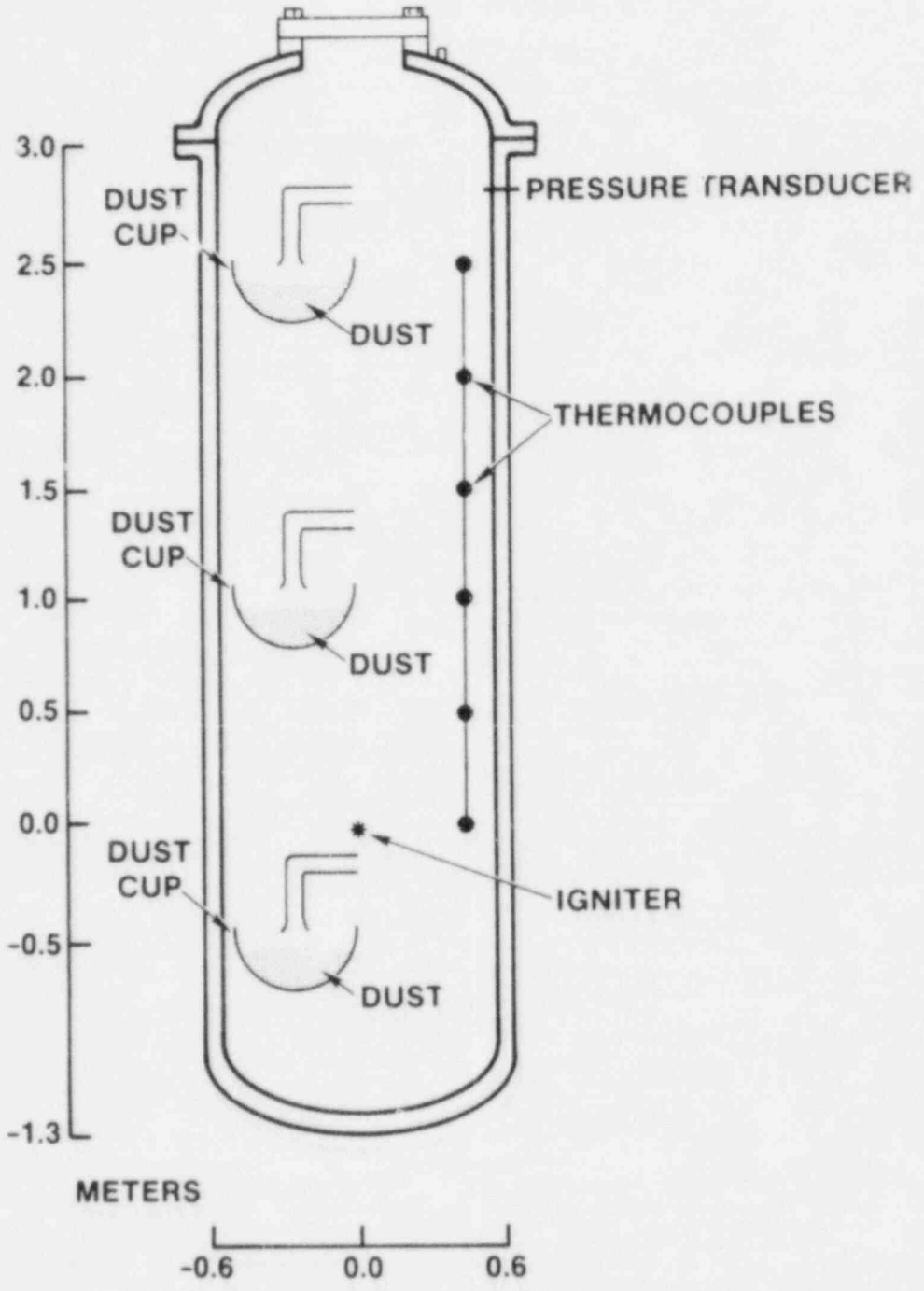

Figure 1.69. Schematic Diagram of the Bowl-Type Powder Dispersal System Installed in the VGES Chamber for CsI-Al_2O_3 Experiments. The dispersers are not drawn to scale, and only three of the six are shown (the other three are at similar levels but at the other side of the tank). Two of the three thermocouple rakes have also been omitted from this figure.

Other analyses are underway and are being performed initially by x-ray fluorescence and gravimetry. Also under investigation by x-ray diffraction is identification of the end product of the cesium portion of the cesium iodide.

1.6.5 Nonpowered Hydrogen Igniters

(L. R. Thorne, 8353; J. V. Volponi, 8353; W. J. McLean, 8353)

During a Loss-Of-Coolant Accident (LOCA) in a Light Water nuclear Reactor (LWR), there is the potential for rapid production of large quantities of hydrogen gas.[1.45] The hydrogen is produced from the reaction of water and steam with the fuel rod cladding. The hydrogen production rate may be so rapid that a flammable or detonable mixture may be produced as the hydrogen mixes with the air in the containment building. If this mixture is ignited, the structural integrity of the containment building might be compromised and serious safety and radiological hazards could result. Therefore, in the event of an LOCA, measures must be taken to either dispose of the hydrogen or otherwise make the mixture inflammable. One such measure is to purposely ignite the mixture at hydrogen concentrations below which there might be serious damage from the ensuing hydrogen combustion and associated pressure rise. This approach has already been implemented at several LWR sites by using hot glow plugs located at various positions within the containment building. One disadvantage of glow plugs, however, is that they require a continuous source of electrical power that may not be available during a serious accident.

Thus, a device which ignites lean hydrogen-air mixtures and does not require an external source of power may be needed. Because of the conditions which may be present within the containment building in an accident situation, other desirable characteristics include insensitivity to high temperature, high humidity, water spray, gas flow velocity, and capability of repeated operation in the event of further hydrogen buildup.

We report here the successful development of a prototype igniter that meets these design objectives. The igniter makes use of the catalytic properties of platinum to accelerate the reaction between hydrogen and oxygen to the point that the heat release rate is sufficiently high to produce the temperatures necessary for gas-phase ignition. First, we present the results of experiments aimed at optimizing the igniter performance, then typical performance of the prototype device is presented, and last, a discussion of those design parameters which should be considered in future igniter designs is given.

The present experimental work follows the earlier work of R. W. Schefer, who has modeled the heat balance and fluid

mechanics of catalytic recombination of hydrogen and oxygen on platinum, of P. A. Thiel, who has studied the reaction of hydrogen and oxygen on platinum surfaces under ultra-high vacuum conditions, and of M. L. Koszkowski and C. F. Melius, who have modeled the chemistry and heat transfer of the boundary layer between the platinum surface and the gas mixture.

Several catalytic igniters were constructed and tested in the apparatus shown schematically in Figure 1.70. It consists of a water-cooled premixed burner to which is attached a quartz chimney. The burner is not operated as a burner, per se, but provides a safe means of stopping the flame front once the hydrogen-air mixture flowing in the chimney is ignited.

In a typical test sequence, the igniter to be tested is placed in the chimney and the valve to the vent is opened and the valve to the burner is closed. Then the flow rates of hydrogen and air are adjusted to produce the desired hydrogen concentration. To initiate the test, the valve to the burner is opened and the valve to the vent is closed quickly. After a short induction time of 30 to 400 s, the catalytic igniter ignites the hydrogen-air mixture and the flame front travels from the point of ignition to the burner surface where it is stabilized. For safety, the apparatus is located within the flow field of a hood which is vented to the outside so that any unburned hydrogen is removed from the laboratory.

The temperature of the igniter is monitored quantitatively with a Chromel/Alumel thermocouple and qualitatively with an infrared-sensitive detector. Because the infrared emission is proportional to the temperature of the igniter to the fourth power, the infrared detector is most sensitive to high temperatures and provides a good indication of the time of ignition. When gas-phase ignition occurs, the temperature of the igniter drops because the flame front moves to the burner surface away from the igniter. One advantage of the infrared detector is that it responds to temperature changes very rapidly. A trace of the temperature of the igniter substrate as measured by a thermocouple and the infrared detector is shown in Figure 1.71 for a typical experiment. The temperature drop after ignition is clearly evident. The infrared signal drops before the thermocouple signal because of the faster response time of the infrared detector. Temperature measurements were also made of the region a few millimeters above the catalytic substrate. In these cases, ignition of the gas-phase mixture was indicated by a rise in temperature.

The hydrogen concentration is controlled by regulating the flow of air and hydrogen supplied to the burner. Tylan mass flow meters were used and were calibrated before this series

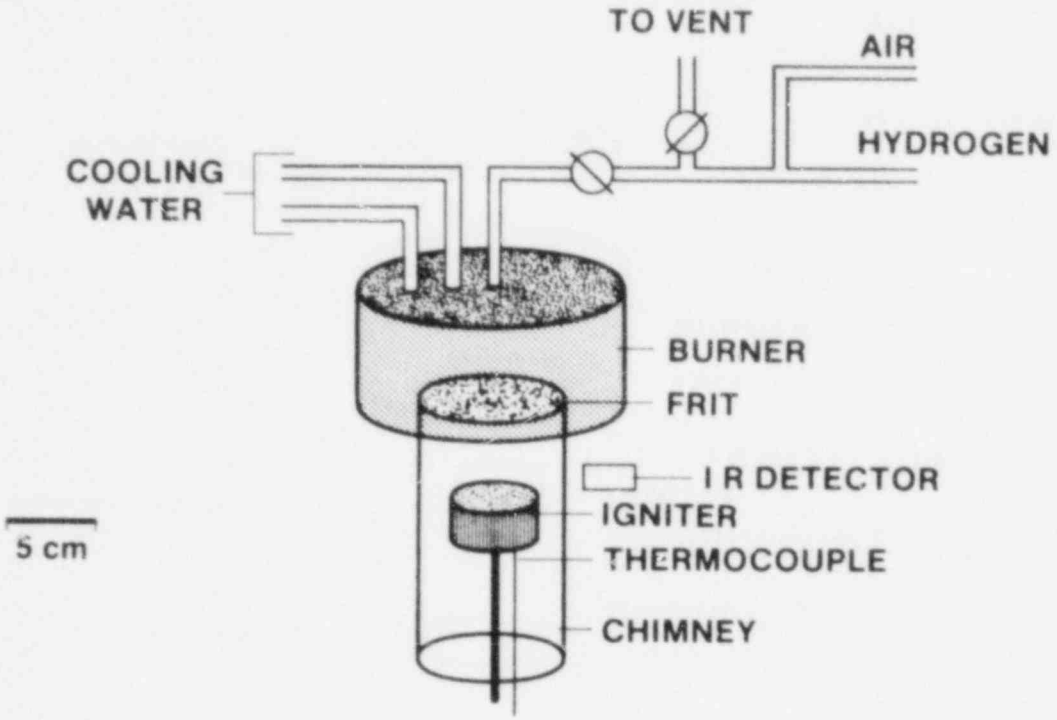

Figure 1.70. Apparatus Used to Test Catalytic Igniter Performance

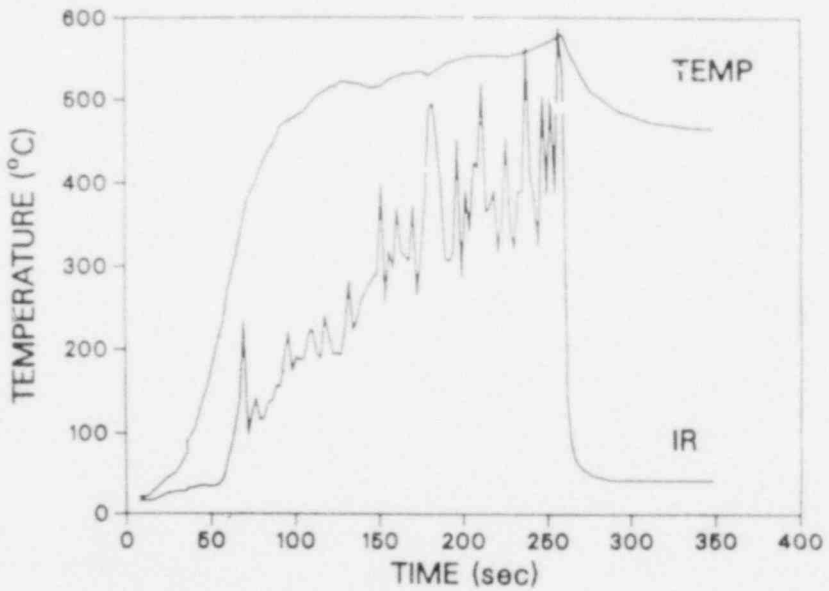

Figure 1.71. Results of a Typical Igniter Test. Upper trace (TEMP) is the temperature of the platinum-coated substrate as measured by a Chromel/Alumel thermocouple. Lower trace (IR) is the infrared emission from the substrate and wires. The infrared emission provides a rapid responding, qualitative measure of the temperature.

of experiments by setting the flow control valve for a specific flow rate while the flow was connected to a wet test meter which measures the volume of gas delivered. The time required for the delivery of a specific volume under standard conditions was then measured. The volume delivered divided by the elapsed time gives the flow rate at standard temperature and pressure and the meter was adjusted to read this value.

The lean ignition limit of hydrogen depends on gas flow velocity, means of ignition, and the direction of flame propagation. Using a spark igniter and with a gas flow velocity of 5.7 cm/s, the leanest mixture which can be ignited in the apparatus is 5.1 percent for upward flame propagation (burner in inverted configuration) and 9.3 percent for downward flame propagation (normal burner configuration). This compares with 4.1 percent and 9 percent, respectively, for measurements made in a standard apparatus.[1.46]

A schematic diagram of the first successful catalytic igniter is shown in Figure 1.72. It consists of a platinum-coated honeycomb and platinum coil which is instrumented with a platinum/platinum-13 percent rhodium thermocouple. Six other designs were tested and are shown in Figures 1.73 through 1.75. The figure captions indicate whether gas-phase ignition was achieved and under what conditions. The design which gave the best performance, that is, ignited the leanest mixtures, is shown in Figure 1.76.

From these tests it was determined that both a substrate coated with high surface area platinum and platinum wires are necessary for the device to ignite very lean mixtures. For these designs, the substrate first warmed, then the wires warmed, and finally the wires glowed red hot and ignited the gas mixture. Small patches glowed on the substrate, but they were much less bright than the wires indicating that the wires reached higher temperatures than the substrate.

That both a high surface area platinum substrate and platinum wires are needed to effect ignition indicates that there exists some interaction between them. This could be mechanical (disruption of the flow around the igniter), chemical (one part may supply a necessary chemical species to the other), or thermal (one igniter part may provide a thermal boost to the other).

The results of two experiments showed that the mode of interaction is primarily thermal. In the first experiment, a platinum wire was heated electrically to a temperature high enough that the chemical surface reaction began to increase rapidly due to the heat release from the reaction

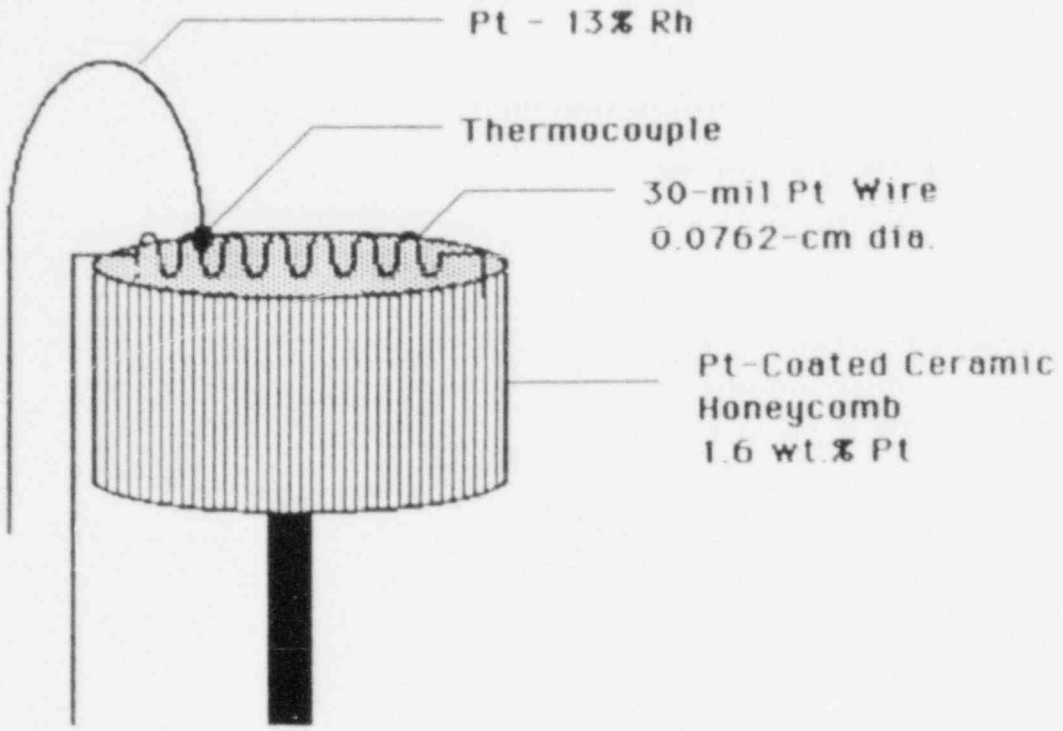

Figure 1.72. First Successful Catalytic Igniter Design

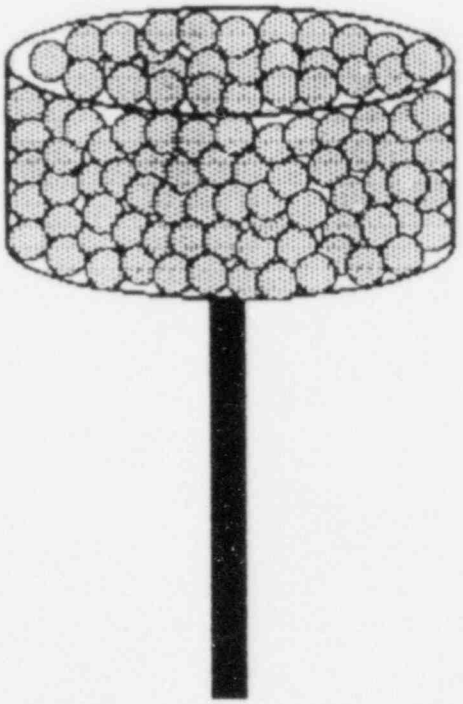

Figure 1.73. Igniter Made From a Stainless Steel Screen Cage Which Holds Platinum-Coated Ceramic Beads. This igniter failed to ignite lean hydrogen-air mixtures up to 12 percent hydrogen.

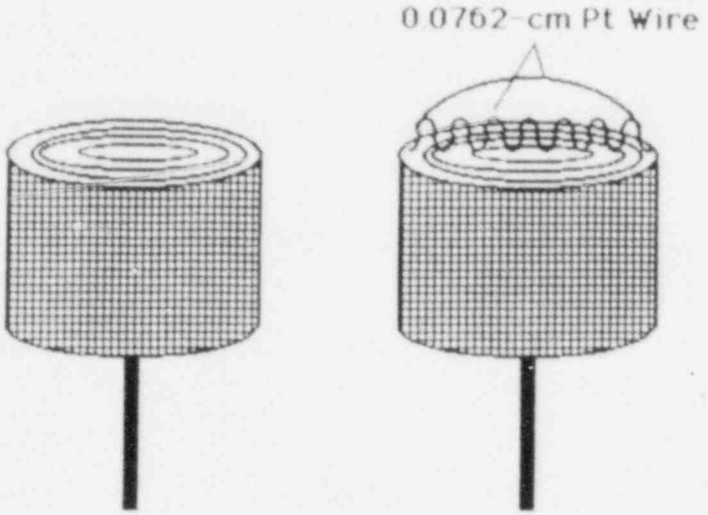

Figure 1.74. Two Igniter Designs Which Use a Coil of Platinum-Coated Wire Screen. The coating contains teflon to reduce the effects of liquid water. Only the igniter which has both wire screen and platinum wire operates successfully. It will ignite concentrations down to 10.5 percent hydrogen, flowing at 5.7 cm/s.

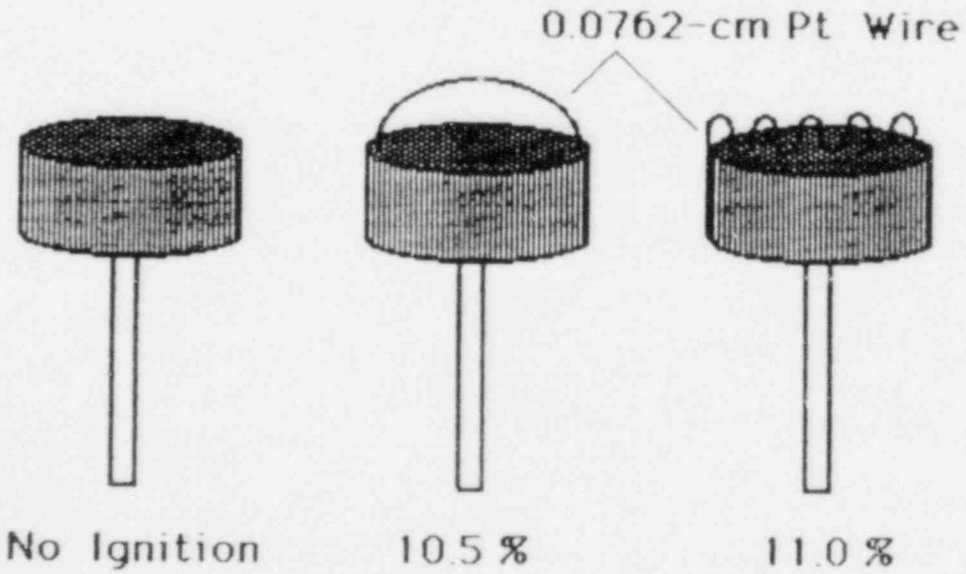

Figure 1.75. Three Igniter Designs Which Use a 1.7 Weight Percent Platinum-Coated Honeycomb. Platinum wire is necessary for successful operation. A wire loop is better than a wire coil.

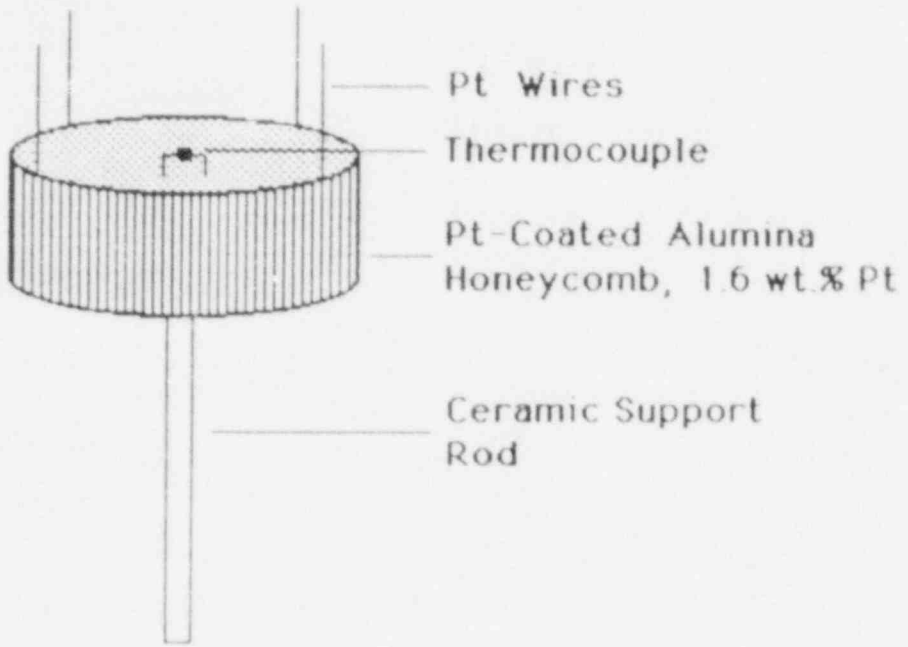

Figure 1.76. Optimized Prototype Catalytic Igniter

itself. The temperature of the wire thus began to rise without additional electrical heating until it was sufficiently hot to ignite the gas mixture. A schematic diagram of the apparatus is shown in Figure 1.77. Only a small temperature boost above room temperature was needed to cause the surface reaction on the wire to begin to increase rapidly. when heated to 80°C, the wire positioned in a vertical direction would ignite mixtures as lean as 8.0 percent hydrogen. This compares to 8.5 percent for a horizontal wire. In the second thermal interaction experiment, the thermal boost was provided by the platinum-coated substrate as shown in Figure 1.78. If the distance between the wire and the platinum-coated substrate was more than 0.1 cm, then the platinum wire would not heat much above room temperature and ignition would not occur even though the substrate heated to the usual temperature.

To test the importance of wire position, the wires were hung below the substrate, that is downstream from the substrate. In this configuration, the igniter failed to ignite an 11 percent hydrogen mixture. Presumably, leaner mixtures would not have ignited either.

From the foregoing experiments it is clear that: (1) both the platinum-coated substrate and the platinum wire are

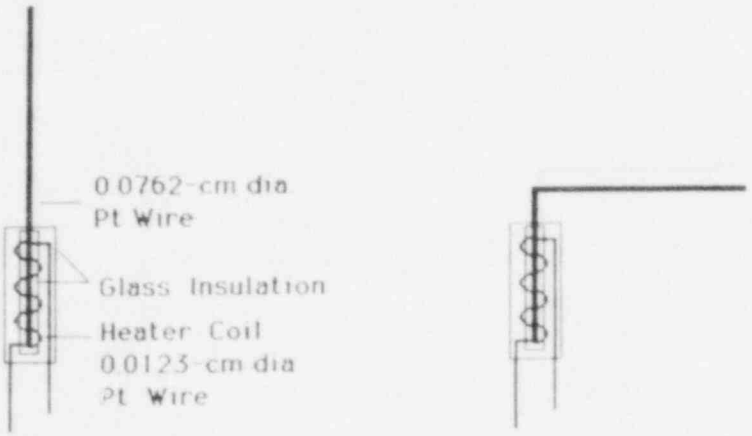

Figure 1.77. Device to Electrically Heat a Platinum Wire to Test the Effects of Thermal Boosting. Vertical wire orientation provides ignition at lower hydrogen concentrations than horizontal orientation.

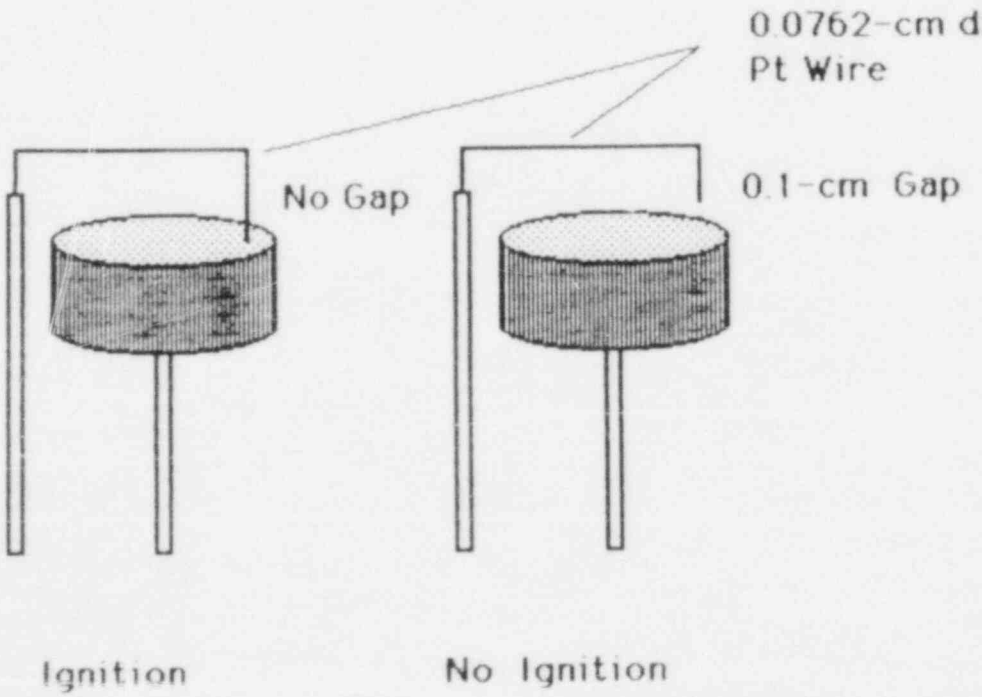

Figure 1.78. Device Used to Test the Thermal Boosting Provided by the Catalytic Honeycomb. The platinum wire must be very close or touching the honeycomb for the igniter to work successfully.

necessary, (2) the primary effect of the substrate is to provide a thermal boost to the platinum wire, (3) that vertical positioning of the platinum wire is more effective than horizontal and that straight wires are better than coils, and (4) that the wires must project away from the substrate into the unreacted mixture.

At this point, experiments were performed to optimize the wire diameter and length. Wire lengths of 1, 2, and 4 cm, and wire diameters of 0.0123, 0.0246, and 0.0735 cm were tested. The results, which are summarized in Table 1.6, showed that long thin wires worked best. This concluded our initial efforts to optimize the igniter design.

The optimized prototype igniter shown in Figure 1.78 was evaluated in terms of its response to hydrogen concentration, gas flow velocity, gas temperature, gas humidity, and water spray. The results are summarized below.

Hydrogen Concentration

For both the inverted and normal burner configurations, the leanest mixtures tested were ignited; 5.5 percent for upward flame propagation and 11.6 percent for downward flame propagation with a gas flow velocity of 2.8 cm/s. In the case of the downward propagation tests, the mixture would actually ignite the gas phase at lower hydrogen concentrations (near 9 percent), but the flame would stabilize on the catalytic substrate or move upward to the edge of the chimney and extinguish. Only at concentrations of 11.6 percent or higher would the flame front propagate downward and stabilize on the burner surface. The performance of the catalytic igniter is quite good as demonstrated by the fact that mixtures nearly as lean as the spark ignition limit can be ignited catalytically.

Flow Velocity

The effects of flow velocity for flows of 1.7, 2.8, 5.7, 8.6, 14.5, and 19.5 cm/s were examined for concentrations in the range of 5.5 to 11.5 percent. The ignition induction time (i.e., the time between the first exposure of the igniter to the hydrogen mixture and the time of the gas-phase ignition) was taken as an indication of the effectiveness of the igniter. Shorter times indicated better performance. The results are shown in Figure 1.79 and indicate that the effects of flow rate are greatest at low velocities with lower hydrogen concentrations being harder to ignite.

Temperature

The effect of gas temperature was investigated with the same apparatus used for the humidity studies except that there

Table 1.6

Results of Optimizing Wire Diameter and Length

Wire Diameter (cm)	Wire Length (cm)	Minimum Hydrogen Concentration Needed for Ignition (%)
0.0123	1.0	6.1
0.0123	2.0	5.5
0.0123	4.0	5.5
0.0246	2.0	5.5
0.0492	2.0	7.5
0.0735	2.0	8.5

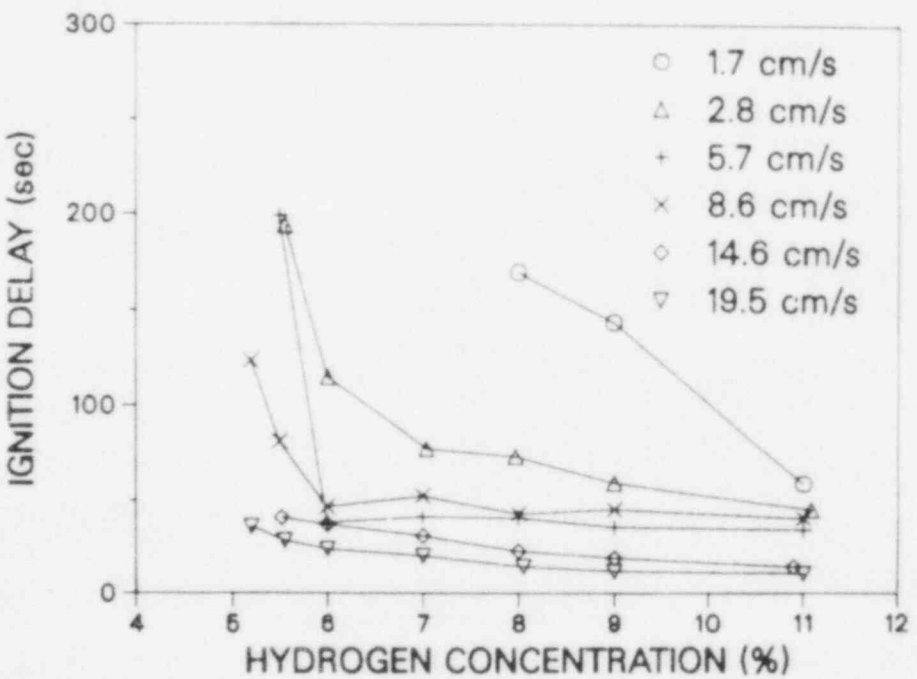

Figure 1.79. Effect of Gas Flow Rate on Igniter Performance. Low concentrations at low flow velocities are most difficult to ignite.

was no water in the bubbler and the entire apparatus was controlled at the same temperature. The results are shown in Figure 1.80. For the temperature interval tested, the data can be approximated by a straight line having a best fit intercept of 72.4 ± 9.5 s and a slope of -0.76 ± 0.22 s/°C.

Humidity

The effects of humidity were tested by adding water vapor to the hydrogen-air mixture. This was accomplished by bubbling the mixture through a temperature-controlled water bath. The water bath consisted of a 5-cm diameter, 20-cm long copper pipe with copper end caps filled with copper turnings. The temperature of the water bath was set to a temperature between 1 to 20°C below the temperature of the rest of the apparatus depending on the desired relative humidity. This provided a humidified mixture at the temperature of the apparatus but at a dew point (saturated vapor temperature) equal to the temperature of the water bath. The relative humidity was computed from psychrometric tables taking the temperature of the apparatus as the dry bulb temperature and the temperature of the water bath as the wet bulb temperature. The relative humidity calculated in this way is only approximate because the gas flow velocities in the apparatus are much lower than those typically used to measure humidity. This means that the relative humidity computed for the apparatus may be slightly higher than the actual humidity.

The results showing the effect of humidity are given in Figure 1.81 and Table 1.7. They indicate that humidified mixtures are more difficult to ignite and that the increase in the ignition delay is about a factor of 3 from the low humidity case to the 100 percent relative humidity case. The ignition delay times versus relative humidity fit reasonably well a straight line having a slope of 3.11 ± 0.40 s/percent and an intercept of 169.7 ± 21.3 s. Thus, the effect of high humidity is to delay the ignition, but not to prevent it.

Water Spray

Fine water droplets were misted onto the igniter until its mass increased by about 10 percent (5 g of water). The igniter failed to warm even when exposed to an 11 percent hydrogen-air mixture. After the liquid water had evaporated (24 hr), the igniter operated normally as before.

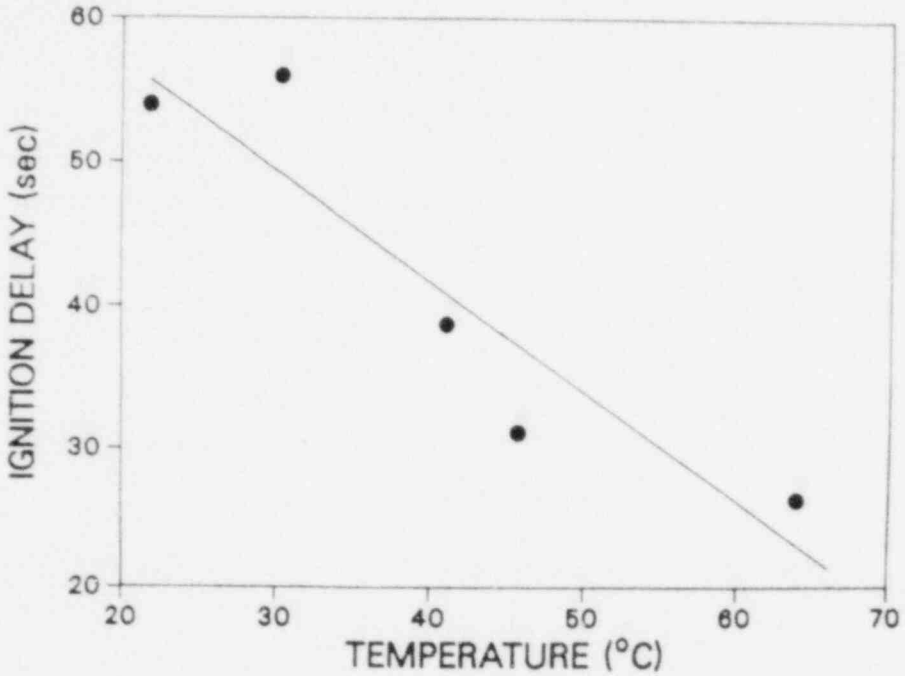

Figure 1.80. Effect of Gas Mixture Temperature. Warmer gas is easier to ignite than cooler gas.

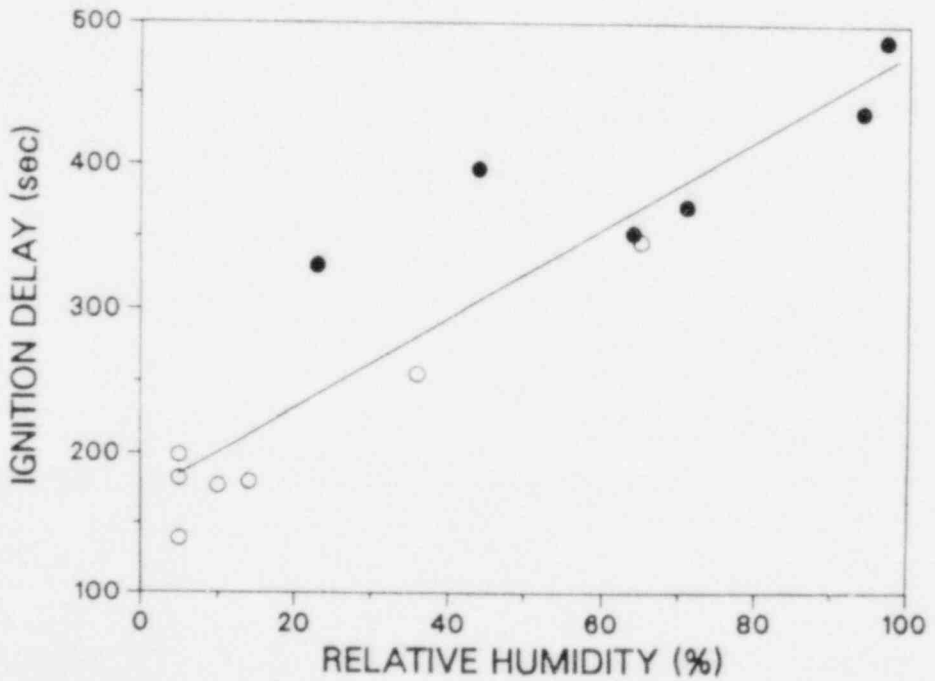

Figure 1.81. Effect of Humidity on Ignition Delay Time. Humidified mixtures are more difficult to ignite.

Table 1.7

Effects of Flow Rate

Flow Velocity (cm/s)	Hydrogen Concentration (%)	Ignition Delay (s)
1.7	8.0	170
	9.0	144
	11.0	60
2.8	5.6	194
	6.0	115
	7.0	78
	8.0	74
	9.0	60
	11.0	46
5.7	5.5	199
	6.0	38
	7.0	41
	8.0	36
	11.0	35
8.6	5.2	124
	5.5	82
	6.0	47
	7.0	53
	8.0	43
	9.0	46
	11.0	41
14.6	5.5	41
	6.0	37
	7.0	31
	8.0	23
	9.0	19
	10.9	14
19.5	5.2	36
	5.6	29
	6.0	24
	7.0	20
	8.0	14
	9.0	12
	11.0	11

1.7 References

1.1 D. H. Cho, W. L. Chan, and R. W. Wright, A Parametric Study of Pressure Generation and Sodium-Slug Energy from Molten-Fuel-Coolant Interactions, Argonne National Laboratories, ANL-8105, 1973.

1.2 C. C. Chu and M. L. Corradini, "Hydrodynamic Fragmentation of Liquid Droplets," Int. Conf. on Nuclear Power, 47 (November 1984).

1.3 F. Kreith, Principles of Heat Transfer, (New York: Educational Publishers, 1973) pp. 165-172.

1.4 R. B. Bird, W. E. Stewart, and E. N. Lightfoot, Transport Phenomena, (New York: Wiley, 1960) pp. 407-411.

1.5 G. Taylor, "The Instability of Liquid Interfaces When Accelerated in a Direction Perpendicular to Their Planes," Proc. Roy. Soc., A201, London, p. 192 (1950).

1.6 J. K. Dienes, "Method of Generalized Coordinates and an Application to Rayleigh-Taylor Instability," Phys. Fluids, 21(5), p. 736 (May 1978).

1.7 D. J. Lewis, "The Instability of Liquid Surfaces When Accelerated in a Direction Perpendicular to Their Planes," Proc. Roy. Soc., A202, London, p. 81 (1950).

1.8 E. T. Emmons, "Taylor Instability of Finite Surface Waves," Journal of Fluid Mechanics, p. 177 (1960).

1.9 D. C. Pack and W. M. Evans, Proc. Phys. Soc., B64, pp. 298-302, pp. 303-310 (1951).

1.10 M. Berman, LWR Safety Research Program Semiannual Report, October 1981-March 1982, Sandia National Laboratories, NUREG/CR-2841, SAND82-1572, December 1982.

1.11 D. E. Mitchell, M. L. Corradini, and W. W. Tarbell, Intermediate Scale Steam Explosion Phenomena: Experiments and Analysis, Sandia National Laboratories, NUREG/CR-2145, SAND81-0124, September 1981.

1.12 L. D. Buxton and W. B. Benedick, Steam Explosion Efficiency Studies, Sandia National Laboratories, NUREG/CR-0947, SAND79-1399, December 1979.

1.13 S. E. Dingman, "BRW Mark III Standard Problem Results," Sandia memorandum to A. L. Camp, May 8, 1984.

1.14 E. E. Zukoski, T. Kubota, and B. M. Cetegen, "Entrainment and Flame Geometry of Fire Plumes," Fire Safety Journal, 3, pp. 107-121 (1980/81).

1.15 A. C. Ratzel, "Data Analysis Work on NTS Premixed Combustion Tests," Sandia memorandum to T. T. Hitchcock and J. H. Linebarger, October 2, 1984.

1.16 H. Uchida, A. Ogama, and Y. Togo, "Evaluation of Post Incident Cooling Systems of Light-Water Power Reactors," Proceedings of the Third International Conference on the Peaceful Uses of Atomic Energy, Geneva Switzerland, 13, pp. 93-104 (1964).

1.17 A. L. Kuhl, M. M. Kamel, and A. K. Oppenheim, "Pressure Waves Generated by Steady Flames," 14th Symp. Int.) on Combustion, pp. 1201-1215 (1973).

1.18 C. M. Guirao, G. G. Bach, and J. H. Lee, "Pressure Waves Generated by Spherical Flames," Comb. & Flame, 27, pp. 341-351 (1976).

1.19 L. I. Sedov, Similarity and Dimensional Methods in Mechanics, 4th Ed., Gostekhizdat, Moscow (English translation edited by M. Holt, Academic Press, New York, 1959).

1.20 A. H. Kuhl, "On the Use of General Equations of State in Similarity Analysis of Flame-Driven Blast Waves," Shock Waves, Explosions, and Detonations, 87, Progress in Astronautics and Astronautics, Ed. J. R. Bowen, N. Manson, A. K. Oppenheim, R. I. Soloukhin, pp. 175-195.

1.21 R. H. Guirguis, M. M. Kamel, and A. K. Oppenheim, "Self-Similar Blast Waves Incorporating Deflagrations of Variable Speed," Shock Waves, Explosions, and Detonations, 87, Progress in Astronautics and Astronautics, Ed. J. R. Bowen, N. Manson, A. K. Oppenheim, R. I. Soloukhin, pp. 121-157.

1.22 A. K. Oppenheim, E. A. Lundstrom, A. L. Kuhl, and M. M. Kamel, "A Systematic Exposition of the Conservation Equations for Blast Waves," J. Appl. Mech., 38, pp. 783-794 (1971).

1.23 A. K. Oppenheim, A. L. Kuhl, E. A. Lundstrom, and M. M. Kamel, "A Parametric Study of Self-Similar Blast Waves," J. Fluid Mech., 52, pp. 657-682 (1972).

1.24 J. H. Lee, R. Knystautas, and C. K. Chan, "Turbulent Flame Propagation in Obstacle Filled Tubes," Proceedings of the 20th Symposium (International) on Combustion, Ann Arbor, Michigan (1984).

1.25 R. Knystautas, J. H. Lee, I. Moen, and H. G. Wagner, "Direct Initiation of Spherical Detonation by a Hot Turbulent Gas Jet," 17tn Symposium (International) on Combustion (1979).

1.26 K. J. Dörge, D. Pangritz, and H. G. Wagner, Acta Astronautica, 3, p. 1067 (1976).

1.27 J. H. Lee and I. O. Moen, "The Mechanism of Transition from Deflagration to Detonation in Vapor Cloud Explosion," Progr. Energy Comb. Sci., 6, p. 359 (1980).

1.28 J. H. Lee, R. Knystautas, and N. Yoshikawa, Acta Astronautica, 5, p. 971 (1978).

1.29 P. A. Urtiew and A. K. Oppenheim, 11th Symposium (International) on Combustion, p. 665 (1967).

1.30 J. H. Lee, R. Knystautas, and C. K. Chan, "Turbulent Flame Propagation in Obstacle Filled Tubes," Proceedings of the 20th Symposium (International) on Combustion, Ann Arbor (to be published).

1.31 H. Pförtner, H. Schneider, W. Drenchen, and C. Koch, "Flame Acceleration and Pressure Buildup in Free and Partially Confined Hydrogen-Air Clouds," Ninth International Colloquium on Dynamics of Explosions and Reactive Systems, Poiters, France (July 1983).

1.32 M. P. Sherman, S. R. Tieszen, W. B. Benedick, J. W. Fisk, and M. Carcassi, "The Effect of Transverse Venting on Flame Acceleration and Transition to Detonation in a Large Channel," 10th Intl. Colloquium on Dynamics of Explosions & Reactive Systems (to be published).

1.33 K. I. Shchelkin and Y. Troshin, Gasdynamics of Combustion (Baltimore, MD: Mono Book Corp., 1965).

1.34 J. H. Lee, R. Knystautas, C. Guirao, W. B. Benedick, and J. E. Shepherd, "Hydrogen-Air Detonations," Proceedings of the Second International Conference on the Impact of Hydrogen on Water Reactor Safety, NUREG/CR-0038, EPRI RP 1932-35, SAND82-2456, pp. 1007-1026, October 1982.

1.35 C. K. Westbrook and P. A. Urtiew, "Chemical Kinetic Prediction of Critical Parameters in Gaseous Detonation," 19th Symp. (Int.) on Combustion, Pittsburgh, PA, pp. 615-623 (1982).

1.36 D. C. Bull, J. E. Elsworth, and P. J. Shuff, "Detonation Cell Structures in Fuel/Air Mixtures," Combustion and Flame, 45, pp. 7-22 (1982).

1.37 Z. M. Shapiro and T. R. Mofette, Hydrogen Flammability Data and Application to PWR Loss-of-Coolant Accident, Bettis Plant, WAPD-SC-545, September 1957.

1.38 S. Gordon and B. J. McBride, "Computer Program for Calculation of Complex Chemical Equilibrium Compositions, Rocket Performance, Incident and Reflected Shocks, and Chapman-Jouguet Detonations," NASA SP-273, 1971.

1.39 R. Knystautas, J. H. Lee, and C. M. Guirao, Combustion and Flame, 48 (1), pp. 63-83 (1982).

1.40 Y. K. Liu, J. H. Lee, and R. Knystautas, Combustion and Flame, 56, pp. 215-225 (1984).

1.41 M. Berman, M. P. Sherman, J. C. Cummings, M. R. Baer, and S. K. Griffiths, Analysis of Hydrogen Mitigation of Degraded Core Accidents in the Sequoyah Nuclear Power Plant, Sandia National Laboratories, NUREG/CR-1762, SAND80-2714, March 1981.

1.42 L. Thompson, "EPRI Large-Scale Hydrogen Combustion Experiments," Designing for Hydrogen in Nuclear Power Plants, Joint ASME/ANS Nuclear Engineering Conference, Portland, Oregon, pp. 9-14 (1984).

1.43 W. H. Walton and W. C. Prewett, "The Production of Sprays and Mists of Uniform Drop Size by Means of Spinning Disc Type Sprayers," Proc. Phys. Soc., 62, pp. 341-350 (1944).

1.44 Reactor Safety Research Quarterly Report: July-September 1984, Sandia National Laboratories, NUREG/CR-3816 (3 of 4), SAND84-1072 (3 of 4), Vol. 31, April 1985.

1.45 M. P. Sherman, et al., The Behavior of Hydrogen During Accidents in Light Water Reactors, Sandia National Laboratories, NUREG/CR-1561, SAND80-1495, August 1980.

1.46 E. F. Coward and G. W. Jones, "Limits of Flammability of Gases and Vapors," Bulletin 503, Bureau of Mines, U.S. Dept. of Interior, 1952.

2. FISSION-PRODUCT SOURCE TERM

2.1 High-Temperature Fission-Product Chemistry and Transport (D. A. Powers, 6422; R. M. Elrick, 6422; R. A. Sallach, 1846)

A draft report[2.1] was written this quarter covering experiments that included iodine in some form: (1) CsI vapor reaction with 304 stainless steel and with Inconel 600 in an atmosphere of steam and hydrogen, (2) reaction of CsI vapor (in argon) with solid silver, and (3) reaction of iodine and HI vapors (in argon) with solid silver. Some results of this work were reported in a preliminary document.[2.2]

A summary of Reference 2.1 follows: The alloys 304 stainless steel and Inconel 600 were oxidized in steam at 1270 K while being exposed to cesium iodide vapor. The structures of the respective oxide layers grown in steam on Inconel 600 and 304 stainless steel are similar in both the CsI and CsOH test series. On Inconel 600 there is a small interaction of CsI vapor with the oxide layer resulting in some retention of cesium but not of iodine. The retained cesium is probably present in combination with silicon as a silicate compound. Although the cesium/silicon correlation coefficients have marginal values--about 0.7 at best--trial correlations with other elements present in the oxide gave much lower values. The amount of retained cesium resulting from exposure to CsI vapor was comparable to the amount retained in the CsOH tests. On 304 stainless steel there was no detectable interaction of CsI vapor with the oxide layers. This is in sharp contrast to the CsOH experiments where cesium was found fully combined with the silicon content of the inner oxide layer as the silicate $Cs_2Si_4O_9$. This lack of interaction is attributed to the greater stability of the CsI molecule, precluding its dissociation on the oxide surface and the subsequent diffusion of a cesium species throughout the oxide layers. Surface reaction rate constants for cesium and iodine in the reactions of CsI with Inconel 600 and with 304SS in steam and hydrogen are summarized in Table 2.1.

Furthermore, cesium iodide vapor in an argon carrier was shown to be stable in the presence of silver at temperatures less than 1223 K. Also, HI and iodine vapors react rapidly with solid silver to form silver iodide at temperatures up to at least 1073 K.

Krishna Vinjamuri of INEL requested equilibrium calculations for the Te-O-H system in order to predict the major tellurium species that could be released under TMI-2 accident conditions. A memo was prepared and sent to INEL. The conclusions drawn in this study are given here.

Table 2.1

Summary of Surface Reaction Rate Constants
and Test Conditions

Conditions	Temperature (K)	H_2(mole) / H_2O(mole)	Chemical Species(mole) H_2O (mole)		Surface Reaction Rate Constant (m/s) Removed by Water (U)	Reacted (R)
CsI/304SS in steam	1270	0.1 to 0.2	~4 x 10^{-5}	Cesium	<3 x 10^{-7}	<3 x 10^{-7}
				Iodine	<3 x 10^{-7}	<3 x 10^{-7}
CsI/Inconel 600 in steam	1270	0.03 to 0.08	~4 x 10^{-5}	Cesium	5 x 10^{-7}	2.5 x 10^{-6}
				Iodine	<2 x 10^{-7}	<2 x 10^{-7}

Uncertainty in surface reaction rate constants ±2X.

Data for the hydrogen/water and tellurium/water ratios are used as input to calculate the equilibrium concentrations of various vapor species containing tellurium. The complete list of species considered for these calculations is given in Table 2.2. Thermochemical data for these species were obtained from the JANAF Tables[2.3] for the hydrogen + oxygen species and from the tabulation of Mills[2.4] for species containing tellurium. One possible vapor species was not considered--the hydrated form of TeO_2 vapor which can be written as $TeO(OH)_2$. This hydrated species was shown to become important relative to the tellurium dioxide vapor species at temperatures above 700°C whenever steam is present.[2.5] However, these oxygen-containing forms can be important major species only when there is an excess of oxygen present (an overall hydrogen-to-oxygen ratio less than 2.0). That is not the case here since the overall hydrogen-to-oxygen ratio is always greater than 2.00. Therefore, no errors are produced by the omission of the hydrated species.

Table 2.2

Vapor Species Considered by the Calculation

Element	Species
Tellurium	$Te, Te_2, TeO, TeO_2, H_2Te$
Hydrogen/Oxygen	H_2, H, HO, H_2O, O, O_2

The input data used for these calculations are presented in Table 2.3. The hydrogen-to-steam and tellurium-to-oxygen ratios are listed for various times to be considered. The former ratios were converted to overall hydrogen-to-oxygen ratios; these are also listed. These hydrogen-to-oxygen ratios are also shown in Figure 2.1. Included in that figure are the square roots of the tellurium/water ratios. (The square roots were used in order to facilitate the presentation of the data.) The correlation of the tellurium release with an excess of hydrogen is clearly evident.

These atomic ratios were the input to the FLUEQU code by which the equilibrium concentrations of the chemical species were calculated. This code was developed at Sandia[2.6] for application to geohydrothermal systems but was later applied to chemical vapor deposition studies and to calculations of fission product species.[2.8] The code is strictly applicable only to wholly vapor systems. If the possibility of vapor condensation may occur, the operator must monitor

Table 2.3

The H/O and Te/O Elemental Ratios
Used for Input Data

Time (min)	H_2/H_2O Ratio	H/O Ratio	Te/O Ratio
153	0.48	2.96	7.0×10^{-6}
158	0.66	3.32	1.3×10^{-5}
163	0.80	3.60	1.4×10^{-5}
168	1.16	4.32	1.1×10^{-5}
173	3.2×10^{-3}	2.0064	1.0×10^{-8}
178	3.2×10^{-3}	2.0064	3.0×10^{-9}
183	0.88	2.44	7.5×10^{-8}
188	1.96	5.92	2.4×10^{-7}
193	3.39	8.78	1.5×10^{-7}
198	5.43	12.86	1.0×10^{-7}
203	1.20	4.40	5.8×10^{-10}
208	0.28	2.56	5.8×10^{-10}
213	0.28	2.56	5.8×10^{-10}

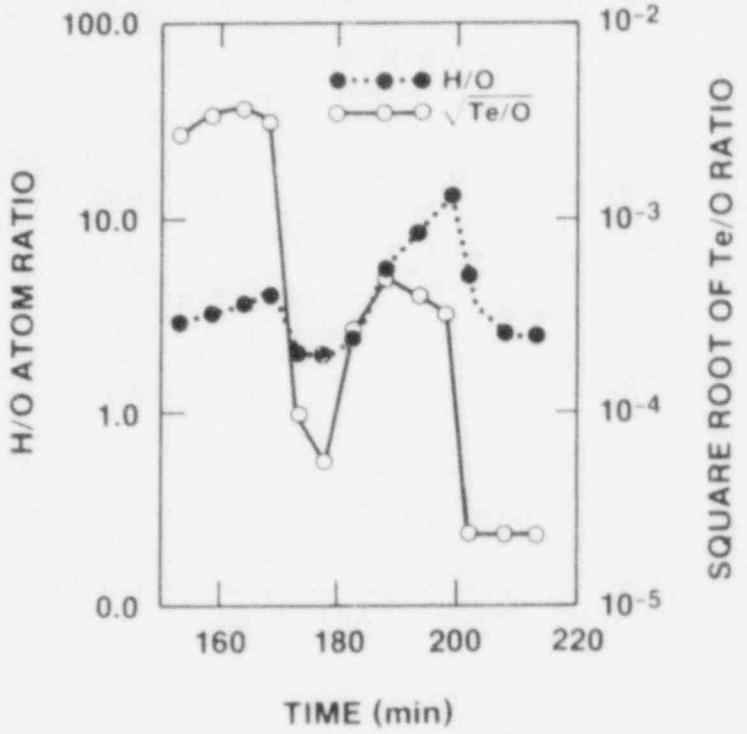

Figure 2.1. The H/O Ratio and Square Root of Te/O Ratio vs. Time

the partial pressure of appropriate vapor species and check for this phenomenon.

Two temperatures and two pressures were considered. The lower temperature, 482°C (900°F), is considered to be a representative temperature for the upper plenum. The higher temperature, 982°C (1800°F), is typical of the region at the top of the core. The higher pressure was 15.2 MPa (about 2250 psi) and represents the operating pressure range. The lower pressure was chosen as 8.2 MPa (about 1200 psi) to represent conditions during steam blowdown. These choices for the system pressure are not critical factors since the calculations will show that the distribution of chemical species does not depend significantly on pressure (for pressures greater than about 1 MPa).

A series of calculations was made to explore the distribution of tellurium species as a function of temperature, total pressure, the extent of steam oxidation, and initial Te/O ratio. The temperatures ranged between 800 and 2000 K; higher temperatures were not considered since the tabulated free energy data does not extend above 2000 K. The pressures ranged between 0.1 MPa (atmospheric pressure) and 20 MPa. The initial Te/O (Te/H_2O) ratios were 1.E-5, 1.E-7, and 1.E-9. The initial H/O ratio was 2.0, corresponding to pure

steam. The amount of oxygen present was then reduced to correspond to 2, 20, 50, 71, 83, and 90 percent reacted (assuming the reaction to be between metal and steam to form the metal oxide with the release of an equivalent amount of hydrogen into the gas phase). These reaction percentages are equivalent to H/O ratios of 2.04, 2.5, 4.0, 7.0, 12.0, and 20.0, respectively.

The calculated partial pressure of some tellurium chemical species at a total pressure of 8.2 MPa are shown in Figures 2.2 and 2.3 for the temperatures 482°C and 982°C, respectively. Only those species whose partial pressures are in excess of 10^{-7} Pa are shown. The preponderant tellurium species is hydrogen telluride (H_2Te) except when there is little hydrogen gas present, i.e., during the burst of steam occurring at 173-178 min. At that time, the partial pressures of the elemental tellurium vapors are comparable to or slightly exceed the partial pressure of H_2Te. At 482°C the preferred elemental form of tellurium is the dimer Te_2 while at 982°C the monomer Te is the predominant elemental species.

The results calculated for 15.2 MPa are very similar, so similar that the results are not graphed. Relative to Figures 2.2 and 2.3 the curve for the partial pressure of H_2Te vapor is shifted upward (by about log(2)) as a result of the increase of total pressure. However the curves for other vapor species containing tellurium do not appear to undergo any significant shift.

Whenever there is large excess of hydrogen gas present (overall hydrogen-to-oxygen ratio greater than 2.5) more than 90 percent of the tellurium is present as H_2Te vapor. Thus, the chemistry of fission-product tellurium is dominated by that vapor species and the interaction of fission-product tellurium with the materials of the reactor system can be interpreted on that basis.

Condensation of elemental tellurium does not appear to occur under the conditions for which these calculations were made. Only at 482°C and 15.2 MPa does the partial pressure of the elemental forms approach the vapor pressure over the liquid phase, and this situation occurs only up to 170 min. At later times the tellurium-to-oxygen(water) ratio becomes reduced and condensation of elemental tellurium is not feasible. Condensation might occur if the local system temperature were to fall to some lower value during early times.

These calculations indicate that for the conditions specified in Table 2.3 the predominant vapor species which contains the fission-product tellurium is H_2Te. Other tellurium vapor species are not really significant except for the short period at 173-178 min where the gaseous environment

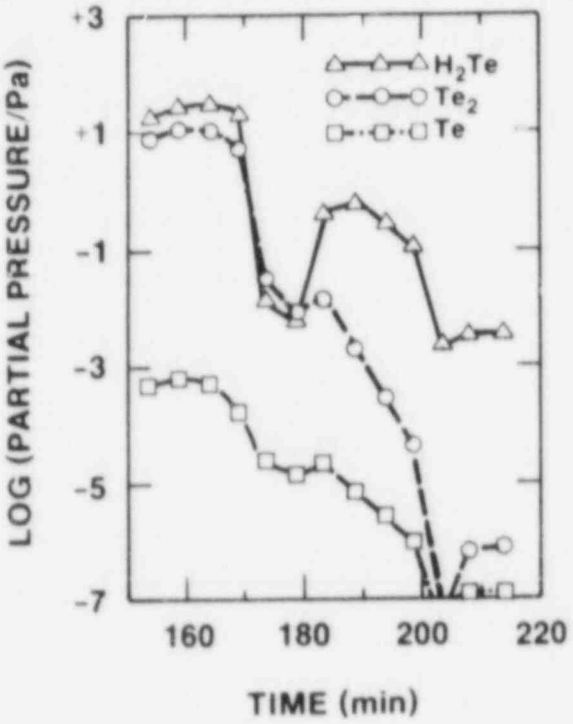

Figure 2.2. Partial Pressure of Tellurium Species at 482°C and 8.2 MPa Total Pressure

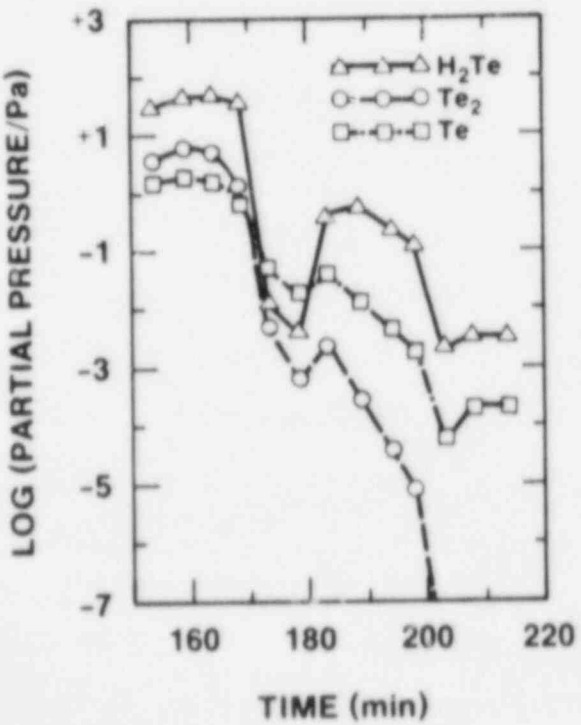

Figure 2.3. Partial Pressure of Tellurium Species at 982°C and 8.2 MPa Total Pressure

is almost pure steam. Thus, the chemistry of fission product tellurium in the present environment is going to be determined by the reactions of H_2Te vapor with the materials of the reactor system.

The calculations also indicate that the system pressure, so long as it is high, is not a significant parameter in regard to the distribution of tellurium-containing species. The dominant parameter determining the distribution of tellurium species is the hydrogen-to-oxygen ratio. Whether this fact is relevant to the correlation between tellurium release into the gas phase and the presence of excess hydrogen gas (as seen in Figure 2.1) is an interesting, but debatable point. The point is worth further consideration.

The apparent correlation between the release of tellurium and an excess hydrogen could arise in several ways. Two suggest themselves readily. Assume the tellurium is bound to a metal surface as a telluride, zirconium telluride, for instance. Then, if the base metal is oxidized by steam, both hydrogen and tellurium would be released into the gas phase. The correlation then is real in that the same process (steam oxidation) is responsible for their production.

Alternately, assume that the tellurium is present in elemental form. Its release (vaporization) is then a function of its temperature. A local equilibrium partial pressure of elemental vapor species would be strived for. However, this local partial pressure would be disturbed whenever hydrogen is brought into the environment. The species H_2Te would be formed at the expense of the elemental forms, reducing their partial pressure and enhancing the rate of vaporization. The hydrogen, of course, derives from steam oxidation. Here, also, the correlation is real but the oxidation and vaporization processes do not occur in the same location.

The second hypothesis can also be applied to the thermal dissociation of metal tellurides in which tellurium vapors are created.

In regard to this second hypothesis, notice in Figures 2.2 and 2.3 that the calculated partial pressures of the elemental vapors (Te or Te_2) do not exhibit a variation with release rate (Figure 2.1), but show a relatively constant value early in the time period, then decay gradually as time progresses. Such behavior might be expected if the second hypothesis is valid.

When the calculations were made for a much broader range of parameters, general trends became evident. Selected data are presented in Figures 2.4 through 2.9 to illustrate these trends and the effect of particular parameters. Our starting

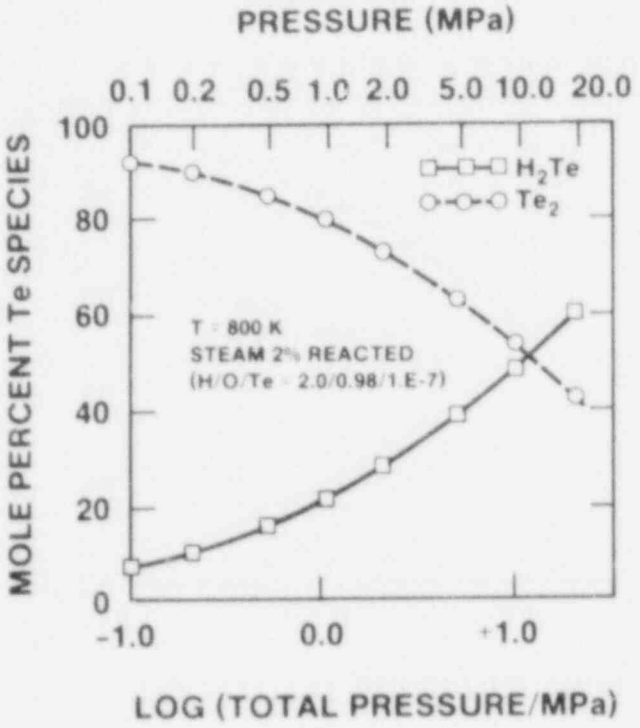

Figure 2.4. Effect of Total Pressure on Composition of Tellurium Species at 800 K and With H/O = 2.04

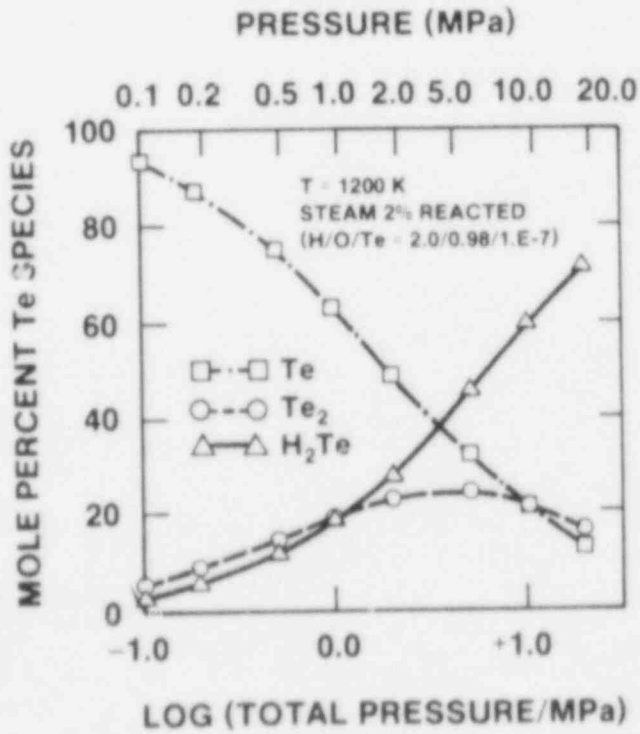

Figure 2.5. Effect of Total Pressure on Composition of Tellurium Species at 1200 K and With H/O = 2.04

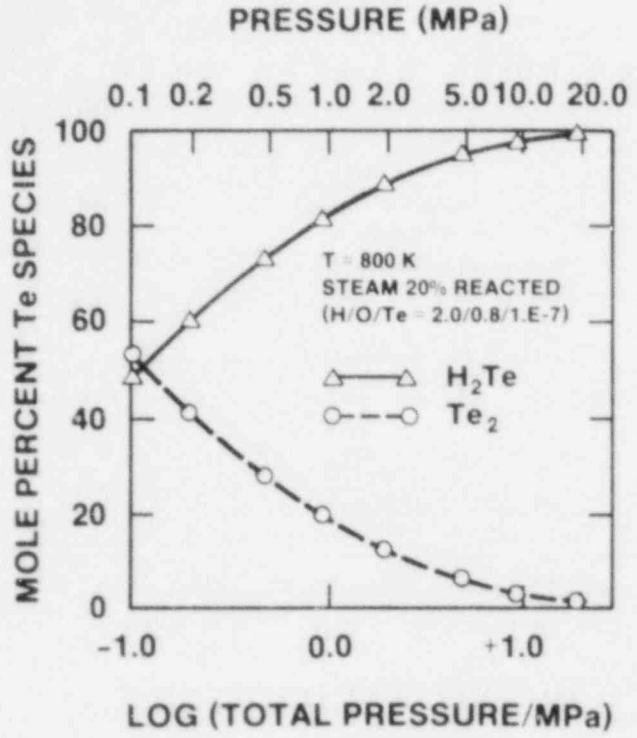

Figure 2.6. Effect of Total Pressure on Composition of Tellurium Species at 800 K and With H/O = 2.5

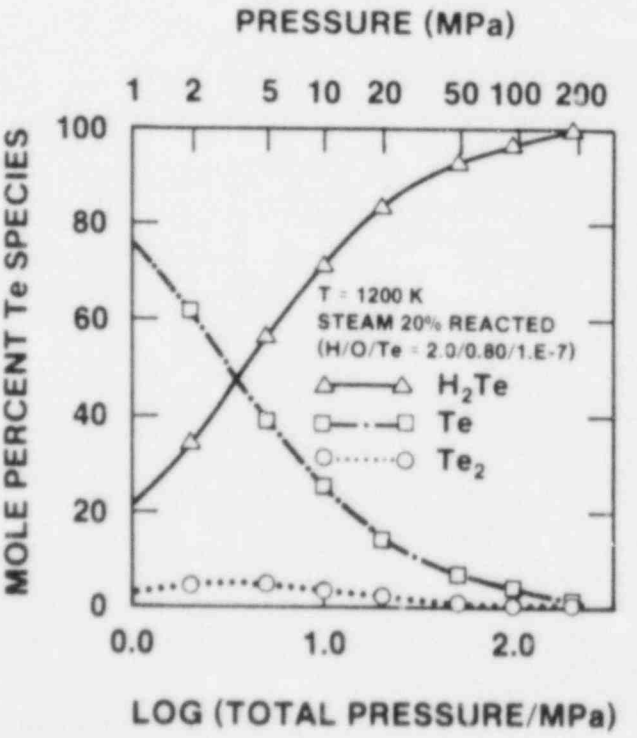

Figure 2.7. Effect of Total Pressure on Composition of Tellurium Species at 1200 K and With H/O = 2.5

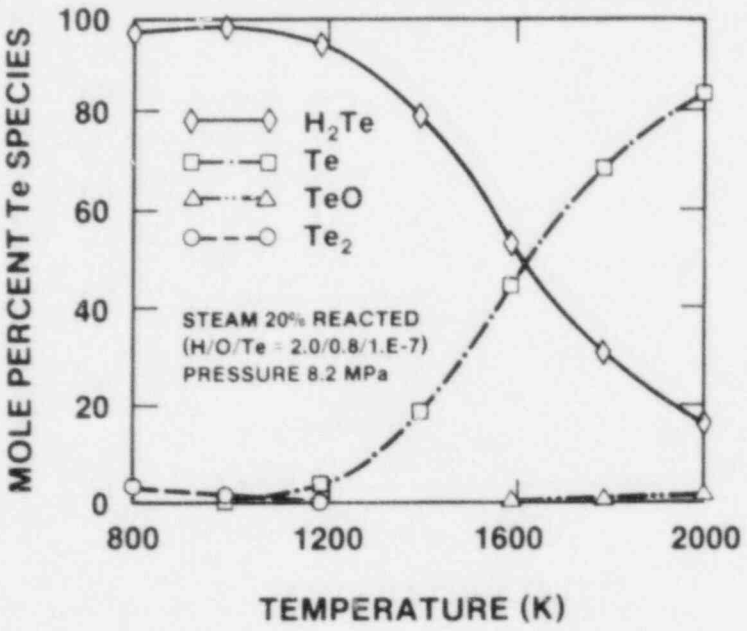

Figure 2.8. Effect of Temperature on Tellurium Species

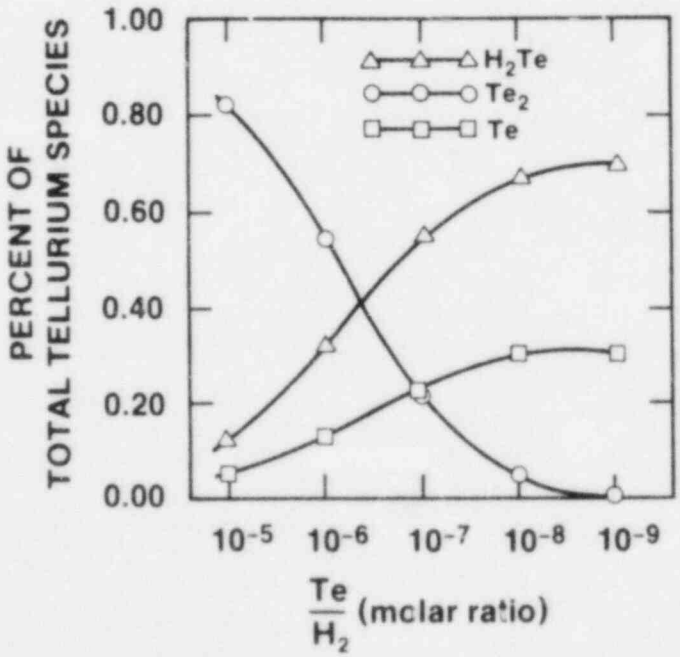

Figure 2.9. Effect of Dilution on Composition of Tellurium Species. Parameters: T = 1200 K; Total Pressure = 8.2 MPa. Composition: H/O/Te = 2.0/0.98/X where X is the abscissa of the graph.

point is the vapor composition in pure steam at atmospheric pressure (0.1 MPa). With no excess hydrogen the stable vapor tellurium species are the elemental vapors: the dimer Te_2 at temperatures <1000 K and the monomer Te at higher temperatures. These elemental vapors persist as the dominant species until about 20 percent of the steam has reacted (H/O about 2.5) when the total pressure is 0.1 MPa (atmospheric pressure). As the total pressure is increased the species H_2Te is formed at the expense of the elemental vapors even when as little as 2 percent of the steam has reacted. High system pressures favor the formation of H_2Te vapor.

The effect of pressure can be countered by increasing the temperature. This is shown in Figure 2.8 for a H/O ratio and a pressure where H_2Te is the predominant species at 800 K. As temperature is increased to 2000 K, thermal dissociation of H_2Te takes place and the elemental forms again become dominant.

The effect of dilution of the tellurium content is shown in Figure 2.9. The dimer Te_2 becomes unstable with respect to the monomer, as would be expected. However, the H_2Te species is also seen to become the major species even for steam-hydrogen mixtures in which the H/O ratio is as low as 2.04.

In summary, the formation of the vapor species H_2Te is favored by the presence of excess hydrogen and by high total system pressures. This species is also favored when the tellurium content of the gas phase is reduced or diluted. Increasing the system temperature will tend to dissociate H_2Te, but temperatures above 1200 K are needed depending on other system parameters.

2.2 ACRR Source Term Tests

(K. O. Reil, 6423; J. Grimley, 6425; P. S. Pickard, 6423)

A unique fission-product sampler system has been designed to provide the ST tests with the capability of sampling fission products as close as possible to the point of release. This is desirable to minimize transport and mitigation effects that require unfolding to interpret the results. The sampler design includes both passive filter sections (for particulates) and active filter sections designed to remove specific fission-product species by chemical reactions.

A schematic of the filter system is shown in Figure 2.10. The first series will include:

1. CsI (particulate) in flowing steam at 1170 K on Inconel-mesh filters, and

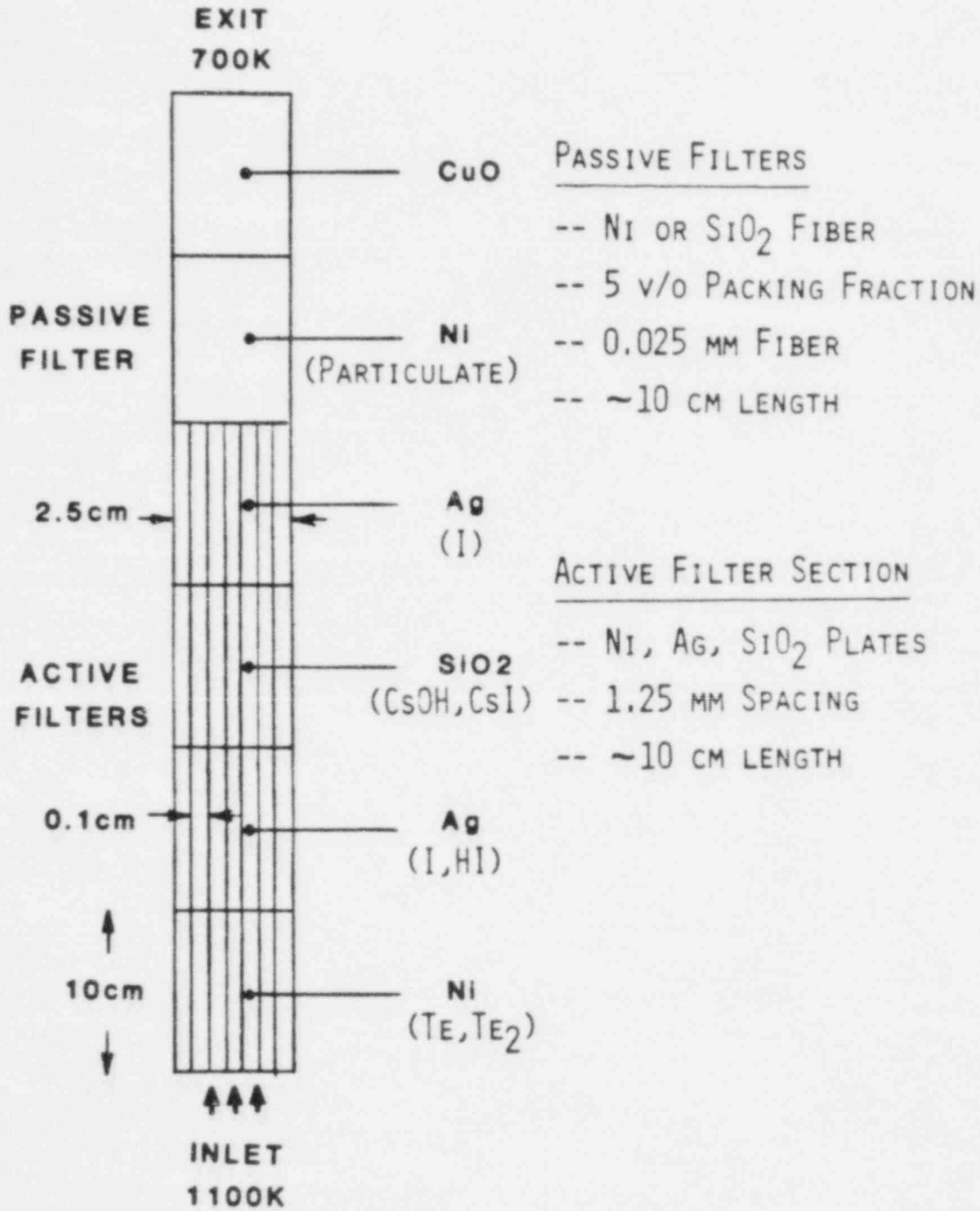

Figure 2.10. ST/DFI Filter System

2. Active (Reactive Filter Tests)

- Cs on SiO_2
- Te on Ni
- I on Ag.

The active filter tests will initially be performed in steam at 1170 K prior to examining temperature and flow effects. The active filter sections are intended to provide some segregation of Cs, Te, and I to enhance posttest analyses as well as provide some additional information on the form of I released (CsI or I_2).

The ST samplers consist of a series of reactive filters (to segregate specific species) and a particulate filter. The reactive filters being examined are Ni(Te), SiO_2(Cs), and Ag(I). Tests have now been completed for the particulate filter (Inconel mesh) and CsI on SiO_2. The efficiency of the particulate filter was tested in steam at 800°C with CsI particulate estimated to be in the micrometer range. Filter efficiency was determined using deposition surfaces before and after the filter section. The measured efficiency of the filter is in excellent agreement with calculated estimates for these conditions. Implied efficiencies for samplers designed for ST tests are >90 percent for the range of anticipated temperatures, pressures, and aerosol sizes. The filters have relatively low pressure drops (~1 psi) across the section. The first test completed on the reactive filters (CsI on SiO_2) showed lower than expected reaction rates of Cs with SiO_2. A repeat of this experiment will be performed after the first series is completed. If these results are confirmed, discrimination between CsI and CsOH can still be obtained by the relative deposition of Cs (from CsOH) on the SiO_2 and (from CsI) in the particulate sections.

Two approaches are being examined that will provide the capability to examine a range of fuel temperatures, gas pressure and composition, and full-clad damage states. The two approaches are illustrated in Figure 2.11, the recirculating system, and Figure 2.12, the once-through steam system.

Another major activity involved demonstration of specific wet chemistry techniques for posttest analysis of fission-product samplers. Although the primary diagnostic for most isotopes of interest is γ-spectroscopy, the use of Ion Chromatography (Cs, Ba, Sr), Ion Selective Electrodes (I), and Voltametry (Te), potentially provide sensitive backup techniques for these elements.

The following is the estimated required sensitivity for ST conditions (based on 100 g fuel samples):

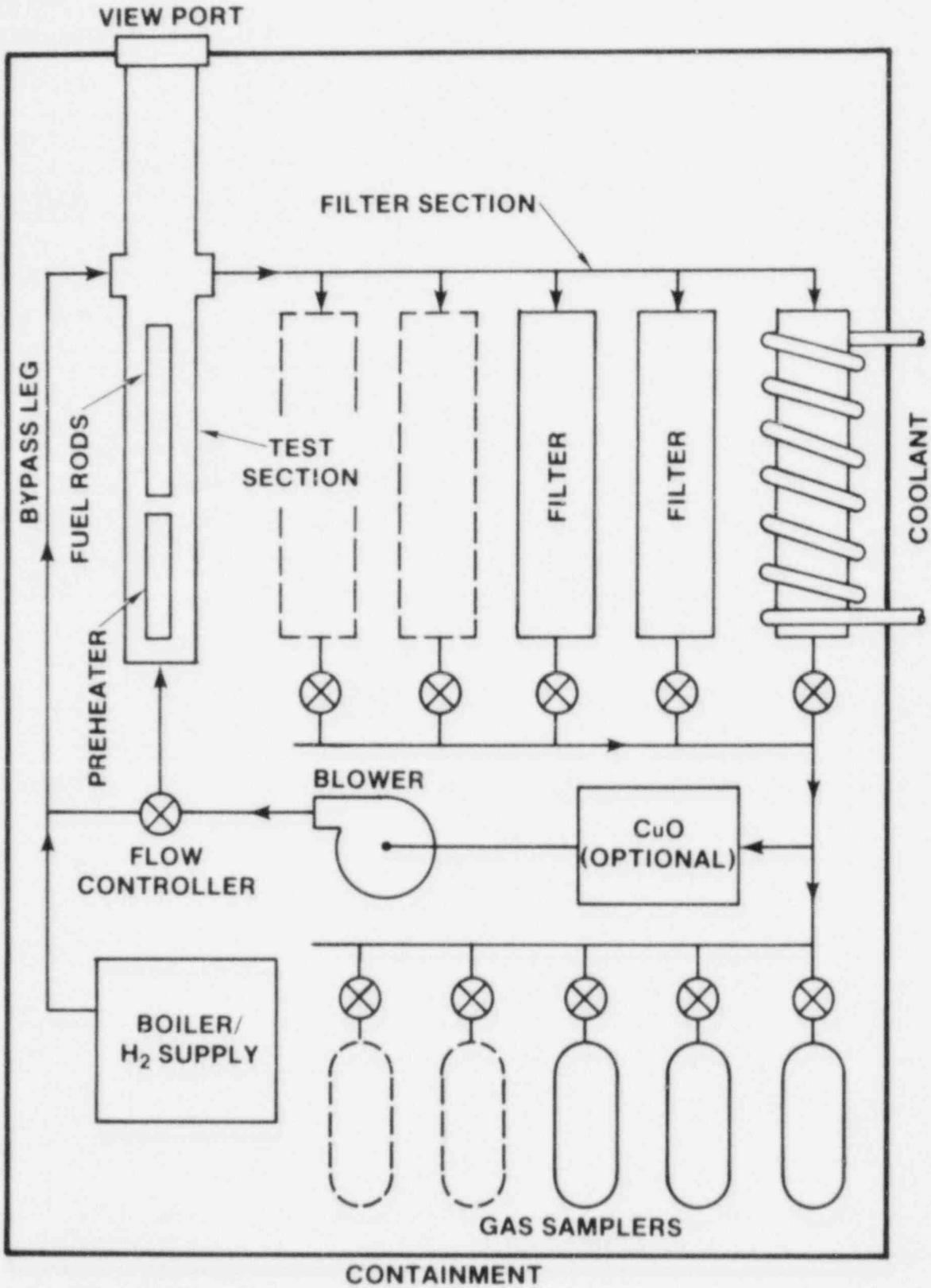

Figure 2.11. Recirculating System Schematic

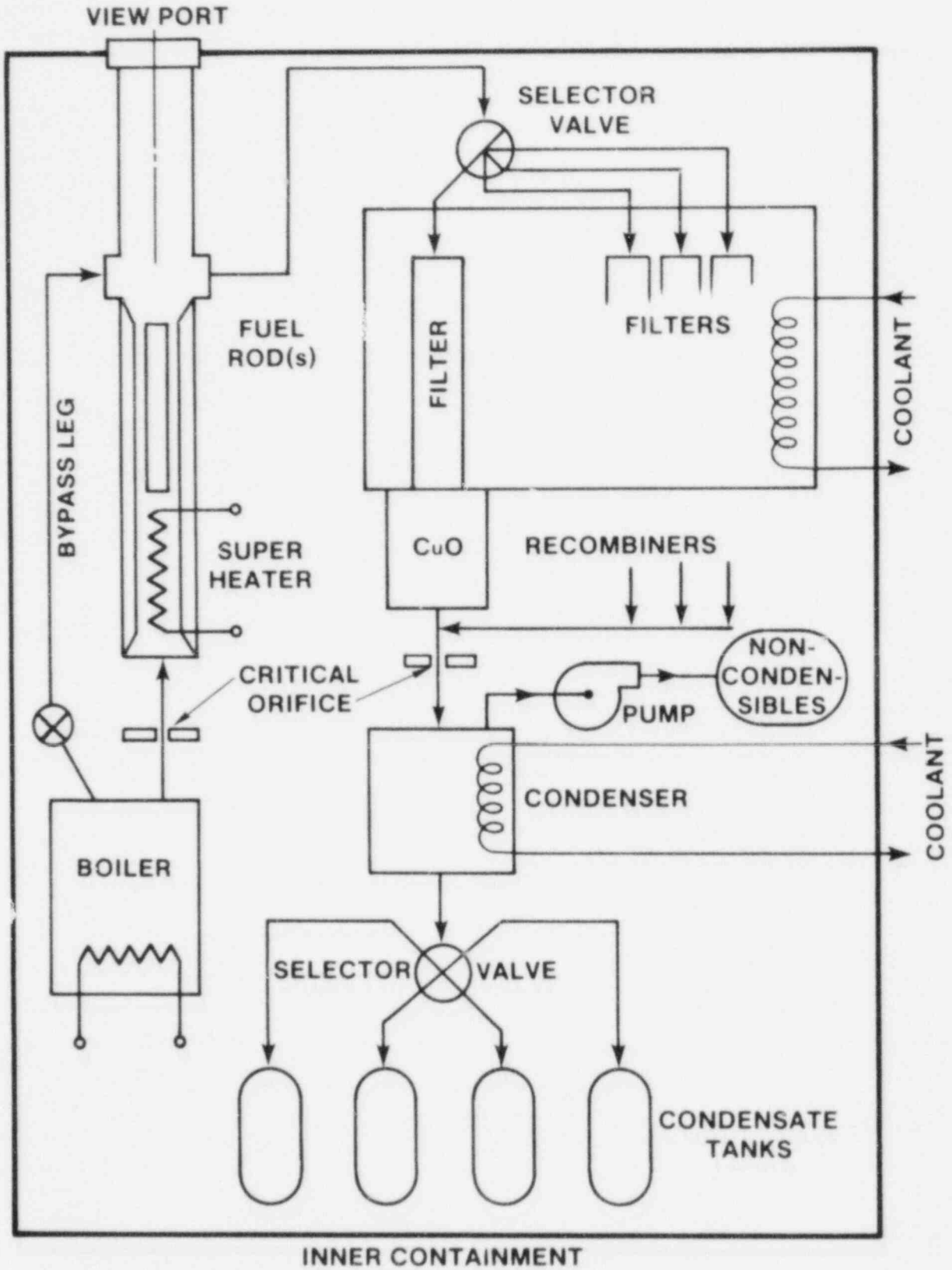

Figure 2.12. Schematic Diagram of Once-Through Steam System for ST Tests

Technique	Isotope	Required Sensitivity Range (ppm)
I.C.	Cs	10-2700
	Ba	40-140
	Sr	10-50
I.S.E.	I	1-200
Voltametry	Te	30-300

Preliminary tests have been completed for Cs and I in solutions of known amounts of contaminants.

Ion-selective electrodes have been tested for iodine analysis under widely varied conditions (pH 1.0 to 13.0, ionic strength 10^{-6}-1 M), and have been used to measure iodide in filter efficiency tests; the response of the electrodes is generally very good. The ion chromatograph was shown to be sensitive to Ba and Sr levels well below 1 ppm, even in the presence of 200 ppm Cs. A literature search indicates that the IC columns should not be damaged by radiation levels below 10^6 rads.

Voltametry tests for Te will be performed early in CY 1985. In preparation for γ-spectroscopy tests, a program has been written to calculate γ response functions for Ge detectors for widely varying counting conditions. Spectra are calculated using semiempirical curves for intrinsic efficiency, double and single escape yields, peak width, peak to Compton, peak to tail (multiple Compton), and Pb absorption coefficients as functions of γ energy. Responses for individual γ's are linearly summed, then nonlinear effects due to high count rate (sum peaks and sum Compton) are calculated and added to the spectrum.

The program will be benchmarked against neutron activation analysis spectra. Future modifications will include improvements on the efficiency of file storage, and variable detector geometries. To date, the program has been useful in determining nuclides most suited for direct γ spectroscopy and neutron activation, and has outlined the optimum counting conditions for detection.

2.3 References

2.1 R. A. Sallach, R. M. Elrick, S. C. Douglas, and A. L. Ouellette, Reaction Between Some Cesium-Iodine Compounds and the Reactor Materials 304 Stainless Steel, Inconel 600 and Silver, Volume II Cesium Iodide Reactions, Sandia National Laboratories, NUREG/CR-3197 (2 of 3), SAND83-0395, November 1984.

2.2 R. A. Sallach, Chemical Aspects of CsI Interaction in Steam with 304 Stainless Steel and Inconel 600, Sandia National Laboratories, SAND84-0749 (to be published).

2.3 JANAF Thermochemical Tables, NSRDS-NBS37 (1971) and Supplements (1974, 1975, and 1978).

2.4 K. C. Mills, "Thermodynamic Data for Inorganic Sulphides, Selenides and Tellurides," London Butterworths (1974).

2.5 A. P. Malinauskas, H. H. Gooch, Jr. and J. D. Redman, "The Interaction of Tellurium Dioxide and Water Vapor," Nucl. Appl. and Tech., 8, p. 52 (1970).

2.6 T. M. Gerlach, "Evaluation of Volcanic Gas Analysis from Kilauea Volcano," J. Volcanology and Geothermal Research, 7, pp. 295-317 (1980).

2.7 E. Randich and T. M. Gerlach, "The Calculation and Use of CVD Phase Diagrams with Applications to the Ti-B-Cl-H System 1200 K-800 K," J. Thin Solid Films (1982).

2.8 R. M. Elrick and R. A. Sallach, "Chemistry of Cesium and Iodine," Chapter 5 of Technical Bases for Estimating Fission Product Behavior During LWR Accidents, NUREG-0772 (1981).

3. LWR DAMAGED FUEL PHENOMENOLOGY

3.1 ACRR Damaged Fuel Relocation and Quench

(A. C. Marshall, 6423; P. S. Pickard, 6423)

The DF-2 experiment was performed in October 1984 to examine the effects of higher initial oxidation on the severity of the fuel damage processes. DF-2 was performed with relatively low steam flow rates (≈0.025 g/s rod) at ~15 atm system pressure with about 15 percent of the upper bundle oxidized prior to the initiation of the transient. A comparison of DF-1 and DF-2 conditions is summarized in Table 3.1.

Table 3.1

DF-2 vs. DF-1 Experiment Conditions

	DF-1	DF-2
System Pressure	45 psi	~220 psi
Rod Internal Pressure (cold)	<1 psi	15 psi
Cladding Fraction Oxidized prior to High Reactor Power (upper half of bundle) --calculated	10%	15%
Steam Inlet Mass Flow Rate	0.036 g/sec/rod	0.025 g/sec/rod
Maximum Reactor Power	1.5 MW	1.5 MW
Maximum Rod Fission Power	2.4 W/g	2 W/g
Axial Power Gradient	flat	flat

3.1.1 Experiment Description

A temperature plot of two upper W/Re TCs is shown in Figure 3.1. The ACRR reactor power history for the DF-2 test is shown in Figure 3.2. The early low-power period was designed to preoxidize the cladding. The mass flow rates of inlet and bypass steam are presented in Figure 3.3. These flow rates are measured at the supply skid, so that package inlet flow is more uniform than shown. The flow interruption was due to accidental closing of isolation valves.

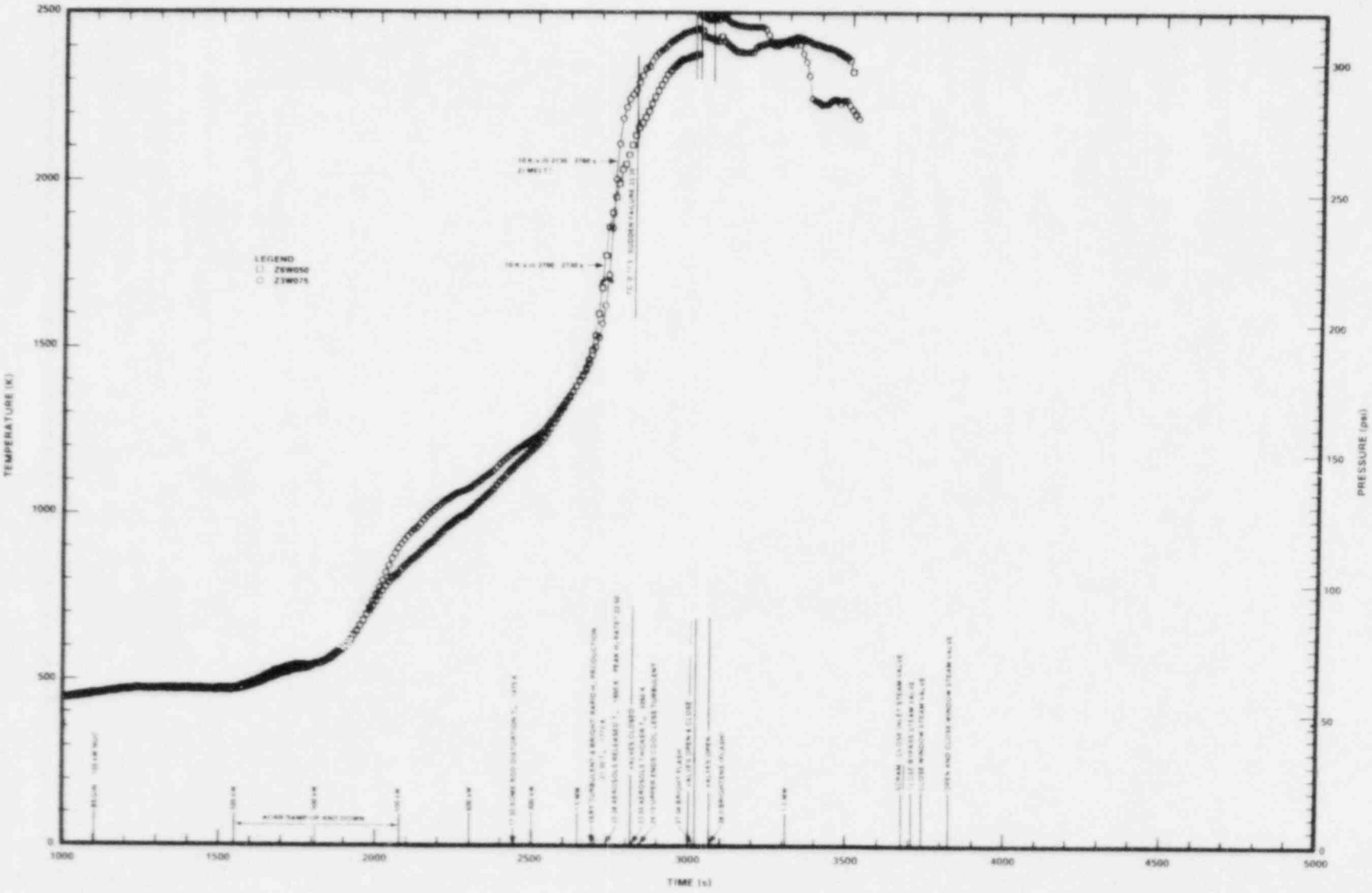

Figure 3.1. DF-2 Thermocouple Data

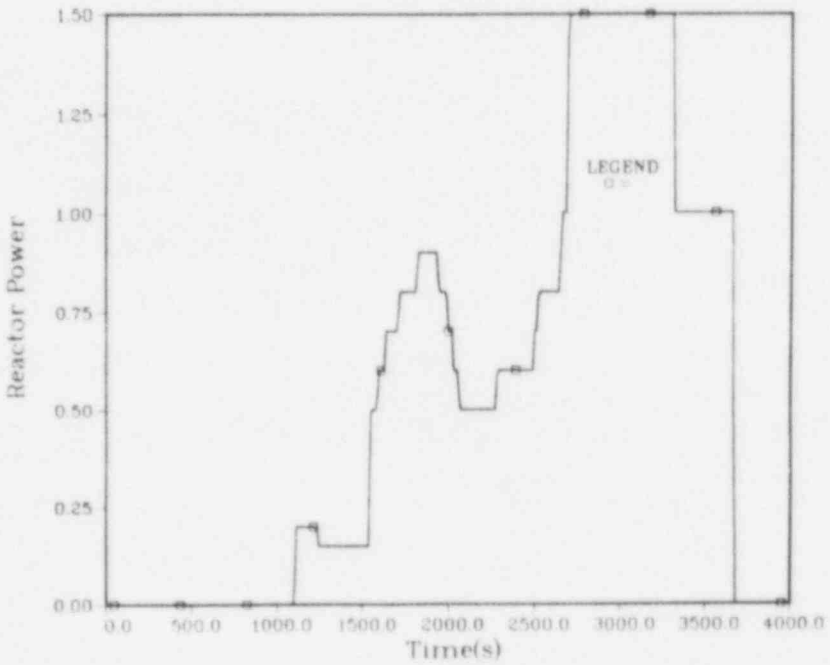

Figure 3.2. DF-2 Power History

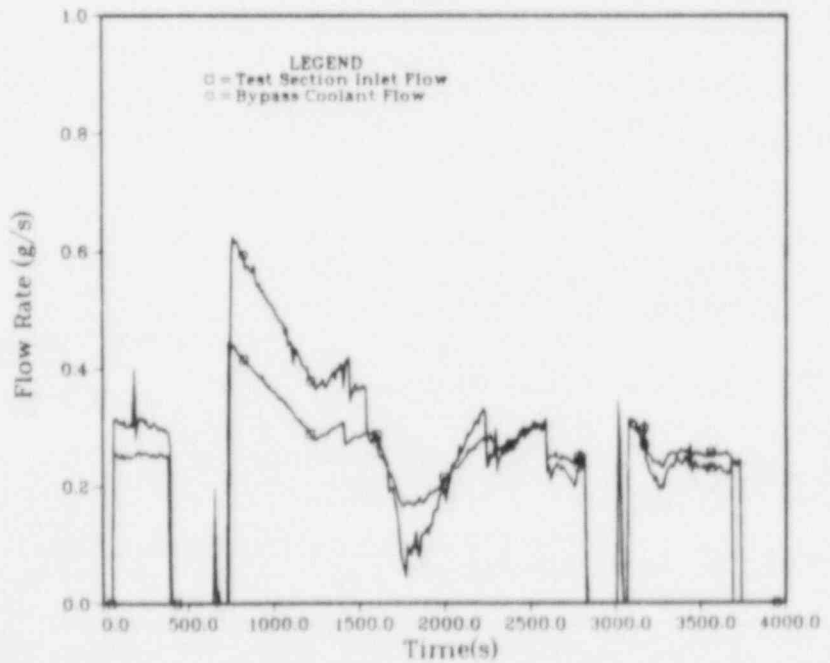

Figure 3.3. Steam Mass Flow Rates

The experiment sequence is summarized in Table 3.2. After about 8 min of low power (150 kW) operation of the reactor power was gradually increased, then adjusted to hold the fuel temperatures in a range that would permit significant oxidation of the cladding prior to initiation of the high power transient. When the fuel reached 1200°C, the fuel rods were observed to have bowed toward the center. At 20 min 50 s, video time (video started about 5 min after reactor power initiation and is listed in Table 3.1), the maximum fuel temperature reached 1400°C. The reactor power was then increased to 1.5 MW to initiate the high power transient. One minute later the CuO temperature indicated a rapid rise in hydrogen production and fuel temperatures reached 1550°C. The fuel rods appeared to have bowed significantly and the video image was bright but difficult to interpret due to increased turbulence. At 22 min 27 s the fuel temperatures in the upper half of the bundle reached 1850°C and were climbing at a rate of 10°C/s. At this time aerosols were observed in the flow channel. About 20 s later the heatup rate in the upper half slowed down while the rate in the lower half increased to 10°C/s. At this time the H_2 production rate appears to have peaked. Also at this time the Pt/Rh thermocouple on the fuel rod near the bottom suddenly failed. One minute later the electrical power to the steam inlet valves was lost and the valves closed, interrupting steam inlet flow. Since the capsule volume is large and the steam pressure was fairly high, steam continued to flow through the fuel bundle (at a lower rate) as the system depressurized. The fuel temperature in the upper region continued to increase with no apparent change in rate. Fuel temperatures in the lower bundle (measured 2 1/2" below fuel center) were observed to drop slightly for about 30 s, then increased at a lesser rate than the rate just before the valves closed.

The upper end fittings were observed on the video monitor to cool down after the valves were shut, probably due to a lack of bypass steam to maintain oxidation heating. Turbulence decreased during this period.

At 26 min 50 s the steam valves were reopened for about 30 s. All fuel temperatures and the H_2 production rate were observed to increase. The measured temperature increase was on the order of 100°C. When the valves closed, the fuel temperature below the centerline and the hydrogen production rate decreased again.

The valves were opened again at 28 min and remained open. At this time only the thermocouple at 2 1/2" below the centerline showed an increase. H_2 production also increased for about 20 s. The rate of temperature increase at this location briefly reached 20°C/s. At about 30 min full pressure and flow were reestablished and the peak temperature was reached in the bottom bundle half. At 36:50 the

Table 3.2

Sequence of Events for Experiment DF-2

Time DAC (sec)	Time Video (min:sec)	Event		Max. Fuel Temperature °C	Max. Fuel Temperature K
1100	-4:50	Begin Reactor Power at 150 kW		350	623
1390	0:0	Start Video		450	723
1600	3:30	Increase Reactor Power to 500 kW ↓ (ramp power up in steps)		550	823
1800	6:50	900 kW ↓ (ramp power up in steps)	Pre-Conditioning Phase	860	1133
2060	11:10	500 kW		1150	1423
2440	17:30	Rods Bowing Toward Center Visible ↓ (ramp power up in steps)		1200	1473
2500	18:30	800 kW ↓		1573	1300
2640	20:50	Increase Reactor Power to 1.5 MW (begin transient)		1400	1673
2700	21:50	Rapid Increase in H_2 Production Very Turbulent; TC Suddenly Fails Near Bottom of Bundle		1550	1823
2738	22:28	Aerosols Release, Max. Heatup Rate of 10°C/s		≥1850	≥2173
2760	22:50	Peak H_2 Production, Upper Bundle Heatup Rate Slows Down		≥1927	≥2200
2820	23:50	Steam Inlet Valves Close,		≥2007	≥2280
		region: temperature upper half of fuel: steady increase lower half of fuel: slight momentary drop then increase at slower rate upper end fittings: cool down			
2840	24:10	Turbulence Decreases		≥2067	≥2340

Table 3.2 (Continued)

Sequence of Events for Experiment DF-2

Time DAC (sec)	Video (min: sec)	Event	Max. Fuel Temperature °C	K
3000	26:50	Steam Inlet Valves Opened, upper fuel half: slight increase peak temperature reached lower fuel half: rapid increase in temperature upper fittings: heatup H_2 production: slight increase	≥2277	>2500
3030	27:20	Valves Close upper fuel half: no change lower fuel half: temp. drop H_2 production: slight drop	≥2277	>2500
3070	28:00	Valves Open and Remain Open upper fuel half: no change lower fuel half: rapid temp. increase (21°C/s) H_2 production: increases for about 20 s, then decreases turbulence increases	≥2277	>2500
3180	29:50	Full Pressure and Flow Reestablished, Max. Temp. Reached in Bottom Fuel Half	≥2197	>2470
3600	36:50	Two Upper W/Re TCs Fail	≥2052	>2325
3680	38:10	Reactor Scrammed, Inlet Valves Shut	>1700	>1973
3830	40:40	Window Steam Valves Opened and Closed Momentarily, Momentary Small Temp. Increase		
4090	45:00	Chunk of Cold Debris Covers View of Rod		
4210	47:00	Chunks of Cold Debris Fall Away, Exposing View of Rods		

two upper W/Re TCs suddenly failed, and at 38 min the reactor was scrammed. At 45 and 47 min cold debris was observed to fall out of view, exposing the hotter fuel rods below.

3.1.2 Radiographs and Photographs

Radiographs were taken of the DF-2 package about 1 week after the experiment. Many of the features observed in the DF-1 radiographs are visible in the DF-2 radiographs: rod distortion, shroud intrusion, fuel dissolution, and refrozen materials in the lower region of the bundle. Fuel damage, as indicated by these features, however, was considerably less for DF-2 than for DF-1. The pinching together of the fuel rods observed on the video monitor and film is also visible in the radiographs.

3.1.3 OMA and Radiometer

A three-dimensional plot of the Optical Multichannel Analyzer (OMA) was done. The spectrum deviates from a black-body curve fairly significantly in the visible range. This deviation is due to the formation of ZrO_2, which has an emissivity that is low in the visible range relative to the infrared and ultraviolet regions of the spectrum. Aerosols released during the experiment also influence the measured spectrum. Thus far, no temperatures have been computed from the OMA data.

Figure 3.4 presents a comparison of the W/Re thermocouple measurements with the radiometry data. The temperatures for the radiometer were obtained using very preliminary data and are inaccurate. However, this data does show an increase and decrease in temperature consistent with the thermocouple traces. The sudden changes in the radiometer indication are due to movement of the radiometer and the presence of aerosols.

3.2 ACRR LWR Degraded Core Coolability

(A. W. Reed, 6425; K. R. Boldt, 6421; T. R. Schmidt, 6421)

DCC-1 consisted of fairly small debris and examined incipient and extended dryout, and quench as a function of temperature and pressure. DCC-2 was similar to DCC-1 except that the particle size was larger and of a different particle size distribution. DCC-3 will be performed in the third quarter of 1985 and consists of a two-layer stratified bed with capability for bottom coolant feed.

The activities this quarter centered on testing and preparation of hardware and instruments for the DCC-3 experiment and obtaining capillary pressure versus saturation data in UO_2-water debris beds for use in the analysis of DCC-1 and DCC-2.

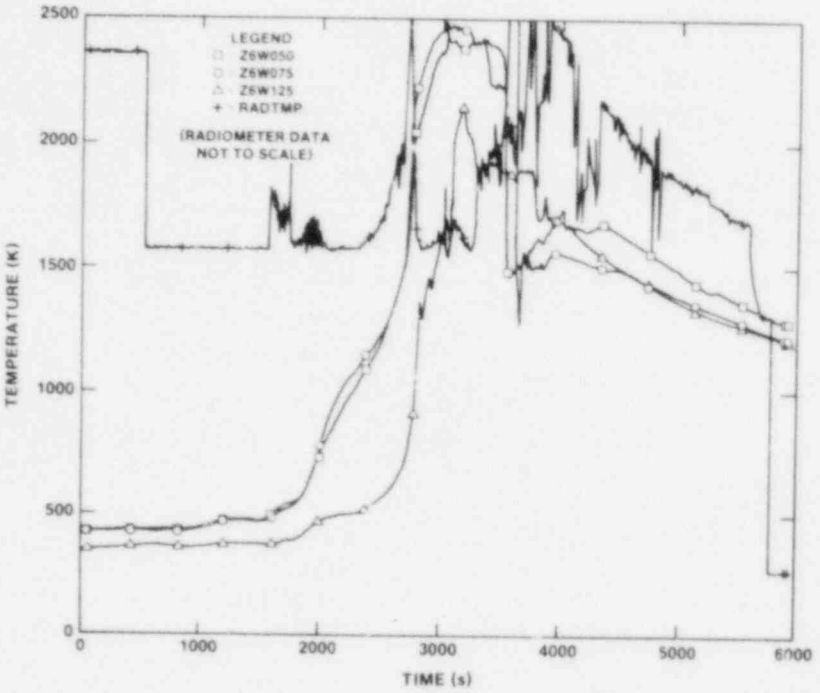

Figure 3.4. Comparison of W/Re Thermocouple Measurements With Radiometry Data

3.2.1 Capillary Pressure Measurements

One of the key components in the Lipinski model for debris bed cooling is the capillary pressure/saturation curve. This relationship describes the pressure difference between liquid and vapor phases in a porous bed, and thus is necessary to the calculation of the liquid and vapor pressure drop in the bed. Additionally, since channels are a surface tension phenomenon, knowledge of this curve is needed to calculate the channel depth. Finally, evidence suggests that liquid and vapor relative permeabilities can be deduced from this curve.

The first complete correlation of capillary pressure/saturation data was reported in 1941 by Leverett.[3.1] In his paper, Leverett demonstrated that the data for unconsolidated sand in the range of 45 μm to 180 μm could be nondimensionalized using the surface tension, bed permeability, and void fraction. After this paper, little data was generated for unconsolidated particulate beds, because the primary interest at the time was in geologic materials, and the capillary pressure is highly dependent upon the microscopic structure of the porous medium. As a result, there is a paucity of capillary pressure data for particulate beds. Because of this, a fit of the original Leverett data is used in the debris bed cooling code, DEBRIS.[3.2]

Due to the importance of the capillary pressure curve to debris bed modeling, we chose to measure capillary pressure on glass-water beds and UO_2-water beds. For beds with narrow particle size distributions, our data agreed well with that of Leverett. For beds composed of wide size distributions, the capillary pressure curve changed drastically. This change calls into question the currently-used method of calculating channel depth, which is of primary importance in the D-10 experiment. The D-10 inpile coolability experiment was conducted at the ACRR using uranium fuel and sodium as the coolant. Additionally, the work of Brooks and Corey[3.3] suggests that the relative permeabilities may also change. This may be important in the explanation of DCC-1. Measurements of capillary pressure for wide particle distributions are planned for the future.

Capillary pressure measurements were made using glass peening shot and depleted UO_2. The test section is glass buchner with a fritted disk (measured breakthrough pressure = 439 mm Hg) in the bottom. Connecting the test section and the vacuum chamber is a glass tube 2 m tall having a nominal I.D. of 8 mm. The vacuum chamber is connected to a vacuum pump with an in-line cold trap. The gauge pressure of the glass tube was measured by a water manometer for pressures up to 1000 mm of water. Pressures higher than this were measured with a mercury manometer which was read by a vertical cathotometer. The cathotometer has a resolution of 0.01 mm.

The porous bed was prepared in the following manner: A line was inscribed on the glass test section 30 mm above the top surface of the fritted disk. The test section was filled to this level with the particulate, forming a dry bed. The porosity of the bed was determined by weighing the bed before and after the loading. By knowing the particulate density (2450 kg/m^3 measured for the glass shot, 10400 kg/m^3 for UO_2), the porosity was calculable.

After the test section was connected, the top of the test section was sealed and the system evacuated. Deionized deaerated water was then introduced at the top of the glass tube and allowed to fill the particulate bed until the top of the bed was covered. The vacuum was then gently broken, and the test section sealing top was replaced with one which allowed the test section to "breath." This second top contained a moist towel which kept the humidity in the test section high, thus reducing the evaporation from the bed.

During the operation of the apparatus, the vacuum tank was kept connected to the test section. This damped the effects of ambient pressure and temperature variations. The water pressure was decreased by cracking the valve between the

vacuum chamber and the glass tube. Water then flowed from the particulate bed into the glass tube. The vacuum valve was then closed and the bed/tank system allowed to come into equilibrium. Equilibrium was determined by observing the water level in the tube as a function of time. At high saturations, the water stopped flowing within several minutes. At lower saturations, 1 or more hours were required for flow to cease.

The water pressure at the bottom of the bed was calculated by adding the gas pressure in the tube, measured by the manometers, to the hydrostatic head of the water in the tube. The saturation of the bed was determined by recording the change in the height of the water in the tube. The volume of the displaced water was calculated using the volume calibration of the tube. This was then divided by the void volume of the particulate bed to arrive at the saturation.

The remaining six particulate beds were composed of depleted UO_2. Table 3.3 summarizes the particle sizes for the experiments. Three of the UO_2 beds were composed of particles from a single sieve bin. Two of the beds were composed of mixtures of particles from adjacent bins. The sixth bed had the same size distribution found in D-10. The equivalent particle diameters for the mixtures were computed using the Fair-Hatch weighting.[3.2]

Figure 3.5 is a plot of the average capillary pressure in the bed as a function of the average bed saturation for all the tests but the bimodal distribution of glass particles and the simulated D-10 bed. The average capillary pressure is defined as the difference between the atmospheric pressure, which is constant throughout the bed, and the liquid pressure in the middle of the bed. A discussion of the error associated with using average quantities instead of point quantities is contained in the analysis section. It is obvious that the capillary pressure is highly dependent upon the particle size. But in spite of the wide range of pressures, the curves share common traits. At saturations close to unity, the breakthrough pressure is clearly defined. The capillary pressure then remains nearly constant over a wide range of intermediate saturations. At low saturations, the capillary pressure increases as the saturation approaches its irreducible value.

Figure 3.6 is plot of the nondimensionalized capillary pressure as a function of the effective saturation. The effective saturation is defined as

$$S_{eff} = \frac{S - S_{irr}}{1 - S_{irr}} \qquad (3.1)$$

Table 3.3

Experiment Particle Sizes

Test Number	Material	Size Range (μm)	Wt. %	$\bar{d}$ (μm)	ϵ	Φ	Bed Volume (cm^3)	Baseline (mm)
1	Glass	50 Mesh	100.	352.	0.379	1.00	219	129.8
2	Glass	150 Mesh	100.	122.	0.380	1.00	220	255.8
3	Glass	50 Mesh	50.					
		150 Mesh	50.	181.2	0.368	1.00	223	259.9
4 (D-10)	UO_2	2800-4000	3.6					
		2000-2800	4.7					
		1400-2000	6.5					
		1000-1400	7.8					
		710-1000	9.2					
		500-710	10.4					
		355-500	10.7					
		250-355	10.8					
		180-250	9.3					
		125-180	9.1					
		90-125	6.8					
		63-90	5.7					
		45-63	3.8					
		38-45	1.6	172.7	0.355	0.78	220	229.6
5	UO_2	250-355	100.	302.5	0.379	0.78	224	246.8
6	UO_2	1000-1400	100.	1200.	0.432	0.78	222	179.3
7	UO_2	710-1000	100.	855.	0.434	0.78	221	225.5

Table 3.3 (Continued)

Experiment Particle Sizes

Test Number	Material	Size Range (μm)	Wt. %	$\bar{d}$ (μm)	ε	Φ	Bed Volume (cm^3)	Baseline (mm)
8	UO_2	125-180	49.5					
		180-250	50.5	178.7	0.423	0.78	222	175.4
9	UO_2	355-500	50.7					
		500-710	49.3	499.8	0.403	0.78	221	216.9

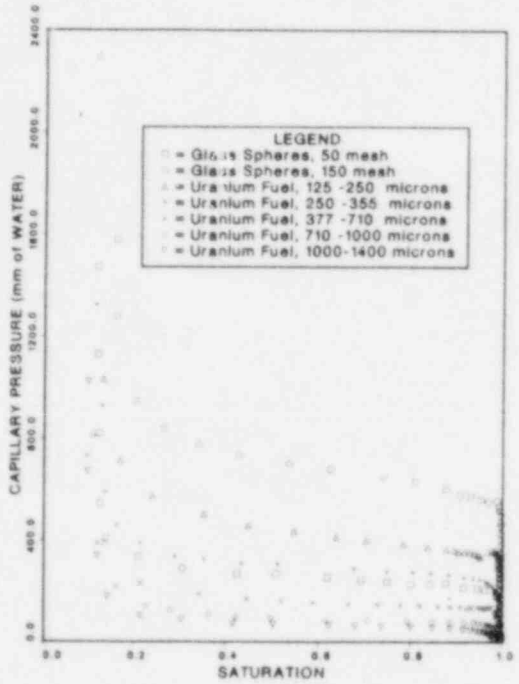

Figure 3.5. Average Capillary Pressure for Narrow Size Distributions

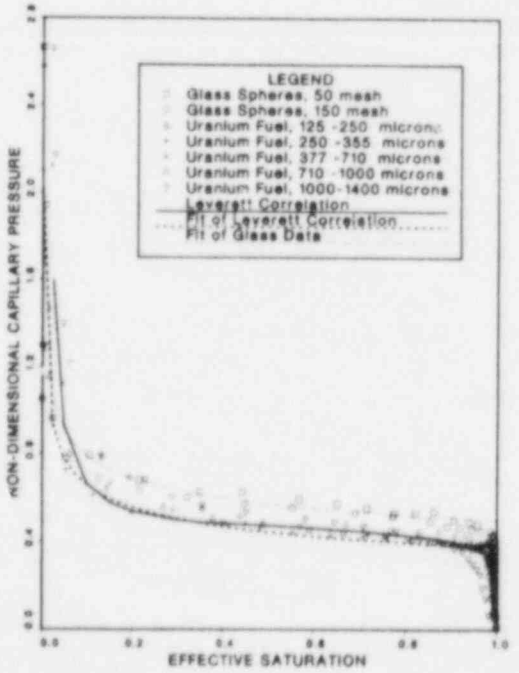

Figure 3.6. Nondimensional Capillary Pressure for Narrow Size Distributions

where S_{irr} is the irreducible saturation. The irreducible saturation was taken as the last data point at the end of an experiment.

The nondimensional capillary pressure (J) is defined as

$$J(S_{eff}) = \frac{P_c(S_{eff})}{\sigma} \frac{d\phi\varepsilon}{\sqrt{150(1-\varepsilon)}} \quad . \tag{3.2}$$

This is the form obtained when the Ergun component[3.2] for laminar permeability is substituted for the permeability in Leverett's nondimensional form. This substitution reflects the fact that Leverett measured permeabilities while we did not. The sphericity (ϕ) used for the UO_2 particles was 0.78, which is what is currently used in DEBRIS.

Figure 3.6 demonstrates that the capillary pressure data for the tests presented can be adequately described by the Leverett correlation. Most of the data lies above the correlation. This is probably because of the difference in nondimensionalization. The choice of nondimensional forms is a matter of convenience. Neither conforms strictly to the requirements of similarity. But as long as the correlation is confined to particulate that is roughly spherical, the correlation should be adequate.

A deviation from the correlation is seen in the D-10 capillary pressure data (Figure 3.7). The problem is not merely one of choosing the proper effective diameter. Changing the effective diameter would displace the curve vertically, but would not change its shape. The data is demonstrating that the pore size distribution of a mixture is very different than that of uniform beds. Since the nondimensionalization is based on the average hydraulic radius, it cannot account for the differential quantity of distribution.

The data generated by this set of measurements has indicated that our knowledge of the capillary effect in the dryout of debris beds is not as complete as was previously thought. Predictions for beds having a narrow particle size distribution will not be greatly affected by the new data. Predictions for beds having broad distributions may be changed.

The D-10 experiment contained particles ranging from 40 μm to 4000 μm. The major uncertainty in the predictions for D-10 was in the channel depth.[3.4] The code DEBRIS predicts channels which are too long. This results in an overprediction of dryout power by about a factor of 3. If the model is modified to reflect the lower bound on channel depth, the resulting predictions are about a factor of 2 too

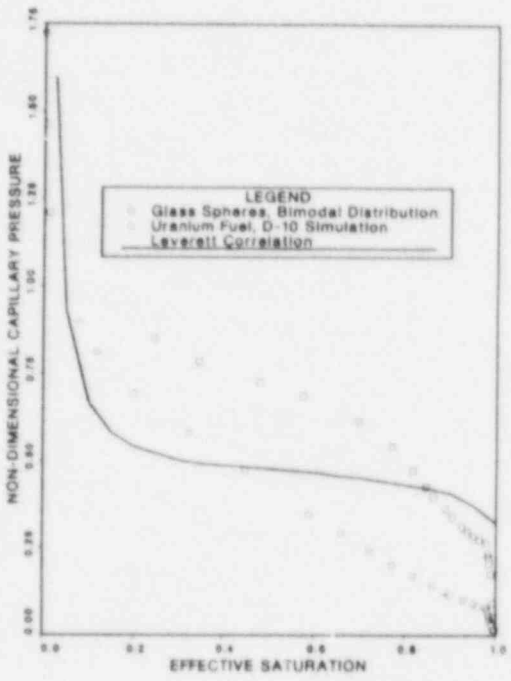

Figure 3.7. Nondimensional Capillary Pressure for Broad Size Distributions

low. An understanding of the physics of channeling in mixed beds is necessary to the successful prediction of D-10 results, and the capillary pressure data is a key part of that understanding.

As was stated in the introduction, Brooks and Corey demonstrated that the relative permeabilities could be related to the capillary pressure/saturation data. The data presented here suggests that the effect of this change on dryout flux should be investigated. A measurement of capillary pressure for the DCC-1 bed is planned for the near future. It is hoped that relative permeabilities derived from this measurement will shed light on the pressure dependence observed in the DCC-1 experiment.

3.2.2 DCC-3

During this period the primary and secondary containments and the crucible have been received and inspected. Most of the other hardware and instrumentation has been received and is in inspection and testing. A proof test vessel for testing the plumbing for the bottom coolant feed pumping and measurement system has been fabricated and proof tested to 7000 psi. This will be used at 3000 psi pressure up to temperatures of 350°C. Manufacture of the doubled-walled

cooling coil has been delayed because the bids were 3 times higher than expected. The UO_2 fuel order is 80 percent complete with the final 5-8 kg to be finished next period.

3.3 References

3.1 M. C. Leverett, "Capillary Behavior in Porous Solids," Trans. A.I.M.E., 142, 1941.

3.2 R. J. Lipinski, A Model for Boiling and Dryout in Particle Beds, Sandia National Laboratories, SAND82-0765, NUREG/CR-2646, 1982.

3.3 R. H. Brooks and A. T. Corey, "Properties of Porous Media Affecting Fluid Flow," J. Irrigation and Drainage Division, ASCE, June 1966.

3.4 A. W. Reed, An Analytical Update of the D-10 Experiment, memo to W. J. Camp, 1985.

4. MELT PROGRESSION PHENOMENOLOGY

(J. E. Kelly, 6425; P. J. Maudlin, 6425; J. L. Tomkins, 6425; M. F. Young, 6425; W. J. Camp, 6425)

4.1 MELPROG Code Development

Work continued on modifying the code to allow the incorporation of the new 2-D FLUIDS module. This work simply involves modifying the data transfer sections of each module. However, a new routine was developed to calculate 2-D fluid flow areas, 2-D hydraulic diameters, 2-D cell fluid volumes, and 2-D structure volume fractions. The routine has been completed and is currently being tested and debugged.

Also, the code was reoverlayed to allow it to be run on the CDC 7600 computer with the new 2-D FLUIDS module. The main development task was making a new input module that combines the input sections of the other modules.

A two-dimensional continuity package for decomposing the corium field into seven components has been developed and incorporated into FLUIDS. The components included are UO_2, Zr, ZrO_2, stainless steel, eutectic, control rod material, and poison rod material. With this package the specific composition of the corium field can be followed during the calculation.

In order to maintain consistency in the code, the number of components treated in the DEBRIS module has also increased. DEBRIS treats the same components as FLUIDS, except for the poison rod material. An equation of state and a continuity equation are solved for each of these components. The relocation of the various components is also correctly treated.

A new routine has been written to calculate the local corium distribution on a two-dimensional basis. This routine is only needed for the 1-D version, since th 2-D code will automatically calculate this distribution. This new routine was needed to allow the debris bed formation model to function properly.

Work continued on developing the VICTORIA fission-product module. Presently, the code has a driver routine that integrates three physics modules: an aerosol behavior module (MAEROS); an equilibrium chemistry module (VCS); and a two-dimensional species continuity module. Work on a fuel release model and testing of VICTORIA has been initiated.

The documentation of the initial version of MELPROG is nearly complete. This document describes the physical modeling in the code in detail and will form the basis for a code user's manual.

4.2 Model Verification

The mechanical models used in the STRUCT module are in the process of being evaluated against more detailed models, in this case the JAC finite element code. JAC is a 2-D code with rx or xy geometries developed in the Applied Mechanics Division at SNLA.

The evaluation has been completed of the plate cell model used to describe perforated plates supported at regular intervals, such as the lower core grid plate. Test included loading at a given plate average temperature and loading with a temperature gradient through the plate thickness. The conclusion of this work was that the assumptions behind the MELPROG model are correct; namely, the grid plate is under low stress and will fail close to the melting point. The presence of a temperature gradient through the plate does not make a significant difference, since, under low stress, the colder part of the plate can hold the load given up by the hot part; this justifies the use of average temperatures in the plate cell model as the input temperature to the mechanical property routines and to the Larson-Miller Parameter routine.

The creep equations for SS304 were also evaluated for the stresses to which the grid plate is subjected over a temperature range from normal operating temperature up to slightly below melt. The result was that creep is very slight over the time scale of interest (a few hours), even at temperatures close to melt. This phenomenon seems to be taken into account by the creep-rupture failure criterion used in MELPROG.

5. ADVANCED REACTOR ACCIDENT ENERGETICS

5.1 Initiation Phase

(S. A. Wright, 6423; P. S. Pickard, 6423; G. Schumacher, 6423)

The third STAR experiment was performed. This was the first STAR experiment to use preirradiated fuel. The purpose of this experiment was to examine fuel and clad motion behavior in an irradiated fuel experiment that reproduced ULOF accident heating conditions.

5.1.1 STAR-3 Geometry and Fuel Type

The STAR-3 capsule was nearly identical to that of the earlier STAR experiments. The major differences were the size of the pin bundle (2 pins) and the location of the mirrors used to view the fuel pins. Figure 5.1 shows the fuel pin bundle and the four views of the pin bundle as seen from above (or as seen by the camera). Two of the images show front and back views of the fissile fuel pin section, and the preirradiated fuel pin is on the inside of the front and back images. Henceforth, these images are denoted as FF and FB. The third image views the transition zone of the fuel pin as seen from the preirradiated fuel pin side (denoted as T, for transition from fuel to blanket), and the last image views the blanket region of the pin bundle from the fresh fuel pin side. (This image is denoted as B.) Figure 5.1 also shows that the bottom of the enriched fuel pin section is placed at the axial centerline of the ACRR.

A cylindrical quartz tube enclosed the fuel pin bundle. The quartz tube had an I.D. of 18 mm and an O.D. of 20 mm. Unfortunately, this results in a large hydraulic diameter of 8.3 mm compared to a prototypic hydraulic diameter of 3.2 mm with wire wrap, or 4.2 mm without wire wrap. (An attempt was made to fabricate an oval-shaped tube to improve the hydraulic diameter, however, the cost and delivery time for these tubes was unacceptable.)

The STAR-3 experiment contained a fresh fuel pin and a preirradiated fuel pin. The preirradiated fuel pin was the lower portion of the EBR-II irradiated PNL10-60 fuel pin. This pin used mixed oxide fuel, had an effective enrichment of 67 percent, a burnup of 5.7 a/o, and a linear heat rating of 26 kW/m. Table 5.1 lists more details of this fuel pin. Pin preparation was performed by sectioning the PNL10-60 into two 16.4-cm-long sections. The lower section was used in this experiment. Once cut, a few mm of the ceramic MOX fuel was removed from both ends of the fuel pin by core drilling to allow the insertion of end plugs. The end plugs were then welded to the irradiated cladding sealing the fuel inside the clad. The pin sections used in the earlier FD experiments were not sealed. Argon at 0.84 bar was used as

Table 5.1

PNL10-60 Preirradiated Fuel Pin Characteristics

Theoretical Density	11.02 g/cm^3
Fabrication Porosity	9.1%
Smear Density	85.5%
PuO_2 Fraction	25%
UO_2 Fraction	75%
U-235 Enrichment	65%
Pu Enrichment	88% (^{238}Pu + ^{242}Pu)
Peak Burnup	5.7 a/o
Peak Linear Heat Rating	255 w/cm
% Fission Gas Release Total Gas Content	70.8 1.1×10^{26} $atom/m^3$
Diameter of Fuel	4.927 mm
I.D. of Cladding	5.080 mm
O.D. of Cladding	5.842 mm
Cladding Type	316 SS, 20% CW

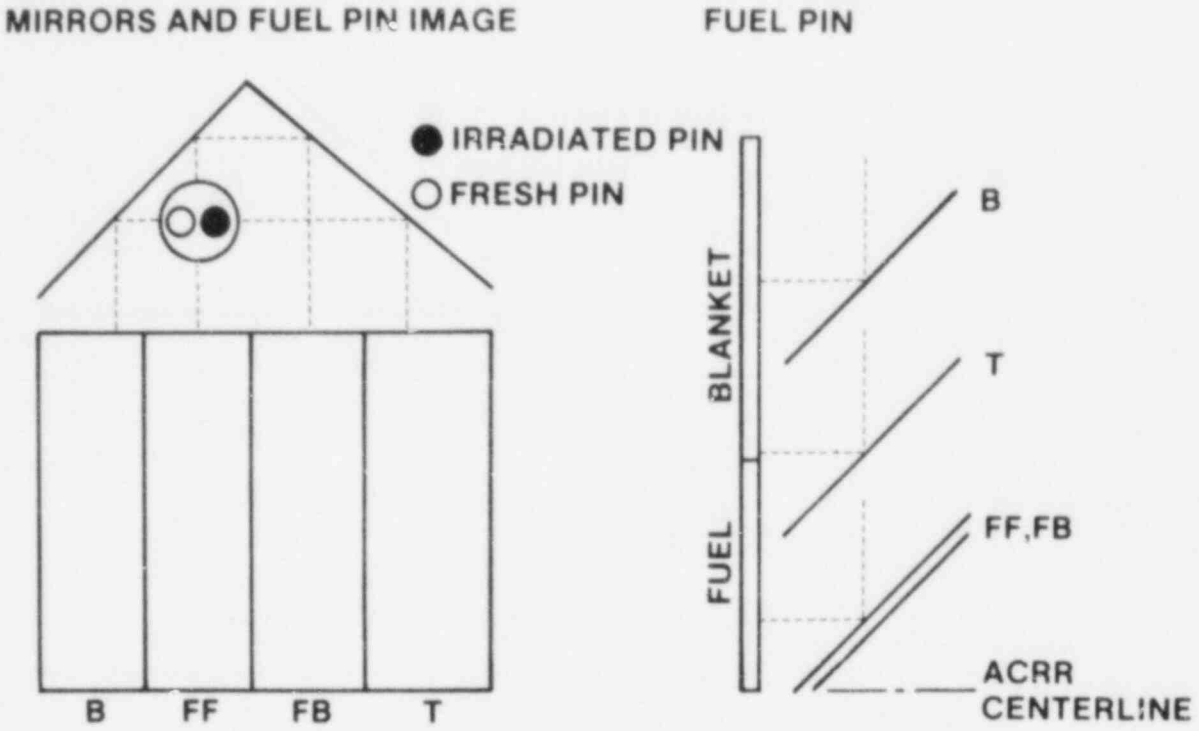

Figure 5.1. View of Two Pins and Location of Imaging Mirrors for STAR-3

the fill gas in the glove box; thus, it is also the fill gas captured in the gap of the pins. Since the end caps had threaded ends, they were screwed to upper and lower extensions to give the fuel pin an overall length of 66.2 cm. In addition, the pin was mounted upside down so axial location of the highest burnup was at the axial centerline of the ACRR. Care was taken in all stages of the pin fabrication to assure good conductivity through the pin cladding so that the electrical preheating would raise the clad temperature to the desired level.

The fresh fuel pin had an enrichment of 66 percent, otherwise it was identical to the pins used in the earlier STAR experiments. The fill gas in the fresh pins was helium at 0.8 bar in contrast to the argon used in the preirradiated fuel pin.

5.1.2 STAR-3 Experimental Conditions

A few hours prior to the actual experiment, a "calorimeter" experiment was performed to determine the coupling factor between the pins and the ACRR. The fresh fuel pin had five thermocouples welded to the cladding. Four of these thermocouples were on the enriched fuel section and the fifth in the upper axial blanket. A small reactor pulse of 30 MJ was used to deposit energy in the fuel. The magnitude of the

temperature rise due to the reactor pulse was then used to determine the coupling factor. A coupling factor of 9.74 J/g/MJ at the bottom of the fuel column was determined. Near the top of the fuel column the coupling factor was 8.04 J/g/MJ (83 percent of the maximum). These values were significantly lower than the TWOTRAN calculated coupling factors, which were predicted to be near 13 J/g/MJ. Because of these lower-than-expected coupling factors, the nuclear preheat was lengthened to clad melting while at nominal power and prior to fuel melting. All of the calorimeter data has not been analyzed at this time, so it will be reported later. The coupling factor measurement technique worked well, and we estimate that the uncertainty in the measurement is $\pm$4 to 8 percent

The STAR-3 experiment required the coordinated timing of electrical preheating, motors, lights, cameras, data acquisition, and the reactor pulse. Table 5.2 lists the times when these events occurred during the experiment sequence.

Table 5.2

Time Sequence for Starting Motors and Cameras

t = 0.000 s	Start Count Down
t = 0.010 s	Start Electrical Heating
t = 30.000 s	Start of Slow Data Acquisition (200 samples/s)
t = 49.40 s	Stop Electrical Heating
t = 64.00 s	Start Backlights
t = 64.50 s	Start Blower
t = 66.00 s	Start Cameras
t = 70.000 s	Start ACRR Power Transient and Fast Data Acquisition (4000 samples/s)
t = 78.000 s	End Fast Data Acquisition
t = 120.00 s	End Slow Data Acquisition

The data acquisition system recorded 23 data signals including thermocouples, a flow meter, inlet and outlet pressure transducers, reactor power monitors, and a watt meter. This instrumentation was nearly identical to the STAR-2 experiment

and, consequently, is not discussed further. Some changes were made in the data acquisition system, however. Three physical devices were used to record the data. One device was a high-speed transient digitizer that recorded eight channels of data at 4000 samples/s. The other device was a similar digitizer that was multiplexed to record 16 channels at 200 samples/s, and the third device was a scanning relay system that recorded 12 channels of data at 4 samples/s. The scanning relay system was capable of displaying the data real time; thus we were able to observe the initial preheat stages of the experiment. This was especially valuable in assuring an adequate electrical preheat.

In addition, a single color pyrometer was used to measure fuel surface temperature during the reactor transient. However, very little information was recorded by this device because of the limited amount of clad motion that occurred during the experiment. The fuel and clad relocation behavior was recorded by two cameras. Both cameras triggered and ran through completion of their film rolls, and the recorded image on the film had a good exposure.

Before describing the experimental data, some of the initial conditions are described. This data, along with more detailed data, is given in Table 5.3. The capsule was originally filled with 0.56 bar of argon 305 K, and the inlet gas flow velocity was 30 m/s. The pressure drop through the bundle was 31 kPa and increased to 36 kPa once fuel and clad motion began.

5.1.3 STAR-3 Results and Data Description

The electrical preheat began at 0.0 s, and deposited 1.5 kW in the cladding of each fuel pin. By 49 s, the cladding temperatures had reached 1340 K. To prevent possible clad melting due to continued heating, the electrical heating was manually turned off. Figure 5.2 shows the cladding temperature as measured by a thermocouple located 12 mm above the bottom of the enriched fuel column of the fresh fuel pin. Due to the extended time before the start of the reactor transient (22 s), the fuel pin cooled substantially as shown in Figure 5.2. Also shown in this figure is an increased rate of cooling due to the starting of the blower at 66 s. When the reactor pulse began at 70.000 s, the cladding temperatures were 1040 K. Thermocouples near the top of the fuel zone indicated temperatures near 1100 K.

The ACRR power transient for this experiment is shown in Figure 5.3. Also shown are the times of a few major events such as the start of fuel disruption and fuel melting. The power transient consisted of a nominal power (P_o) nuclear preheat that lasted for 6 s (70.0 to 76.0 s) followed by a slow to moderate increase in power to 5 x P_o. Nominal power

Table 5.3

Initial Conditions at Start of ACRR Transient

Coupling Factor	9.74 J/(g * MJ)
Total Number of Pins	2
Number of Preirradiated Pins	1
Effective Enrichment	67%
Gas Inlet Temperature	305 K
Gas Inlet Pressure	58 kPa
Inlet Flow Velocity	30 m/s
Quartz Tube I.D.	18 mm
Hydraulic Diameter	8.2 mm
Electrical Preheat Temperature	1035 K

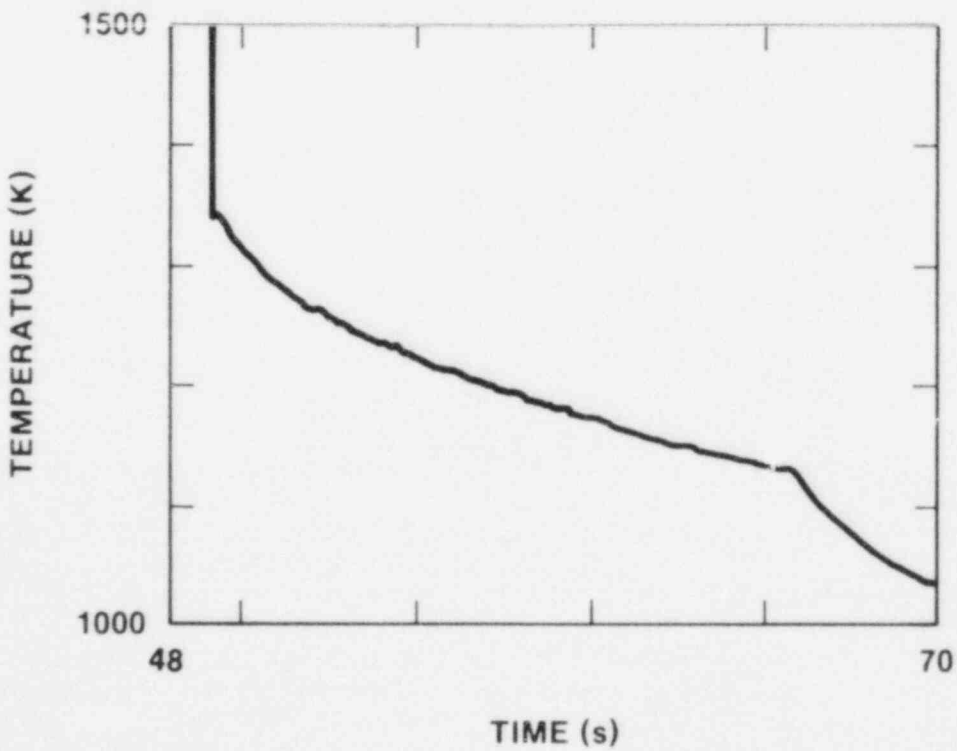

Figure 5.2. Clad Temperature at Bottom of Fuel Zone Just After the Electrical Preheat and Prior to the ACRR Transient

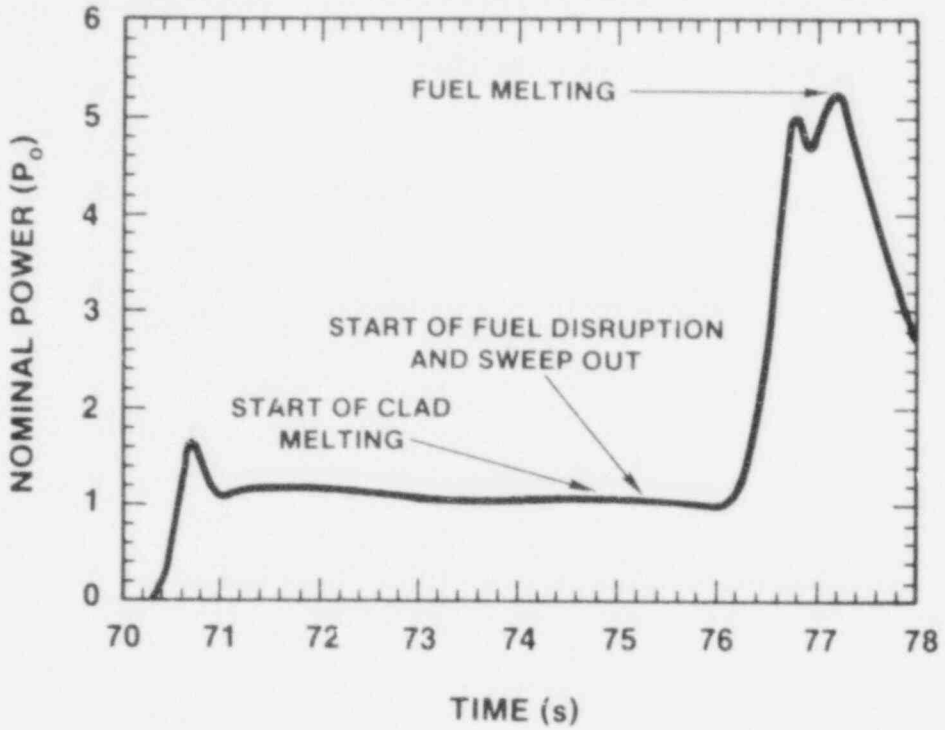

Figure 5.3. Measured Power Transient for STAR-3 (Nominal power is 150 w/g)

power in this report is assumed to be 150 W/g or about 300 W/cm. This power transient was designed to cause clad melting near 74 s, and allow enough time for clad motion to occur prior to fuel disruption. As mentioned earlier, fuel disruption was expected to occur because of fuel melting (at 77.0 s) and fission gas-induced fuel frothing and foaming. Instead, very early fuel breakup and axial sweepout were observed.

The following paragraphs describe the observed results. Photographic prints of selected frames from this experiment are reproduced in Figure 5.4. Also of interest are the SANDPIN calculated temperature histories given in Figure 5.5 and the times of the observed major events given in Table 5.4. The temperature calculations (for various radial locations in the fuel pin and at the bottom of the fuel zone), were performed using the precalculation input parameters except for the coupling factor and the reactor power transient which used the actual measured values. Thus, the model is essentially a precalculation, except for the coupling factor and the power transient. In addition, the geometric model for these calculations used a single-pin model (rather than two pins) so some care should be used in generalizing results based on these data.

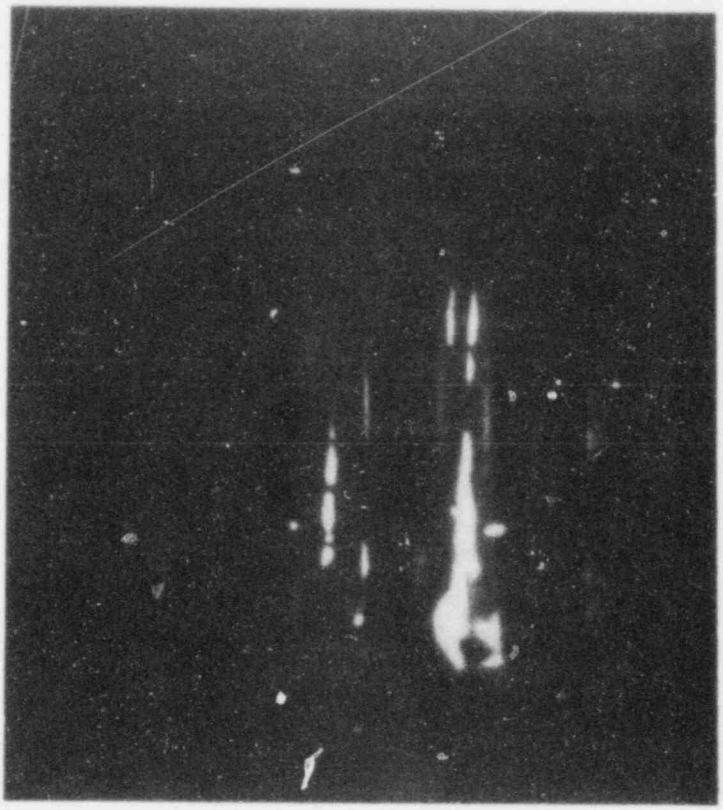

Figure 5.4a. Fuel Crumbling, t = 75.232 s

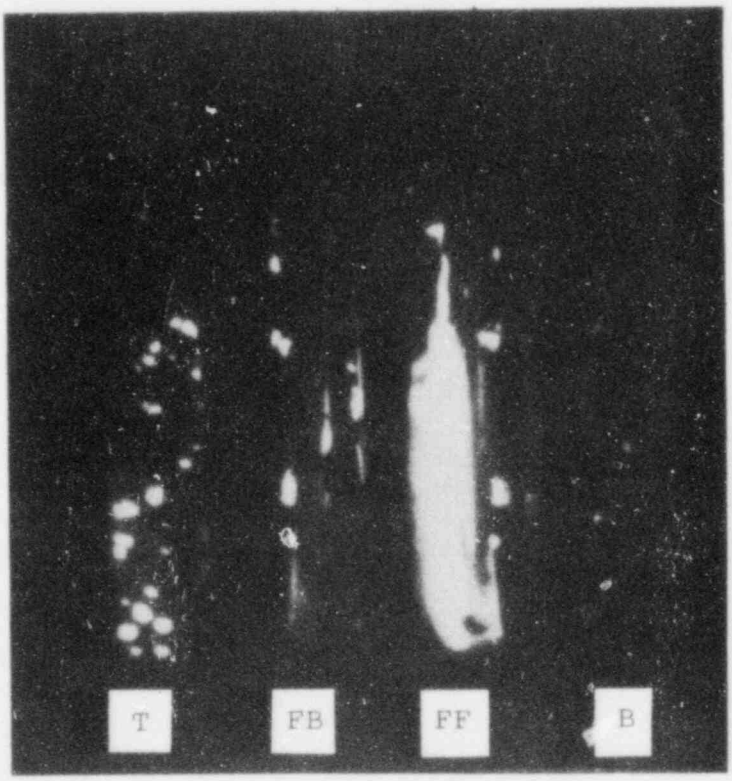

Figure 5.4b. Crumbling and Sweepout, t = 75.341 s

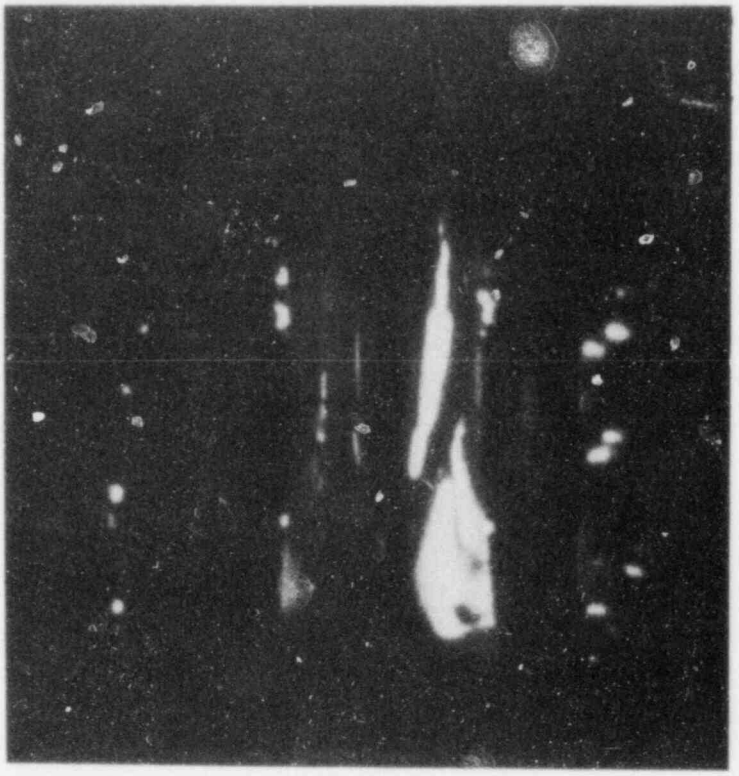

Figure 5.4c. Clad Peeling, t = 75.382 s

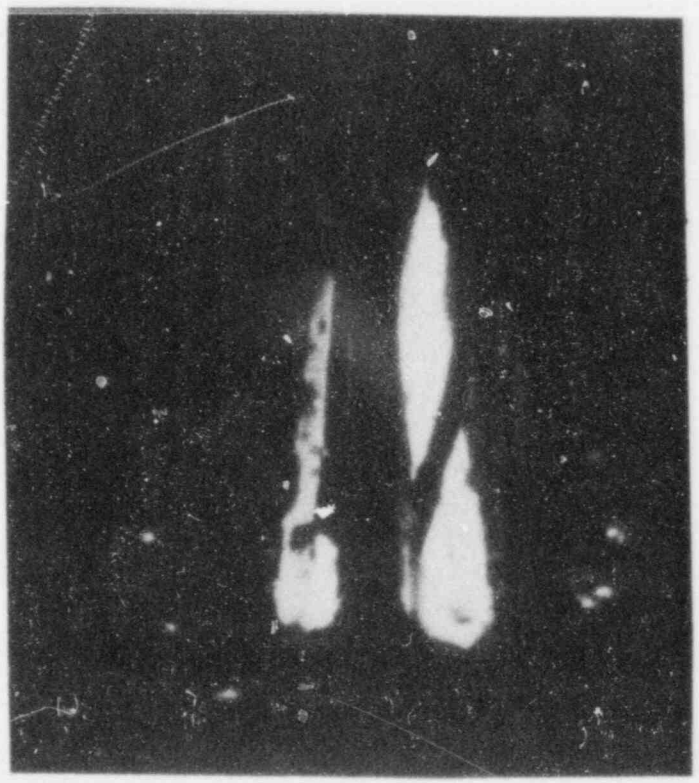

Figure 5.4d. Clad Drops on Fresh Fuel, t = 76.024 s

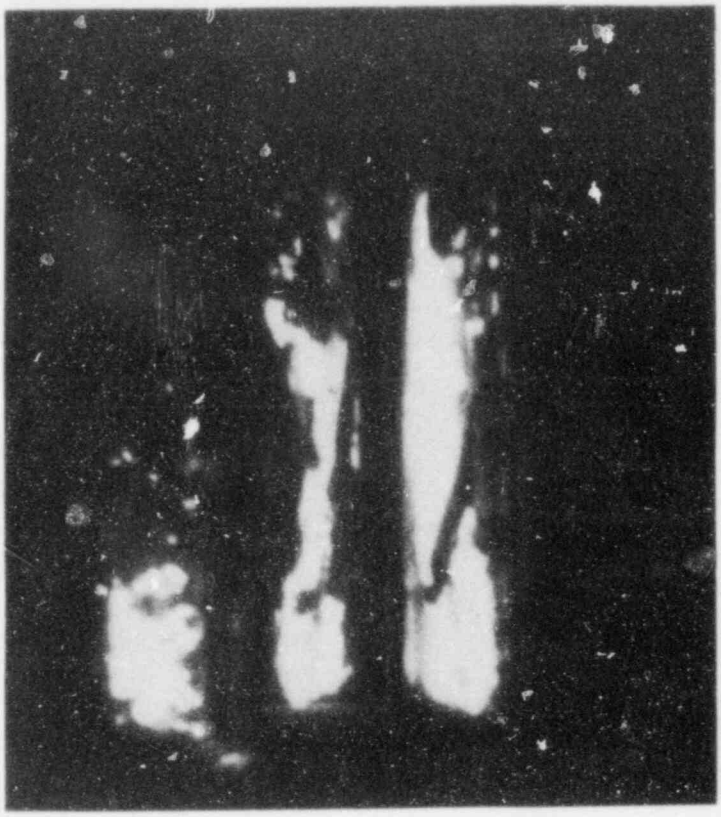

Figure 5.4e. Crumbling in Transition Zone, t = 76.459 s

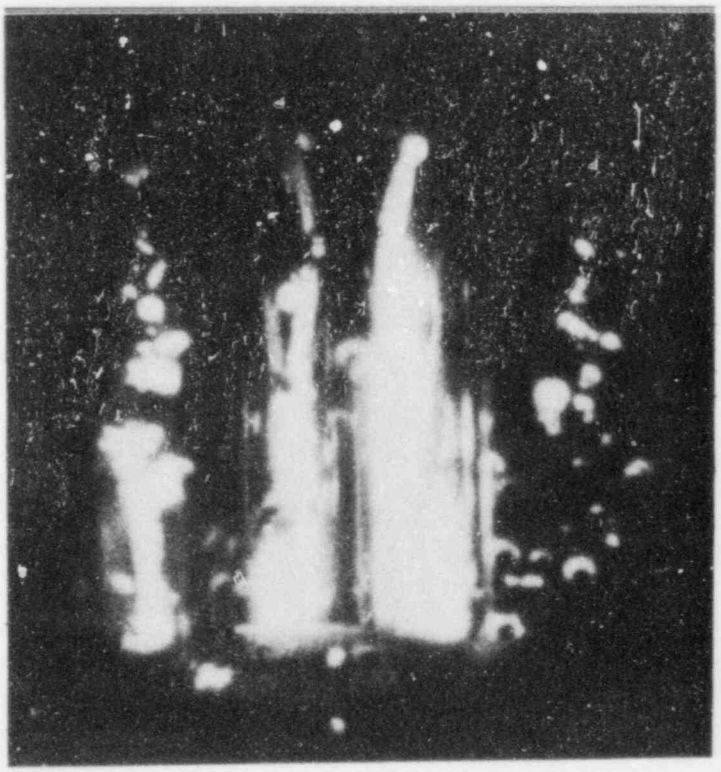

Figure 5.4f. Fuel Melting and Sweepout, t = 76.867 s

Table 5.4

Time Sequence for the Major Events as Observed in the STAR-3 High-Speed Film

	STAR-3 EVENTS	TIME (s)
1.	Aerosol appears at bottom of fuel column, fuel pins are visible (glowing) a dull orange.	73.699
2.	Image of brightly glowing cladding, twisted fuel pins are visible.	74.523
3.	Aerosol ejection through the irradiated fuel pin cladding about 4 cm above the bottom of the fuel column on the back image.	74.564
4.	Clad melting. The bright spot above the aerosol spot is a rip in the cladding on the irradiated fuel pin. Beginnings of clad droplet formation on the back image, and also on the front image. ($T_{clad} \simeq T_{solidus}$)	74.625
5.	Clad melting and drop formation are more pronounced.	75.064
6.	More clad melting. A fuel particle is ejected about 2.5 cm above bottom on the back image. Particle ejection is from the preirradiated fuel pin. Very clear drop formation and pin bowing are visible. Transition region is now visible. Two pins are visible when only one should be. Clad melting extends 8-9 cm.	75.191
7.	Fuel disruption, and entrainment. Cladding begins to rip open and large fuel particles (1-3mm) fall out and are entrained "crumbling." Some evidence of clad bridging.	75.232
8.	Continued ripping and fuel crumbling with sweepout. Entrained velocities (v = 2-3 m/s).	75.272
9.	Continued clad ripping and fuel crumbling, entrained fuel particles are in transition zone; some particles are entering the blanket zone.	75.341
10.	Clad peels from the fuel with continued fuel crumbling and sweepout. Initial fuel removal has slowed.	75.382

Table 5.4 (Continued)

Time Sequence for the Major Events as Observed in the STAR-3 High-Speed Film

	STAR-3 EVENTS	TIME (s)
11.	Entrained fuel particles escape flow channel through the top. Cladding is forming large drops on the fresh fuel pin which is still intact.	75.450
12.	Mature clad drop formation on fresh fuel pin, drops are 10 mm long and 5 mm high. Bowed fresh fuel pin overlays irradiated fuel pin. Pellet interfaces are visible on fresh pin. Clad melting in the lower portion of the transition region begins (10 cm from bottom).	76.024
13.	Clad melting on fresh pin extends entire length of fuel height. Preirradiated pin clad melting in transition zone is observed. Direct view shows distinct pins.	76.398
14.	Clad removal on irradiated pin in transition zone begins and fuel crumbling and sweepout occur. Large drops of cladding are on fresh pin in the back image.	76.459
15.	Crumbled fuel from transition zone is swept out of channel.	76.500
16.	Apparent fuel melting and increased fuel motion.	76.867
17.	More fuel melting and motion.	77.076
18.	Definite fuel melting.	77.115

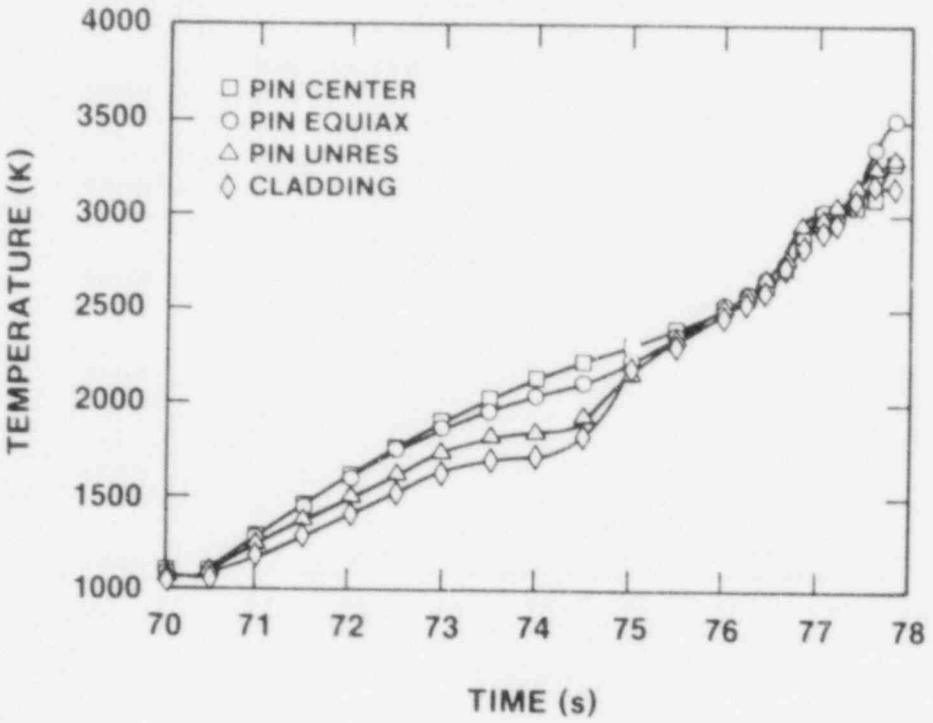

Figure 5.5. Calculated Temperature Histories at Various Radial Locations at the Bottom of the Fuel Zone

Several surprises occurred in this experiment. Clad melting and relocation were expected well before fuel disruption and melting. Early clad melting was indeed observed (t = 74.62 s). However, it was preceded by an early ejection of aerosols. The first aerosol ejection was observed very early at 73.70 s which, according to the thermal calculations given in Figure 5.5, corresponded to clad melting (the cladding was passing through the heat of fusion). Even though the gas flow through the coolant channel was near 30 m/s, this aerosol plated out on the quartz tube and appeared as a dark spot on the lower portion of the FF image. The dark spot was apparent throughout the remainder of the experiment. The second and more prominent aerosol ejection (t = 74.625 s) occurred just after the cladding exceeded the liquidus temperature. Unlike the first aerosol ejection, this one remained visible for only 1 to 2 ms and then was swept completely out of the channel.

Shortly after clad melting occurred, the cladding began to form drops and waves as in all of the previous experiments; however, no clad motion occurred. Then at 75.19 s a few particles of fuel (less than one mm in diameter) were

ejected from the preirradiated fuel pin (Figure 5.4c). These particles were then quickly swept upwards out of the fuel zone.

One should also note that the pins were twisted. This twisting was not apparent at the beginning of the transient, so it can be presumed that it occurred because of the thermal expansion or possibly some influence of the original wire wrap. The wire wrap, which was not present during the STAR experiment, was originally twisted around the pins with a pitch of 30.4 cm.

At 75.23 s a long strip of cladding ripped open (over a length of about 5 cm), and the fuel fell into the coolant channel and was swept axially out of the coolant channel. The fuel particles had diameters from 1 to 3 mm, and it appeared that they came only from the unrestructured region of the fuel pin. Photographs of the original fuel showed that the unrestructured zone was heavily cracked, probably due to cool-down effects after the initial irradiation in EBR-II.

This kind of fuel disruption resembles "crumbling" because the fuel particles were not driven out of the fuel matrix. We will refer to this behavior as crumbling to distinguish it from the "cracking" type disruption in which the fuel particles are forced from the fuel matrix. (The cracking type of fuel disruption was achieved in experiment STAR-4.) During the next several hundred milliseconds, the fuel continued to crumble and the fuel particles were swept upwards out of the fuel zone at velocities of 2 to 3 m/s. This "crumbling" and sweepout occurred while the pin power levels were still very low (approximately 1 x P_o), and all of the fuel was still solid. This process of fuel crumbling and sweepout occurred axially up the entire length of the fuel pin. At 75.6 it was observed in the transition (T) zone. The irradiated pin as seen in the FF and FB images is the inside pin.

Shortly after the onset of fuel disruption and sweepout, continued clad melting was observed. However, very little clad relocation was observed. Instead, a long strip of cladding peeled away from the irradiated fuel pin column. The strip was approximately 7 to 8 cm long (t = 75.38 s). Later (t = 76.024), very clear drops of molten cladding were observed on the fresh fuel pin, but not on the irradiated pin. In addition, there was no axial cladding relocation on the fresh fuel pin. Two phenomena were occurring: (1) cladding drop formation began on the fresh pin as in the earlier fresh fuel experiments, but because it was a two-pin experiment with a large hydraulic diameter, bypass flow occurred and no axial clad relocation was observed; and (2) no clad relocation was observed on the preirradiated pin because the fuel surface breaks up at the start of clad

relocation. Thus, there was no substrate upon which the cladding could move. It also appeared that the initial drop formation on the irradiated fuel was altered due to the presence of fission products because of the clad ripping and peeling that occurred. This could also be caused by internal pressure effects due to the sealed pin.

Late in the experiment, near the peak of the power transient at t = 77.13 s, fuel melting was observed in what fuel remained. At this time even more axial fuel sweepout was seen. This is due to local fuel frothing caused by fuel melting and results in very large volume increases (6 to 10 times the original volume). Such large amounts of swelling cause fuel which is not completely molten to break up and be swept out. This behavior was clearly seen in the FD 2.6 experiment. It is difficult to estimate the amount of fuel that was swept out of the fissile fuel zone, but it appears to be greater than 40 to 50 percent of the preirradiated fuel pin.

The responses of three in-core diagnostic devices are also useful in interpreting the observed fuel and clad motion. These devices are a thermocouple, the pressure drop through the channel, and the flow rate through the channel. Their responses during the ACRR power transient are given in Figures 5.6, 5.7, and 5.8.

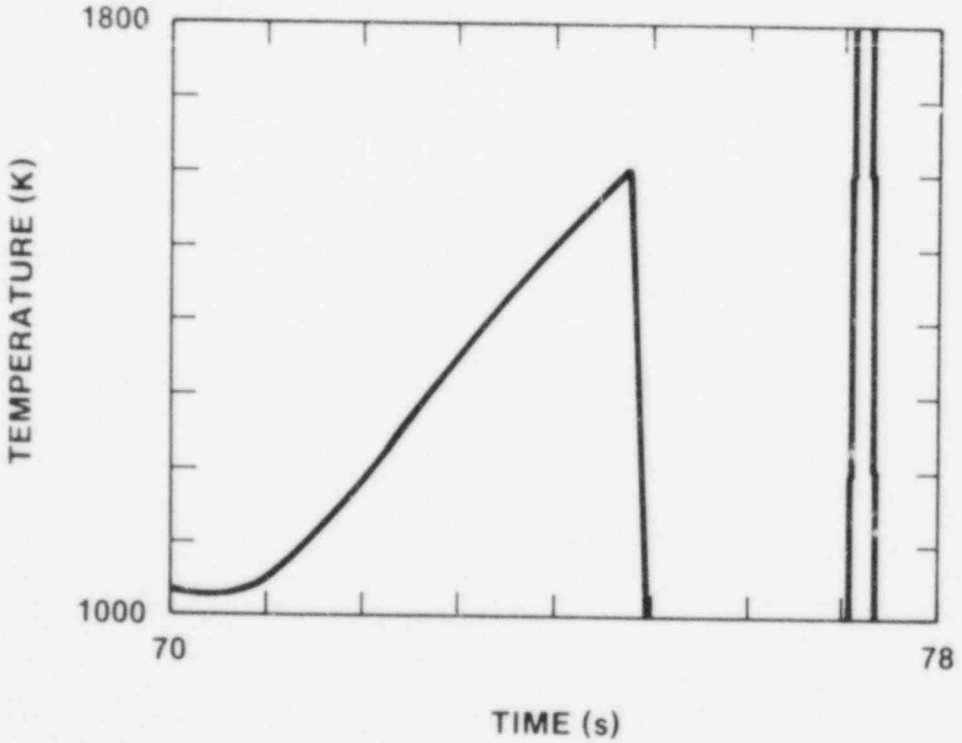

Figure 5.6. Measured Temperature of Cladding at the Bottom of the Fuel Column During the ACRR Power Transient

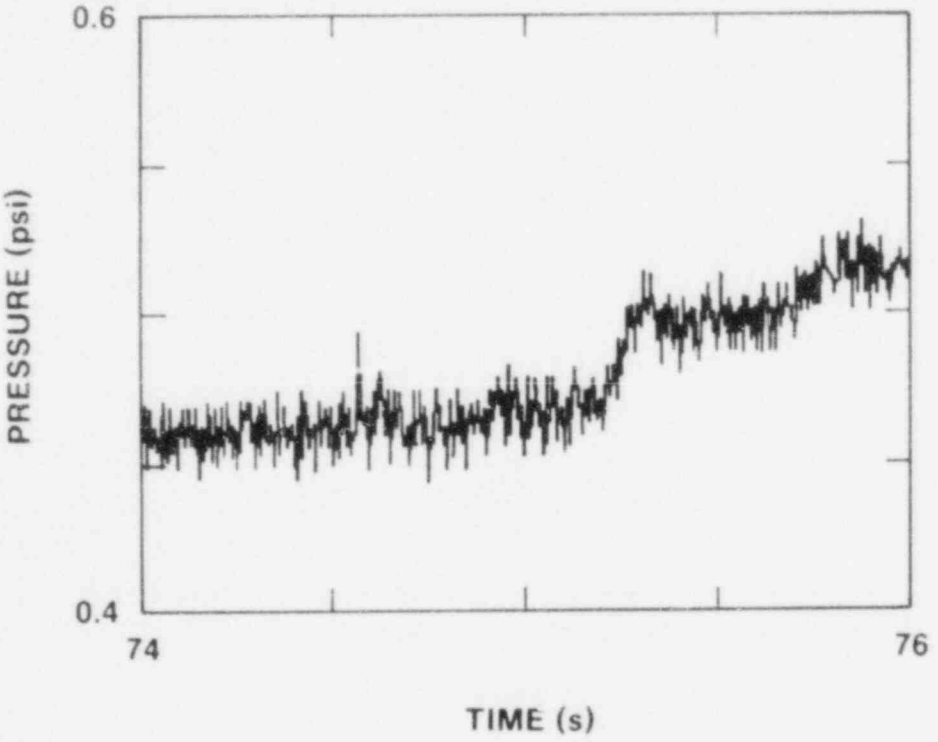

Figure 5.7. Measured Pressure Drop Across the Coolant Channel During the ACRR Power Transient

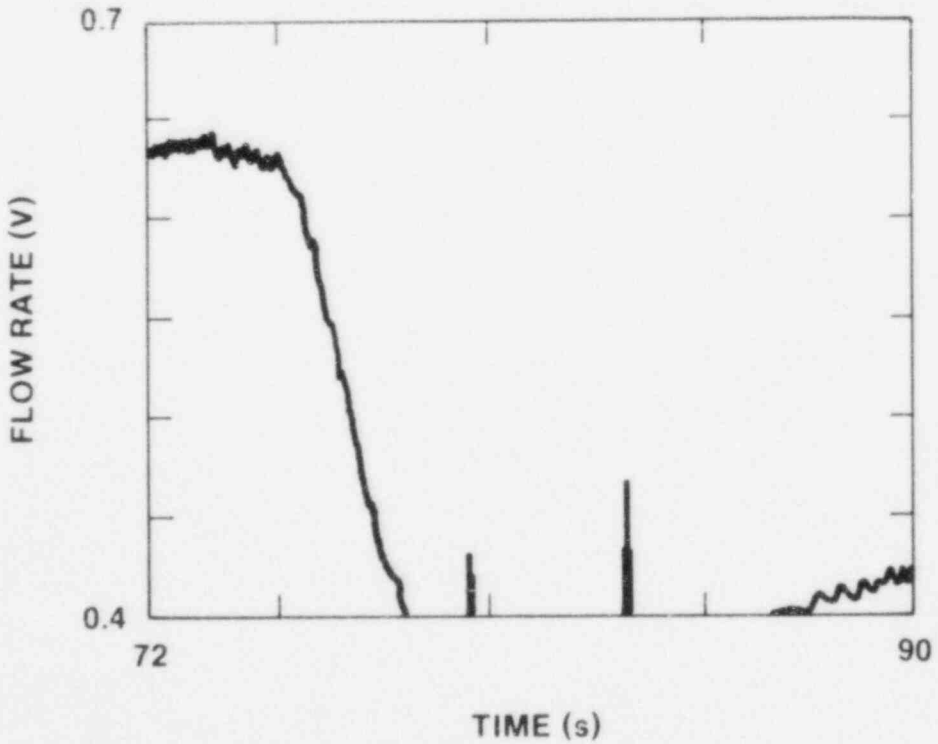

Figure 5.8. Measured Flow Rate and Conversion Equation to Give the Inlet Coolant Velocity for STAR-3

Figure 5.6 shows the thermocouple response to the reactor power transient from t = 70.0 s to 78.0 s. This thermocouple was welded to the cladding of the fresh fuel pin about 12 mm above the bottom of the enriched fuel section. The figure shows that the initial electrical preheat raised the clad temperatures to 1040 K, and beginning at 71 s the temperature begins to increase at steady rate due to the nominal power nuclear preheat. At 74.8 s the thermocouple becomes dislodged from the cladding due to incipient melting. The measured temperature at this time was 1600 K, while the calculated temperature was 2000 K. This discrepancy is probably due to some inaccuracies in the SANDPIN model, such as a lower gap conductivity through the irradiated fuel pin than modeled. This inaccuracy is consistent with the observations made in the films since they indicate (see Table 5.4) that at 74.6 s the cladding is near the clad solidus temperature.

Figure 5.7 shows the measured pressure drop through the flow channel. The pressure drop is about 0.45 psi until 75.3 s, when it increases to 5.0 psi. This increase in pressure corresponds to the fuel disruption and sweepout observed in events 7 through 10 in Table 5.4. The results of the measured flow rate, see Figure 5.8, are also consistent with this data. At 75.5 s a very rapid decrease in the flow rate is observed. Initially, it was 30 m/s, and then it decreased to almost half this value. If this was caused by a reduction in the flow area, then the constriction would have to reduce the flow area by 50 percent. The figure also shows that the flow recovers somewhat, but this is probably due to cool-down effects late in time. The flow never fully recovers.

5.1.4 Conclusions and Discussion of the STAR-3 Experiment

The crumbling mode of fuel disruption was not predicted by the SANDPIN/CMOT fission gas analysis. Figure 5.9 shows the SANDPIN predicted cracking criteria based on fission gas pressurization in the fuel matrix. This figure clearly shows that the maximum cracking criterion achieved in the unrestructured zone at the bottom of the fuel zone was 0.4. This value represents the small intergranular bubbles. This cracking criterion does reach the maximum value at the approximate time that the crumbling was observed. In spite of the present difficulty in predicting the crumbling type of fuel disruption, it is consistent with some of the earlier FD work and some of the DEH experiments. Unfortunately, there are no integral-type experiments that have used a similar power transient and fuel type (burnup and linear heat rating) that can be used for comparison.

In at least one of the FD2/4 experiments (namely the sister experiment FD2.6) a few small pieces of fuel fell out of the fuel column shortly after clad melting and drainage. It

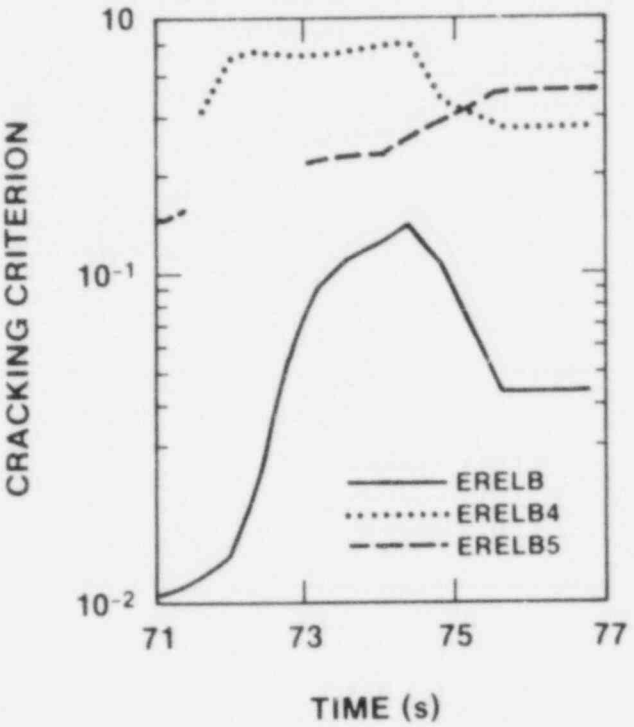

Figure 5.9. SANDPIN Calculated Cracking Criterion for STAR-3

appears that this is what happened in STAR-3 but on a larger scale, since fuel crumbling was observed over the entire length of the fuel pin. This crumbling could have been aided by fuel pin bowing as described later.

Similar fuel breakup behavior was also seen in some of the DEH experiments (DEH-IC). In these experiments the fuel was actually ejected from the fuel column once the cladding had melted and drained away. The power levels at the time of fuel breakup were at or near nominal power. This behavior was correlated with fuel pins having a high cesium content, and it was proposed by Dimelfi (ANL) that cesium pressurization coupled with the sudden removal of the cladding was causing the disruption. As already mentioned, cesium equilibrium pressures in the fuel clad gap are predicted to be 7 to 10 bar. Cesium pressures in the pore volume in the unrestructured zone are even higher (approximately 20 to 100 bar). Thus, it seems feasible that cesium, if not causing the disruption, is at least contributing to it. A simple cesium pressurization model will be included in SANDPIN/CMOT cracking criteria model to see if earlier cracking can be predicted.

Another contributing factor to the crumbling fuel behavior could be significant pin bowing and twisting due to thermal

expansion. This bowing and twisting has also been observed in the TREAT experiments. The outer unrestructured zone of the fuel pin is very brittle and quite weak. Karstens has made fracture measurements of LMFBR fuel pins and concludes that this fuel is already fractured on a microscopic level. External stresses, such as pin bowing, may be sufficient to further crack the fuel so that it has no self-integrity and thus can fall apart once its cladding support is removed.

Another possible contributing factor, as mentioned earlier, is cool-down cracks. The PNL10-60 fuel pin used in this experiment is heavily cracked, especially in the unrestructured zone. If the crumbling is due to the cool-down cracks, then it may be necessary to precondition the fuel prior to the power transient. However, this is not practical in the ACRR. Since the CABRI reactor can pulse from nominal power, this issue could be answered in future CABRI tests.

Most of this discussion has focused on the early crumbling of the fuel. During the later portions of the transient, significant fuel melting occurred. At this time, the entrained fuel changes from angular objects to spheres. Also, early examination of the films indicates that even more fuel sweepout was seen at these times. Thus, the fuel frothing breaks up the outer (still intact) regions of the fuel and causes even more rapid fuel sweepout.

The major events observed in the STAR-3 experiment imply early fuel removal and delayed clad removal. A significant fraction of the irradiated fuel was swept out of the fissile section. Subsequent analysis will be performed to estimate the rate of fuel mass removal, and the final distribution. SIMMER analysis will also be used to examine the fuel relocation behavior since it contains a fluid flow regime that consists of solid particles. In addition, future experiments with similar fuel types and power transients will be performed to understand better the "crumbling" type fuel behavior.

5.2 Transition Phase

(R. O. Gauntt, 6423; P. S. Pickard, 6423; A. Furutani, 6423)

5.2.1 B-Series Experiments

Experiment B-4 will investigate the upward injection of a pure UO_2 melt into a bare clad 5-pin partial LMFBR bundle which has been preheated to 1173 K such that the interface temperature between the clad and the molten UO_2 is above the steel melting point. These conditions are analogous to those employed in the annular channel experiment, B-3. Experiment B-5 also will use a 5-pin bundle but will include a stainless steel wire wrap around the pins. The wire wrap

is expected to greatly enhance the potential for steel entrainment through the vigorous convective action of the flowing melt and possibly alter the freezing process.

Fuel for the loading of experiment B-4 has been received. Work is currently focused upon assembly of the 5-pin freezing channel structure for experiment B-4. In experiment B-4, the entire length of the flow channel (1.3 m) is to be instrumented with 20-mm chromel-alumel thermocouples which will provide a time record of the bulk melt flow up the channel. The initial bulk melt will consist of nearly 300 g of pure UO_2 heated in the double pulse mode to around 3600 K. The double pulse heating is necessary to generate a sufficiently uniform melt temperature with all fuel above the solidus.

The five freezing channel pins will be loaded with ceramic zirconia rather than the alumina inserts which were originally to be used. This is to avoid the formation of a relatively low temperature eutectic between refrozen fuel and exposed alumina, which might complicate the experiment interpretation.

A detailed neutronic analysis of the 3-pin melting configuration in radial-azimuthal geometry is underway to insure that an accurate fission profile is determined. This is necessary in order to reduce the uncertainties in the thermal analysis of the fuel melting pulse design as well as the analysis of the low temperature calorimetry experiment performed to determine the experiment coupling factor. Other factors contributing to uncertainty in coupling factor measurements are fuel thermal conductivity and fuel gap conduction. These are being investigated along with fission profile effects through thermal calculations using the heat conduction code TAC-2D.

5.2.2 Gap Experiment

The annular fuel melting configuration used in the GAP experiment has been analyzed extensively using the TWOTRAN-II neutron transport code. Deficiencies in the geometry description that were discovered in the GAP-1 problem input were corrected, and rerunning the corrected problem yields a coupling factor significantly lower than the original numbers reported for GAP-1 and in line with the measured values for that experiment. From this benchmark, a redesign of the GAP-2 package was begun. By increasing fuel enrichment, increasing neutron moderation to the inner annular fuel surface, thinning the annular fuel thickness, decreasing the fuel density, and decreasing parasitic absorption in steel structures, the predicted coupling factor was increased from the GAP-1 value of about 7 J/g/MJ to a revised value for

GAP-2 of about 11 J/g/MJ. This new design adequately compensates for the decrease in ACRR performance observed with the GAP-1 package. An order is being placed for new fuel based upon this analysis.

5.2.3 TRAN Analysis

The SIMMER-II core disruption code was used to analyze the fuel melting phase of the planned B-4 and B-5 experiments. The unique aspect of these calculations is the prediction of early fuel motion at the time of melt due to the sudden release of trapped porosity gas. A sensitivity study revealed that double-pulsing of the fuel in the melting phase of the experiment tends to minimize the undesired early motion by driving off gas contained in the open fuel porosity. Also determined in the study was the effectiveness of a melt-away base plate at the bottom of the test fuel stack in discouraging early downward fuel motion. A variant of the design studied will be used in the B-4 experiment.

Precalculations using the PLUGM code for the B-4 experiment indicate that a coherent bulk flow of fuel is likely to result through the entire length of the freezing channel without the slug blow-through experienced in the earlier mass-limited TRAN experiments. This is providing that a sufficient fraction of the initial fuel melt can be encouraged to enter the channel section.

6. POSTACCIDENT HEAT REMOVAL

6.1 Debris Bed Coolability

(C. A. Ottinger, 6421; T. R. Schmidt, 6421; A. W. Reed, 6425)

Most of the activity this period centered on satisfying the increased security requirements for experiments involving Category I quantities of special nuclear material, which includes D-13. Extensive security upgrades would be needed at the sodium fill facility in TAIII in order to permit the fuel for D-13 to be present. The decision was made to modify a building within TAV to accommodate the fuel loading and sodium filling operations. This necessitated numerous safety reviews for radiological and fire safety as well as development of facilities for loading the fuel into the experiment, assembly and welding of the containment, and a sodium transfer system for taking high-purity sodium from the sodium fill facility and loading it into the D-13 experiment. The high temperature thermocouples were completed by the manufacturer and received by the laboratory. This completed acquisition of all hardware and instrumentation for the experiment.

The procedures for D-13 have been reviewed and finalized. Inputs have been received from both PNC and Ispra and have been incorporated into the procedures.

The procedures are for the first session only. Procedures for any additional sessions will be determined following the first session.

The first portion of the experiment (startup through packed bed incipient dryout) is similar to the procedures used in D-10, with two exceptions. First, the emphasis in D-13 will be to complete the packed bed incipient dryout investigations prior to any channeling investigations. Second, instead of using helium mass flow as the variable for downward cooling, the temperature measured by the thermocouples below the heat flux plate (C1 and C2) will be varied.

One area of debris coolability modeling which is currently lacking in data is the modeling of steady-state dry zone thickness as a function of power. Such a model, when combined with the knowledge of dry zone conductivity, can yield prediction of the incipient melt power (as opposed to the incipient dryout power) for a bed. Steady-state extended dry zone thickness data can only be obtained with a high-temperature crucible. This data was obtained only in the channeled state for D-10. D-13 offers a new bed morphology regime and the opportunity to investigate dry zone thickness vs. power in both the packed and channeled states.

For this reason, it is very desirable to obtain as much steady-state dry zone thickness data from D-13 as possible before channeling occurs (and possibly causes a permanent bed change). Thus, it is recommended to investigate extended dryout with the limitation that channeling be avoided as long as possible.

In a stratified bed the most important parameter in the channel formation (or bed disruption) is believed to be the thickness of the subcooled zone (assuming the bed porosity and aspect ratio are fixed). This is because as the subcooled zone thickness decreases, the overburden on the boiling zone decreases. In addition, the top of the boiling zone enters regions of smaller and smaller particles, allowing a greater pressure in the vapor to develop because of the capillary forces. The combined effect is to make the subcooled zone thickness a very influential parameter in the channel formation criterion, much more so than specific power.

By the time extended dry zone investigations arise in the D-13 operations, a considerable range of subcooled zone thicknesses will have been achieved. The smallest thickness will probably have occurred at dryout with 600°C bulk sodium and maximum downward cooling. This thickness can be used as a criterion for avoiding channeling during the extended dryout investigations. As long as the subcooled zone thickness is kept greater than this previously determined value, channeling should not occur.

If channeling does occur, the magnitude of the disruption is probably fairly independent of the bed boundary conditions, provided the power is somewhere near the incipient dryout power. This is again because the event will not occur until the subcooled zone thickness achieves a value which is fairly independent of bed boundary conditions. Thus, one should proceed with the largest subcoolings first in the extended dryout investigations (but try to avoid channeling) before the lower subcooling runs so as to maximize the amount of data collected before channeling. One should not expect an undue increase in the expected consequences from such a procedure, if channeling does occur.

Therefore, the extended dryout investigations will be made with a series of small power steps allowing for steady-state at each step and with 350°C bulk sodium and a low (~300°C) heat flux plate temperature before continuing to the investigations with 600°C bulk sodium.

Following the extended dryout studies, the channeling investigations will be made using power ramps of about 0.1 W/g per minute rather than the fast ramps used during D-10 to

avoid a bed disturbance. The high-temperature extended dryout investigations will be performed with a fast power ramp of about 1.0 W/g within 20 seconds.

Preliminary predictions of incipient dryout have been performed as a function of downward cooling using sticking factors of 1.0 and 10.0 as shown in Figure 6.1. The sticking factor is the ratio between the force exerted by the vapor on the solid particles and the buoyant weight of the particles. The sticking factor was estimated to be about 7 for D-10. For the D-13 bed, in a sodium pool at 300°C, channeling will not occur before incipient dryout without some downward cooling. With increasing downward cooling, the thickness of the upper subcooled zone decreases until the vapor pressure is sufficient to displace the particles. At this point, channeling occurs.

For a sticking factor of unity, channel forms between 10 and 20 kW/m^2. The channel depth increases with increasing downward cooling until about 80 kW/m^2. As the downward cooling increases beyond this point, the thickness of the downward boiling zone increases, causing a corresponding decrease in the thickness of the upward boiling zone. This, in turn, causes a decrease in channel depth. At a downward cooling of 400 kW/m^2, the channels are predicted to be 70 mm deep.

For a sticking factor of 10, channeling is predicted to occur between cooling rates of 300 and 400 kW/m^2. At cooling levels below this, the unchanneled bed exhibits dryout levels lower than those of the channeled configuration by as much as a factor of 3. Regardless of the sticking factor, the bed becomes coolable when the downward cooling becomes about 400 kW/m^2. The dryout heat flux at this point should be about 1 MW/m^2, corresponding to about 1.1 W/g of fuel which would be coolable for the decay heat power levels in most accident scenarios.

6.2 Dry Debris Melt Progression

(T. R. Schmidt, 6421; J. E. Kelly, 6425; J. T. Hitchcock, 6427)

The two experiments in the series have been completed. DC-1 was performed in-pile in the ACRR and examined the heat transfer of dry, solid urania particulate as a function of temperature up to melt. The urania debris was then heated until half (~1 kg) of the bed formed a molten pool with an overlying void. This experiment was designed to determine the effective thermal conductivity of dry debris at three temperatures on the approach to melt and then to examine the melt progression, pool formation, and heat transfer during the molten phase of the experiment. This is the first experiment to produce a sizeable molten pool of urania with intrinsic heating and full instrumentation.

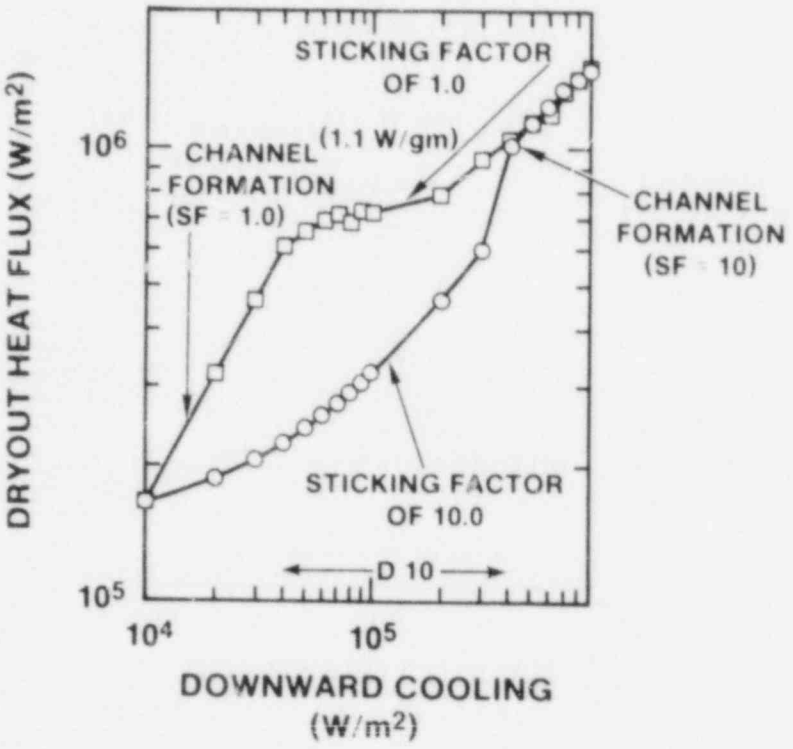

Figure 6.1. D-13 Dryout Predictions. Bulk temperature: 350°C.

The DC-2 experiment investigated a dry debris bed composed of UO_2 and stainless steel. It was top-and bottom-cooled and side-insulated to reduce radial heat losses.

Several steady-state conditions were established spanning the temperature range below melt to obtain data on the bed thermal conductivity. High-temerature data provided unique information on the total effective conductivity in the range where radiative heat transfer dominates. In the second phase of the experiment, the bed was taken into steel melt to observe the agglomeration and migration of steel in a composite bed.

Mechanisms of melt progression and steel migration and agglomeration are being obtained in the posttest microscopic examination of the debris. This work, which is currently in progress, will be used to verify models of material motion during melting. Also, phenomenological understanding will be obtained on how the melt interacts with the solid debris and how voiding and crust formation occurs. Figures 6.2 and

6.3 show the vertical sections of DC-1 and DC-2, respectively. In DC-1 approximately 50 percent of the UO_2 melted and formed a pool of molten material. A dense stable crust formed around the pool by sintering and densification. The crust was a fairly dense lenticular structure with nonconnected porosity. There was then a transition layer between the lenticular structure and the unsintered UO_2 debris. Some areas exhibited a well-defined columnar grain structure, particularly at the sides of the debris in the region of the molten pool surface. This material is not thought to be previously molten material. Also shown in the figure are two ultrasonic thermometers (UTs) and one type-C thermocouple. The thermocouple failed at 2700°C during formation of the molten pool and the UTs worked for 30 min into the molten phase. In the molten zone the sheaths and insulation have been dissolved.

In the DC-2 section, the molten stainless steel is the dark phase material. The heat transfer in the bed was increased substantially (~40 percent) subsequent to steel melting. It was anticipated that significant migration of the steel occurred; however, examination of the debris shows only small agglomerations and no preferential migration. This behavior is markedly different than observed in earlier furnace tests and in the Molten Pool series. It was noted in DC-2 that the UO_2 was well wetted by the molten steel and there was some evidence of urania sintering. These may be the predominant mechanisms for pinning the steel in localized regions. Microscopic analyses will be performed on both experiments.

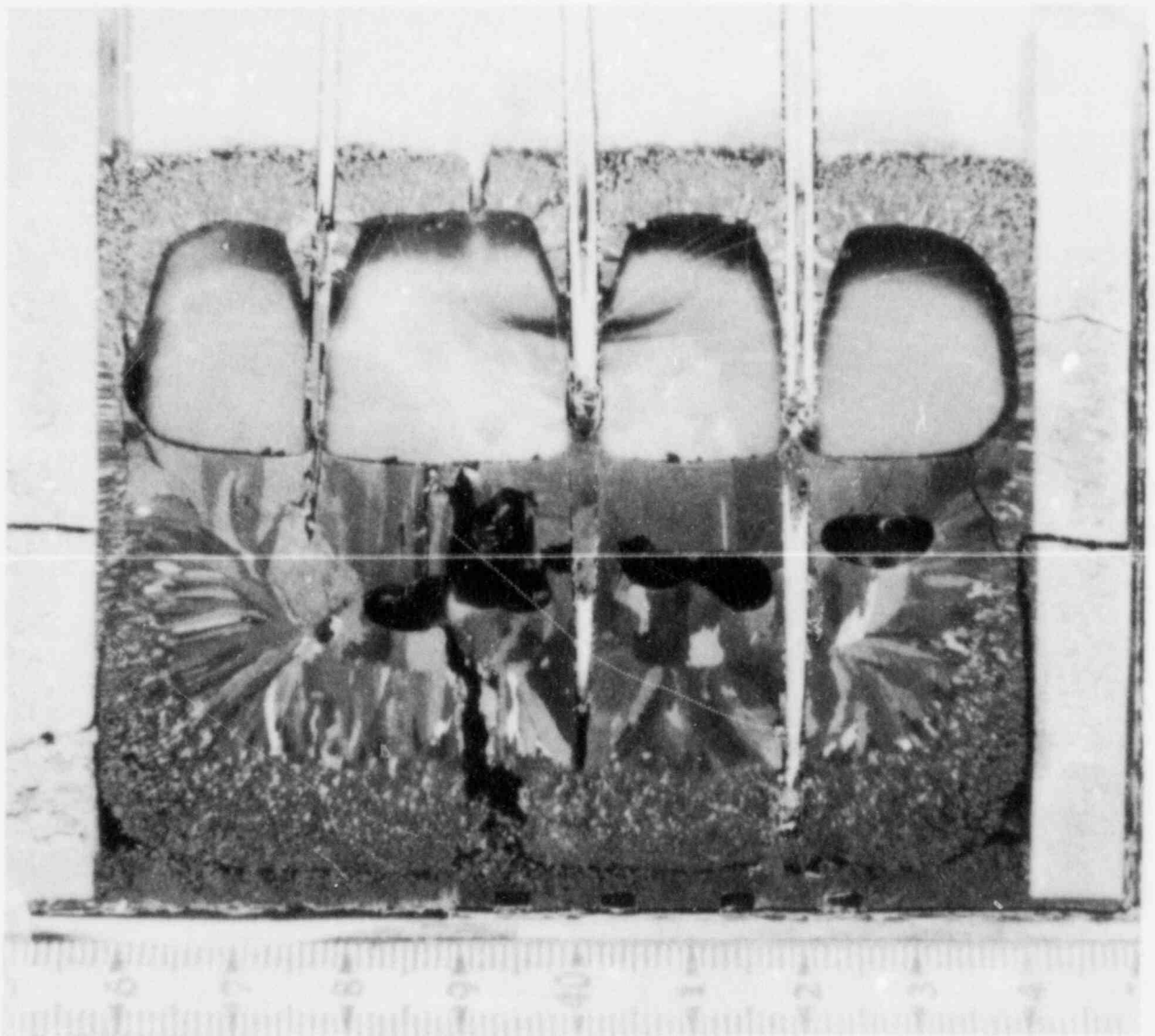

Figure 6.2. DC-1 Vertical Section

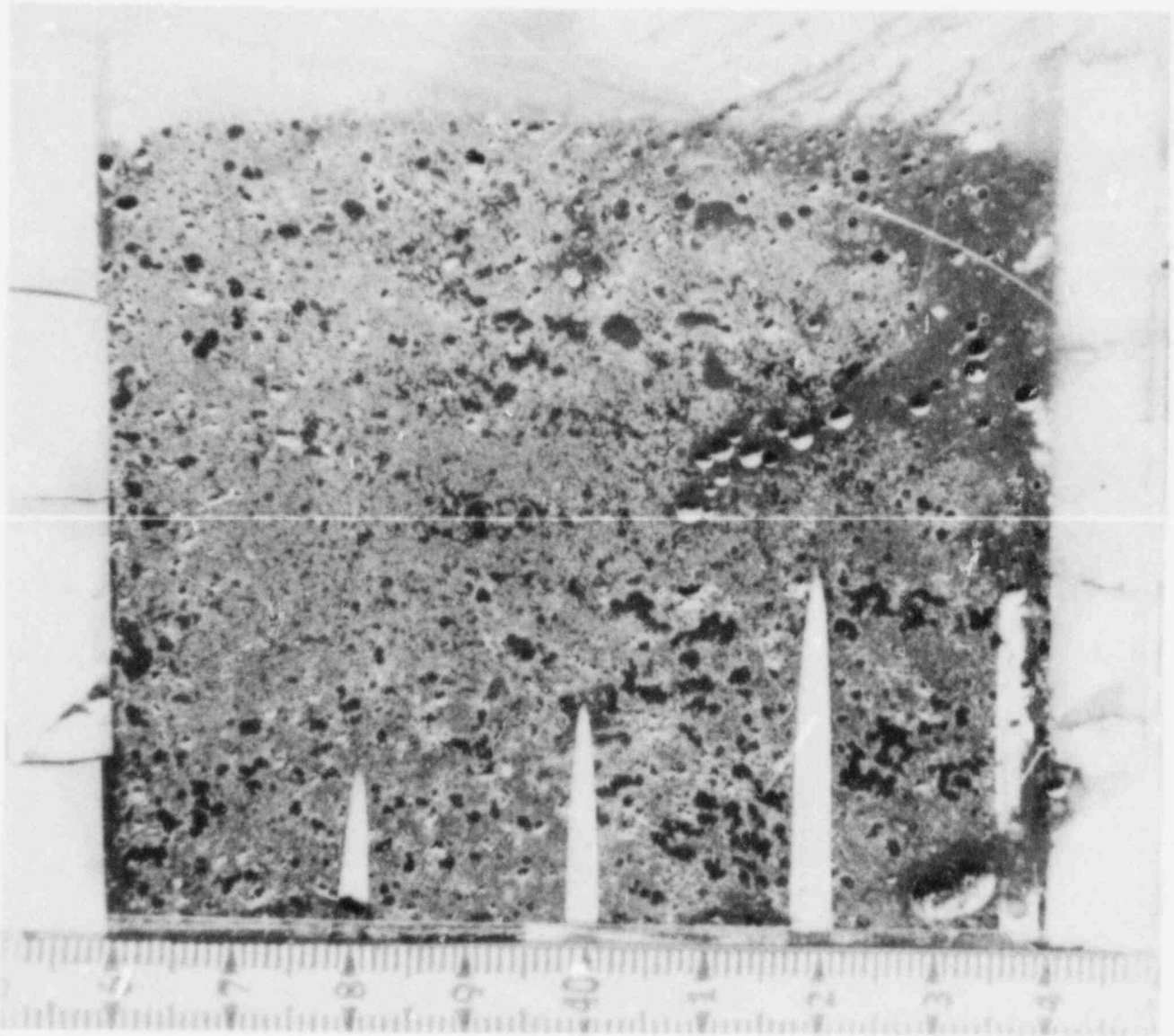

Figure 6.3. DC-2 Vertical Section

DISTRIBUTION:

U.S. Government Printing Office
Receiving Branch (Attn: NRC Stock)
8610 Cherry Lane
Laurel, MD 20707
(330 Copies for R3 and R7)

U.S. Nuclear Regulatory Commission (10)
Division of Accident Evaluation
Office of Nuclear Regulatory Research
Washington, DC 20555
Attn: C. N. Kelber
G. Marino
K. G. Steyer
P. Worthington
R. T. Curtis, Chief
Containment Systems Research Branch
S. B. Burson
Containment Systems Research Branch
M. Silberberg, Chief
Fuel Systems Research Branch
L. Chan
Fuel Systems Research Branch
J. Telford
Fuel Systems Research Branch
R. W. Wright
Fuel Systems Research Branch

U.S. Nuclear Regulatory Commission (12)
Office of Nuclear Reactor Regulation
Washington, DC 20555
Attn: V. Benaroya
W. R. Butler
G. W. Knighton
J. K. Long
J. F. Meyer
R. Palla
K. I. Parczewski
G. Quittschreiber
Z. Rosztoczy
T. M. Su
C. G. Tinkler
D. D. Yue

R. W. Barber
U.S. Department of Energy
Office of Nuclear Safety Coordination
Washington, DC 20545

U.S. Department of Energy (2)
Albuquerque Operations Office
PO Box 5400
Albuquerque, NM 87185
Attn: J. R. Roeder, Director
Transportation Safeguards Division
R. Y. Lowrey, Director
Energy Research Technology Division
For: C. B. Quinn
R. N. Holton

Argonne National Laboratory
9700 South Cass Avenue
Argonne, IL 60439
Attn: H. M. Chung

Battelle Columbus Laboratory
505 King Avenue
Columbus, OH 43201
Attn: R. Denning

Brookhaven National Laboratory (2)
Upton, NY 11973
Attn: R. A. Vari
T. Pratt

Los Alamos National Laboratory
PO Box 1663
Los Alamos, NM 87545
Attn: M. Stevenson

Los Alamos National Laboratory
TD-7 M/S-231
Los Alamos, NM 87545
Attn: Dr. W. Stratton

University of Michigan
Nuclear Engineering Department
Ann Arbor, MI 48104

University of Michigan
Department of Aerospace Engineering
Ann Arbor, MI 47109

Purdue University
School of Nuclear Engineering
West Lafayette, IN 47907
Attn: T. G. Theofanous

McGill University
315 Querbes
Outremont, Quebec
Canada, H2V 3W1
Attn: J. H. S. Lee

Northwestern University
Chemical Engineering Department
Evanston, IL 60201
Attn: S. G. Bankoff

UCLA
Nuclear Energy Laboratory
405 Hilgard Avenue
Los Angeles, CA 90024
Attn: I. Catton

University of Wisconsin
Nuclear Engineering Department
1500 Johnson Drive
Madison, WI 53706
Attn: M. L. Corradini

AEC Ltd. (2)
Whiteshell Nuclear Research
Establishment
Pinawa, Manitoba, Canada
Attn: D. Liu
H. Tamm

Projekt Schneller Brueter (4)
Kernforschungszentrum Karlsruhe GMBH
Postfach 3640
D75 Karlsruhe
Federal Republic of Germany
Attn: Dr. Kessler
Dr. Heusener
Dr. S. Hagen
Dr. J. P. Hosemann

Gesellschaft fur Reaktorsicherheit (GRS)
Postfach 101650
Glockengasse 2
5000 Koeln 1
Federal Republic of Germany

Institute für Kernenergetik
und Energiesysteme (2)
University of Stuttgart
Stuttgart
Federal Republic of Germany
Attn: G. Froehlich
M. Buerger

Battelle Institut E. V.
Am Roemrhof 35
6000 Frankfurt am Main 90
Federal Republic of Germany
Attn: Dr. Werner Baukal

Kraftwerk Union (2)
Hammerbacher Strasse 12 14
Postfach 3220
D-8520 Erlangen 2
Federal Republic of Germany
Attn: Dr. K. Hassman
Dr. M. Peehs

UKEA Safety and Reliability
Directorate (4)
Wigshaw Lane
Culcheth
Warrington WA3 4NE
Cheshire
UK
Attn: J. H. Gittus (2)
J. J. Haynes (2)

AERE Harwell (2)
Didcot
Oxfordshire OX11 ORA
UK
Attn: J. R. Matthews
Theoretical Physics Division

UKEA (2)
Risley
Warrington WA3 6AT
Cheshire
UK
Attn: B. Cowking, FRDD
D. Hicks, TRDD

UKEA, Culham Laboratory
Abingdon
Oxfordshire OX14 3DB
UK
Attn: F. Briscoe

UKEA, AEA Winfrith
Dorset DT2 8DH
UK
Attn: A. Briggs
M. Bird
A. J. Potter
A. Wickett

Simon Engineering Laboratory
University of Manchester
M139PL,
United Kingdom
Attn: Prof. W. B. Hall

National Nuclear Corp. Ltd.
Cambridge Road
Whetestone, Leicester, LE83LH
United Kingdom
Attn: R. Ray

CNEN NUCLIT
Rome, Italy
Attn: A. Morici

Dipartmento Di Costruzioni
Meccaniche E Nucleari
Facolta Di Ingegneria
Via Diotisalvi 2
56100 - Italy
Attn: M. Carcassi

Director of Research, Science Education
CEC
Rue De La Loi 200
1049 Brussels
Belgium
Attn: B. Tolley

Power Reactor Nuclear Fuel Development
Corporation (PNC)
Fast Freeder Reactor Development
Project (FBR)
9-13, 1-Chome, Akasaka
Minato-Ku, Tokyo
Japan
Attn: Dr. Watanabe

Japan Atomic Energy Research Institute
Tokai-mura, Naka-gun, Ibaraki-ken,
319-11
Japan
Attn: Dr. K. Soda
Fuel Reliability Laboratory No. 2

General Electric Corporation
Advanced Reactor Systems Department
PO Box 3508
Sunnyvale, CA 94088
Attn: M. I. Temme, Mgr.
Probabilistic Risk Assessment

General Electric Corporation
175 Curtner Avenue
Mail Code N 1C157
San Jose, CA 95125
Attn: K. W. Holtzclaw

Power Authority State of NY
10 Columbus Circle
New York, NY 10019

Offshore Power System
8000 Arlington Expressway
Box 8000
Jacksonville, FL 32211

Electric Power Research Institute (3)
3412 Hillview Avenue
Palo Alto, CA 94303
Attn: J. J. Haugh
K. A. Nilsson
G. Thomas

Fauske Associates
627 Executive Drive
Willowbrook, IL 60521
Attn: R. Henry

Mississippi Power & Light
PO Box 1640
Jackson, MS 39205
Attn: S. H. Hobbs

Duke Power Co. (2)
PO Box 33189
Charlotte, NC 28242
Attn: F. G. Hudson
A. L. Sudduth

Westinghouse Corporation (3)
PO Box 355
Pittsburgh, PA 15230
Attn: N. Liparulo
J. Olhoeft
V. Sprinivas

General Physics Corporation
1000 Century Plaza
Columbia, MD 21044
Attn: Chester Kupiec

TVA
400 Commerce W9C157-CD
Knoxville, TN 37902
Attn: Wang Lau

EG&G Idaho
Willow Creek Building, W-3
PO Box 1625
Idaho Falls, ID 83415
Attn: Server Sadik

Dr. Roger Strehlow
505 South Pine Street
Champaign, IL 61820

Applied Sciences Association, Inc.
PO Box 2687
Palos Verdes Pen., CA 90274
Attn: D. Swanson

Acurex Corporation
485 Clyde Avenue
Mountain View, CA 94042

Astron
2028 Old Middlefield Way
Mountain View, CA 94043

Bechtel Power Corporation
PO Box 3965
San Francisco, CA 94119
Attn: R. Tosetti

Thompson Associates
639 Massachusetts Avenue
Third Floor
Cambridge, MA 02139
Attn: Timothy Woolf

Factory Mutual Research Corporation
PO Box 688
Norwood, MA 02062
Attn: R. Zalosh

Institute of Nuclear Power Operation
Suite 1500
1100 Circle 75 Parkway
Atlanta, GA 30339
Attn: Henry Piper

Sandia Distribution:
1131 W. B. Benedick
1510 J. W. Nunziato
Attn: 1512 J. C. Cummings
1512 J. E. Shepherd
1513 S. N. Kempka
1513 A. C. Ratzel
1530 L. W. Davison
Attn: 1534 J. R. Asay
1541 H. C. Hardee
1830 M. J. Davis
1840 R. J. Eagan
Attn: 1846 R. A. Sallach
1846 R. K. Quinn
3141 C. M. Ostrander (5)
3151 W. L. Garner
6400 A. W. Snyder
6410 J. W. Hickman
6411 A. Benjamin
6412 A. L. Camp
6420 J. V. Walker (2)
6420 D. B. Hente
6421 T. R. Schmidt
6422 D. A. Powers
6422 J. E. Brockmann
6422 R. M. Elrick
6422 J. E. Gronager
6422 W. W. Tarbell
6423 P. S. Pickard
6423 A. Furutani
6423 R. O. Gauntt
6423 A. C. Marshall
6423 K. Muramatsu
6423 S. A. Wright
6425 W. J. Camp
6425 D. R. Bradley
6425 W. Frid
6425 J. E. Kelly
6425 A. W. Reed
6425 M. F. Young
6427 M. Berman
6427 J. T. Hitchcock
6427 M. S. Krein
6427 B. W. Marshall, Jr.
6427 L. S. Nelson
6427 M. P. Sherman
6427 S. R. Tieszen
6427 C. C. Wong
6440 D. A. Dahlgren
6449 K. D. Bergeron
6450 J. A. Reuscher
Attn: 6451 T. F. Luera
6452 M. Aker
6454 G. L. Cano

7530 T. B. Lane (1)
Attn: 7537 N. R. Keltner
7537 R. U. Acton
7537 T. Y. Chu
7550 T. S. Edrington
Attn: 7551 O. J. Burchett
7552 J. H. Gieske
8024 M. A. Pound

NRC FORM 335 (2 84) NRCM 1102, 3201, 3202

U.S. NUCLEAR REGULATORY COMMISSION

BIBLIOGRAPHIC DATA SHEET

SEE INSTRUCTIONS ON THE REVERSE

1. REPORT NUMBER (Assigned by TIDC add Vol. No., if any)

NUREG/CR-3816 (4of4)
SAND84-1072 (4of4)

2. TITLE AND SUBTITLE

REACTOR SAFETY RESEARCH QUARTERLY REPORT
October-December 1984

3. LEAVE BLANK

4. DATE REPORT COMPLETED

MONTH: May YEAR: 1985

5. AUTHOR(S)

Reactor Safety Research Department
Sandia National Laboratories

6. DATE REPORT ISSUED

MONTH: August YEAR: 1985

7. PERFORMING ORGANIZATION NAME AND MAILING ADDRESS (Include Zip Code)

Sandia National Laboratories
Albuquerque, NM 87185

8. PROJECT/TASK/WORK UNIT NUMBER

9. FIN OR GRANT NUMBER

A-1016 etc.

10. SPONSORING ORGANIZATION NAME AND MAILING ADDRESS (Include Zip Code)

U. S. Nuclear Regulatory Commission
Washington, DC 20555

11a. TYPE OF REPORT

progress-technical

b. PERIOD COVERED (Inclusive dates)

October-December 1984

12. SUPPLEMENTARY NOTES

13. ABSTRACT (200 words or less)

Sandia National Laboratories is conducting, under the USNRC's sponsorship, phenomenological research related to the safety of commercial nuclear power reactors. The research includes experiments to simulate the phenomenology of the accident conditions and the development of analytical models, verified by experiment, which can be used to predict reactor and safety systems perfomance and behavior under abnnormal conditions. The objective of this work is to provide NRC requisite data bases and analytical methods to (1) identify and define safety issues, (2) understand the progression of risk-significant accident sequences, and (3) conduct safety assessments. The collective NRC-sponsored effort at Sandia National Laboratories is directed at enhancing the technology base supporting licensing decisions.

14. DOCUMENT ANALYSIS - a. KEYWORDS/DESCRIPTORS

b. IDENTIFIERS/OPEN-ENDED TERMS

15. AVAILABILITY STATEMENT

u

16. SECURITY CLASSIFICATION

(This page) u

(This report) u

17. NUMBER OF PAGES

18. PRICE

☆ U.S. Government Printing Office 1985-576-051/21,001